POLITECNICO DI MILANO
DIPARTIMENTO DI MATEMATICA
F. BRIOSCHI
DOCTORAL PROGRAMME IN MATHEMATICAL MODELS AND METHODS IN ENGINEERING

FEM FOR PDES WITH UNFITTED INTERFACES: APPLICATION TO FLOW THROUGH HETEROGENEOUS MEDIA AND MICROCIRCULATION

Doctoral Dissertation of:
Laura Cattaneo

Supervisor:
Prof. Paolo Zunino

Co-Advisor:
Prof. Davide Ambrosi

Tutor:
Prof. Davide Ambrosi

The Chair of the Doctoral Program:
Prof. Roberto Lucchetti

2014 – XXVI Cycle

A Filippo

Acknowledgments

At first, I would like to thank Prof. Paolo Zunino, who gives me the great opportunity of working with him.
During these years, he has continuously stimulated my research towards new directions, providing new suggestions and ideas. He has always encouraged me to analyze in a rigorous way every problem, trying to find the best solution. I would like also to thank him for the terrific opportunity he gives me to spend some months in Pittsburgh. It was a really great experience! Thanks Paolo!!

I am very grateful to Prof. Davide Ambrosi for his precious advices and for his guidelines and to Dr. Carlo D'Angelo for the precious support to initiate this work.

I would like to thank my reviewers: Prof. Riccardo Sacco and Prof. Christian Vergara for the many observations and stimulating remarks.

Thanks to Prof. Alfio Quarteroni and Prof. Luca Formaggia. The MOX family is a great family thanks to your precious job!

I acknowledge the European Research Council Advanced Grant Mathcard, Mathematical Modelling and Simulation of the Cardiovascular System, which supports my work.

I was really really lucky, since I spend these three years with the best group possible! I thank my friends Nadia, Paolo, Andrea, who have these days so funny!!
Special thanks to my 'Pranzo al Poli' group: Matteo, Matteo, Elena, Elena, Simone, Alessandro, Susanna, Ilario, Chiara. You are very special friends! I love you!
In particular, thanks to 'zia' Elena, who shares with me every new event of my life, especially the most important!!
Thanks to Raimondo, who is the greatest PhD student I know. It was a pleasure to spend time together!!
Thanks to all my MOX friends and collegues: Simone, Michele, Marco, Viola, Simone, Guido, Elisabetta, Franco, Laura, Alessia, Anna . . . and all the others! You are all smart and fantastic people!

Thanks to Claudia . . . even if we are far, you always are my biggest support and irreplaceable friend! And thanks also to the others Lausanne friends, especially to Matteo. Thanks to Rana, who made my Pittsburgh days funny and gave me the opportunity to know a different culture and to create a very special friendship!

Thanks to all my old friends, who always walk by my side: Sara, Greta, Laura, Ciolly, Maddy, Francy, Tia, Roby, Cecio, Pech, Mauri and so on . . .
Thanks to Meri, we made beautiful trips on the train and also great breakfasts! . . . Beautiful and great as our friendship!

Finally I would like to thank my 'old' family, my mother, my father and my sister Alice and my 'new' family, I mean, my husband Mauro, for their support and their so precious love. I love you too.
But a very very special thanks to my new life, who is just coming . . . Filippo, this work is dedicated to you. Thanks to stay with me and live with me this really special part of my life. I love you, now and ever.

Abstract

In this thesis we will focus on the modeling of fluid flows and mass transport in different kinds of heterogeneous media, where there exists thin structures embedded in the considered domain.
In particular, we will investigate multidomain problems with homogeneous and heterogeneous dimensionality. On one hand we will study a problem characterized by two regions of the same dimensionality separated by an interface. On the other hand, we will focus on a problem where a one dimensional structure is completely embedded into a three dimensional one. In both situations, the different parts of the system feature different physical properties, therefore the solutions of problems obtained through mathematical modeling, involve discontinuities, singularities or high gradients.
The first problem has many geophysical applications, such as groundwater flows or two-phase flows. The second one describes the exchange of fluid and mass between microvessels and interstitial tissue.
The aim of this work is to study and develop numerical methods characterized by the use of computational meshes that do not fit the geometry of the embedded structures.
In particular, in the first part of the work, we analyze the eXtended finite element method (XFEM) to solve elliptic and saddle point contrast problems. Then, in the second part, we study tissue perfusion and biochemical transport in vascularized tumor tissue. The latter problem is addressed using a new approach, called the Embedded Multiscale method.
Both numerical methods allow to discretize the external domain independently of the internal structure.

Contents

Introduction

Mathematical models and numerical methods have emerged as fundamental tools in the investigation of life sciences. In the real world many problems, that we want to describe through mathematical models, are characterized by field quantities that change rapidly over length scales that are small with respect to the observed domain. These kind of problems arise from different fields, such as geosciences, nanotechnologies, bioengineering and systems biology.

For example, in plate tectonics and basin evolution, mantles, plates and sedimentary layers can be modeled as heterogeneous viscous fluids, featuring non standard frictional interactions at their interfaces. Again, many geophysical applications, such as groundwater flows or two-phase flows for oil migration, are characterized by the presence of strong heterogeneities of the model parameters and the permeability of the considered medium (the ground, or, at a larger scale, a geological basin) may easily span several orders of magnitude.

In many bioengineering studies, in order to handle the heterogeneous coupling between blood flow and plasma filtration, we need to develop numerical models capable to deal with extremely variable parameters, such as the blood viscosity and Darcy's permeability of the arterial walls and the external tissue.

The heterogeneities that characterize these systems are described also by the geometry of the systems themselves. Indeed the different layers of a basin are separated by fractures or interfaces and, in a similar way, the vessels walls separate the blood system from the external tissue.

Therefore, in order to predict in a proper way the model results, it is needed to well describe both the physical and the geometrical properties of the system.

At the same time, the geometrical description could be too difficult, so it is very important to find a correct trade off between the accurate description of the included structures and the reduction of the geometrical complexity of the system. On one hand it is fundamental to use real geometries for the computational modeling, since they allow for an accurate description of the non-smooth behavior of the system. In this direction, for example, the enormous development of clinical imaging such as magnetic resonance or computed tomography opens a new way toward a detailed patient-specific description of the actual geometry. On the other hand it could be computational too expensive to

describe in details the embedded structures because at the level of the numerical solver, we may have to use refined meshes or graded meshes.
For all these reasons, it is fundamental to study and develop reduced numerical models able to simplify the geometrical complexity without loss of information.

In this thesis we will focus on the mathematical and numerical modeling of partial differential equations with unfitted interfaces.
On one hand we will study multidomain problems with homogeneous dimensionality, i.e. problems characterized by two means of the same dimension separated with one another through an interface.
On the other hand, we will focus on multidomain problems with heterogeneous dimensionality, that is the case where a one dimensional structure is completely embedded into a three dimensional structure.
In both situations, the different parts of the system feature different physical properties and, depending on the problem, the solution involves discontinuities, singularities or high gradients.
As anticipated, the common strategy to solve both kinds of problems plans to *develop numerical models characterized by the use of computational meshes that do not fit the geometry of the embedded structures*. The discretization of the external domain and the discretization of the internal structure are therefore *completely independent*.

The thesis is divided in two parts, each of which is focused on the study of a different model problem.

The first part of this thesis is focused on multidomain problems with homogeneous dimensionality. We study contrast problems, which is the case where different means of the same dimensions are separated by an interface.
To solve these kind of problems we apply the *eXtended Finite Element Method*, (XFEM), that is based on the local enrichment of the approximation space of the classical FEM, such that the non-smooth solution properties are accounted for correctly, independently of the mesh.

In the *first chapter* of the thesis we start with the approximation of diffusion-reaction equations, where two different domains are separated by a planar interface, [118].
In order to improve the unsatisfactory behavior of Lagrangian elements for this kind of contrast problem, we enrich the approximation space, involving all the elements cutted by the interface and we combine this enrichment with a Nitsche's technique to enforce the interface matching conditions. Firstly, we analyze the H^1-stability of the finite element space with respect to the position of the interface. This analysis, applied to the conditioning of the discrete system of equations, shows that the scheme may be ill posed for some configurations of the interface. Secondly, we propose a stabilization strategy, based on a scaling technique, which restores the standard properties of a Lagrangian finite element space and results to be very easily implemented. We also address the behavior of the scheme with respect to large contrast problems ending up with a choice of Nitsche's penalty terms such that the extended finite element scheme with penalty is robust for the worst case among small sub-elements and large contrast

problems.

In the *second chapter* we will address a two-phase Stokes problem, namely the coupling of two fluids with different kinematic viscosities, where the domain is crossed by an interface corresponding to the surface separating the two fluids, [26].
We observe that the interface conditions allow the pressure and the velocity gradients to be discontinuous across the interface. XFEM is applied to accommodate the weak discontinuity of the velocity field across the interface and the jump in pressure. Numerical evidences show that the discrete pressure approximation may be unstable in the neighborhood of the interface, even though the spatial approximation is based on *inf-sup* stable finite elements. Clearly, XFEM enrichment locally violates the satisfaction of the stability condition for mixed problems. For this reason, resorting to some pressure stabilization technique in the region of elements cut by the unfitted interface is recommended. In particular we consider the application of stabilized equal order pressure / velocity XFEM discretizations and we analyze their approximation properties. On one side, this strategy increases the flexibility on the choice of velocity and pressure approximation spaces. On the other side, some pressure stabilization operators, such as local pressure projection methods or the Brezzi-Pitkaranta scheme, seem to be effective to cure the additional source of instability arising from the XFEM approximation. These operators could be applied *locally*, namely only in proximity of the interface. We perform some numerical results and we conclude the chapter discussing some benchmark cases, in order to thoroughly compare the performance of different variants of the method.

The second part of the thesis is focused on multidomain problems with heterogeneous dimensionality. We develop a multiscale method to study blood flow and transport phenomena in living tissues, applying a special coupling between a microcirculation network surrounded by a permeable medium.
We use the *Immersed Boundary (IB) method* developed in [32] to couple the one-dimensional with the three-dimensional flow through the network and the interstitial volume, respectively. The main idea consists in replacing the immersed three dimensional network with an equivalent concentrated source term. In this way we facilitate the analysis of complex capillary bed configurations and we end up with an heterogeneous system characterized by one dimensional channels embedded into a porous medium. The main methodological and theoretical aspects of the method have already been addressed in the works by Carlo D'Angelo [32–34].
The resulting numerical method is characterized by the fact that the partitions into elements of the one dimensional network and the three dimensional tissue are completely independent.

The aim of the *third chapter* is to develop a computational model able to capture the interplay between microcirculation and interstitial flow, [28].
Such phenomena are at the basis of the exchange of nutrients, wastes and pharmacological agents between the cardiovascular system and the organs. We develop a model applicable at the microscopic scale, where the capillaries and the interstitial volume can be described as independent structures capable to propagate flow. After discussing the

details for the implementation of a computational solver, we apply it to compare flow within healthy and tumor tissue samples.

The objective of the *fourth chapter* is to derive a new pharmacokinetic model to study the delivery of drugs to tumors, in particular we want to perform a comparative computational study testing vascular targeting of tumors using drug delivery from bolus and nanoparticle injection, [27].
Starting from the fundamental laws of filtration and transport in biological tissues, we develop a mathematical model able to capture the interplay between blood perfusion, fluid exchange with the interstitial volume, mass transport in the capillary bed, through the capillary walls and into the surrounding tissue. These phenomena are accounted at the microscale level, where the capillary bed and the interstitial volume are viewed as two separate regions. The capillary bed is described as a network of vessels carrying blood flow.
We apply the model to study drug delivery to tumors. Owing to its general foundations, the model can be adapted to describe and compare various treatment options. In particular, we consider drug delivery from bolus injection and from nanoparticles, which are in turn injected into the blood stream. The computational approach is prone to perform a systematic quantification of the treatment performance, enabling the analysis of interstitial drug concentration levels, drug metabolization rates, cell surviving fractions and the corresponding timecourses. This study shows that for the treatment based on bolus injection, the drug dose is not optimally delivered to the tumor interstitial volume. Using nanoparticles as intermediate drug carriers overrides the shortcomings of the previous delivery approach.
The present work shows that the proposed theoretical and computational framework represents a promising tool to compare the efficacy of different treatments of cancer based on chemotherapy. Being directly derived from the fundamental laws of flow and transport, the model may be also adapted to study different types of cancer, provided that suitable metrics are available to quantify the transport properties of a specific tumor mass. The generality of the theoretical framework also enables the extension to different delivery platforms, such as liposomes.

CHAPTER 1

Multiscale models for fluid flow in porous media

In the real world we find a huge number of examples in which fields quantities change rapidly over length scales that are small with respect to the observed domain. The solutions of these phenomena, obtained through mathematical modeling, involve discontinuities, singularities or high gradients.
The first objective of this work is modeling fluid flows and mass transport in heterogeneous media or fractured domain, where there exists thin planar fractures or vessels embedded in the considered domain. When the dimensional gap between the three dimensional domain space and the manifold representing the fracture or the vessels is high, for instance when the fractures are thin tubes, the solution may be strongly singular on the fracture.
Reduced models of this kind have an high interest due to their potential applications in different fields, and have been studied in some works, see for example [75] and references therein.
Typically we consider an heterogenous N-dimensional domain, made of regions featuring different characteristic, such as, for example, permeabilities. These heterogeneities should be clearly distinct, since two or more separated regions of the domain are characterized by different properties. Otherwise smaller inclusions have the dimension of pores and they are dispersed in the domain, forming the so called porous medium. In the first case, the regions are separate by inclusions, fractures or simple interfaces. In the second case the porous medium is even crossed by fractures or vessels, forming a very complex structure.
In our work we will investigate both possibilities, studying two different kinds of problems: on one hand we investigate the situation in which two different media, in particular two fluids, are separate by a thin interface. On the other hand we study the case of a porous domain, representing a portion of tissue, spanned by a complex network

of vessels. In both these two cases we want to apply suitable reduced models, in order to simplify the numerical solution. Indeed the numerical approximation might require excessive mesh refining and increasing computational costs, if it wants to take into account for the presence of fractures and vessels as N-dimensional regions. To apply reduced models, the transverse dimension of interfaces or vessels should be negligible when compared to the dimension of the considered domain. In particular, we implement reduced model in which fractures are represented as N-1 manifolds and vessel are represented as N-2 manifolds in a N=3-dimensional region, as depicted in figure 1.1.

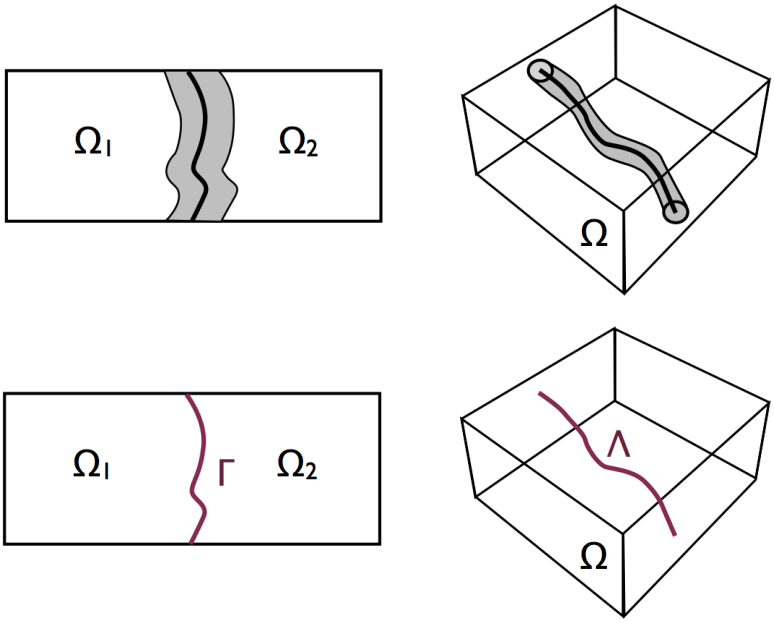

Figure 1.1: *On the top: reference geometries for the problem considered. On the right, a 2D fracture in a 2D domain. On the left, a 3D vessel in a 3D domain. On the bottom: reduced models, both fracture and vessel are in this case represented as 1D manifold.*

We will make a clear distinction between these two kind of problems. Indeed, in the first case we are actually considering the fracture as a simple interface of dimension $N-1$, which separates two different media of dimension N. The presence of the interface allows for special coupling conditions between the different parts of the domain. These conditions are required to close the problem. This model problem has applications in many fields, like for example geophysics or hydrogeology but we will apply it to describe two-phase flows, through Stokes equations.
The second problem describes tissue perfusion and transport of nutrients from capillary vessels to cells. We address the coupling of a Darcy model for fluid flow in a porous domain, with a Navier-Stokes model of fluid flow within the vessels embedded in the domain. In this case the coupling is between the embedded $N-2$ dimension structure and the external N dimension domain.
The solutions of these reduced problems are characterized by discontinuities and singularities. In particular the interface problem is handled with a *weak* discontinuity, while the solution of the Darcy equations in the porous domain is singular on the vessels net-

work.

Beyond the first objective of this work, the second big aim is to find a strategy to approximate the solution of these problems on a computational mesh that does not fit the geometry of the 2D-1D manifolds, as reported in Figure 1.2. This means that we want to study and develop numerical methods able to solve both the problems in such a way that the discretization of the external domain and the discretization of interfaces and vessels are *completely independent*.

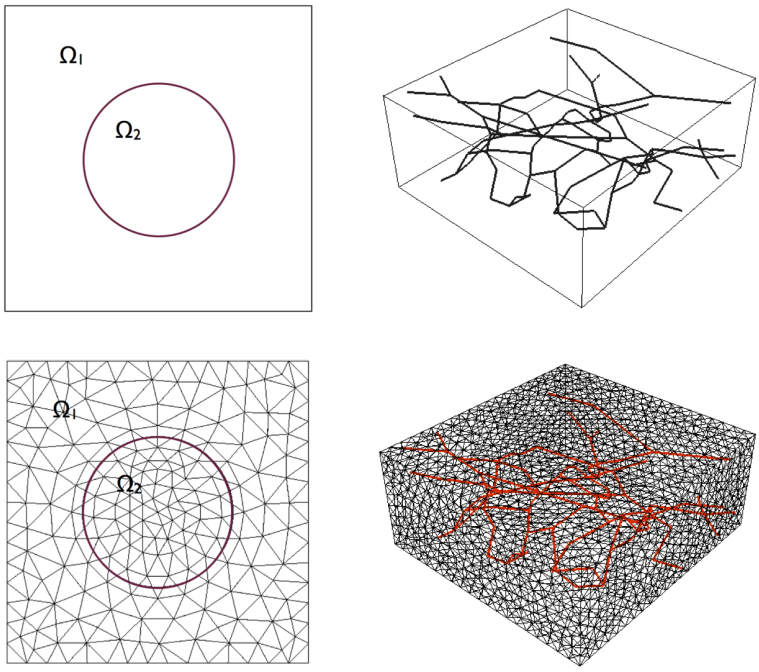

Figure 1.2: *On the top: reduced model geometries. On the bottom: computational meshes do not fit the geometry of the manifolds.*

1.1 Multidomain problems with homogeneous dimensionality

We consider a model problem characterized by two or more means separated with one another through interfaces. This is the case of several situations, such as multiphase and free surface flows, possibly extended to multi-physics environments, by including heat or mass transport problems and reaction phenomena. For this reason, it is prone to embrace a wide spectrum of complex physical problems and related models. In this context, challenging applications emerge from geosciences. In plate tectonics and basin evolution, mantles, plates and sedimentary layers can be modeled as heterogeneous viscous fluids, featuring non standard fractional interactions at their interfaces. As an example, the evolution of sedimentary basins can be modeled as a stratified creeping flow. Obviously the more interesting situation is solving time dependent or non-linear problems where the interface moves with time or during iteration.
To introduce the reduced model problem we start from a simple case, that is the sta-

tionary heat conduction problem with contrast between coefficients across a smooth internal interface.
In the sequel we consider a bounded convex polygonal domain $\Omega \cup \mathbb{R}^d$ with $d = 1, 2$ space dimensions, we define its boundary $\partial\Omega$ and we denote with Γ an internal interface of dimension $d-1$, separating Ω into two subregions Ω_1 and Ω_2, as reported in figure 1.1 for the particular case of $d = 2$. Let $\mathbf{n}$ be a fixed unit normal vector on Γ. For the sake of simplicity, we assume that Γ is either a piecewise linear curve for $d = 2$ or a connected collection of planar surfaces for $d = 3$. On each subregion Ω_i with $i = 1, 2$, we denote by ϵ_i the diffusion coefficients, with the assumptions that there exists $\underline{\epsilon} > 0$ such that $\epsilon_i \geq \underline{\epsilon}$. We aim to approximate the solution u_i of the following problem:

$$\begin{cases} -\nabla \cdot (\epsilon_i \nabla u_i) = f_i & \text{in } \Omega_i \\ u_i = 0 & \text{on } \partial\Omega \cap \partial\Omega_i \\ u_1 = u_2 & \text{on } \Gamma \\ \epsilon_1 \partial_n u_1 = \epsilon_2 \partial_n u_2 & \text{on } \Gamma \end{cases} \tag{1.1}$$

where $\partial_n u$ denotes $\nabla u \cdot \mathbf{n}$. The first coupling condition ensures the continuity of the solution through the interface Γ, i.e. $u_1 = u_2$. The second one ensures the continuity of the flux, but since $\epsilon_1 \neq \epsilon_2$, the solution features a jump in its gradient. This type of singularity is usually called a weak discontinuity.
Starting from this model problem, we are particularly interested in studying coupled heterogeneous problems with large contrast between coefficients. In particular we focus on symmetric elliptic equations with large contrast between diffusion coefficients. Then, we analyze the approximation of saddle point problem, in particular we address a two-phase Stokes problem, namely the coupling of two fluids with different kinematic viscosities. In both cases, we will combine the Nitsche's method for weakly enforcing interface conditions, originally proposed in [87], with piecewise linear finite elements, which are locally enriched to capture a weak discontinuity of the solution. The first part of the thesis is clearly more focused on the numerical analysis of such methods, as we aim to develop suitable finite element schemes that are robust with respect to the heterogeneity of the coefficients.
We will explain the variational scheme with more details in chapter 2, while in the next section of this chapter we will present the local enrichment of the basis function.

1.2 Multidomain problems with heterogeneous dimensionality

We fix a domain Ω composed two parts, Ω_v and Ω_t, the capillary bed and the tissue interstitium respectively, both of them having dimension $d = 3$. Assuming that the capillaries can be described as cylindrical vessels, we denote with Γ the outer surface of Ω_v, with R its radius and with Λ the centerline of the capillary network. Figure 1.3 shows a description of the geometrical model. We consider R constant and any physical quantity of interest, such as the blood pressure p and the blood velocity $\mathbf{u}$, is a function of space $\mathbf{x} \in \Omega$ and time t. These quantities obey different balance laws, depending on the portion of the domain of interest and, in general, they are not continuous at the interface between subdomains. We consider the tissue interstitium Ω_t as an isotropic porous medium, such as the Darcy's law applies, while we start assuming a Newtonian

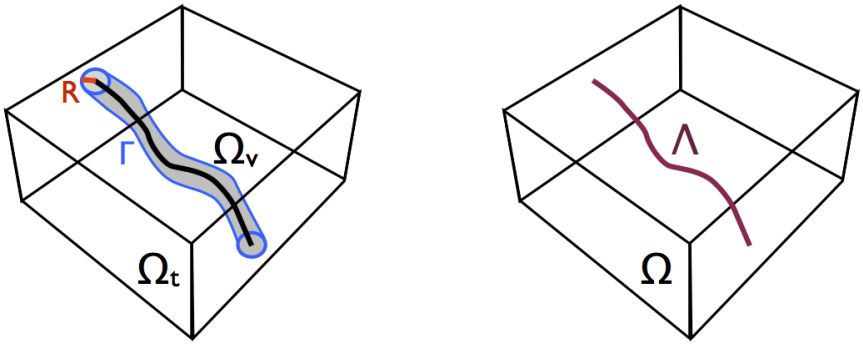

Figure 1.3: *On the left: description of the interstitial tissue with embedded capillary network. On the right: reduction from three-dimensional to one-dimensional description of capillary vessels.*

model for the blood flow in the capillaries. As a consequence of all these modelling assumptions, the fluid problem in the entire domain Ω reads as follows:

$$\begin{cases} \nabla \cdot \mathbf{u}_t = 0 & \text{in } \Omega_t \\ \mathbf{u}_t = -\dfrac{k}{\mu}\nabla p_t & \text{in } \Omega_t \\ \rho\dfrac{\partial \mathbf{u}_v}{\partial t} + \rho(\mathbf{u}_v \cdot \nabla)\mathbf{u}_v = -\nabla p_v + \mu\Delta \mathbf{u}_v & \text{in } \Omega_v \\ \nabla \cdot \mathbf{u}_v = 0 & \text{in } \Omega_v \end{cases} \tag{1.2}$$

where μ and k denote the dynamic blood viscosity and the constant tissue permeability, respectively, and ρ is the blood density. At the interface $\Gamma = \partial\Omega_v \cap \partial\Omega_t$ we impose continuity of the flow:

$$\mathbf{u}_v \cdot \mathbf{n} = \mathbf{u}_t \cdot \mathbf{n} = L_p(p_v - p_t) \quad \mathbf{u}_t \cdot \boldsymbol{\tau} = 0, \quad \text{on } \Gamma \tag{1.3}$$

where $\mathbf{n}$ is the outward unit vector normal to the capillary surface. The fluid flux across the capillary wall is obtained in this simple example on the basis of the Starling law and L_p represents the hydraulic conductivity of the vessel wall.

Starting from this model problem we will apply a reduced method, which allows us to describe the $3D$ embedded network as a $1D$ manifold, as depicted in figure 1.3. This method, called Immersed Boundary method, makes use of average operations to transfer the coupling informations from the vessels interface Γ to the 1D manifold Λ. The resulting $3D$ model is characterized by a solution that features a strong singularity where the tissue is crossed by the $1D$ manifold.

1.2.1 The Immersed Boundary method

The immersed boundary method was originally developed by Charles S. Peskin [90] with the aim of improve the computer simulation of fluid-structure interaction, especially to study biological fluid dynamics with a particular attention for flow patterns around heart valves. Afterwards the idea has been modified and improved by Wing

Kam Liu et al., [77, 78, 115], where, starting from the immersed boundary method, they propose different variations of it, such as the immersed finite element method or the extended immersed boundary method (EIBM) [114]. Also these alternative methods are proposed for the solution of complex fluid and deformable structure interaction problems. For example, in the immersed finite element the Dirac function is replaced by the reproducing kernel particle method (RKPM) delta function, which ensure the continuity between the fluid and solid sub-domains.
The idea of coupling two different structures with a Dirac delta function was then taken by Carlo D'Angelo et al., [32–34]. In particular they use the original idea of Peskin to study a different kind of problems, i.e. no more fluid-structure interaction problems, but elliptic problems in fractured domains, where the coupling terms are seen as Dirac measures concentrated on the fractures. In particular in these works they consider the coupling between two diffusion-reaction problems, one taking place in a three-dimensional domain and the other in a one-dimensional subdomain. This coupled problem wants to represent the simplest model of fluid flow in a three-dimensional porous medium featuring fractures that can be described by one-dimensional manifolds. The mass conservation that should be guaranteed at the interface between the porous medium and the one dimensional manifold has to be taken into account by means of a measure term in the 3D equation. In particular, the 3D solution is singular on the one dimensional network, [34].
We will apply this model to reduce the system of equations (1.2), describing the multiscale analysis of blood flow through tissues. We detail the procedure to couple the blood flow and the tissue perfusion through the Dirac delta source term in Chapter 4. In the following we report the resulting coupled problem for microcirculation and interstitial flow which consists to find the pressure fields p_t, p_v and the velocity fields $\mathbf{u}_t$, $\mathbf{u}_v$ such that

$$\begin{cases} -\nabla \cdot \left(\dfrac{k}{\mu}\nabla p_t\right) - |\gamma(s)| f(\overline{p}_{t/v})\delta_\Lambda = 0, & \text{in } \Omega \\ \mathbf{u}_t = -\dfrac{k}{\mu}\nabla p_t & \text{in } \Omega \\ -\dfrac{\pi R^4}{8\mu}\dfrac{\partial^2 p_v}{\partial s^2} + |\gamma(s)| f(\overline{p}_{t/v}) = 0, & s \in \Lambda \\ \mathbf{u}_v = -\dfrac{R^2}{8\mu}\dfrac{\partial p_v}{\partial s}\boldsymbol{\lambda} & s \in \Lambda \end{cases} \tag{1.4}$$

where the term $|\gamma(s)| f(\overline{p}_{t/v})$ is taking into account for the flux released by the actual interface Γ and we denote with $\boldsymbol{\lambda}$ an arbitrary orientation that defines the increasing direction of the arc length along the network Λ.
The full Navier-Stokes equations is replaced by a one-dimensional model for blood flow and transport in the capillary system. We observe that the source term in the tissue equation is actually a Dirac measure. Therefore the solution p_t is characterized by a strong singularity on the vessels network.
We will apply the immersed boundary method both to study tissue perfusion and mass delivery in vascularized tumor tissue. The second part of the thesis is therefore more focused on the application of such method on new and challenging biomedical prob-

lems.

1.3 Numerical approximation of interface problems on unfitted meshes

The problems that we have previously introduced handle with non-smooth solutions, characterized by discontinuities and singularities. For the numerical approximation of these kind of solutions there exist two different approaches, [57]:

- the first strategy involves meshes that *conform* the discontinuities and are refined near singularities and high gradients. In particular, if we want to study the evolution of such phenomena, we need to reconstruct and refine the mesh at each time step.
- the second choice is to find a strategy able to model the non-smooth solutions *independently* of the domain mesh.

In this work we study and analyze two numerical methods that belong to the second category.
We apply the **eXtended Finite Element Method** (XFEM) to solve the interface problem.
Regarding the vessels transport problem, we construct two independent meshes to describe separately the tissue domain and the 1D vessels network. Then we need to construct suitable interpolation operators in order to compute the averaged quantities that appear in the reduced model (1.4). We detail now these two numerical methods.

1.3.1 The eXtended Finite Element method

The extended finite element method (XFEM), also known as generalized finite element method (GFEM) or partition of unity method (PUM) is a numerical technique that generalizes the classical finite element method (FEM) approach by extending the solution space. The extended finite element method was developed to overcome difficulties in solving problems with localized features. The work of Belytschko et al. [49] is one of the pioneering work towards the local enrichment of the approximation field. One of the initial applications was the modeling of fractures in a material [11, 39, 83]. In this original implementation, discontinuous basis functions are added to standard polynomial basis functions for nodes that belonged to elements that are intersected by a crack to provide a basis that can include crack opening displacements. A key advantage of XFEM is that in such problems the finite element mesh does not need to be updated to track the crack path. Subsequent research has illustrated the more general use of the method for problems involving singularities, material interfaces and other problems where a localized feature can be described by an appropriate set of basis functions. The incorporation of any function, typically non-polynomials, is realized through the notion of partition of unity. Thanks to this property, it is then possible to incorporate any kind of function to locally approximate the field. These functions may include any analytical solution of the problem or any a priori knowledge of the solution from the experimental test results.
The enriched basis is formed by the combination of the nodal shape functions associated with the mesh and the product with discontinuous functions. This construction

allows modeling of geometries that are independent of the mesh. Additionally the enrichment is added only locally, i.e. where the domain is required to be enriched. The resulting algebraic system of equations consists of two types of unknowns, classical degrees of freedom and enriched degrees of freedom. It was shown that for some problems, such an embedding of the problem's feature into the approximation space can significantly improve convergence rates and accuracy. Moreover, treating problems with discontinuities with eXtended Finite Element Methods suppresses the need to mesh and re-mesh the discontinuity surfaces, thus alleviating the computational costs. All of the above features provide the method with distinct advantages over standard finite element for modeling arbitrary discontinuities or singularities.

XFEM approximation spaces

The enrichment of the finite element method is obtained by using the partition of unity method (PUM), [4, 82]. The idea of PUM is to construct an approximation space for a specific family of partial differential equations by combining the functions arising from a partition of unity of the domain with local approximation spaces that are able to capture the nature of the problem at hand. In the XFEM the partition of unity is obtained from a finite element space relative to an admissible partition of the domain, a mesh. The local approximation space coincides with special functions that resemble the singularities of the solution at particular locations, such as crack tips in solid mechanics. To build up the partition of unity, we consider here piecewise affine Lagrangian finite elements defined on the family of meshes $\mathcal{T}_h$, characterized by the parameter h. We denote with V^h the finite element space. One of the characteristic features of XFEM is to use local enrichment functions. Then, given $\mathcal{I}$ the set of indexes numbering the mesh nodes with the corresponding (piecewise affine Lagrangian) basis functions $N_i(\mathbf{x})$, we denote by $\mathcal{I}^* \subset \mathcal{I}$ the subset of enriched nodes. Then, following [56], we adopt the corrected XFEM approximation space, whose functions $u^h(\mathbf{x}) \in V^h$ can be represented as

$$u^h(\mathbf{x}) = \sum_{i \in \mathcal{I}} N_i(\mathbf{x}) u_i + \sum_{i \in \mathcal{I}^*} N_i^*(\mathbf{x}) R(\mathbf{x}) [\psi(\mathbf{x}) - \psi(\mathbf{x}_i)] u_i^* \tag{1.5}$$

The coefficients u_i belong to the standard finite element part and u_i^* are additional nodal unknowns. The function $\psi(\mathbf{x})$ is called an *enrichment function* and it is this function that incorporates the special knowledge about a solution (e.g. jumps, kinks, singularities, etc.) into the approximation space. $R(\mathbf{x})$ is a ramp function that is necessary to localize the enrichment function. Then, all nodes of the domain where this localized enrichment function in non-zero are enriched.
In the following we will refer to some works by P. Hansbo and A. Hansbo to properly choose the enrichment function $\psi(\mathbf{x})$, [63, 64]. We will detail the construction of these functions in chapter 2.

1.3.2 The Immersed Boundary method.

The application of the immersed boundary method allows for a special coupling between the immersed capillary network and the external tissue. The big advantage of such a method is the geometrical complexity reduction. From now on we do no more need to solve the full 3D geometry of the embedded structure. Moreover, at the discrete

level, another advantage of this problem formulation is that the partition of the domains Ω and Λ into elements are completely independent.
We define a mesh for the tissue domain, constructing an admissible family of partitions of Ω into tetrahedrons. We also assume that Ω has a simple shape, such that it can be exactly represented by a collection of elements. For the discretization of the capillary bed, each branch of the whole network Λ is partitioned into a sufficiently large number of linear segments E, whose collection represents a finite element mesh on a one-dimensional manifold. On both mesh, we will define a suitable Lagrangian finite element basis and the two sets of bases are completely independent, since the 3D and 1D meshes do not conform. In particular, let us denote with $\{\psi_t^i\}$, $i = 1, \dots, N_t^h$ the Lagrangian piecewise linear finite element basis on the tissue mesh. To solve the variational form of the system of equations (1.4), we need to compute the average of ψ_t^j, i.e $\overline{\psi}_t^j$, on the circle of radius R and we have to project both the values of ψ_t^j and $\overline{\psi}_t^j$ on the 1D discrete space. In particular, on one hand we will construct a discrete operator able to interpolate the tissue piecewise linear finite elements on the linear finite element space defined on the capillary mesh. On the other hand we will interpolate the tissue degrees of freedom on some additional degrees of freedom, defined on the discretization of the vessels perimeter. This perimeter is a circle of radius R defined on the orthogonal plane to Λ at each point of the 1D mesh. The additional degrees of freedom are required to interpolate the value of the tissue concentration profile on the actual interface. Once interpolating, these values are used to compute the mean value of ψ_t^i in correspondence of every point of the 1D mesh.
The construction of these two operators is the core part of the numerical method which refers to the immersed boundary method, since they allow to solve the reduced problem using two completely independent meshes. We will detail better the definition and the implementation of such discrete operators in Chapter 4

Part I

Multidomain problems with homogeneous dimensionality

CHAPTER 2

An unfitted interface penalty method for the approximation of contrast problems

2.1 Introduction

In this first part of the thesis we will analyze multidomain problems with homogeneous dimensions. The main application we have in mind is the numerical approximation of contrast problem, that are characterized by non smooth solutions.
Finite element method is one of the most common numerical tool for finding the approximate solutions of partial differential equations. It has been applied successfully in many areas of engineering sciences to study, model and predict the behavior of materials and structures. The FEM makes use of polynomials as approximation functions, hence they often require smooth solutions in order to obtain optimal accuracy. However, if the solution contains a non smooth behavior, like high gradients, singularities or strong discontinuities, then the FEM methodology becomes computationally expensive and the optimal convergence is not guaranteed. Also, we often rely with structures that present internal interfaces separating different means. The parametric description of the interface boundary with the subsequent mesh generation, represents a further difficulties for the application of finite element methods, since the interface does not necessarily conform with the mesh, and the finite element method may be defined on sub-elements. This additional difficulty may be taken into account by constructing a mesh that doesn't conform with the interface and by enriching the approximation space with additional basis functions that lay on a portion of the mesh elements. Such technique is called the extended finite element method (XFEM) and it has been successfully applied to different applications such as crack propagation problems [39], free interface problems in fluid dynamics [61, 94] and modeling fractures in porous media [36]. For the approximation by XFEM of second order problems with interface conditions we

mention for instance [30, 38, 58, 66, 84]. It has been observed in [17, 19, 20, 94] that the stability and the condition number of the finite element scheme depend on how the interface cuts the computational mesh.

In this chapter, we focus on the development of an extended finite element method for interface problems governed by symmetric elliptic equations with large contrast between diffusion coefficients. The approximation of elliptic interface problems with XFEM has been already investigated in recent works. The discretization scheme that we consider is closely inspired by [63, 64], where an extended finite element method has been combined with a Nitsche's technique to enforce the matching conditions between elliptic problems. Such method turns out to be stable and convergent, but the resulting discrete problem may be ill conditioned in presence of small sub-elements. To cure this drawback, the application of interior penalty stabilization techniques has been successfully considered in a sequel of papers [17, 19, 20]. The idea of such stabilization methods is to introduce in the discrete formulation an artificial diffusion term to ensure the positivity of the discrete bilinear form for any configuration of the boundary or interface.

A second relevant question involves the behavior of the scheme addressed in [63] when we have to approximate large contrast problems. Also in this case the problem results to be ill conditioned.

With the present work, already published in [118], we aim to improve the understanding of the aforementioned drawbacks of XFEM combined with Nitsche's treatment of interface conditions for large contrast problems and to develop a finite element scheme that is robust with respect to the configuration of sub-elements as well as the heterogeneity of the diffusion coefficients. We first extend to the case of H^1 norm the stability analysis of linear XFEM already performed in [94] in the L^2 norm. In other words, we analyze the condition number of XFEM mass and stiffness matrices in presence of small sub-elements and we conclude that their optimal condition number, see [108] for a discussion of this indicator, is uniformly independent of how the interface cuts the mesh. This means that the simple application of a diagonal preconditioner allows us to stabilize the scheme with respect to small sub-elements. This analysis of the XFEM space is closed by the proof of discrete inequalities that will be useful to address the stability and conditioning of the scheme proposed in [63].

The previous robustness result is partially spoiled by the application of Nitsche's method for the implementation of interface conditions, because for such technique both large contrast of diffusion coefficients and small sub-elements negatively affect the condition number of the discrete problem. For the former issue, Nitsche's method becomes stable if the penalty term is tuned as illustrated in [21], while stability in case of the latter issue is ensured when the penalty is selected as in [63]. Unfortunately, these criteria can be contradictory. However, owing to the present analysis, we finally show that it is possible to blend the two different criteria to select Nitsche's penalty terms in order to make sure that the considered XFEM scheme is robust for the worse case among small sub-elements and large contrast problems.

In conclusion, we show that it is possible to develop a robust discretization scheme based on extended finite elements for the approximation of large contrast interface problems on meshes that do not fit the interface. The robustness is gained thanks to a suitable choice of the parameters that define the penalty technique combined with the

application of a diagonal preconditioner to the solution of the discrete system of equations. A remarkable advantage of this stabilization strategy consist in the simplicity of implementation. Some concluding numerical experiments confirm the efficiency of the scheme for the approximation of large contrast problems independently of the location of the interface.

2.2 Problem set up

In the sequel we consider a bounded convex polygonal domain $\Omega \cup \mathbb{R}^d$ with $d = 1, 2, 3$ space dimensions, we define its boundary $\partial\Omega$ and we denote with Γ an internal interface separating Ω into two subregions Ω_1 and Ω_2. Let $\mathbf{n}$ be a fixed unit normal vector on Γ. For the sake of simplicity, we assume that Γ is either a piecewise linear curve for $d = 2$ or a connected collection of planar surfaces for $d = 3$. A more precise characterization of the interface will be presented later on.

On each subregion Ω_i with $i = 1, 2$, we denote by ϵ_i and μ_i the diffusion and reaction coefficients respectively, with the assumptions that $\mu_i \geq 0$ and there exists $\underline{\epsilon} > 0$ such that $\epsilon_i \geq \underline{\epsilon}$. We aim to approximate the solution u_i of the following problem:

$$\begin{cases} -\nabla \cdot (\epsilon_i \nabla u_i) + \mu_i u_i = f_i & \text{in } \Omega_i \\ u_i = 0 & \text{on } \partial\Omega \cap \partial\Omega_i \\ u_1 = u_2 & \text{on } \Gamma \\ \epsilon_1 \partial_n u_1 = \epsilon_2 \partial_n u_2 & \text{on } \Gamma \end{cases} \tag{2.1}$$

where $\partial_n u$ denotes $\nabla u \cdot \mathbf{n}$. In what follows, we denote by $H^s(\cup\Omega_i)$ with $s \geq 1$ the broken Sobolev space of functions that belong to H^s in each subregion Ω_i with $i = 1, 2$. Let $(\cdot, \cdot)_{0,\Omega}$ be the $L^2(\Omega)$ inner product, for any $v, w \in H^1(\cup\Omega_i)$. We write $(\nabla v, \nabla w)_{0,\cup\Omega_i} := \sum_{i=1,2} (\nabla v_i, \nabla w_i)_{0,\Omega_i}$ and we also apply a similar notation for the corresponding induced norm, i.e. $\|\nabla v\|^2_{0,\cup\Omega_i} := \sum_{i=1,2} \|\nabla v_i\|^2_{0,\Omega_i}$. We write $x \lesssim y$ if there exists a generic constant c such that $x \leq cy$. Furthermore, if there exist such $\underline{c}$, $\overline{c}$ that $\underline{c}y \leq x \leq \overline{c}y$ we write $x \simeq y$. Constants $\underline{c}, \overline{c}$ are assumed to be independent of the configuration of Γ and ϵ_i, μ_i, h, unless differently specified.

Let $\mathcal{T}_h$ be a family of shape regular and quasi uniform triangulations of Ω. On domains with simple shape, it may be a family of uniform triangulations. Let K be a generic element of $\mathcal{T}_h$ and let h_K be its diameter (the radius of the smallest ball containing this set). Since we deal with regular meshes, we will also refer to $h := \max_{K \in \mathcal{T}_h} h_K$. The collection of elements that are intersected by Γ is denoted with

$$\mathcal{G}_h := \{K \in \mathcal{T}_h : \ K \cap \Gamma \neq \emptyset\}$$

and let $\Gamma^K := K \cap \Gamma$ the hyperplane cutting the element K.

We start defining the standard linear Lagrangian elements on $\mathcal{T}_h$,

$$V_h^\Omega := \{v \in C^0(\Omega) : v|_K \in \mathbb{P}^1(K) \ \forall K \in \mathcal{T}_h\},$$

and we rely with the following assumption:

Assumption 2.2.1. Poincaré inequality is applicable to V_h^Ω. If $\Omega \setminus \mathcal{G}_h$ is a non connected set, then Poincaré inequality must hold on each disconnected part.

Let $\mathcal{I}(V_h^\Omega)$ be the set of indexes numbering the nodes associated with V_h^Ω and let $\mathcal{V}(V_h^\Omega) := \{x_k\}_{k\in\mathcal{I}(V_h^\Omega)}$ be the corresponding set of points on Ω, with which we associate the basis functions ϕ_k such that $V_h^\Omega = \text{span}\{\phi_k\}_{k\in\mathcal{I}(V_h^\Omega)}$. Let $\pi_h^\Omega : C^0(\Omega) \to V_h^\Omega$ be the Lagrangian interpolant on V_h^Ω.

The position of the interface Γ can be described in multiple ways. For instance, Γ can be defined as a parametrized curve or surface. Alternatively, it can be implicitly represented by means of the level set of a distance function. The second strategy seems to be very natural and attractive in the context of finite elements and it motivates the first of the forthcoming assumptions.

Assumption 2.2.2. The interface Γ is such that:

i) There exists a discrete implicit surface (or hypersurface when $d = 3$) $\varphi_h \in V_h^\Omega$ that defines Γ as its zero level set.

ii) Let $\mathcal{P}_k$ be the patch corresponding to a generic vertex $x_k \in \mathcal{V}(V_h^\Omega)$, i.e. $\mathcal{P}_k = \text{supp}(\phi_k)$. We assume that

$$\mathcal{P}_k \cap \big(\Omega \setminus \mathcal{G}_h\big) \neq \emptyset, \quad \forall\, x_k \in \mathcal{V}(V_h^\Omega)$$

Let us denote by Γ_h the trace mesh corresponding to Γ, i.e. $\Gamma_h := \cup_{K\in\mathcal{G}_h}\Gamma^K$, and for any integrable function v we define,

$$\int_{\Gamma_h} v := \sum_{\Gamma^K\in\Gamma_h} \int_{\Gamma^K} v$$

Proceeding similarly, we denote by $\mathcal{F}_h$ the collection of edges or faces, F, on the external boundary $\partial\Omega$ and we denote by h_F their diameter. The boundary mesh $\mathcal{F}_h$ can be further split into its parts $\mathcal{F}_{h,i}$ relative to each subregion Ω_i.

2.3 An extended finite element space

We begin the development of the approximation method from the definition and the analysis of a suitable finite element space, that should be capable to approximate the discontinuity of the derivative of the field u on a computational mesh that does not capture the interface Γ. To this purpose, we enrich the space V_h^Ω with additional basis functions. For simplicity of notation we will omit the subscript h and write v instead of v_h. We start by defining the following restriction operator :

$$R_i :\ L^2(\Omega) \to L^2(\Omega), \quad R_i v := \begin{cases} v|_{\Omega_i} & \text{in } \Omega_i \\ 0 & \text{in } \Omega \setminus \Omega_i \end{cases}$$

As already proposed in [63, 94] for H^1-nonconforming approximations of the solution at the interface, the enriched finite element space V^h is defined as follows:

$$V^h := R_1 V_h^\Omega \oplus R_2 V_h^\Omega$$

as also reported in figure 2.1

To proceed, we consider the alternative representation of V^h proposed in [94], which exploits a hierarchical representation in terms of a standard Lagrangian finite element

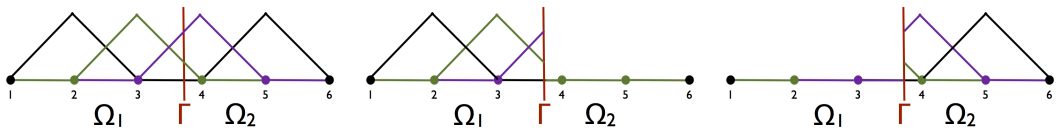

Figure 2.1: *Starting from the left: standard finite element space V_h^Ω, $R_1 V_h^\Omega$ and $R_2 V_h^\Omega$.*

space, enriched with additional basis functions over cut elements. This new setting will allow us to put into evidence how the enrichment functions affect the standard properties of the finite element space.

We define collections of nodes neighboring the interface and we use them to construct enrichment spaces,

$$\mathcal{I}_i^\Gamma(V_h^\Omega) := \{k \in \mathcal{I}(V_h^\Omega) : \ x_k \in \Omega_j, \ \text{supp}(\phi_k) \cap \mathcal{G}_h \neq \emptyset\}, \ \forall i, j = 1, 2, \ j \neq i$$
$$V_{h,i}^\Gamma := \text{span}\{R_i \phi_k : \ k \in \mathcal{I}_i^\Gamma(V_h^\Omega)\}$$

Owing to Theorem 2 in [94], the following direct decomposition holds:

$$V^h = V_h^\Omega \oplus V_{h,1}^\Gamma \oplus V_{h,2}^\Gamma$$

i.e. any function $v \in V^h$ can be uniquely decomposed as $v = v^\Omega + v_1^\Gamma + v_2^\Gamma$ with $v^\Omega \in V_h^\Omega$, $v_i^\Gamma \in V_{h,i}^\Gamma$, as depicted in figure 2.2.

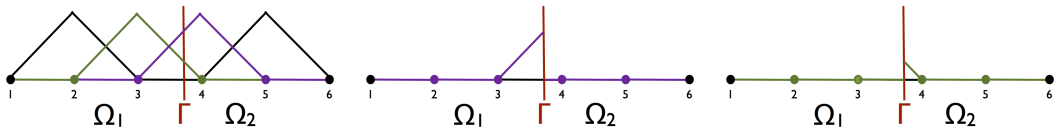

Figure 2.2: *Starting from the left: standard finite element space V_h^Ω, $V_{h,1}^\Gamma$ and $V_{h,2}^\Gamma$.*

To characterize function v_i^Γ, we set up suitable extensions of each subregion Ω_i, i.e. $\Omega_i^+ := \cup_{K \in \mathcal{T}_h} \{K \cap \Omega_i \neq \emptyset\}$ and we denote by $\mathcal{T}_{h,i}^+$ the corresponding triangulation. We denote by $V_{h,i}^+$ the Lagrangian finite element space relative to $\mathcal{T}_{h,i}^+$ and we observe that for any $v \in V^h$ there exists a unique discrete function $v_i^+ \in V_{h,i}^+$ such that $R_i v = v_i^+|_{\Omega_i}$. As a result of that, we introduce the extension operator:

$$E_i : R_i V^h \to V_{h,i}^+, \quad E_i R_i v := v_i^+$$

By means of this definition, it is possible to provide an explicit characterization of functions v_i^Γ in the decomposition $v = v^\Omega + v_1^\Gamma + v_2^\Gamma$. More precisely we have:

$$v^\Omega = \pi_h^\Omega v \tag{2.2}$$
$$v_i^\Gamma = \sum_{k \in \mathcal{I}_i^\Gamma} \beta_k^i \phi_k|_{\Omega_i}, \ \text{where} \ \sum_{k \in \mathcal{I}_i^\Gamma} \beta_k^i \phi_k|_{\Omega_i^+} = E_i R_i v - \pi_h^\Omega v|_{\Omega_i^+} \tag{2.3}$$

We notice that the spaces $V_{h,1}^\Gamma$ and $V_{h,2}^\Gamma$ are L^2-orthogonal on Ω, because their basis functions share disjoint supports, as we can observe from figure 2.2.

Before to start with the analysis, we first introduce some indicators that quantify how the interface cuts the computational mesh. For any $K \in \mathcal{G}_h$ we set:

$$\nu_i^K := \frac{|K \cap \Omega_i|}{|K|}, \quad \lambda_i^K := h_K \frac{|\Gamma_h^K|}{|K \cap \Omega_i|},$$

where $\nu_1^K + \nu_2^K = 1$ for any $K \in \mathcal{G}_h$. It can be seen that for any shape regular mesh $\mathcal{T}_h$, there exists a positive and bounded constant S such that

$$0 < \nu_i^K \lambda_i^K \leq S, \ \forall K \in \mathcal{G}_h \tag{2.4}$$

Furthermore, let $x_k \in \mathcal{I}_i^\Gamma$ be any vertex associated with the enrichment spaces $V_{h,i}^\Gamma$, let ϕ_k be the corresponding basis function and $\mathcal{P}_k$ be its patch. The indicators that affect the conditioning of a finite element method with respect to small sub-elements can be defined as

$$\underline{\nu}_i := \min_{k \in \mathcal{I}_i^\Gamma} \frac{|\mathcal{P}_k \cap \Omega_i|}{|\mathcal{P}_k|}, \quad \overline{\nu}_i := \max_{k \in \mathcal{I}_i^\Gamma} \frac{|\mathcal{P}_k \cap \Omega_i|}{|\mathcal{P}_k|}$$

$$\nu := \min_i \min_{k \in \mathcal{I}_i^\Gamma} \frac{|\mathcal{P}_k \cap \Omega_i|}{|\mathcal{P}_k|}$$

As shown in [94] Lemma 2, under Assumption 2.2.2 there exist a constant $0 < c_{cs}^0 < 1$, uniformly independent of ν and h, such that the following strengthened Cauchy-Schwarz inequality holds true for any $v^\Omega \in V_h^\Omega, \ v^\Gamma \in V_{h,1}^\Gamma \oplus V_{h,2}^\Gamma$,

$$(v^\Omega, v^\Gamma)_{0,\Omega} \leq c_{cs}^0 \|v^\Omega\|_{0,\Omega} \|v^\Gamma\|_{0,\Omega} \tag{2.5}$$

Exploiting the decomposition $v = v^\Omega + v_1^\Gamma + v_2^\Gamma$ together with Pythagoras Theorem, straightforward computations show that

$$\begin{aligned}(1 - c_{cs}^0)(\|v^\Omega\|_{0,\Omega}^2 + \|v_1^\Gamma\|_{0,\Omega}^2 + \|v_2^\Gamma\|_{0,\Omega}^2) \\ \leq \|v\|_{0,\Omega}^2 \leq 2(\|v^\Omega\|_{0,\Omega}^2 + \|v_1^\Gamma\|_{0,\Omega}^2 + \|v_2^\Gamma\|_{0,\Omega}^2)\end{aligned} \tag{2.6}$$

For the case of linear finite elements, the previous results can be extended to the gradient of discrete functions.

Lemma 2.3.1. *Under Assumptions 2.2.1 and 2.2.2, there exists a constant* $0 < c_{cs}^1(h) < 1$ *uniformly independent of* ν *but possibly dependent on* h*, such that for any* $v^\Omega \in V_h^\Omega, \ v^\Gamma \in V_{h,1}^\Gamma \oplus V_{h,2}^\Gamma$ *it holds*

$$(\nabla v^\Omega, \nabla v^\Gamma)_{0,\cup\Omega_i} \leq c_{cs}^1(h) \|\nabla v^\Omega\|_{0,\cup\Omega_i} \|\nabla v^\Gamma\|_{0,\cup\Omega_i}. \tag{2.7}$$

Proof. Owing to Cauchy-Schwarz inequality we get

$$\begin{aligned}(\nabla v^\Omega, \nabla v^\Gamma)_{0,\cup\Omega_i} &= \sum_i (\nabla v^\Omega, \nabla v_i^\Gamma)_{0,\Omega_i \cap \mathcal{G}_h} \leq \sum_i \|\nabla v^\Omega\|_{0,\Omega_i \cap \mathcal{G}_h} \|\nabla v_i^\Gamma\|_{0,\Omega_i \cap \mathcal{G}_h} \\ &\leq \sqrt{\sum_i \|\nabla v^\Omega\|_{0,\Omega_i \cap \mathcal{G}_h}^2} \sqrt{\sum_i \|\nabla v_i^\Gamma\|_{0,\Omega_i \cap \mathcal{G}_h}^2} \leq \|\nabla v^\Omega\|_{0,\mathcal{G}_h} \|\nabla v^\Gamma\|_{0,\cup\Omega_i}\end{aligned}$$

Then, exploiting assumption 2.2.1 and 2.2.2 (ii) we prove that there exist elements $K \in \Omega \setminus \mathcal{G}_h$ where $\nabla v^\Omega \neq 0$. This is equivalent to assert that there exists $c(h)$ such that

$$0 < c(h) := \inf_{v^\Omega \in V_h^\Omega,\ \|\nabla v^\Omega\|_{0,\mathcal{G}_h} \neq 0} \frac{\|\nabla v^\Omega\|_{0,\Omega\setminus\mathcal{G}_h}}{\|\nabla v^\Omega\|_{0,\mathcal{G}_h}} \tag{2.8}$$

Such definition shows that $c(h)$ depends on $\mathcal{G}_h$ solely, but not on the configuration of the interface within this crust of elements; thus, it is uniformly lower bounded with respect to ν. Then, it holds

$$c(h)\|\nabla v^\Omega\|_{0,\mathcal{G}_h} \leq \|\nabla v^\Omega\|_{0,\Omega\setminus\mathcal{G}_h},\ \|\nabla v^\Omega\|_{0,\mathcal{G}_h} \leq \sqrt{\frac{1}{1+c^2(h)}}\|\nabla v^\Omega\|_{0,\Omega}\ \forall v^\Omega \in V_h^\Omega$$

and the desired result is verified with $c_{cs}^1(h) = \sqrt{\frac{1}{1+c^2(h)}} < 1$.

To conclude, we provide a lower bound for $c(h)$ which suggests that $c(h)$ scales as $h^{\frac{1}{2}}$. To this aim, we notice that the restriction of v^Ω to $\mathcal{G}_h$ is identified by degrees of freedom laying on $\partial\mathcal{G}_h$ solely, denoted by $\mathbf{v}_{\partial\mathcal{G}_h}$. Then, by merging the following inequalities,

$$\|v^\Omega\|_{0,\mathcal{G}_h}^2 \leq ch^d\|\mathbf{v}_{\partial\mathcal{G}_h}\|^2 \text{ on } \mathcal{G}_h, \quad ch^{d-1}\|\mathbf{v}_{\partial\mathcal{G}_h}\|^2 \leq \|v^\Omega\|_{0,\partial\mathcal{G}_h}^2 \text{ on } \partial\mathcal{G}_h$$

there exists c, independent of h, such that

$$\|v^\Omega\|_{0,\mathcal{G}_h}^2 \leq c^2 h\|v^\Omega\|_{0,\partial\mathcal{G}_h}^2$$

which combined with the inverse inequality gives,

$$\|\nabla v^\Omega\|_{0,\mathcal{G}_h}^2 \leq c_I^2 h^{-2}\|v^\Omega\|_{0,\mathcal{G}_h}^2 \leq c^2 c_I^2 h^{-1}\|v^\Omega\|_{0,\partial\mathcal{G}_h}^2.$$

We now look at $\partial\mathcal{G}_h$ as a subset of the boundary of $\Omega \setminus \mathcal{G}_h$ and we assume that Poincaré inequality holds for the restriction of V_h^Ω to $\Omega \setminus \mathcal{G}_h$. As a result of that, combining Poincaré and trace inequalities, we obtain

$$\|v^\Omega\|_{0,\partial\mathcal{G}_h}^2 \leq \|v^\Omega\|_{0,\partial(\Omega\setminus\mathcal{G}_h)}^2 \leq c_T^2\|v^\Omega\|_{1,\Omega\setminus\mathcal{G}_h}^2 \leq c_T^2(1+c_P^2)\|\nabla v^\Omega\|_{0,\Omega\setminus\mathcal{G}_h}^2.$$

In conclusion, we get

$$\|\nabla v^\Omega\|_{0,\mathcal{G}_h} \leq c\, c_I c_T\sqrt{1+c_P^2}h^{-\frac{1}{2}}\|\nabla v^\Omega\|_{0,\Omega\setminus\mathcal{G}_h}$$

that is

$$\inf_{v^\Omega \in V_h^\Omega,\ \|\nabla v^\Omega\|_{0,\mathcal{G}_h} \neq 0} \frac{\|\nabla v^\Omega\|_{0,\Omega\setminus\mathcal{G}_h}}{\|\nabla v^\Omega\|_{0,\mathcal{G}_h}} \geq h^{\frac{1}{2}}\left(c\, c_I c_T\sqrt{1+c_P^2}\right)^{-1}.$$

□

As already observed for (2.5), inequality (2.7) directly implies that

$$\begin{aligned}(1-c_{cs}^1(h))(\|\nabla v^\Omega\|_{0,\Omega}^2 + \|\nabla v_1^\Gamma\|_{0,\Omega}^2 + \|\nabla v_2^\Gamma\|_{0,\Omega}^2) \\ \leq \|\nabla v\|_{0,\Omega}^2 \leq 2(\|\nabla v^\Omega\|_{0,\Omega}^2 + \|\nabla v_1^\Gamma\|_{0,\Omega}^2 + \|\nabla v_2^\Gamma\|_{0,\Omega}^2)\end{aligned} \tag{2.9}$$

where $(1-c_{cs}^1(h))$ is asymptotically equivalent to h.

2.3.1 Stability of the finite element space in the H^1 norm

The aim of this section is to extend the stability analysis of $V_{h,i}^{\Gamma}$ in L^2 norm, previously developed in [94], to the case of H^1 norm. For the sake of completeness, first we briefly remind the L^2 stability analysis and second we extend it to the gradients of functions. The presented results are valid in $d = 1, 2, 3$ space dimensions. We remind that all the results addressed here are only valid for linear finite element functions.

Our primary objective is to analyze the stability of $V_{h,i}^{\Gamma}$ with respect to the position of the interface Γ. The stability of a standard finite element space in the L^2 norm is ensured by the following estimate, where $\underline{c}, \overline{c}$ denote generic positive constants and v_k^{Ω} are the nodal values of $v^{\Omega} \in V_h^{\Omega}$,

$$\underline{c} \sum_{k=1}^{n} (v_k^{\Omega})^2 \|\phi_k\|_{0,\Omega}^2 \leq \|v^{\Omega}\|_{0,\Omega}^2 \leq \overline{c} \sum_{k=1}^{n} (v_k^{\Omega})^2 \|\phi_k\|_{0,\Omega}^2 \quad \forall v^{\Omega} \in V_h^{\Omega} \tag{2.10}$$

As shown in [94], Lemma 3, this result can be extended to the enriched finite element space. Indeed, for any $v_i^{\Gamma} \in V_{h,i}^{\Gamma}$ there exist positive constants $\underline{c}_0^{\Omega}, \overline{c}_0^{\Omega}$, independent of how the interface Γ cuts the mesh $\mathcal{T}_h$, such that

$$\underline{c}_0^{\Omega} \sum_{k \in \mathcal{I}_i^{\Gamma}} \left(\beta_k^i\right)^2 \|R_i \phi_k\|_{0,\Omega}^2 \leq \|v_i^{\Gamma}\|_{0,\Omega}^2 \leq \overline{c}_0^{\Omega} \sum_{k \in \mathcal{I}_i^{\Gamma}} \left(\beta_k^i\right)^2 \|R_i \phi_k\|_{0,\Omega}^2 \tag{2.11}$$

The extension of this analysis to the H^1 norm requires to prove the following result, which relies on the fact that gradients of the local basis functions on $V_{h,i}^{\Gamma}$ are linearly independent. We notice that this latter property would not hold true in the space V_h^{Ω}.

Lemma 2.3.2. *For any $v_i^{\Gamma} \in V_{h,i}^{\Gamma}$ there exist positive constants $\underline{c}_1^{\Omega}, \overline{c}_1^{\Omega}$, independent of how the interface Γ cuts the mesh $\mathcal{T}_h$, such that*

$$\underline{c}_1^{\Omega} \sum_{k \in \mathcal{I}_i^{\Gamma}} \left(\beta_k^i\right)^2 \|R_i \nabla \phi_k\|_{0,\Omega}^2 \leq \|\nabla v_i^{\Gamma}\|_{0,\Omega}^2 \leq \overline{c}_1^{\Omega} \sum_{k \in \mathcal{I}_i^{\Gamma}} \left(\beta_k^i\right)^2 \|R_i \nabla \phi_k\|_{0,\Omega}^2 \tag{2.12}$$

Proof. Let $K \in \mathcal{G}_h$ be a generic interface element with $K_i = K \cap \Omega_i$ and let $\mathcal{I}_i^{\Gamma}(K) := \{k \in \mathcal{I}(V_h^{\Omega}) : \ x_k \in \Omega_j, \ \text{supp}(\phi_k) \cap (\mathcal{G}_h \cap K) \neq \emptyset\}$ be the degrees of freedom of the enriched space on this element. For simplicity, we restrict our analysis to the element level, since for any $v_i^{\Gamma} \in V_{h,i}^{\Gamma}$ we have

$$\|\nabla v_i^{\Gamma}\|_{0,\Omega}^2 = \sum_{K \in \mathcal{G}_h} \Big\| \sum_{k \in \mathcal{I}_i^{\Gamma}(K)} \beta_k^i R_i \nabla \phi_k \Big\|_{0,K}^2 = \sum_{K \in \mathcal{G}_h} \Big\| \sum_{k \in \mathcal{I}_i^{\Gamma}(K)} \beta_k^i \nabla \phi_k \Big\|_{0,K_i}^2$$

Owing to the fact that $\nabla \phi_k$ are constant functions, there exists a real matrix $A_{loc,i}$, with $[A_{loc,i}]_{rs} := (\nabla \phi_r, \nabla \phi_s)_{0,K}$ for any $r, s \in \mathcal{I}_i^{\Gamma}(K)$, independent of how the interface Γ_h^K cuts the element K, such that

$$\| \sum_{k \in \mathcal{I}_i^{\Gamma}(K)} \beta_k^i \nabla \phi_k \|_{0,K_i}^2 = \frac{|K_i|}{|K|} \boldsymbol{\beta}_i' A_{loc,i} \boldsymbol{\beta}_i$$

We observe that $A_{loc,i}$ is symmetric and positive definite, since functions $\nabla\phi_k$ with $k \in \mathcal{I}_i^\Gamma(K)$ are linearly independent. We also define $D_{loc,i} = \mathrm{diag}(A_{loc,i})$ such that,

$$\sum_{k\in\mathcal{I}_i^\Gamma(K)} \left(\beta_k^i\right)^2 \|\nabla\phi_k\|_{0,K_i}^2 = \frac{|K_i|}{|K|}\boldsymbol{\beta}_i' D_{loc,i}\boldsymbol{\beta}_i$$

Clearly, the eigenproblem $A_{loc,i}\boldsymbol{\beta}_i = \lambda D_{loc,i}\boldsymbol{\beta}_i$ admits a spectrum of positive eigenvalues $\lambda(K) \in [\lambda_{min}(K), \lambda_{max}(K)]$, where $\lambda_{min}(K), \lambda_{max}(K)$ only depend on the shape of the element K, but not on the interface Γ_h^K. Then, the following local estimate holds true,

$$\lambda_{min}(K) \sum_{k\in\mathcal{I}_i^\Gamma(K)} \left(\beta_k^i\right)^2 \|\nabla\phi_k\|_{K_i}^2 \le \|\nabla v_i^\Gamma\|_{K_i}^2 \le \lambda_{max}(K) \sum_{k\in\mathcal{I}_i^\Gamma(K)} \left(\beta_k^i\right)^2 \|\nabla\phi_k\|_{K_i}^2$$

Finally, summing up over all elements $K \in \mathcal{G}_h$, we obtain (2.11) with constants $\underline{c}_1^\Omega := \min_{K\in\mathcal{G}_h} \lambda_{min}(K)$ and $\overline{c}_1^\Omega := \max_{K\in\mathcal{G}_h} \lambda_{max}(K)$.

□

We will extensively apply the following inequalities relating the L^2 norms of finite element functions with the corresponding euclidean norms of degrees of freedom. Let $\mathbf{v}$ denote the vector of degrees of freedom that identify a generic function $v \in V^h$ and let $\mathbf{v}_i^\Gamma$ and $\mathbf{v}^\Omega$ be the vectors relative to $v_i^\Gamma \in V_{h,i}^\Gamma$ and $v^\Omega \in V_h^\Omega$, respectively. It is well known that for any $v^\Omega \in V_h^\Omega$ there exist positive constants $\underline{c}^\Omega, \overline{c}^\Omega$ such that,

$$\underline{c}^\Omega h^d \|\mathbf{v}^\Omega\|^2 \le \|v^\Omega\|_{0,\Omega}^2 \le \overline{c}^\Omega h^d \|\mathbf{v}^\Omega\|^2 \tag{2.13}$$

where $\|\mathbf{v}\|$ denotes the Euclidean norm. Owing to (2.3), for any $v \in V^h$ the upper bound of (2.13) can be also extended to the local finite element spaces $V_{h,i}^+$ as follows, $\|E_i R_i v\|_{0,\Omega}^2 \lesssim h^d\big(\|\mathbf{v}^\Omega\|^2 + \|\mathbf{v}_i^\Gamma\|^2\big)$. For the enriched finite element spaces, the corresponding results are affected by the position of the interface Γ.

Lemma 2.3.3. *For any $v_i^\Gamma \in V_{h,i}^\Gamma$ there exist positive constants $\underline{c}_0^\Gamma, \overline{c}_0^\Gamma$, independent of ν, h, such that*

$$\underline{c}_0^\Gamma h^d \underline{\nu}_i^{2/d+1} \|\mathbf{v}_i^\Gamma\|^2 \le \|v_i^\Gamma\|_{0,\Omega}^2 \le \overline{c}_0^\Gamma h^d \overline{\nu}_i^{2/d+1} \|\mathbf{v}_i^\Gamma\|^2 \tag{2.14}$$

Furthermore, there exists $\underline{v}_i^\Gamma \in V_{h,i}^\Gamma$ such that

$$\|\underline{v}_i^\Gamma\|_{0,\Omega}^2 \le \overline{c}_0^\Gamma h^d \underline{\nu}_i^{2/d+1} \|\underline{\mathbf{v}}_i^\Gamma\|^2 \tag{2.15}$$

Proof. Owing to the the lower bound of (2.11), we observe that

$$\Big(\min_{k\in\mathcal{I}_i^\Gamma} \|R_i\phi_k\|_{0,\Omega}^2\Big)\|\mathbf{v}_i^\Gamma\|^2 \lesssim \|v_i^\Gamma\|_{0,\Omega}^2$$

We aim to estimate the smallest $\|R_i\phi_k\|_{0,\Omega_i}^2$ by splitting the integrals over the subelements that belong to the patch of $R_i\phi_k$ and then applying a suitable quadrature formula. We notice that the measure of the support where the integrals are evaluated is proportional to $h^d\underline{\nu}_i$ while the pointwise evaluations of the function to be integrated can

be at most equivalent to $(\underline{\nu}_i^{1/d})^2$. The upper bound is obtained replacing the smallest $\|R_i\phi_k\|^2_{0,\Omega_i}$ with the largest. Then, we conclude that

$$\min_{k\in\mathcal{I}_i^\Gamma}\|R_i\phi_k\|^2_{0,\Omega_i}\simeq h^d\underline{\nu}_i^{2/d+1},\quad \max_{k\in\mathcal{I}_i^\Gamma}\|R_i\phi_k\|^2_{0,\Omega_i}\simeq h^d\overline{\nu}_i^{2/d+1}$$

which proves (2.14). By the same argument (2.15) holds true if we select $\underline{v}_i^\Gamma := R_i\phi_k$ corresponding to $\min_{k\in\mathcal{I}_i^\Gamma}\|R_i\phi_k\|^2_{0,\Omega}$. □

Exploiting lemma 2.3.2 we also show that a similar result holds in the space $\nabla V_{h,i}^\Gamma$, with a different scaling with respect to ν.

Lemma 2.3.4. *For any $v_i^\Gamma\in V_{h,i}^\Gamma$ there exist positive constants $\underline{c}_1^\Gamma,\overline{c}_1^\Gamma$, independent of ν,h such that*

$$\underline{c}_1^\Gamma h^{d-2}\underline{\nu}_i\|\mathbf{v}_i^\Gamma\|^2\le\|\nabla v_i^\Gamma\|^2_{0,\Omega}\le\overline{c}_1^\Gamma h^{d-2}\overline{\nu}_i\|\mathbf{v}_i^\Gamma\|^2 \tag{2.16}$$

Furthermore, there exists $\underline{v}_i^\Gamma\in V_{h,i}^\Gamma$, the same function of lemma 2.3.3, such that

$$\|\nabla\underline{v}^\Gamma\|^2_{0,\Omega}\le\overline{c}_1^\Gamma h^{d-2}\underline{\nu}_i\|\underline{\mathbf{v}}^\Gamma\|^2 \tag{2.17}$$

Proof. The proof follows from the same reasoning of lemma 2.3.3 combined with (2.12). However, we notice that $\|R_i\nabla\phi_k\|^2_{0,K_i}\simeq h^{d-2}\nu_i^K$, because $R_i\nabla\phi_k$ are constant functions proportional to h^{-1}. □

Let us denote by N_h the dimension of V^h and let $M\in\mathbb{R}^{N_h\times N_h}$ and $L\in\mathbb{R}^{N_h\times N_h}$ be the standard mass and stiffness matrices in the finite element space V^h, precisely

$$\mathbf{v}'M\mathbf{w}=(v,w)_{0,\Omega},\quad \mathbf{v}'L\mathbf{w}=(\nabla v,\nabla w)_{0,\cup\Omega_i},\quad \forall v,w\in V^h$$

which feature the following block decomposition

$$M=\begin{bmatrix}M^\Omega & M_1^{\Omega\Gamma} & M_2^{\Omega\Gamma}\\ (M_1^{\Omega\Gamma})' & M_1^\Gamma & 0\\ (M_2^{\Omega\Gamma})' & 0 & M_2^\Gamma\end{bmatrix}\quad L=\begin{bmatrix}L^\Omega & L_1^{\Omega\Gamma} & L_2^{\Omega\Gamma}\\ (L_1^{\Omega\Gamma})' & L_1^\Gamma & 0\\ (L_2^{\Omega\Gamma})' & 0 & L_2^\Gamma\end{bmatrix}$$

where, reminding the decomposition $v=v^\Omega+v_1^\Gamma+v_2^\Gamma$, for any $v^\Omega,w^\Omega\in V_h^\Omega$ and $w_j^\Gamma\in V_{h,j}^\Gamma,\ j=1,2$, we have,

$$\begin{aligned}&(\mathbf{v}^\Omega)'M^\Omega\mathbf{w}^\Omega:=(v^\Omega,w^\Omega)_{0,\Omega},\quad (\mathbf{v}^\Omega)'L^\Omega\mathbf{w}^\Omega:=(\nabla v^\Omega,\nabla w^\Omega)_{0,\cup\Omega_i}\\ &(\mathbf{v}_i^\Gamma)'M_i^\Gamma\mathbf{w}_i^\Gamma:=(v_i^\Gamma,w_i^\Gamma)_{0,\Omega},\quad (\mathbf{v}_i^\Gamma)'L_i^\Gamma\mathbf{w}_i^\Gamma:=(\nabla v_i^\Gamma,\nabla w_i^\Gamma)_{0,\cup\Omega_i}\\ &(\mathbf{v}^\Omega)'M_j^{\Omega\Gamma}\mathbf{w}_j^\Gamma:=(v^\Omega,w_j^\Gamma)_{0,\Omega},\quad (\mathbf{v}^\Omega)'L_j^{\Omega\Gamma}\mathbf{w}_j^\Gamma:=(\nabla v^\Omega,\nabla w_j^\Gamma)_{0,\cup\Omega_i}\end{aligned}$$

We remark that inequalities (2.6), (2.9) are fundamental to show that

$$\mathbf{v}'M\mathbf{v}\simeq(\mathbf{v}^\Omega)'M^\Omega\mathbf{v}^\Omega+(\mathbf{v}_1^\Gamma)'M_1^\Gamma\mathbf{v}_1^\Gamma+(\mathbf{v}_2^\Gamma)'M_2^\Gamma\mathbf{v}_2^\Gamma \tag{2.18}$$

$$\mathbf{v}'L\mathbf{v}\simeq(\mathbf{v}^\Omega)'L^\Omega\mathbf{v}^\Omega+(\mathbf{v}_1^\Gamma)'L_1^\Gamma\mathbf{v}_1^\Gamma+(\mathbf{v}_2^\Gamma)'L_2^\Gamma\mathbf{v}_2^\Gamma \tag{2.19}$$

with lower bound constant $\underline{c}_{cs}(h)=(1-c_{cs}(h))$, being $c_{cs}(h):=\max(c_{cs}^0,c_{cs}^1(h))$, and upper bound constant $\overline{c}=2$ that are uniformly independent of ν. However, according to lemma 2.3.1, the lower bound is asymptotically proportional to h, namely $\underline{c}_{cs}(h):=ch$.

Given a real square matrix B, we denote by $\mathrm{diag}(B)$ the square matrix corresponding to its diagonal. The following result is a simple reinterpretation at the algebraic level of inequality (2.11) and (2.12).

Corollary 1. *There exist positive constants $\underline{c}^{M^\Gamma}, \overline{c}^{M^\Gamma}$, uniformly independent of ν and h, such that*

$$\underline{c}^{M^\Gamma}(\mathbf{v}_i^\Gamma)'\mathrm{diag}(M_i^\Gamma)\mathbf{v}_i^\Gamma \leq (\mathbf{v}_i^\Gamma)'M_i^\Gamma\mathbf{v}_i^\Gamma \leq \overline{c}^{M^\Gamma}(\mathbf{v}_i^\Gamma)'\mathrm{diag}(M_i^\Gamma)\mathbf{v}_i^\Gamma,\ \forall v_i^\Gamma \in V_{h,i}^\Gamma \quad (2.20)$$

There exist positive constants $\underline{c}^{L^\Gamma}, \overline{c}^{L^\Gamma}$, uniformly independent of ν but possibly dependent on h, such that

$$\underline{c}^{L^\Gamma}(\mathbf{v}_i^\Gamma)'\mathrm{diag}(L_i^\Gamma)\mathbf{v}_i^\Gamma \leq (\mathbf{v}^\Gamma)'L_i^\Gamma\mathbf{v}_i^\Gamma \leq \overline{c}^{L^\Gamma}(\mathbf{v}_i^\Gamma)'\mathrm{diag}(L_i^\Gamma)\mathbf{v}_i^\Gamma,\ \forall v_i^\Gamma \in V_{h,i}^\Gamma \quad (2.21)$$

Looking at the *optimal condition number*, i.e. given $A \in \mathbb{R}^{N\times N}$

$$K_{opt}(A) := \min_{D\in\mathbb{R}^{N\times N}} K_2(DAD)$$

Corollary 1 implies that $K_{opt}(M+L)$ does not depend on ν.

2.3.2 Discrete inequalities

We conclude the analysis of $V_{h,i}^\Gamma$ with a discussion on how the fundamental discrete inequalities must be modified in this space.

Let us start with the inverse inequality, which in V_h^Ω reads as

$$h\|\nabla v^\Omega\|_{0,\Omega} \lesssim \|v^\Omega\|_{0,\Omega}$$

for any $v^\Omega \in V_h^\Omega$. It is easy to verify that such property can be straightforwardly extended to $V_{h,i}^+$ as follows,

$$h^2\|\nabla v\|_{0,\cup\Omega_i}^2 \lesssim \|v\|_{0,\cup\Omega_i^+}^2 := \sum_{i=1,2}\|E_iR_iv\|_{0,\Omega_i^+}^2,\ \forall v \in V^h \quad (2.22)$$

However, a qualitative analysis in the one-dimensional case is sufficient to show that such inequality does not hold uniformly with respect to ν when restricted to each subregion Ω_i, because the space $R_iV_h^\Omega$ contains an element of size $h\underline{\nu}_i$.

Lemma 2.3.5. *For any $v_i^\Gamma \in V_{h,i}^\Gamma$ the following inequality holds true*

$$h^2\underline{\nu}_i^{2/d}\frac{\underline{\nu}_i}{\overline{\nu}_i}\|\nabla v_i^\Gamma\|_{0,\Omega_i}^2 \lesssim \|v_i^\Gamma\|_{0,\Omega_i}^2 \quad (2.23)$$

Proof. Owing to the upper bound of (2.16) we have,

$$\sup_{v_i^\Gamma\in V_{h,i}^\Gamma}\frac{\|\nabla v_i^\Gamma\|_{0,\Omega_i}^2}{\|\mathbf{v}_i^\Gamma\|^2} \leq \overline{c}h^{d-2}\overline{\nu}_i$$

which is equivalent to

$$\inf_{v_i^\Gamma\in V_{h,i}^\Gamma}\frac{\|\mathbf{v}_i^\Gamma\|^2}{\|\nabla v_i^\Gamma\|_{0,\Omega_i}^2} \geq (\overline{c}h^{d-2}\overline{\nu}_i)^{-1}$$

Combining the previous inequality with the lower bound of (2.14) we obtain,

$$\inf_{v_i^\Gamma\in V_{h,i}^\Gamma}\frac{\|v_i^\Gamma\|_{0,\Omega_i}^2}{\|\nabla v_i^\Gamma\|_{0,\Omega_i}^2} \geq (\overline{c}h^{d-2}\overline{\nu}_i)^{-1}\underline{c}h^d\underline{\nu}_i^{2/d+1} \geq \underline{c}h^2\underline{\nu}_i^{2/d}\frac{\underline{\nu}_i}{\overline{\nu}_i}$$

that is the desired result. □

Proceeding similarly, we notice that the discrete inequality

$$h_K\|v^\Omega\|^2_{0,\partial K} \lesssim \|v^\Omega\|^2_{0,K},\ \forall v^\Omega \in V_h^\Omega \tag{2.24}$$

will be affected by the position of the interface when applied to the enriched spaces.

Lemma 2.3.6. *For any $v_i^\Gamma \in V_{h,i}^\Gamma$ and $K_i = |K \cap \Omega_i|$ with $K \in \mathcal{G}_h$ the following inequality holds true*

$$h_K(\nu_i^K)^{1/d}\|v_i^\Gamma\|^2_{0,\Gamma_h^K} \lesssim \|v_i^\Gamma\|^2_{0,K_i},\ \forall v_i^\Gamma \in V_{h,i}^\Gamma \tag{2.25}$$

Proof. Owing to (2.11) we have,

$$\|v_i^\Gamma\|^2_{0,\Gamma_h^K} \leq \overline{c}_0^\Omega \sum_{k\in\mathcal{I}_i^\Gamma} \left(\beta_k^i\right)^2 \|R_i\phi_k\|^2_{0,\Gamma_h^K}$$

with $\|R_i\phi_k\|^2_{0,\Gamma_h^K} \simeq h^{d-1}(\nu_i^K)^{1/d+1}$. Then, we obtain

$$\|v_i^\Gamma\|^2_{0,\Gamma_h^K} \leq \overline{c}_0^\Omega \sum_{k\in\mathcal{I}_i^\Gamma} \left(\beta_k^i\right)^2 h^{d-1}(\nu_i^K)^{1/d+1}$$

which, owing to (2.14), can be combined with

$$\sum_{k\in\mathcal{I}_i^\Gamma} \left(\beta_k^i\right)^2 h^d(\nu_i^K)^{2/d+1} \leq \|v_i^\Gamma\|^2_{0,K_i}$$

to obtain the desired result. □

We finally address the Poincaré-Friedrichs inequality, providing control on the L^2-norm by means of a modified H^1-seminorm, i.e.

$$\|v^\Omega\|^2_{0,\Omega} \leq c^{PF}\|\nabla v^\Omega\|^2_{0,\Omega} + \sum_{i=1,2}\int_{\mathcal{F}_{h,i}} (h_F)^{-1}(v^\Omega)^2,\ \forall v^\Omega \in V_h^\Omega$$

Concerning the enriched finite element space, we observe that the discrete functions $v_i^\Gamma \in V_{h,i}^\Gamma$ vanish by construction on a collection of the inner boundaries of elements in $\mathcal{T}_{h,i}^+$ that are intersected by Γ. Let us denote by $\Sigma_i := \partial(\mathcal{G}_h \cap \Omega_i) \setminus \partial\Omega_i$ such line or surface and by $H^1_{\Sigma_i}(\Omega_i)$ the subspace of $H^1(\Omega_i)$ of functions whose traces vanish on Σ_i. Since $V_{h,i}^\Gamma \subset H^1_{\Sigma_i}(\Omega_i)$, the previous Poincaré-Friedrichs inequality reduces the usual Poincaré inequality,

$$\|v_i^\Gamma\|^2_{0,\Omega_i} \leq c_i^P\|\nabla v_i^\Gamma\|^2_{0,\Omega_i}$$

which holds true with a constant c_i^P that is uniformly bounded with respect to ν and h, because c^P depends on the number of space dimensions, d, the diameter of the domain, but not on its aspect ratio.

2.4 The unfitted interface penalty method

Following [63], we aim to apply Nitsche's method to enforce the coupling conditions between the finite element approximations of u_i on $R_i V_h^\Omega$.

First, we denote by v^-, v^+ the two limit values of any sufficiently regular function on the two sides of the interface Γ, where the notation $\pm$ refers to the orientation of $\mathbf{n}$, and we define

$$[\![v]\!] := v^- - v^+, \quad \{v\}_w := w^- v^- + w^+ v^+, \quad \{v\}^w := w^+ v^- + w^- v^+$$

Then, we introduce the following bilinear forms and functionals,

$$\begin{aligned}
a_i(u,v) &:= \int_{\Omega_i} \left(\epsilon_i \nabla u_i \cdot \nabla v_i + \mu_i u_i v_i\right) \\
b_{h,i}(u,v) &:= \int_{\mathcal{F}_{h,i}} \left(\gamma \epsilon_i h_F^{-1} u_i v_i - \epsilon_i \partial_n u_i v_i - \epsilon_i \partial_n v_i u_i\right) \\
c_h(u,v) &:= \int_{\Gamma_h} \left(\gamma \{\epsilon\}_w (h_K)^{-1} [\![u]\!][\![v]\!] - \{\epsilon \partial_n u\}_w [\![v]\!] - \{\epsilon \partial_n v\}_w [\![u]\!]\right) \\
a_h(u,v) &:= \sum_{i=1,2} \left(a_i(u,v) + b_{h,i}(u,v)\right) + c_h(u,v) \\
F(v) &:= \int_\Omega f v
\end{aligned}$$

where $\gamma > 0$ is a stabilization parameter that will be suitably selected later on. Our discrete problem reads as follows:

$$\text{find } u_h \in V^h \text{ such that } a_h(u_h, v_h) = F(v_h),\ \forall v_h \in V^h \tag{2.26}$$

We notice that (2.26) is strongly consistent with the weak solution of (2.1), as ensured by lemma 1 in [63], which straightforwardly applies to the present case. The natural norms to perform the stability and error analysis of the scheme are:

$$\begin{aligned}
\|v\|^2_{\pm\frac{1}{2},\mathcal{F}_{h,i}} &:= \int_{\mathcal{F}_{h,i}} (h_F)^{\mp 1} v^2 \\
\|v\|^2_{\pm\frac{1}{2},\Gamma_h} &:= \int_{\Gamma_h} (h_K)^{\mp 1} v^2 \\
|||v|||^2_{1,\Omega_i} &:= a_i(v,v) + \|\epsilon_i^{\frac{1}{2}} v\|^2_{+\frac{1}{2},\mathcal{F}_{h,i}} \\
|||v|||^2_{1,h,\cup\Omega_i} &:= \sum_{i=1,2} |||v|||^2_{1,\Omega_i} + \|\{\epsilon\}_w^{\frac{1}{2}} [\![v]\!]\|^2_{+\frac{1}{2},\Gamma_h}
\end{aligned}$$

We remind that the coupling term $c_h(u,v)$ admits an alternative skew symmetric formulation,

$$\hat{c}_h(u,v) := \int_{\Gamma_h} \left(\gamma \{\epsilon\}_w (h_K)^{-1} [\![u]\!][\![v]\!] - \{\epsilon \partial_n u\}_w [\![v]\!] + \{\epsilon \partial_n v\}_w [\![u]\!]\right)$$

Although we will not analyze in detail this option, we observe that the main conclusions on the robustness of the scheme (2.26) will equivalently hold in this latter case.

Finally, we observe that for the numerical scheme (2.26) we have exploited a weak enforcement of Dirichlet boundary conditions. As a result of that, assumption 2.2.1 is not valid because Poincaré inequality is not applicable to this case. However, by means of Poincaré-Friedrichs generalization, lemma 2.3.1 can be extended to norm $|||v|||^2_{1,\Omega_i}$ without the need of assumption 2.2.1. More precisely, there exists a constant $\underline{c}^*_{cs}(h)$ uniformly independent of ν but asymptotically proportional to h, such that for any $v \in V^h$ it holds,

$$\underline{c}^*_{cs}(h)(|||v^\Omega|||^2_{1,\Omega_i} + |||v^\Gamma_i|||^2_{i,\Omega_i}) \lesssim |||v|||^2_{1,\Omega_i} \lesssim (|||v^\Omega|||^2_{1,\Omega_i} + |||v^\Gamma_i|||^2_{i,\Omega_i}) \tag{2.27}$$

2.4.1 Stability and conditioning of the finite element scheme

We start from the following result, which extends lemma 4 in [63]. Let w_i be the averaging weights defining $\{\cdot\}_w, \{\cdot\}^w$ that appear in $c_h(\cdot,\cdot)$.

Lemma 2.4.1. *There exists positive constants $c^\nu_w, c^\epsilon_w > 1$ such that*

$$\|\epsilon_i^{\frac{1}{2}} w_i^{\frac{1}{2}} \partial_n R_i v\|^2_{-\frac{1}{2},\Gamma_h} \lesssim c^\nu_w \|\epsilon_i^{\frac{1}{2}} \nabla R_i v\|^2_{0,\Omega_i}, \forall v \in V^h \tag{2.28}$$

$$\|\{\epsilon\}_w^{\frac{1}{2}} v_i^\Gamma\|^2_{+\frac{1}{2},\Gamma_h} \lesssim c^\nu_w c^\epsilon_w h^{-2} \|\epsilon_i^{\frac{1}{2}} v_i^\Gamma\|^2_{0,\Omega_i}, \forall v_i^\Gamma \in V^\Gamma_{h,i} \tag{2.29}$$

where

$$c^\nu_w := \max_{i=1,2} \max_{K\in\mathcal{G}_h} (\nu_i^K)^{-1} w_i$$

$$c^\epsilon_w := \max_{i,j=1,2,\, j\neq i} \max_{K\in\mathcal{G}_h} \left(1 + \frac{(\epsilon_j w_j)|_K}{(\epsilon_i w_i)|_K}\right)$$

Proof. For the first inequality we notice that

$$\begin{aligned} w_i h_K \int_{\Gamma_h^K} \epsilon_i \partial_n R_i v^2 &\leq w_i h_K \frac{|\Gamma_h^K|}{|K\cap\Omega_i|} \|\epsilon_i^{\frac{1}{2}} \nabla R_i v\|^2_{0,K_i} \\ &= \lambda_i^K \nu_i^K (\nu_i^K)^{-1} w_i \|\epsilon_i^{\frac{1}{2}} \nabla R_i v\|^2_{0,K_i} \leq S(\nu_i^K)^{-1} w_i \|\epsilon_i^{\frac{1}{2}} \nabla R_i v\|^2_{0,K_i} \end{aligned}$$

where S is the constant of (2.4).

For the second property we apply (2.25) to show that for $i,j = 1,2$ with $j \neq i$ it holds

$$\int_{\Gamma_h^K} (h_K)^{-1} \{\epsilon\}_w (v_i^\Gamma)^2 \lesssim h_K^{-2} w_i (\nu_i^K)^{-1/d} \left(1 + \frac{(\epsilon_j w_j)|_K}{(\epsilon_i w_i)|_K}\right) \|\epsilon_i^{\frac{1}{2}} v_i^\Gamma\|^2_{0,K_i}$$

Observing that $(\nu_i^K)^{-1/d} \leq (\nu_i^K)^{-1}$, the result is proved by summing over the elements $K \in \Omega_h$. □

Lemma 2.4.1, together with the choice $w_i = \nu_i^K$ for any $K \in \Omega_h$, guarantees that the stability of the scheme does not depend on how the interface cuts the mesh. However, this choice is not optimal for the robustness of the scheme with respect to the heterogeneity of the diffusion coefficients. Indeed, it is shown in [21, 41] that it is possible to suitably select the weights to make sure that c^ϵ_w is independent of ϵ_i/ϵ_j for

$i, j = 1, 2,\ j \neq i$, but this requirement may be in conflict with the previous one. A few alternatives to treat this intrinsic drawback of (2.26) will be discussed in section 2.4.2.

Reminding that there exists $\underline{\epsilon} > 0$ such that $\epsilon_i \geq \underline{\epsilon}$ for $i = 1, 2$ and $\mu_i \geq 0$ being ϵ_i, μ_i the diffusion and reaction coefficients respectively, we set

$$\underline{\mu} := \min_{i=1,2} \mu_i, \quad \overline{\mu} := \max_{i=1,2} \mu_i$$

$$\underline{\epsilon} := \min_{i=1,2} \epsilon_i, \quad \overline{\epsilon} := \max_{i=1,2} \epsilon_i$$

$$\underline{\alpha} := \underline{\epsilon} \quad \overline{\alpha} := \max[\overline{\mu}, \overline{\epsilon}]$$

Then, the fundamental properties that characterize the robustness of the scheme are summarized in the following result.

Theorem 2.4.2. *Let $a_h(\cdot,\cdot)$ be the symmetric bilinear form of (2.26), where the averaging weights are selected as $w_i = \nu_i^K$. Let $\mathbf{v} \in \mathbb{R}^{N_h}$ be the vector of degrees of freedom associated with a generic $v_h \in V^h$ and let $\|\mathbf{v}\|$ be its Euclidean norm. Let A_h be the finite element matrix corresponding to the bilinear form $a_h(\cdot,\cdot)$ and the discrete space V^h. The following properties hold true with generic positive constants $\underline{c}$ and $\overline{c}$:*

i) Provided that $\gamma > c_w^\nu$, for any $v \in V^h$

$$\underline{c}|||v|||^2_{1,h,\cup\Omega_i} \leq a_h(v,v) \leq \overline{c}c_w^\nu|||v|||^2_{1,h,\cup\Omega_i}$$

ii) There exist positive constants $\underline{\kappa}, \overline{\kappa}$ with

$$\underline{\kappa} := \underline{\alpha}\,\underline{c}^*_{cs}(h)h^d \min\left[c^{PF}\underline{c}^\Omega, \min_{i=1,2}\underline{\nu}_i\big((\underline{\mu}/\underline{\epsilon})\underline{c}_0^\Gamma\underline{\nu}_i^{2/d} + \underline{c}_1^\Gamma h^{-2}\big)\right]$$
$$\overline{\kappa} := \overline{c}\,\overline{\alpha}h^{d-2}\max\left[\overline{c}^\Omega, \max_{i=1,2}\overline{\nu}_i\big((h^2 + c_w^\nu c_w^\epsilon)\overline{c}_0^\Gamma\overline{\nu}_i^{2/d} + \overline{c}_1^\Gamma\big)\right]$$

such that

$$\underline{\kappa}\|\mathbf{v}\|^2 \leq |||v|||^2_{1,h,\cup\Omega_i} \leq \overline{\kappa}\|\mathbf{v}\|^2,\ \forall v \in V^h$$

iii) There exist functions $\underline{v}, \overline{v} \in V^h$ and positive constants $\underline{\sigma}, \overline{\sigma}$ with

$$\underline{\sigma} := \overline{c}\,\overline{\alpha}h^{d-2}\min_{i=1,2}\underline{\nu}_i\big((h^2 + c_w^\nu c_w^\epsilon)\overline{c}_0^\Gamma\underline{\nu}_i^{2/d} + \overline{c}_1^\Gamma\big)$$
$$\overline{\sigma} := \underline{c}\,\underline{\alpha}\,\underline{c}^*_{cs}(h)c^{PF}\underline{c}^\Omega h^{d-2}$$

such that

$$|||\underline{v}|||^2_{1,h,\cup\Omega_i} \leq \underline{\sigma}\|\underline{\mathbf{v}}\|^2, \quad \overline{\sigma}\|\overline{\mathbf{v}}\|^2 \leq |||\overline{v}|||^2_{1,h,\cup\Omega_i}$$

iv) The spectral condition number of A_h satisfies the following bounds

$$\frac{\overline{\sigma}}{\underline{\sigma}} \leq K_2(A_h) \leq c_w^\nu\frac{\overline{\kappa}}{\underline{\kappa}}$$

i.e $K_2(A_h) \simeq \nu^{-1}$ in the asymptotic limit $\nu \to 0$.

Proof. Part (i): to prove the coercivity of the bilinear form we start from the consistency and symmetry terms. We observe that for any $a_i, b \in \mathbb{R},\ 0 < \delta < 1$ and positive weights $0 \leq w_i \leq 1$ this inequality holds,

$$2\Big(\sum_{i=1,2} w_i \epsilon_i a_i\Big) b \leq \sum_{i=1,2} \left(\delta w_i \epsilon_i a_i^2 + \delta^{-1} w_i \epsilon_i b^2\right) \leq \delta \sum_{i=1,2} \epsilon_i a_i^2 + \delta^{-1} \{\epsilon\}_w b^2$$

which combined with lemma (2.28) gives,

$$2 \int_{\Gamma_h} \{\epsilon \partial_n v\}_w [\![v]\!] \leq \delta c_w^\nu \sum_i \|\epsilon_i^{\frac{1}{2}} \nabla R_i v\|_{0,\Omega_i}^2 + \delta^{-1} \|\{\epsilon\}_w^{\frac{1}{2}} [\![v]\!]\|_{+\frac{1}{2},\Gamma_h}^2,\ \forall v \in V^h$$

Proceeding as in the standard Nitsche's method for the boundary conditions, we conclude that, provided that $\gamma > c_w^\nu$, it holds $a_h(v,v) \gtrsim |||v|||_{1,h,\cup\Omega_i}^2$ for any $v \in V^h$. The proof of the upper bound follows from the application of Cauchy-Schwarz inequalities to derive upper bounds of each term of $a_h(\cdot,\cdot)$. In particular, for any $u, v \in V^h$ the following inequality

$$\begin{aligned}\int_{\Gamma_h} \{\epsilon \partial_n u\}_w [\![v]\!] &\leq \sum_{i=1,2} \|(\epsilon_i w_i)^{\frac{1}{2}} \partial_n u\|_{-\frac{1}{2},\Gamma_h} \|\{\epsilon\}_w^{\frac{1}{2}} [\![v]\!]\|_{+\frac{1}{2},\Gamma_h} \\ &\leq c_w^\nu \sum_{i=1,2} \|\epsilon_i^{\frac{1}{2}} \nabla u_i\|_{0,\Omega_i} \|\{\epsilon\}_w^{\frac{1}{2}} [\![v]\!]\|_{+\frac{1}{2},\Gamma_h}\end{aligned}$$

motivates the presence of c_w^ν in the continuity constant of the bilinear form.

Part (ii): for the lower bound we have,

$$\begin{aligned}|||v|||_{1,h,\cup\Omega_i}^2 &\geq \sum_{i=1,2} |||v|||_{1,\Omega_i}^2 \geq \underline{c}_{cs}^*(h) \sum_{i=1,2} \left(|||v^\Omega|||_{1,\Omega_i}^2 + |||v_i^\Gamma|||_{1,\Omega_i}^2\right) \\ &\geq \underline{\alpha}\, \underline{c}_{cs}^*(h) \Big[c^{PF} \|v^\Omega\|_{0,\Omega}^2 + \sum_{i=1,2} \left((\underline{\mu}/\underline{\epsilon}) \|v_i^\Gamma\|_{0,\Omega_i}^2 + \|\nabla v_i^\Gamma\|_{0,\Omega_i}^2\right)\Big] \\ &\geq \underline{\alpha}\, \underline{c}_{cs}^*(h) h^d \Big[c^{PF} \underline{c}^\Omega \|\mathbf{v}^\Omega\|^2 + \sum_{i=1,2} \left((\underline{\mu}/\underline{\epsilon}) \underline{c}_0^\Gamma \underline{\nu}_i^{2/d+1} + \underline{c}_1^\Gamma h^{-2} \underline{\nu}_i\right) \|\mathbf{v}_i^\Gamma\|^2\Big] \\ &\geq \underline{\alpha}\, \underline{c}_{cs}^*(h) h^d \min\Big[c^{PF} \underline{c}^\Omega, \min_{i=1,2} \left((\underline{\mu}/\underline{\epsilon}) \underline{c}_0^\Gamma \underline{\nu}_i^{2/d+1} + \underline{c}_1^\Gamma h^{-2} \underline{\nu}_i\right)\Big] \|\mathbf{v}\|^2\end{aligned}$$

Exploiting (2.29), for the upper bound we obtain,

$$\begin{aligned}|||v|||_{1,h,\cup\Omega_i}^2 &\lesssim \sum_{i=1,2} \left(|||v|||_{1,\Omega_i}^2 + c_w^\nu c_w^\epsilon h^{-2} \|\epsilon_i^{\frac{1}{2}} v_i^\Gamma\|_{0,\Omega_i}^2\right) \\ &\lesssim \sum_{i=1,2} \left(|||v^\Omega|||_{1,\Omega_i}^2 + |||v_i^\Gamma|||_{1,\Omega_i}^2 + c_w^\nu c_w^\epsilon h^{-2} \|\epsilon_i^{\frac{1}{2}} v_i^\Gamma\|_{0,\Omega_i}^2\right) \\ &\lesssim \overline{\alpha}\Big[h^{-2} \|v^\Omega\|_{0,\Omega}^2 + \sum_{i=1,2} \left((1 + c_w^\nu c_w^\epsilon h^{-2}) \|v_i^\Gamma\|_{0,\Omega_i}^2 + \|\nabla v_i^\Gamma\|_{0,\Omega_i}^2\right)\Big] \\ &\lesssim \overline{\alpha} h^{d-2}\Big[\overline{c}^\Omega \|\mathbf{v}^\Omega\|^2 + \sum_{i=1,2} \left((h^2 + c_w^\nu c_w^\epsilon) \overline{c}_0^\Gamma \overline{\nu}_i^{2/d+1} + \overline{c}_1^\Gamma \overline{\nu}_i\right) \|\mathbf{v}_i^\Gamma\|^2\Big] \\ &\lesssim \overline{\alpha} h^{d-2} \max\Big[\overline{c}^\Omega, \max_{i=1,2} \left((h^2 + c_w^\nu c_w^\epsilon) \overline{c}_0^\Gamma \overline{\nu}_i^{2/d+1} + \overline{c}_1^\Gamma \overline{\nu}_i\right)\Big] \|\mathbf{v}\|^2\end{aligned}$$

Part (iii): to show that $|||\underline{v}|||^2_{1,h,\cup\Omega_i} \leq \underline{\sigma}\|\underline{\mathbf{v}}\|^2$ we select $\underline{v} = \underline{v}_i^\Gamma$, as in lemma 2.3.3 with $i = \arg\min \underline{\nu}_i$ and proceeding exactly as for the upper bound of part (ii) with $v^\Omega = 0$, we obtain

$$|||\underline{v}|||^2_{1,h,\cup\Omega_i} \lesssim \overline{\alpha} h^{d-2} \min_{i=1,2} \left((h^2 + c_w^\nu c_w^\epsilon)\overline{c}_0^\Gamma \underline{\nu}_i^{2/d+1} + \overline{c}_1^\Gamma \underline{\nu}_i \right) \|\underline{\mathbf{v}}\|^2$$

We notice that the previous bound is not optimal in the parameter h and for Lagrangian finite elements it would be possible to refine it until h^d. However, this seems to be hardly feasible for $V_{h,i}^\Gamma$, because such space does not enjoy an approximation property.

For the lower bound, we select $\overline{v} := v^\Omega$, i.e. $v_1^\Gamma = v_2^\Gamma = 0$. In this case, we rely on the standard finite element framework. More precisely, by choosing v^Ω as a global shape function, see for instance [43] Theorem 9.14, there exists a constant $\underline{c}$ such that $\|\nabla v^\Omega\|^2_{0,\Omega} \geq \underline{c} h^{-2} \|v^\Omega\|^2_{0,\Omega}$. Proceeding as for the lower bound of part (ii) we obtain,

$$|||\overline{v}|||^2_{1,h,\cup\Omega_i} \geq \underline{c\alpha}\, \underline{c}^*_{cs}(h) c^{PF} \underline{c}^\Omega h^{d-2} \|\overline{\mathbf{v}}\|^2$$

Part (iv): reminding that $a_h(v,v) = \mathbf{v}' A_h \mathbf{v}$ for any $v \in V^h$, when A_h is symmetric the result is a straightforward application of (i), (ii) and (iii) combined with

$$\lambda_{min} = \min_{\mathbf{v}\neq\mathbf{0}} \frac{\mathbf{v}' A_h \mathbf{v}}{\|\mathbf{v}\|^2}, \quad \lambda_{max} = \max_{\mathbf{v}\neq\mathbf{0}} \frac{\mathbf{v}' A_h \mathbf{v}}{\|\mathbf{v}\|^2}$$

As a result of that, we immediately obtain,

$$\underline{\kappa} \lesssim \lambda_{min} \lesssim \underline{\sigma}, \quad \overline{\sigma} \lesssim \lambda_{max} \lesssim c_w^\nu \overline{\kappa}$$

We finally notice that in the asymptotic limit $\nu \to 0$ we have $\underline{\kappa}, \underline{\sigma} \simeq \nu$ while $\overline{\sigma}, \overline{\kappa}$ are independent of ν. This allows us to conclude that $K_2(A_h) \simeq \nu^{-1}$. We remind that c_w^ν is independent of ν under the condition $w_i = \nu_i^K$. □

To analyze how the solution of (2.26) converges to the one of (2.1) we refer to [63], where an equivalent scheme is addressed. The only significant modification that should be introduced in the present setting to perform the convergence analysis, consists in the definition of the interface Γ. Indeed, Γ must be a smooth curve or surface, in order to ensure that the solution of (2.1) is regular enough to prove the approximation properties of V^h. To comply with this requirement, we have to address a smooth level set function φ that defines the continuous interface as its zero level set. According to assumption 2.2.2, the discrete interface Γ_h will be provided by φ_h, a finite element approximation of φ in V_h^Ω.

2.4.2 Stabilization of the scheme

Theorem 2.4.2 shows that problem (2.26) is ill posed when the discrete interface Γ cuts the computational mesh in such way that very small sub-elements are generated, i.e. $\nu \to 0$. As illustrated in section 2.3.1, this is not a major limitation, because the singularity of the matrix in the limit case can be cured by means of a diagonal scaling technique. The application of this preconditioning strategy to the specific case of (2.26) is addressed below.

We start from the following estimate,

$$\begin{aligned}\sum_{i=1,2}|||v|||^2_{1,\Omega_i} &\lesssim |||v|||^2_{1,h,\cup\Omega_i}\\ &\lesssim \sum_{i=1,2}|||v|||^2_{1,\Omega_i} + \{\epsilon\}_w h^{-2}\sum_{i=1,2}\|v_i^\Gamma\|^2_{0,\Omega_i}\\ &\lesssim \sum_{i=1,2}|||v|||^2_{1,\Omega_i} + c_w^\nu c_w^\epsilon h^{-2}\|\epsilon^{\frac{1}{2}}v\|^2_{0,\Omega}\\ &\lesssim (1+c_w^\nu c_w^\epsilon h^{-2})\sum_{i=1,2}|||v|||^2_{1,\Omega_i},\ \forall v\in V^h \end{aligned} \tag{2.30}$$

which shows the equivalence between $|||\cdot|||^2_{1,h,\cup\Omega_i}$ and $\sum_{i=1,2}|||\cdot|||^2_{1,\Omega_i}$ for any discrete functions, uniformly with respect to $\underline{\alpha}, \overline{\alpha}$ and ν. Then we study the generalized mass matrix,

$$\mathbf{v}'(M_\mu + L_{h,\epsilon})\mathbf{v} = \sum_i |||v|||^2_{1,\Omega_i}$$

where M_μ and $L_{h,\epsilon}$ are the scaled mass and stiffness matrices with respect to the reaction and diffusion coefficients, i.e.

$$\begin{aligned}\mathbf{v}'M_\mu\mathbf{w} &:= \sum_{i=1,2}(\mu_i^{\frac{1}{2}}v_i, \mu_i^{\frac{1}{2}}w_i)_{0,\Omega_i}\\ \mathbf{v}'L_{h,\epsilon}\mathbf{w} &:= \sum_{i=1,2}\left[(\epsilon_i^{\frac{1}{2}}\nabla v_i, \epsilon_i^{\frac{1}{2}}\nabla w_i)_{0,\Omega_i} + \int_{\mathcal{F}_{h,i}}\epsilon_i h_F^{-1}v_i w_i\right]\end{aligned}$$

which can be represented as follows,

$$M_\mu = \begin{bmatrix} M_\mu^\Omega(\mu_1,\mu_2) & \mu_1 M_1^{\Omega\Gamma} & \mu_2 M_2^{\Omega\Gamma}\\ (\mu_1 M_1^{\Omega\Gamma})' & \mu_1 M_1^\Gamma & 0\\ (\mu_2 M_2^{\Omega\Gamma})' & 0 & \mu_2 M_2^\Gamma\end{bmatrix}\ L_{h,\epsilon} = \begin{bmatrix} L_{h,\epsilon}^\Omega(\epsilon_1,\epsilon_2) & \epsilon_1 L_1^{\Omega\Gamma} & \epsilon_2 L_2^{\Omega\Gamma}\\ (\epsilon_1 L_1^{\Omega\Gamma})' & \epsilon_1 L_1^\Gamma & 0\\ (\epsilon_2 L_2^{\Omega\Gamma})' & 0 & \epsilon_2 L_2^\Gamma\end{bmatrix}$$

As already mentioned, the primary objective is to cure the instability arising when very small sub-elements are generated. A secondary and more challenging objective, is to simultaneously reduce the stiffness of the system in the case of large contrast problems. A first difficulty arises from inequality (2.23), which shows that any diagonal or block diagonal preconditioner based on mass matrix would never be sufficient to eliminate the ill conditioning arising from small sub-elements. A second difficulty emerges from the discussion of lemma 2.4.1, which highlights that the scheme (2.26) with averaging weights $w_i = \nu_i^K$ may be affected by instabilities in the case of large contrast problems. As a result of these observations, we propose the following preconditioner

$$P := \begin{bmatrix} M_\mu^\Omega & 0 & 0\\ 0 & \mu_1\mathrm{diag}(M_1^\Gamma) & 0\\ 0 & 0 & \mu_2\mathrm{diag}(M_2^\Gamma)\end{bmatrix} + \begin{bmatrix} L_{h,\epsilon}^\Omega & 0 & 0\\ 0 & \epsilon_1\mathrm{diag}(L_1^\Gamma) & 0\\ 0 & 0 & \epsilon_2\mathrm{diag}(L_2^\Gamma)\end{bmatrix}$$

that will be further combined with a particular choice of the weights w_i. The performance of P applied to matrix A_h is summarized in the following result.

Theorem 2.4.3. *There exist two positive constants* $\underline{c}^P, \overline{c}^P \simeq c_w^\nu\big(1 + c_w^\nu c_w^\epsilon h^{-2}\big)$ *independent of* $\nu, \underline{\alpha}, \overline{\alpha}$*, but possibly dependent on* h*, such that*

$$\underline{c}^P \mathbf{v}' P \mathbf{v} \leq \mathbf{v}' A_h \mathbf{v} \leq \overline{c}^P \mathbf{v}' P \mathbf{v}. \tag{2.31}$$

Proof. Let T_h be the generalized mass matrix corresponding to norm $|||\cdot|||_{1,h,\cup\Omega_i}$. Theorem 2.4.2 (i) ensures that

$$\mathbf{v}' T_h \mathbf{v} \lesssim \mathbf{v}' A_h \mathbf{v} \lesssim c_w^\nu \mathbf{v}' T_h \mathbf{v}$$

Reminding that $\mathbf{v}'(M_\mu + L_{h,\epsilon})\mathbf{v} = \sum_i |||v|||^2_{1,\Omega_i}$, inequality (2.30) is equivalent to,

$$\mathbf{v}'(M_\mu + L_{h,\epsilon})\mathbf{v} \lesssim \mathbf{v}' A_h \mathbf{v} \lesssim c_w^\nu\big(1 + c_w^\nu c_w^\epsilon h^{-2}\big)\mathbf{v}'(M_\mu + L_{h,\epsilon})\mathbf{v}$$

Then, the result follows from the combination of (2.27) with (2.20), (2.21). □

The aim of Theorem 2.4.3 is to emphasize how the enrichment of the finite element space affects the conditioning of problem (2.26). Since the blocks referring to the standard finite element space, namely M_μ^Ω, $L_{h,\epsilon}^\Omega$, are not diagonalized, this result does not provide any significant information about how to cure the stiffness arising from heterogeneity of diffusion coefficients. It is well known that for large contrast among ϵ_1 and ϵ_2, the continuous problem (2.1) can be ill posed too. A suitable approximation method may help to reduce this intrinsic difficulty of the problem. Preliminary considerations addressed in [22] suggest that the weak enforcement of interface conditions by means of Nitsche's method, together with the averaging weights proposed in [21, 41], could be particularly effective to this purpose.

On the basis of (2.31) and in particular the fact that the constant $\overline{c}^P$ of the upper bound is proportional to $(c_w^\nu)^2 c_w^\epsilon$, we propose a strategy to select the averaging weights of the scheme (2.26) that aims to maximize the efficiency of the preconditioner P as well as the robustness of the method with respect to the location of the interface and the heterogeneity of diffusion coefficients.

We first notice that the definition of the weights is taken at the element level, for any element $K \in \mathcal{G}_h$, and that the two weights w_i are uniquely identified by a single parameter w such that $w_1 = w$ while $w_2 = 1 - w$. The element-based counterpart of constant $\overline{c}^P$ is

$$\begin{aligned}
\overline{c}_w^P|_K &:= c_w^\nu|_K\big(1 + c_w^\nu|_K c_w^\epsilon|_K h^{-2}\big) \\
c_w^\nu|_K &:= \max_i \big(w_i|_K (\nu_i^K)^{-1}\big) \\
c_w^\epsilon|_K &:= \max_i \big(1 + \frac{(\epsilon_j w_j)|_K}{(\epsilon_i w_i)|_K}\big)
\end{aligned}$$

where we have highlighted the dependence on w.

We consider a simple approach to make sure that $\overline{c}_w^P|_K$ does not depend on the worse case among small sub-elements and highly heterogeneous coefficients across the interface. Let $w_i^\nu|_K = \nu_i^K$ be the optimal weights to ensure robustness for small sub-elements, and let $w_i^\epsilon|_K = \epsilon_j/(\epsilon_i + \epsilon_j)$ the weights that ensure robustness in case of large contrast problems according to [21]. Indeed, it is easy to verify that $c_{w^\nu}^\nu|_K = 1$

and $c^{\epsilon}_{w^{\epsilon}}|_K = 2$. Then, two function evaluations followed by an *if* statement on each element $K \in \mathcal{G}_h$ allow to find the weights such that,

$$w^*|_K = \arg \min_{*=\nu,\epsilon} \overline{c}^P_{w^*}|_K$$

Since the choice of the weights influence the constant c^{ν}_w, owing to theorem 2.4.2 the penalty parameter γ should be tuned accordingly.

We will verify the efficiency of the latter strategy by means of numerical experiments. A few computations show that this choice of the weights is also optimal in the sense that it coincides with the solution of the following minimization problem,

$$w^{opt}|_K = \arg \min_{w\in[0,1]} \overline{c}^P_w|_K$$

The main advantage of the proposed technique for a robust approximation of problem (2.1) in the framework of XFEM consists in the simplicity of implementation, since it is applied at the algebraic level, without modifications to the structure of (2.26). However, for discrete problems featuring both small cut elements and large contrast of diffusion coefficients the present scheme should be further improved.

An heuristic approach consists in the application of the modified XFEM space proposed in [94]. The idea is to slightly modify the configuration of the interface to avoid the usage of enrichment functions of very small support. The optimal approximation properties of the enriched finite element space can be maintained, provided that the threshold below which the small cut elements are discarded is sufficiently small with respect to the mesh characteristic size. By this way, the quantity ν^{-1} becomes uniformly upper bounded with respect to the configuration of the interface and consequently the averaging weights in (2.26) can be exploited to cure the instability arising from the large contrast of coefficients.

A more sound approach is based on the application of a stabilization operator to problem (2.26). In [20] Burman and Hansbo propose the following stabilized formulation of problem (2.26),

$$a_h(u_h, v_h) + g_h(u_h, v_h) = F_h(v_h), \ \forall v_h \in V_h \tag{2.32}$$

where $g_h(\cdot,\cdot)$ is the so called *ghost penalty* stabilization term for piecewise affine approximations. Let $\mathcal{E}_h$ be the set of element edges in the boundary zone, more precisely,

$$\mathcal{E}_h := \{F = K \cap K', \text{ where either } K \in \mathcal{G}_h \text{ or } K' \in \mathcal{G}_h\}$$

Then, the stabilization operator is given by a penalty on the jumps of the gradients over the set of element edges in the boundary zone,

$$g_h(u_h, v_h) := \sum_{F\in\mathcal{E}_h} \gamma_g h_F([\![\nabla u_h \cdot \mathbf{n}_F]\!], [\![\nabla v_h \cdot \mathbf{n}_F]\!])_{0,F}$$

where $\mathbf{n}_F$ is the reference unit normal vector relative to each edge. The enhanced stability obtained by adding $g_h(\cdot,\cdot)$, is reflected in the coercivity estimate

$$\|v_h\|^2_{1,h,\Omega} \lesssim a_h(v_h, v_h) + g_h(v_h, v_h), \quad \forall v_h \in V_h$$

which holds true uniformly with respect to ν for any possible choice of the averaging weights of (2.26). Again, the stabilized unfitted interface method can be complemented by the most suitable averaging weights for the approximation of large contrast

problems. In our view, the main drawback of this approach consists in the difficulty to build up the finite element matrix corresponding to $g_h(\cdot,\cdot)$, especially in the three-dimensional case. Furthermore, a thorough investigation of how this artificial diffusion term affects the approximation of the solution and of its gradients in the neighborhood of the interface is still missing.

2.5 Numerical results

The numerical scheme (2.26) has been implemented in one and two space dimensions. In particular, for the one dimensional case, we perform numerical simulations using Matlab®, while for the two dimensional problem we implement a code using FreeFem++, [67].
For the definition of the degrees of freedom and the construction of matrix A_h, we have exploited the decomposition $V^h = V_h^\Omega \oplus V_{h,1}^\Gamma \oplus V_{h,2}^\Gamma$.

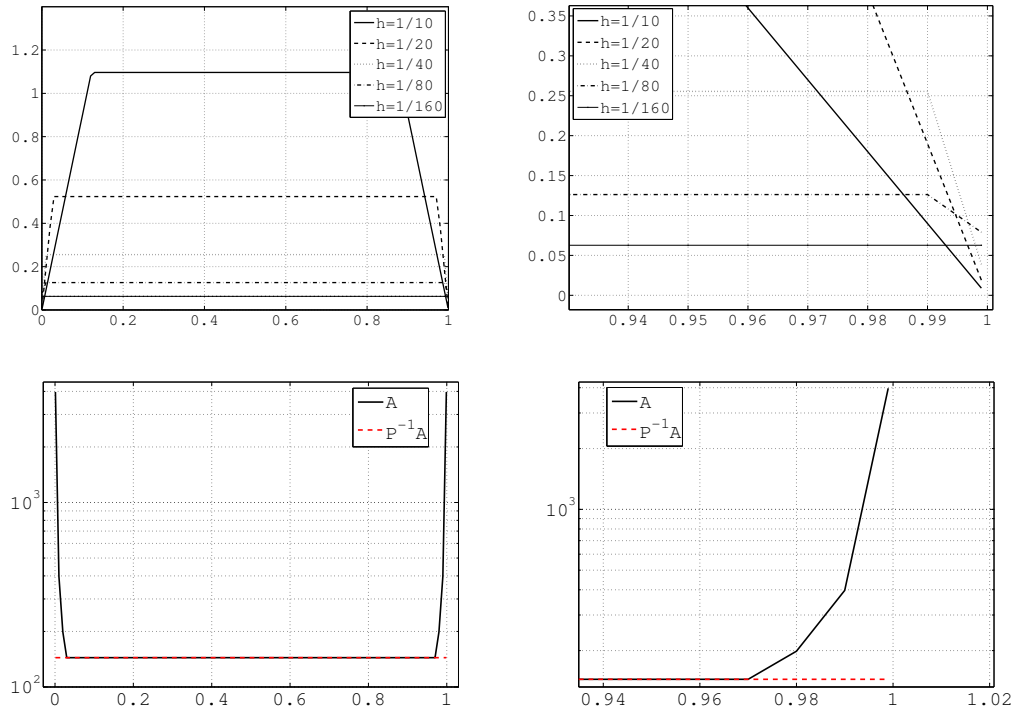

Figure 2.3: *The dependence of $\lambda_{min}(A_h)$ from $\nu_1 \in (0,1)$ is depicted on the top for different values of the characteristic mesh size h. We observe that $\underline{\nu}_1 + \underline{\nu}_2 = 1$ and thus $\underline{\nu} = \min[\underline{\nu}_1, (1-\underline{\nu}_1)]$. On the bottom, we compare how $\underline{\nu}_1$ influences the spectral condition number of A_h and $P^{-\frac{1}{2}} A_h P^{-\frac{1}{2}}$, for $h = 0.05$. A zoom in correspondence of $\underline{\nu}_1 = 1$ is reported on the right for each plot.*

The one-dimensional case allows for a simple control of the position of the interface, which is a single point on the interval $(0,1)$ where problem (2.1) is defined. In particular, on a uniform finite element partition of size h, Γ splits one of the sub-intervals in two parts of length $h\nu_1$ and $h\nu_2$ with $\nu_1 + \nu_2 = 1$ and $\nu = \min_i \nu_i$. For the sake of simplicity, we have considered a purely diffusive problem, i.e. $\mu_i = 0$, with uniform coefficients $\epsilon_i = 1$.

With the one dimensional model, we have first analyzed how the spectrum of A_h depends on ν. The results, reported in figure 2.3, closely follow the estimates of theorem 2.4.2. We notice that the minimum eigenvalue of A_h follows the same trend of constant $\underline{\kappa}$, which is proportional to

$$\min\left[c^{PF}\underline{c}^{\Omega}, \min_{i=1,2}\underline{\nu}_i\big((\underline{\mu}/\underline{\epsilon})\underline{c}_0^{\Gamma}\underline{\nu}_i^{2/d} + \underline{c}_1^{\Gamma}h^{-2}\big)\right]$$

In agreement to theorem 2.4.3, we observe that the diagonal scaling is effective to reduce the high condition numbers that appear when the interface Γ approaches one of the vertexes of the finite element partition, i.e. $\nu \to 0$.

A second test is aimed to verify the efficiency of the averaging weights w^{opt} to guarantee the robustness of the scheme. We observe that constant $\overline{c}^P$ is an upper bound for the spectrum of the following generalized eigen-problem, $A_h\mathbf{v} = \lambda P\mathbf{v}$. We have shown that for a generic choice of w, constant $\overline{c}^P$ could be extremely large in the case of large contrast problems or small sub-elements. Then, we consider a moderately large contrast problem with $\epsilon_1 = 1$ and $\epsilon_2 = 0.1$ and we analyze the behavior of the largest eigenvalue λ_{max} with respect to $\nu \in (0, 1)$. In particular, the comparison of the three cases w^{ϵ}, w^{ν} and w^{opt} reported in figure 2.4 shows that the weights w^{opt} are optimal and they ensure that scheme (2.26) is fully robust.

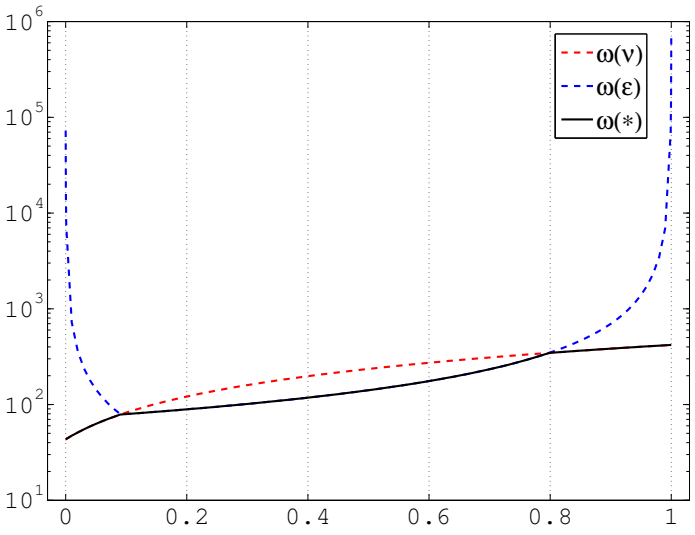

Figure 2.4: *The dependence of λ_{max} on $\underline{\nu}_1$ for three choices of the weights, w^{ϵ}, w^{ν} and $w^{opt} = w^*$*

To further illustrate the analysis that has been performed, we consider a second test case in two space dimensions. It consist on the approximation of problem (2.1) on the unit square $(0, 1) \times (0, 1)$ with a planar interface Γ defined by $x = 0.51, y \in (0, 1)$, which does not fit the computational mesh consisting on a structured triangulation based on a uniform partition of the interval $(0, 1)$ in 16 nodes, see figure 2.5.

For this test case, we qualitatively analyze the approximation of a problem with homogeneous coefficients, i.e. $\epsilon_i = 1, \mu_i = 0$, and a contrast problem with $\epsilon_1 = 1, \epsilon_2 = 0.1, \mu_i = 0$. On one hand, see figure 2.6 (left), the former test confirms that

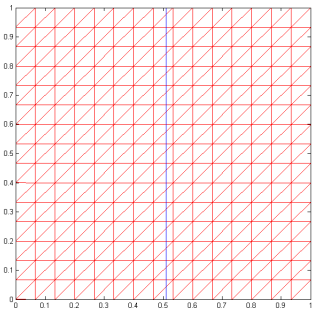

Figure 2.5: *The computational mesh $\mathcal{T}_h$ and the interface Γ for the two dimensional numerical experiments.*

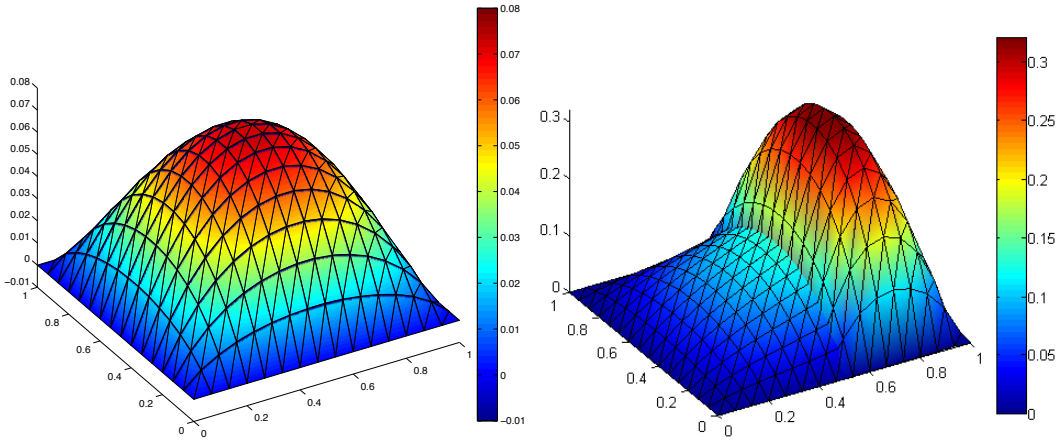

Figure 2.6: *Numerical solution of problem* (2.1) *approximated by* (2.26) *on the finite element mesh illustrated in figure* 2.5*. On the left we report the solution with $\epsilon_i = 1, \mu_i = 0$, while on the right we show the case $\epsilon_1 = 1, \epsilon_2 = 0.1, \mu_i = 0$.*

the behavior of the unfitted penalty method is satisfactory also in the case of a regular solution with continuous normal derivatives across the interface. On the other hand, the latter test shows that the enrichment of the finite element space allows to capture the discontinuity in the fluxes along an interface that does not coincide with a mesh line, as illustrated in figure 2.6 (right).

CHAPTER 3

A stabilized unfitted interface penalty method for the approximation of saddle point problems

3.1 Introduction

We continue the investigation of multidomain problems with homogeneous dimensions, where the model problem is characterized by high contrast coefficients.
As we have already discuss in the previous chapter, the extended finite element methods represent a vivid subject of research in the field of computational mechanics [57, 94], with the aim of enabling the accurate approximation of problems whose solutions involve jumps, kinks, singularities and other locally non-smooth features within elements. This is achieved by enriching the polynomial approximation space of the classical finite element method with non-smooth functions that resemble the true solution near interfaces.

In this chapter we aim to investigate the application of XFEMs, in particular of the method proposed in [63], to the approximation of saddle point problems. This method combines weak enforcement of interface conditions using Nitsche's method with XFEM approximation spaces, as we have already done in Chapter 2. From now on, we will refer to this family of methods as the Nitsche-XFEM schemes, as proposed in [60]. In particular, we apply the eXtended finite element method method to address a two-phase Stokes problem, namely the coupling of two fluids with different kinematic viscosities. Recently, XFEM has been applied to flow problems with moving interfaces, such as the numerical simulation of flows involving immiscible fluids, see for example [60] for a broad introduction or [99] for more specific applications. In this context, different types of enrichment strategies for the finite element approximation spaces have been proposed.

The method originally proposed in [63] for the approximation of the Laplace equa-

tion with contrast coefficients, that we have already discussed in the previous chapter, is particularly effective, owing to the good approximation properties and the simplicity of implementation. Indeed, it has been successfully extended to the approximation of saddle point problems in [3, 10, 18, 65]. The main drawback of the method consists in the lack of robustness when the interface cuts the mesh in a way that very small sub-elements are created, as we have already discussed in the previous chapter. We indeed observe that the interface conditions allow the pressure and the velocity gradients to be discontinuous across the interface. The XFEM is applied to accommodate both the weak discontinuity of the velocity field and the pressure jump across the interface on computational meshes that do not fit the interface itself. Numerical evidence shows that the discrete pressure approximation may be unstable in the neighborhood of the interface, even though the spatial approximation is based on *inf-sup* stable finite elements. As it will be confirmed by the numerical experiments reported in this chapter, for saddle point problems, additional instabilities arise because the enrichment of the Lagrange multiplier space (the pressure) affects the satisfaction of the *inf-sup* condition [14]. For this reason, resorting to pressure stabilization techniques in the region of elements cut by the unfitted interface is mandatory.

There are two possible solutions of this issue. On one hand, the enrichment method could be modified. This strategy has been investigated in a series of works [3,23,107]. It seems to be a promising method. However, a complete stability analysis of the proposed approximation spaces is not available yet. On the other hand, the stabilization methods developed to cure the instabilities with respect to small cut-elements may also help to stabilize the pressure. This is the approach successfully adopted in [10, 65].

Choosing a different strategy, we consider the application of stabilized equal order pressure / velocity XFEM discretizations and we analyze their approximation properties. On one side, this strategy increases the flexibility on the choice of velocity and pressure approximation spaces. On the other side, symmetric pressure stabilization operators, such as local pressure projection methods or the Brezzi-Pitkaranta scheme, seem to be effective to cure the additional source of instability arising from the XFEM approximation. We will show that these operators can be applied either *locally*, namely only in proximity of the interface, or *globally*, that is on the whole domain when combined with equal order approximations.

In the first part of this chapter we analyze the stability of the scheme, then we focus on the approximation properties and on the conditioning number of the scheme. We conclude the chapter with some numerical results and we discuss some benchmark cases, in order to thoroughly compare the performance of different variants of the method.

3.2 Problem set up

We consider again a domain $\Omega \subset \mathbb{R}^2$ crossed by an interface, that corresponds to a surface separating two fluids. We call Γ the interface that divides Ω into two open sets, Ω_1 and Ω_2. We solve:

$$\begin{cases} -\nabla \cdot (\mu_i \nabla \mathbf{u}) + \nabla p = \mathbf{f} & \text{in } \Omega_i, \\ \nabla \cdot \mathbf{u} = 0 & \text{in } \Omega_i, \\ \mathbf{u} = 0 & \text{on } \partial\Omega, \\ [\![\mathbf{u}]\!] = 0 & \text{on } \Gamma, \\ [\![p\mathbf{n} - \mu \nabla \mathbf{u} \cdot \mathbf{n}]\!] = 0 & \text{on } \Gamma. \end{cases} \tag{3.1}$$

The parameter μ_i plays the role of fluid viscosity and is constant in each subdomain Ω_i. Here, since $\mu_1 \neq \mu_2$, the continuity of stresses across Γ induces a kink on the velocity field and a strong discontinuity on pressure (also called jump discontinuity). This is a consequence of the interface conditions $(3.1)_{d,e}$ where $[\![v]\!] = v|_{\Omega_1} - v|_{\Omega_2}$ denotes the jump across Γ. Accordingly, $\mathbf{n}$ is the unit normal vector on Γ pointing from Ω_1 to Ω_2. The equilibrium condition between the normal component of the stresses may be generalized to include surface tension as follows:

$$[\![p\mathbf{n} - \mu \nabla \mathbf{u} \cdot \mathbf{n}]\!] = \tau \kappa \mathbf{n} \quad \text{on } \Gamma$$

where κ is the curvature of Γ and τ is the surface tension coefficient [60]. This more general condition can be naturally embedded in the numerical method that we will develop, giving rise to an additional right hand side proportional to $\tau\kappa\mathbf{n}$. Surface tension introduces a jump discontinuity across the interface in the pressure field, which can be accurately captured by the scheme. As a consequence, most of the results that we will present remain valid when surface tension is accounted for. Only the error analysis (Theorem 3.4.7) should be carefully reviewed, because the additional forcing term corresponding to surface tension features a poor regularity, which in turn affects the maximal regularity that can be assumed by the exact solution of the problem [95].

As we have already discussed, an approach based on finite elements where the computational mesh does not fit to the interface is not suitable for these kind of problems, because it does not satisfy optimal approximation properties. To preserve accuracy, the strong or weak discontinuities in the solution must coincide with mesh edges. However, for many time-dependent problems such as two-phase flows or fluid-structure interaction, non-matching grid formulations become an interesting option because they avoid re-meshing [99, 116, 117].

Mixed finite elements are a typical choice of approximation spaces for the discrete formulation of a saddle point problem without interface. It would be natural to expect that the same finite element spaces would be adequate also to solve the Nitsche-XFEM formulation interface problem. The numerical experiment shown in Figure 3.1 reveals that XFEM spaces do not inherit the *inf-sup* stability of the underlying FEM approximation. More precisely, Figure 3.1 suggests that pressure oscillations, resembling the checkerboard instability, appear in the neighborhood of the interface, even if the initial approximation space is *inf-sup* stable. In this case, the Nitsche-XFEM formulation is applied to solve problem (3.1) on a quasi uniform mesh cut by a circular interface separating two regions characterized by heterogeneous viscosities.

Following the approach already adopted in [10, 65], we investigate how to avoid these oscillations by the choice of suitable enriched finite element spaces and stabilization terms. Actually, instead of stabilization techniques based on the interior penalty technique, we study the behavior of the well known Brezzi-Pitkaranta stabilization

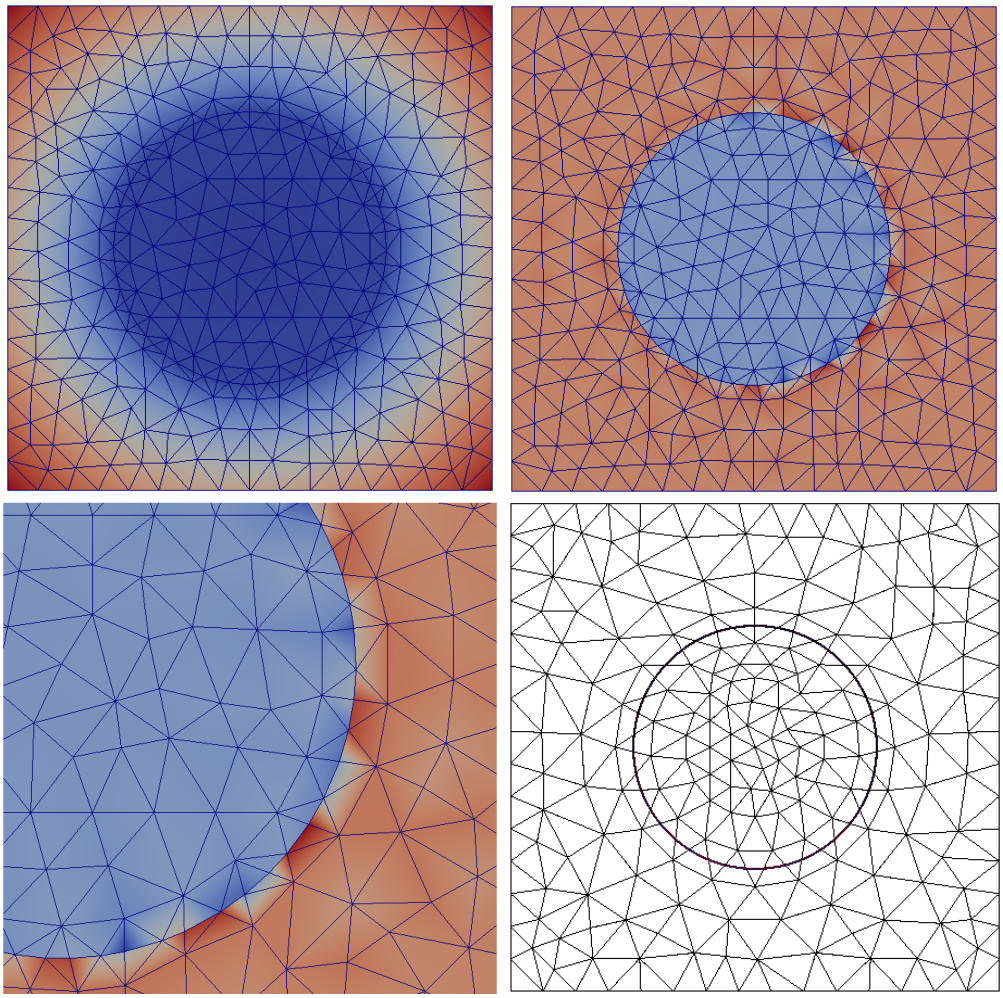

Figure 3.1: *For the test case #3 reported in Section 3.5, we show the typical checkerboard pattern of instabilities for the pressure in the cut region (b), while velocity approximation is not affected by instabilities, as confirmed by the visualization of the velocity field magnitude (a). In picture (c), a zoom on the pressure instabilities and in picture (d) the mesh that has been used for testing the conditioning of the problem, which results are also reported in Section 3.5*

technique [15] applied to this new context. Finally, we address the properties of the algebraic system of equations arising from the proposed discretization method. In particular, we study the spectrum of the Schur complement matrix, showing that the stabilization method is essential to ensure that the conditioning of the system does not depend on the diameter of cut-elements. This result has an important consequence: it confirms that the classical solution methods for algebraic saddle point problems, such as the Uzawa method, can be successfully combined with this approximation scheme.

3.3 Finite element formulation

We solve (3.1) on a conforming triangulation $\mathcal{T}_h$ of Ω, which is independent of the location of the interface Γ. However, we need to make some assumptions concerning the intersection between Γ and the mesh. Let us recall some definition, in particular let

$\mathcal{G}_h = \{K \in \mathcal{T}_h$ such that $K \cap \Gamma \neq \emptyset\}$ be the subset of cut elements and in the following, we call this subset *cut region*. Moreover, let us define the triangulated extended and restricted sub-domains, Ω_i^+, Ω_i^-, respectively, with $\Omega_i^- \subset \Omega_i^+$ as follows

$$\Omega_i^+ = \{\mathbf{x} \in K, \forall K \text{ such that } K \cap \Omega_i \neq \emptyset\}, \quad \Omega_i^- = \{\mathbf{x} \in K, \forall K \text{ such that } K \subset \Omega_i\}.$$

We observe that $\Omega_i^- \subset \Omega_i^+$ and

$$\Omega = \Omega_1^- \bigcup \Omega_2^- \bigcup \mathcal{G}_h, \quad \Omega_i^+ = \Omega_i^- \bigcup \mathcal{G}_h.$$

Starting from some assumptions made in the previous chapter, we highlight that:

Assumption 3.3.1. For any element K in the cut region and $i = 1, 2$ there exists a patch formed by the union of the element K with some of the elements of Ω_i^- sharing with it an edge (see figure 3.2a). This collection of elements is called a macro-element of K and it is denoted with $M_{K,i}$. Furthermore, we assume that the restriction of each macro-element to Ω_i^- is not empty, namely $M_{K,i}^- := M_{K,i} \cap \Omega_i^- \neq \emptyset$. Finally, we observe that $M_{K,i}^-$ contains at least an element of $\mathcal{T}_h$, such that the ratio $|M_{K,i}|/|M_{K,i}^-|$ is always upper bounded, where the symbol $|\cdot|$ represents the measure of a subset in $\mathbb{R}^2$.

Assumption 3.3.2. Γ intersects each element boundary ∂K exactly twice, and each (open) edge at most once.

Assumption 3.3.3. The interface is defined by the zero isoline of a level set function; the level set function is then approximated by linear interpolation on the computational mesh. The interface is thus represented by a chain of straight segments. We assume that the straight line segment Γ_h^K connecting the points of intersection between Γ and ∂K is a good approximation of $\Gamma_K = \Gamma \cap K$ in a sense that is detailed in [63], Assumption 3. This construction can be generalized to three space dimensions.

The first assumption is satisfied if the mesh is uniform, at least in the region neighboring the interface Γ. The last two hypotheses imply that the discrete approximation of the interface subdivides elements into simple shapes (a triangle and a quadrilateral or a couple of triangles).

We can now define the *extended cut region* $\mathcal{S}_h$ as the union of $\mathcal{G}_h$ and all the elements $K \in \mathcal{T}_h$ sharing an edge with at least a cut element (see figure 3.2b). This is equivalent to define $\mathcal{S}_h$ as the set of all the elements contained in at least one macro-element for all $K \in \mathcal{G}_h$:

$$\mathcal{S}_h := \bigcup_{K \in \mathcal{G}_h} \bigcup_{i=1,2} M_{K,i}$$

The proposed XFEM method doubles the degrees of freedom in the elements that are crossed by the discontinuity interface, as shown in figure 3.4. This is achieved by a suitable definition of the approximation spaces. Let $\mathcal{T}_{h,i}^+$ be conforming triangulations of Ω_i^+ such that the union of $\mathcal{T}_{h,1}^+$ and $\mathcal{T}_{h,2}^+$ gives $\mathcal{T}_h$ and for every triangle $K \in \mathcal{T}_{h,1}^+ \cap \mathcal{T}_{h,2}^+$ we have $K \cap \Gamma \neq \emptyset$. Moreover, we define $\mathcal{T}_{h,i}^- = \mathcal{T}_{h,i}^+ \setminus \mathcal{G}_h$. Let us define the following couple of *inf-sup* stable spaces on Ω,

$$V(\Omega) := [\{\phi_h \in C^0(\Omega), \text{ such that } \phi_h|_K \in \mathbb{P}^1, \forall K \in \mathcal{T}_h\} \cap H_0^1(\Omega) \oplus B]^2,$$
$$Q(\Omega) := \{\phi_h \in C^0(\Omega), \text{ such that } \phi_h|_K \in \mathbb{P}^1, \forall K \in \mathcal{T}_h\}$$

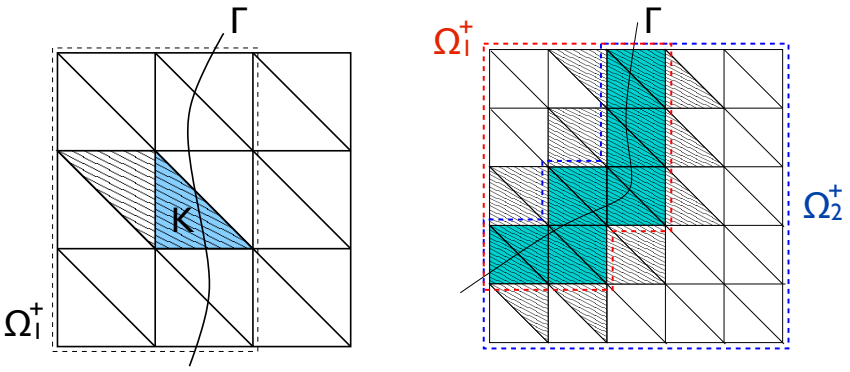

Figure 3.2: *(a) Filled with the diagonal line pattern, a macro-element for an element $K \in \mathcal{G}_h$ (in light blue). This macro-pattern is composed by K and its adjacent elements that shares an edge with it. (b) Definition of Ω_i^+, in light blue the set $\mathcal{G}_h$ and filled with the diagonal line pattern the extended cut region $\mathcal{S}_h$. As we can see, the extended region contains all the elements near to the cut region, meaning that they share an edge with at least one cut element.*

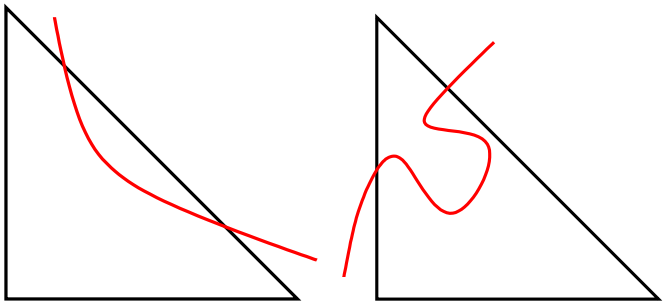

Figure 3.3: *Second (a) and third (b) assumption about the intersection between Γ and $\mathcal{T}_h$ are not satisfied.*

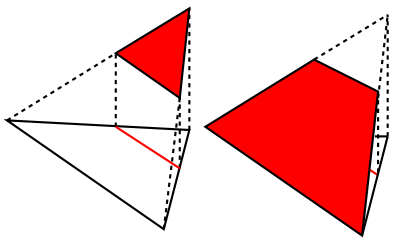

Figure 3.4: *Linear basis function in an element crossed by Γ. The local basis functions ϕ on a cut element K must be discontinuous across Γ:*

$$\phi = \phi_1 \text{ in } K_1 = K \cap \Omega_1, \qquad \phi_2 \text{ in } K_2 = K \cap \Omega_2.$$

Since ϕ_1 and ϕ_2 must be independent, we need to double the degrees of freedom on K so that ϕ_1 can be represented in K_1 by its nodal values and the same holds for ϕ_2.

where $B = \{b \text{ such that } b|_K \in \mathbb{P}^3 \cap H_0^1(K), \forall K \in \mathcal{T}_h\}$.

In alternative, we may use the plain $\mathbb{P}^1 - \mathbb{P}^1$ elements,

$$V(\Omega) := [\{\phi_h \in C^0(\Omega), \text{ such that } \phi_h|_K \in \mathbb{P}^1, \forall K \in \mathcal{T}_h\}]^2,$$
$$Q(\Omega) := \{\phi_h \in C^0(\Omega), \text{ such that } \phi_h|_K \in \mathbb{P}^1, \forall K \in \mathcal{T}_h\}$$

that will be combined with a stabilization term defined below. We now introduce the couple of *inf-sup* stable spaces on the restricted sub-domains Ω_i^-,

$$V_{h,i}^- := \{\phi_h \in V(\Omega_i^-), \text{ such that } \phi_h = 0 \text{ on } \Gamma\},$$
$$Q_{h,i}^- := Q(\Omega_i^-)$$

Let $\mathcal{I}_\Gamma = \{1, ..., n\}$ be the set of all vertexes in the *cut region* $\mathcal{G}_h$ and let

$$W_h = \{\phi_h \in C^0(\Omega), \text{ such that } \phi_h|_K \in \mathbb{P}^1, \forall K \in \mathcal{T}_h\} \cap H_0^1(\Omega)$$

be a standard linear finite element space on the triangulation $\mathcal{T}_h$ of the domain Ω and let $\{\phi_h^j\}$ be the Lagrangian basis of W_h. We can now define a couple of finite element spaces on the *cut region*:

$$V_h^{cut} := [span\{\phi_h^j \in W_h\}_{j\in\mathcal{I}_\Gamma}]^2, \quad Q_h^{cut} := span\{\phi_h^j \in W_h\}_{j\in\mathcal{I}_\Gamma}.$$

The definition of the finite element spaces for the approximation of our problem follows:

$$V_{h,i} := V_{h,i}^- \oplus V_h^{cut}, \quad Q_{h,i} := Q_{h,i}^- \oplus Q_h^{cut}.$$

The enrichment of the *cut region* is obtained by overlapping the spaces $V_{h,i}$ and $Q_{h,i}$ in $\mathcal{G}_h$ which entails that the degrees of freedom of the elements $K \in \mathcal{G}_h$ are doubled. We seek $(\mathbf{u}_{h,i}, p_{h,i}) \in V_{h,i} \times Q_{h,i}$, $i = 1, 2$ such that $\mathbf{u}_h = (\mathbf{u}_{h,1}, \mathbf{u}_{h,2})$ and $p_h = (p_{h,1}, p_{h,2})$ satisfy:

$$\mathcal{B}_h[(\mathbf{u}_h, p_h), (\mathbf{v}_h, q_h)] + s_h(p_h, q_h) = (\mathbf{f}, \mathbf{v}_h)_\Omega \,, \forall (\mathbf{v}_h, q_h) \in V_h \times Q_h \tag{3.2}$$

where $V_h = V_{h,1} \times V_{h,2}$, $Q_h = Q_{h,1} \times Q_{h,2}$ and

$$\begin{aligned}
\mathcal{B}_h[(\mathbf{u}_h, p_h), (\mathbf{v}_h, q_h)] := \quad & a_h(\mathbf{u}_h, \mathbf{v}_h) + b_h(p_h, \mathbf{v}_h) - b_h(q_h, \mathbf{u}_h) \\
a_h(\mathbf{u}_h, \mathbf{v}_h) := & \sum_{i=1,2} \int_{\Omega_i} \mu_i \nabla \mathbf{u}_{h,i} \cdot \nabla \mathbf{v}_{h,i} dx - \int_\Gamma \{\mu \nabla \mathbf{u}_h \cdot \mathbf{n}\} [\![\mathbf{v}_h]\!] ds \\
& - \int_\Gamma \{\mu \nabla \mathbf{v}_h \cdot \mathbf{n}\} [\![\mathbf{u}_h]\!] ds + \sum_{K\in\mathcal{G}_h} \int_{\Gamma_K} \gamma_u h_K^{-1} \mu_{max} [\![\mathbf{u}_h]\!][\![\mathbf{v}_h]\!] ds \\
b_h(p_h, \mathbf{v}_h) := & - \sum_{i=1,2} \int_{\Omega_i} p_{h,i} \nabla \cdot \mathbf{v}_{h,i} dx + \int_\Gamma \{p_h\} [\![\mathbf{v}_h \cdot \mathbf{n}]\!] ds
\end{aligned}$$

where h_K is the diameter of the generic element K. We fix $\mu_{max} = \max_\Omega \mu$ and we have defined the average operator as $\{v\}_\Gamma = \omega_1 v|_{\Omega_1} + \omega_2 v|_{\Omega_2}$. For each element $K \in \mathcal{G}_h$, it must hold $\omega_1 + \omega_2 = 1$. For this scheme it is important that the weights depend of the measure of cut elements, for example $\omega_i = |K \cap \Omega_i|/|K|$. In particular, we use the following definition proposed in [1]:

$$\omega_i := \frac{|K \cap \Omega_i|/\mu_i}{|K \cap \Omega_1|/\mu_1 + |K \cap \Omega_2|/\mu_2}. \tag{3.3}$$

We remark that in the homogeneous case we have $\mu_1 = \mu_2$, so that the last two definitions coincide.
The term $s_h(p_h, q_h)$ is the stabilization operator defined on the cut region. We are interested in analyzing the properties of the Brezzi-Pitkaranta stabilization technique [15] applied to this new context. For this reason, we consider the following operator acting on the pressure approximation near the interface:

$$s_h(p_h, q_h) := \sum_{i=1,2} \sum_{K \in \mathcal{S}_h} \gamma_s \mu_i^{-1} h_K^2 \int_K \nabla p_{h,i} \cdot \nabla q_{h,i} dx, \tag{3.4}$$

where $\mathcal{S}_h$ is the *extended cut region* previously defined. We remark that the integral in (3.4) is on the entire *cut* element K. This is crucial to prevent a bad conditioning of the algebraic problem.
As we have already pointed out, our choice of spaces $V_{h,i}^-$ and $Q_{h,i}^-$ is *inf-sup* stable on the restricted sub-domains. In the case of equal-order stabilized velocity/pressure formulation we add to the discrete problem formulation the additional stabilization term $c_h(p_h, q_h)$. Although $c_h(p_h, q_h)$ can be chosen among the family of symmetric stabilization operators, observing the definition of $s_h(p_h, q_h)$, the most natural choice is the Brezzi-Pitkaranta stabilization:

$$c_h(p_h, q_h) := \sum_{i=1,2} c_{h,i}(p_h, q_h), \quad \text{where} \quad c_{h,i}(p_h, q_h) := \sum_{K \in \mathcal{T}_{h,i}^-} \gamma_s \mu_i^{-1} h_K^2 \int_K \nabla p_{h,i} \cdot \nabla q_{h,i} dx.$$

In this case, we aim to find $\mathbf{u}_h = (\mathbf{u}_{h,1}, \mathbf{u}_{h,2}) \in V_h$ and $p_h = (p_{h,1}, p_{h,2}) \in Q_h$ such that

$$\mathcal{B}_h[(\mathbf{u}_h, p_h), (\mathbf{v}_h, q_h)] + c_h(p_h, q_h) + s_h(p_h, q_h) = (\mathbf{f}, \mathbf{v}_h)_\Omega, \forall (\mathbf{v}_h, q_h) \in V_h \times Q_h. \tag{3.5}$$

In the forthcoming sections, we will analyze the two proposed variants of the Nitsche-XFEM scheme.
A final remark concerns mass conservation. It is well known that stabilization techniques of Brezzi-Pitkaranta type introduce a consistency error in the mass conservation equation which is, in the classical setting, of order h^2. We wish to point out that in our proposed technique for $\mathbb{P}_b^1 - \mathbb{P}^1$ elements, the stabilization term is activated only in the subset $\mathcal{S}_h$ of elements adjacent to the interface Γ. Since the number of elements in $\mathcal{S}_h$ scales like h^{-1} (and not h^{-2} as the total number of mesh elements), the error in mass conservation introduced by our proposed method is of order h^3. Thus, in our opinion, it is acceptable in practice.

3.4 Analysis of the scheme

First of all, let us define the following norms on the trace of a function on Γ:

$$\|v\|_{1/2,h,\Gamma}^2 := \sum_{K \in \mathcal{G}_h} h_K^{-1} \|v\|_{0,\Gamma_K}^2, \qquad \|v\|_{-1/2,h,\Gamma}^2 := \sum_{K \in \mathcal{G}_h} h_K \|v\|_{0,\Gamma_K}^2$$

Then, we introduce the following broken Sobolev spaces: $H_b^k = \{v : v|_{\Omega_i} \in H^k(\Omega_i), i = 1, 2\}$ with the corresponding norms

$$\|\mathbf{v}\|_{k,\Omega}^2 := \sum_{i=1,2} \|\mathbf{v}\|_{k,\Omega_i}^2, \quad \|\mathbf{v}\|_{k,\Omega,\mu}^2 := \sum_{i=1,2} \|\mu_i^{1/2}\mathbf{v}\|_{k,\Omega_i}, \quad \|q\|_{k,\Omega^\pm,\mu}^2 := \sum_{i=1,2} \|\mu_i^{-1/2} q\|_{k,\Omega_i^\pm},$$

$$|||\mathbf{v}|||^2 := \|\mathbf{v}\|_{1,\Omega,\mu}^2 + \|\mu_{max}^{1/2}[\![\mathbf{v}]\!]\|_{1/2,h,\Gamma}^2 + \|\mu_{max}^{-1/2}\{\mu\nabla_{\mathbf{n}}\mathbf{v}\}\|_{-1/2,h,\Gamma}^2,$$

$$\|(\mathbf{v}, q)\|_{\Omega^+}{}^2 := |||\mathbf{v}|||^2 + \|q\|_{0,\Omega^+,\mu}^2 + \|\mu_{max}^{-1/2}\{q\}\|_{-1/2,h,\Gamma}^2.$$

Let us define $b_{h,i}(p_h, q_h)$ as the restrictions of $b_h(p_h, q_h)$ on the domains Ω_i,

$$b_{h,i}(p_h, q_h) := -\int_{\Omega_i} p_{h,i}\nabla \cdot \mathbf{v}_{h,i} dx,$$

and let us introduce the discrete trace inequality

$$h_k\|v\|_{0,\Gamma_K}^2 \leq C\|v\|_{0,K}^2, \tag{3.6}$$

that will be necessary for the theoretical analysis, as in [65], and proved thanks to [13] and [63]. Thanks to this inequality, taking $q_h \in Q_h$, we have,

$$\begin{aligned}
\|\mu_{max}^{-1/2}\{q\}\|_{-1/2,h,\Gamma}^2 &\leq \|\{\mu^{-1/2}q_h\}\|_{-1/2,h,\Gamma}^2 = \sum_{K\in\mathcal{G}_h} h_K\|\{\mu^{-1/2}q_h\}\|_{0,\Gamma_K}^2 \\
&\leq \sum_{K\in\mathcal{G}_h} h_K(\|\mu_1^{-1/2}k_1 q_{h,1}\|_{0,\Gamma_K}^2 + \|\mu_2^{-1/2}k_2 q_{h,2}\|_{0,\Gamma_K}^2) \\
&\leq C\sum_{i=1,2}\sum_{K\in\mathcal{G}_h} \|\mu_i^{-1/2}k_i q_{h,i}\|_{0,K}^2 \\
&\leq C\sum_{i=1,2}\sum_{K\in\mathcal{G}_h} \|\mu_i^{-1/2}q_{h,i}\|_{0,K}^2 \\
&\leq C\sum_{i=1,2}\sum_{K\in\mathcal{T}_{h,i}^+} \|\mu_i^{-1/2}q_{h,i}\|_{0,K}^2 = C\|q_h\|_{0,\Omega^+,\mu}^2.
\end{aligned}$$

In particular, the following equivalence of discrete norms holds true,

$$|||\mathbf{v}|||^2 + \|q_h\|_{0,\Omega^+,\mu}^2 \leq \|(\mathbf{v}, q_h)\|_{\Omega^+}{}^2 \leq |||\mathbf{v}|||^2 + (1 + C)\|q_h\|_{0,\Omega^+,\mu}^2. \tag{3.7}$$

3.4.1 Stability analysis

The first part of our theoretical analysis focuses on the stability of the scheme.

Theorem 3.4.1. *We assume that our finite element scheme is inf-sup stable away from the cut region, i.e. there exist constants C_{p1} and C_{p2}, independent of the mesh size, such that $\forall p_{h,i} \in Q_{h,i}$ there exists $\mathbf{v}_{p_{h,i}} \in V_{h,i} : \mathbf{v}_{p_{h,i}}|_{\mathcal{G}_h} = 0$, such that*

$$\|\mathbf{v}_{p_{h,i}}\|_{1,\Omega_i^-,\mu} \leq C_{p1}\|p_{h,i}\|_{0,\Omega_i^-,\mu}, \tag{3.8}$$

$$C_{p2}\|p_{h,i}\|_{0,\Omega_i^-,\mu} \leq b_{h,i}(p_{h,i}, \mathbf{v}_{p_{h,i}}) + c_{h,i}(p_{h,i}, p_{h,i}). \tag{3.9}$$

These are sufficient conditions for the stability of the approximation on the subregion Ω_i^-, see [42]. Under this assumption, there exists a positive constant C_s, independent of the mesh characteristic size such that, for any $(\mathbf{u}_h, p_h) \in V_h \times Q_h$ it holds:

$$C_s\|(\mathbf{u}_h, p_h)\|_{\Omega^+} \leq \sup_{(\mathbf{v}_h,q_h)\in V_h\times Q_h} \frac{\mathcal{B}_h[(\mathbf{u}_h, p_h), (\mathbf{v}_h, q_h)] + c_h(p_h, q_h) + s_h(p_h, q_h)}{\|(\mathbf{v}_h, q_h)\|_{\Omega^+}}. \tag{3.10}$$

We remark that (3.8) implies

$$\|\mathbf{v}_{p_{h,i}}\|_{1,\Omega_i^-,\mu} \leq C_{p1}\|p_{h,i}\|_{0,\Omega_i^+,\mu}.$$

To prove (3.10), we start showing some properties of the bilinear forms $a_h(\mathbf{u}_h, \mathbf{v}_h)$, $b_h(\mathbf{v}_h, p_h)$, $c_h(p_h, q_h)$ and $s_h(p_h, q_h)$.

Lemma 3.4.2. *The bilinear discrete form $a_h(\mathbf{u}_h, \mathbf{v}_h)$ is continuous on V_h and coercive, provided γ_u is chosen sufficiently large. That is, there exist two constants C_m and C_a, independent of the mesh size such that*

$$a_h(\mathbf{u}_h, \mathbf{v}_h) \leq C_m|||\mathbf{u}_h||| \, |||\mathbf{v}_h|||, \quad \forall \mathbf{v}_h \in V_h, \tag{3.11}$$

$$a_h(\mathbf{v}_h, \mathbf{v}_h) \geq C_a|||\mathbf{v}_h|||^2, \quad \forall \mathbf{v}_h \in V_h. \tag{3.12}$$

Let $\mathbf{v}_h \in V_h$, $p_h \in Q_h$ and $q_h \in Q_h$. There exist three constants C_b, C_{s1} and C_{s2}, independent of the mesh size, such that

$$b_h(\mathbf{v}_h, p_h) \leq C_b|||\mathbf{v}_h|||(\|p_h\|_{0,\Omega^+,\mu} + \|\mu_{max}^{-1/2}\{p_h\}\|^2_{-1/2,h,\Gamma}) \tag{3.13}$$

$$c_h(p_h, q_h) \leq C_{s1}\|p_h\|_{0,\Omega^+,\mu}\|q_h\|_{0,\Omega^+,\mu}, \tag{3.14}$$

$$s_h(p_h, q_h) \leq C_{s2}\|p_h\|_{0,\Omega^+,\mu}\|q_h\|_{0,\Omega^+,\mu}. \tag{3.15}$$

Furthermore, owing to (3.11) and (3.13), the bilinear discrete form $\mathcal{B}_h[(\mathbf{u}_h, p_h), (\mathbf{v}_h, q_h)]$ is continuous on $V_h \times Q_h$,

$$\mathcal{B}_h[(\mathbf{u}_h, p_h), (\mathbf{v}_h, q_h)] \leq C_B\|(\mathbf{u}_h, p_h)\|_{\Omega^+}\|(\mathbf{v}_h, q_h)\|_{\Omega^+}. \tag{3.16}$$

Proof. To prove (3.12), we first prove the following generalized inverse estimate,

$$\|\{\mu\nabla_{\mathbf{n}}\mathbf{v}_h\}\|^2_{-1/2,h,\Gamma} \leq C_I\mu_{max}\|\mathbf{v}_h\|^2_{1,\Omega,\mu} \tag{3.17}$$

where $\nabla_{\mathbf{n}}\mathbf{v}_h = (\nabla\mathbf{v}_h)\mathbf{n}$. where $\nabla_{\mathbf{n}}\mathbf{v}_h = (\nabla\mathbf{v}_h)\mathbf{n}$. This estimate holds true when linear finite elements and the weights ω_i defined in (3.3) are used. In this particular case the constant C_I is such that $C_I \leq 2$. For the proof of (3.17) we observe that, since $\mathbf{v}_h$ is

linear in $\mathcal{G}_h$, for every $K \in \mathcal{G}_h$ we have,

$$\begin{aligned}
\|\{\mu\nabla_{\mathbf{n}}\mathbf{v}_h\}\|^2_{-1/2,h,\Gamma_K} &= h_K|\Gamma_K|\left(k_1\mu_1\nabla_{\mathbf{n}}\mathbf{v}_{h,1} + k_2\mu_2\nabla_{\mathbf{n}}\mathbf{v}_{h,2}\right)^2 \\
&\leq h_K \sum_{i=1,2} \frac{|\Gamma_K|}{|K\cap\Omega_i|} k_i^2\mu_i^2 \|\nabla\mathbf{v}_{h,i}\|^2_{0,K\cap\Omega_i} \\
&= h_K \sum_{i=1,2} \frac{|\Gamma_K|}{|K\cap\Omega_i|} \frac{|K\cap\Omega_i|^2/\mu_i^2}{\big(\sum_{j=1,2}|K\cap\Omega_j|/\mu_j\big)^2} \mu_i^2 \|\nabla\mathbf{v}_{h,i}\|^2_{0,K\cap\Omega_i} \\
&= h_K|\Gamma_K| \frac{1}{\big(\sum_{j=1,2}|K\cap\Omega_j|/\mu_j\big)^2} \sum_{i=1,2} \frac{|K\cap\Omega_i|}{\mu_i} \|\mu_i^{1/2}\nabla\mathbf{v}_{h,i}\|^2_{0,K\cap\Omega_i} \\
&\leq h_K|\Gamma_K| \frac{1}{|K\cap\Omega_1|/\mu_1 + |K\cap\Omega_2|/\mu_2} \sum_{i=1,2} \|\nabla\mathbf{v}_{h,i}\|^2_{0,K\cap\Omega_i,\mu} \\
&\leq \frac{h_K|\Gamma_K|}{|K|}\mu_{max}\|\nabla\mathbf{v}_h\|^2_{0,K,\mu} \\
&= C_{I,K}\mu_{max}\|\nabla\mathbf{v}_h\|^2_{0,K,\mu}.
\end{aligned}$$

We point out that, under the assumption of shape-regular mesh, the constant $C_{I,K}$ is bounded independently of the mesh size and the location of the interface Γ. Indeed it is simple to prove that $C_{I,K} \leq 2$. Summing over all the elements K $\in \mathcal{G}_h$ and setting $C_I = \max_K C_{I,K}$ we have

$$\begin{aligned}
\|\{\mu\nabla_{\mathbf{n}}\mathbf{v}_h\}\|^2_{-1/2,h,\Gamma} &\leq \sum_{K\in\mathcal{G}_h} C_{I,K}\mu_{max}\|\nabla\mathbf{v}_h\|^2_{0,K,\mu} \\
&\leq C_I\mu_{max}\sum_{K\in\mathcal{T}_h}\|\nabla\mathbf{v}_h\|^2_{0,K,\mu} \\
&= C_I\mu_{max}\|\nabla\mathbf{v}_h\|^2_{0,\Omega,\mu}.
\end{aligned}$$

We are now ready to prove coercivity.

$$\begin{aligned}
a_h(\mathbf{v}_h,\mathbf{v}_h) &= \sum_{i=1,2}\int_\Omega \mu_i(\nabla\mathbf{v}_{h,i})^2dx - 2\int_\Gamma [\![\mathbf{v}_h]\!]\{\mu\nabla_{\mathbf{n}}\mathbf{v}_h\}\,ds + \int_\Gamma \gamma_u\mu_{max}h_K^{-1}([\![\mathbf{v}_h]\!])^2ds \\
&\geq \|\mathbf{v}_h\|^2_{1,\Omega,\mu} + \gamma_u\|\mu_{max}^{1/2}[\![\mathbf{v}_h]\!]\|^2_{1/2,h,\Gamma} - 2\|\mu_{max}^{1/2}[\![\mathbf{v}_h]\!]\|_{1/2,h,\Gamma}\|\mu_{max}^{-1/2}\{\mu\nabla_{\mathbf{n}}\mathbf{v}_h\}\|_{-1/2,h,\Gamma} \\
&\geq \|\mathbf{v}_h\|^2_{1,\Omega,\mu} + (\gamma_u-\epsilon)\|\mu_{max}^{1/2}[\![\mathbf{v}_h]\!]\|^2_{1/2,h,\Gamma} - \frac{1}{\epsilon}\|\mu_{max}^{-1/2}\{\mu\nabla_{\mathbf{n}}\mathbf{v}_h\}\|^2_{-1/2,h,\Gamma}.
\end{aligned}$$

Then, it follows from (3.17) that

$$\begin{aligned}
a_h(\mathbf{v}_h,\mathbf{v}_h) \geq \frac{1}{2}\|\mathbf{v}_h\|^2_{1,\Omega,\mu} &+ \left(\frac{1}{2} - \frac{2C_I}{\epsilon}\right)\|\mathbf{v}_h\|^2_{1,\Omega,\mu} \\
&+ \frac{1}{\epsilon}\|\mu_{max}^{-1/2}\{\mu\nabla_{\mathbf{n}}\mathbf{v}_h\}\|^2_{-1/2,h,\Gamma} + (\gamma_u-\epsilon)\|\mu_{max}^{1/2}[\![\mathbf{v}_h]\!]\|^2_{1/2,h,\Gamma}.
\end{aligned}$$

Taking $\epsilon = 4C_I$ and choosing $\gamma_u > 4C_I$ the coercivity of $a_h(\mathbf{u}_h,\mathbf{v}_h)$ follows, since

$$a_h(\mathbf{v}_h,\mathbf{v}_h) \geq \min\{\frac{1}{2}, C_{\gamma_u}, \frac{1}{4C_I}\}(\|\mathbf{v}_h\|^2_{1,\Omega,\mu} + \|\mu_{max}^{1/2}[\![\mathbf{v}_h]\!]\|^2_{1/2,h,\Gamma} + \|\mu_{max}^{-1/2}\{\mu\nabla_{\mathbf{n}}\mathbf{v}_h\}\|^2_{-1/2,h,\Gamma})$$

where $C_{\gamma_u} = (\gamma_u - 4C_I)$. This completes the proof. Continuity of the discrete form $a_h(\mathbf{u}_h, \mathbf{v}_h)$ follows directly from its definition, while to prove the continuity of $b_h(p_h, \mathbf{v}_h)$ we proceed as follows,

$$\begin{aligned} b_h(p_h, \mathbf{v}_h) &= -\sum_{i=1,2} \int_{\Omega_i} p_{h,i} \nabla \cdot \mathbf{v}_{h,i} dx + \int_\Gamma \{p_h\} [\![\mathbf{v}_h \cdot \mathbf{n}]\!] ds \\ &\leq \|p_h\|_{0,\Omega^+,\mu} \|v_h\|_{1,\Omega,\mu} + \|\mu_{max}^{-1/2} \{p_h\}\|_{-1/2,h,\Gamma} \|\mu_{max}^{1/2} [\![\mathbf{v}_h \cdot \mathbf{n}]\!]\|_{1/2,h,\Gamma} \\ &\leq C_b |||\mathbf{v}_h||| (\|p_h\|_{0,\Omega^+,\mu} + \|\mu_{max}^{-1/2} \{p_h\}\|_{-1/2,h,\Gamma}). \end{aligned}$$

Continuity of the stabilization operator $c_h(p_h, q_h)$ is proved as follows,

$$\begin{aligned} c_h(p_h, q_h) &= \sum_{i=1,2} \sum_{K \in \mathcal{T}_{h,i}^-} \gamma_s \mu_i^{-1} h_K^2 \int_K \nabla p_{h,i} \cdot \nabla q_{h,i} dx \\ &\leq \sum_{i=1,2} \sum_{K \in \mathcal{T}_{h,i}^-} \gamma_s h_K^2 h_K^{-2} \|\mu_i^{-1/2} p_h\|_{0,K} \|\mu_i^{-1/2} q_h\|_{0,K} \\ &\leq C_{s1} \|p_h\|_{0,\Omega^+,\mu} \|q_h\|_{0,\Omega^+,\mu}. \end{aligned}$$

Here the first inequality follows from the inverse inequality. The continuity of $s_h(p_h, q_h)$ is actually obtained in the same way. Summing estimates (3.11) and (3.13) and using the definition of the norm $\|(\cdot,\cdot)\|_{\Omega^+}$ yield the result (3.16). □

To prove the *inf-sup* condition, we first consider a stability estimate for a projection operator.

Lemma 3.4.3. *The L^2 projection operator on a macro-element $M_{K,i}$, namely $\Pi_h : H^1(M_{K,i}) \mapsto \mathbb{P}^1(M_{K,i})$, satisfies the following property:*

$$\|p_{h,i}\|_{0,\Omega_i^+,\mu}^2 \leq C \left(\|p_{h,i}\|_{0,\Omega_i^-,\mu}^2 + \gamma_{h,i}(p_{h,i}, p_{h,i}) \right), \tag{3.18}$$

where

$$\gamma_{h,i}(p_{h,i}, q_{h,i}) := \sum_{K \in \mathcal{G}_h} \int_{M_{K,i}} \gamma_s \mu_i^{-1} (1-\Pi_h) p_{h,i} (1-\Pi_h) q_{h,i}, \quad \gamma_h(p_h, q_h) := \sum_{i=1,2} \gamma_{h,i}(p_{h,i}, q_{h,i})$$

and C is a constant dependent on the total number of elements that can form a macro-element $M_{K,i}$ with a generic element $K \in \mathcal{G}_h$.

Proof. Since $\Pi_h p_{h,i}$ is a linear function on a macro-element, it holds that:

$$\|\Pi_h p_{h,i}\|_{0,M_{K,i}}^2 \lesssim \frac{|M_{K,i}|}{|M_{K,i}^-|} \|\Pi_h p_{h,i}\|_{0,M_{K,i}^-}^2,$$

where, as we have introduced in the previous chapter, the notation $x \lesssim y$ represents the existence of a generic constant c such that $x \leq cy$. We represent $p_{h,i}|_{M_{K,i}}$ as the sum of the linear part and a residual: $p_{h,i}|_{M_{K,i}} = \Pi_h p_{h,i} + r_{h,i}$. It follows that

$$\begin{aligned} \|p_{h,i}\|_{0,M_{K,i}}^2 &= \|\Pi_h p_{h,i} + r_{h,i}\|_{0,M_{K,i}}^2 \\ &= \|\Pi_h p_{h,i}\|_{0,M_{K,i}}^2 + \|r_{h,i}\|_{0,M_{K,i}}^2 \\ &\lesssim \frac{|M_{K,i}|}{|M_{K,i}^-|} \|\Pi_h p_{h,i}\|_{0,M_{K,i}^-}^2 + \|r_{h,i}\|_{0,M_{K,i}}^2. \end{aligned}$$

Owing to assumption 3.3.1, the ratio between the measure of the entire macro-element and its restriction is upper bounded. We now consider the second member of the last inequality, where we identify $\beta = |M_{K,i}|/|M^-_{K,i}|$ in order to simplify the notation:

$$\begin{aligned}
\beta\|\Pi_h p_{h,i}\|^2_{0,M^-_{K,i}} + \|r_{h,i}\|^2_{0,M_{K,i}} &= \beta\|\Pi_h p_{h,i}\|^2_{0,M^-_{K,i}} - \beta\|r_{h,i}\|^2_{0,M_{K,i}} + (1+\beta)\|r_{h,i}\|^2_{0,M^-_{K,i}} \\
&\leq \beta \int_{M^-_{K,i}} (\Pi_h p_{h,i} - r_{h,i})(\Pi_h p_{h,i} + r_{h,i}) + (1+\beta)\|r_{h,i}\|^2_{0,M_{K,i}} \\
&\leq \frac{\beta\epsilon}{2}\|\Pi_h p_{h,i} - r_{h,i}\|^2_{0,M_{K,i}} + \frac{\beta}{2\epsilon}\|p_{h,i}\|^2_{0,M^-_{K,i}} + (1+\beta)\|r_{h,i}\|^2_{0,M_{K,i}} \\
&\leq \frac{\beta\epsilon}{2}\|\Pi_h p_{h,i}\|^2_{0,M_{K,i}} + \frac{\beta\epsilon}{2}\|r_{h,i}\|^2_{0,M_{K,i}} + \frac{\beta}{2\epsilon}\|p_{h,i}\|^2_{0,M^-_{K,i}} \\
&\quad + (1+\beta)\|r_{h,i}\|^2_{0,M_{K,i}}.
\end{aligned}$$

Since

$$\|p_{h,i}\|^2_{0,M_{K,i}} = (1 - \frac{\beta\epsilon}{2})\|p_{h,i}\|^2_{0,M_{K,i}} + \frac{\beta\epsilon}{2}\|\Pi_h p_{h,i}\|^2_{0,M_{K,i}} + \frac{\beta\epsilon}{2}\|r_{h,i}\|^2_{0,M_{K,i}},$$

we obtain

$$\begin{aligned}
&(1 - \frac{\beta\epsilon}{2})\|p_{h,i}\|^2_{0,M_{K,i}} + \frac{\beta\epsilon}{2}\|\Pi_h p_{h,i}\|^2_{0,M_{K,i}} + \frac{\beta\epsilon}{2}\|r_{h,i}\|^2_{0,M_{K,i}} \\
&\quad\lesssim \frac{\beta\epsilon}{2}\|\Pi_h p_{h,i}\|^2_{0,M_{K,i}} + \frac{\beta\epsilon}{2}\|r_{h,i}\|^2_{0,M_{K,i}} + \frac{\beta}{2\epsilon}\|p_{h,i}\|^2_{0,M^-_{K,i}} + (1+\beta)\|r_{h,i}\|^2_{0,M_{K,i}},
\end{aligned}$$

from which it follows that

$$\|p_{h,i}\|^2_{0,M_{K,i}} \lesssim \frac{2\beta}{2\epsilon(2-\beta\epsilon)}\|p_{h,i}\|^2_{0,M^-_{K,i}} + \frac{2(1+\beta)}{2-\beta\epsilon}\|r_{h,i}\|^2_{0,M_{K,i}}. \tag{3.19}$$

Choosing a suitable ϵ, for instance $\epsilon = \beta^{-1}$ we have

$$\|p_{h,i}\|^2_{0,M_{K,i}} \lesssim \|p_{h,i}\|^2_{0,M^-_{K,i}} + \|r_{h,i}\|^2_{0,M_{K,i}},$$

and, because of the equivalence of the discrete norms,

$$\|\mu^{-1/2}p_{h,i}\|^2_{0,M_{K,i}} \lesssim \|\mu^{-/2}p_{h,i}\|^2_{0,M^-_{K,i}} + \|\mu^{-1/2}r_{h,i}\|^2_{0,M_{K,i}}.$$

To conclude, we sum over all elements of Ω^+_i and rescale all norms using $\mu_i^{-1/2}$, to obtain

$$\begin{aligned}
\|p_{h,i}\|^2_{0,\Omega^+_i,\mu} &= \|p_{h,i}\|^2_{0,\Omega^-_i,\mu} + \sum_{K\in\mathcal{G}_h}\|\mu_i^{-1/2}p_{h,i}\|^2_{0,K} \\
&\leq \|p_{h,i}\|^2_{0,\Omega^-_i,\mu} + \sum_{K\in\mathcal{G}_h}\|\mu_i^{-1/2}p_{h,i}\|^2_{0,M_{K,i}} \\
&\lesssim \|p_{h,i}\|^2_{0,\Omega^-_i,\mu} + \sum_{K\in\mathcal{G}_h}\left(\|\mu_i^{-1/2}p_{h,i}\|^2_{0,M^-_{K,i}} + \|\mu_i^{-1/2}r_{h,i}\|^2_{0,M_{K,i}}\right) \\
&\lesssim C(\mathcal{T}_h)\left(\|p_{h,i}\|^2_{0,\Omega^-_i,\mu} + \gamma_{h,i}(p_{h,i},p_{h,i})\right).
\end{aligned}$$

We remark that, since we are summing on the macro-elements of all $K \in \mathcal{G}_h$, some elements will be counted more than once. The mesh-dependent constant $C(\mathcal{T}_h)$ that appear in the proof takes into account this fact. □

This result gives origin to several families of stabilization methods. Notably the ghost penalty methods as well as the Brezzi-Pitkaranta stabilization can be seen as schemes to control the local operator.

Lemma 3.4.4. *The stabilization term*

$$s_h(p_h, q_h) = \sum_{i=1,2} \sum_{K \in \mathcal{S}_h} \gamma_s \mu_i^{-1} h_K^2 \int_K \nabla p_{h,i} \cdot \nabla q_{h,i} dx$$

dominates on the local projection stabilization, that is

$$\gamma_h(q_h, q_h) \lesssim s_h(q_h, q_h). \tag{3.20}$$

Proof. We use the following result [17, 42]:

$$\|q_{h,i} - \Pi_h q_{h,i}\|_{0,M_{K,i}} \leq Ch \|\nabla q_{h,i}\|_{L^2(M_{K,i})}, \quad \forall q_{h,i} \in Q_{h,i},$$

where the constant C is independent of the mesh size. We can now write,

$$\begin{aligned}
\gamma_h(q_h, q_h) &= \sum_{i=1,2} \sum_{K \in \mathcal{G}_h} \gamma_s \mu_i^{-1} \|(1 - \Pi_h) q_{h,i}\|^2_{0,M_{K,i}} \\
&\leq \sum_{i=1,2} \sum_{K \in \mathcal{G}_h} C \gamma_s \mu_i^{-1} h_K^2 \|\nabla q_{h,i}\|^2_{0,M_{K,i}} \\
&\leq C(\mathcal{T}_h) \sum_{i=1,2} \sum_{K \in \mathcal{S}_h} \gamma_s \mu_i^{-1} h_K^2 \|\nabla q_{h,i}\|^2_{0,K} \\
&\lesssim s_h(q_h, q_h).
\end{aligned}$$

where $C(\mathcal{T}_h)$ depends on the number of elements that form each macro-element. □

The following property is a consequence of lemmas 3.4.3 and 3.4.4:

$$\|p_{h,i}\|^2_{0,\Omega_i^+,\mu} \lesssim \|p_{h,i}\|^2_{0,\Omega_i^-,\mu} + s_h(p_{h,i}, p_{h,i}). \tag{3.21}$$

It shows that in the Nitsche-XFEM method, the discrete pressure can be controlled provided that an inf-sup stable velocity/pressure approximation is combined with the Brezzi-Pitkaranta operator restricted to the neighborhood of the cut region. Using standard arguments, see [10], we now prove that the scheme is stable in the sense specified in Theorem 3.4.1.

Proof. For the proof of theorem 3.4.1], as first step we prove the *inf-sup* stability on the domain Ω, given the local stability estimates (on the restricted sub-domains):

$$b(p_h, \mathbf{v}_{p_h}) + c_h(p_h, p_h) + s_h(p_h, p_h) \gtrsim C_{p2} \|p_h\|^2_{0,\Omega^+,\mu}. \tag{3.22}$$

We take a $\mathbf{v}_{p_h} = (\mathbf{v}_{p_{h,1}}, \mathbf{v}_{p_{h,2}})$ satisfying the assumptions of the theorem and, reminding that $\mathbf{v}_{p_{h,i}}$ are null on the *cut region* since their support is limited to the restricted sub-domain Ω_i^-, we can write:

$$b(p_h, \mathbf{v}_{p_h}) = -\sum_{i=1,2} \int_{\Omega_i} p_{h,i} \nabla \cdot \mathbf{v}_{p_{h,i}} dx + \int_\Gamma \{p_h\} [\![\mathbf{v}_{p_h} \cdot \mathbf{n}]\!] ds = \sum_{i=1,2} b_{h,i}(p_{h,i}, \mathbf{v}_{p_{h,i}})$$

$$\sum_{i=1,2} \big(b_{h,i}(p_{h,i}, \mathbf{v}_{p_{h,i}}) + c_{h,i}(p_{h,i}, q_{h,i}) \big) = b_h(p_h, \mathbf{v}_{p_h}) + c_h(p_h, p_h) \gtrsim \sum_{i=1,2} C_{p2} \|p_{h,i}\|_{0,\Omega_i^-,\mu}.$$

Using inequality (3.21), we are now able to prove the global *inf-sup* stability (3.22):

$$b_h(p_h, \mathbf{v}_{p_h}) + c_h(p_h, p_h) + s_h(p_h, p_h) \geq \sum_{i=1,2} C_{p2} \|p_{h,i}\|_{0,\Omega_i^-,\mu} + s_h(p_h, p_h)$$
$$\gtrsim C_{p2} \|p_h\|^2_{0,\Omega^+,\mu}.$$

We are now ready to complete the proof. Using the test functions $\mathbf{v}_h = \mathbf{u}_h + \eta \mathbf{v}_{p_h}$ and $q_h = p_h$, we obtain that

$$\|(\mathbf{v}_h, q_h)\|_{\Omega^+} = \|(\mathbf{u}_h + \eta \mathbf{v}_{p_h}, p_h)\|_{\Omega^+} \leq \|(\mathbf{u}_h, p_h)\|_{\Omega^+} + \|(\eta \mathbf{v}_{p_h}, 0)\|_{\Omega^+}$$
$$= \|(\mathbf{u}_h, p_h)\|_{\Omega^+} + |||\eta \mathbf{v}_{p_h}||| = \|(\mathbf{u}_h, p_h)\|_{\Omega^+} + \|\eta \mathbf{v}_{p_h}\|_{1,\Omega,\mu}$$

and using (3.8) we get,

$$\|\eta \mathbf{v}_{p_h}\|^2_{1,\Omega,\mu} = \eta^2 \|\mathbf{v}_{p_h}\|^2_{1,\Omega,\mu} \leq \eta^2 \sum_{i=1,2} C^2_{p1} \|p_{h,i}\|^2_{0,\Omega_i^-,\mu}$$
$$\leq \eta^2 \sum_{i=1,2} C^2_{p1} \|p_{h,i}\|^2_{0,\Omega_i^+,\mu} \leq \eta^2 C^2_{p1} \|(\mathbf{u}_h, p_h)\|_{\Omega^+}{}^2$$

which allows us to write,

$$\|(\mathbf{v}_h, q_h)\|_{\Omega^+} \leq \|(\mathbf{u}_h, p_h)\|_{\Omega^+} + \eta C_{p1} \|(\mathbf{u}_h, p_h)\|_{\Omega^+} = (1 + \eta C_{p1}) \|(\mathbf{u}_h, p_h)\|_{\Omega^+} \lesssim \|(\mathbf{u}_h, p_h)\|_{\Omega^+}.$$

Now we develop the term $\mathcal{B}_h[(\mathbf{u}_h, p_h), (\mathbf{v}_h, q_h)]$ as

$$\mathcal{B}_h[(\mathbf{u}_h, p_h), (\mathbf{v}_h, q_h)] = a_h(\mathbf{u}_h, \mathbf{u}_h + \eta \mathbf{v}_{p_h}) + b_h(p_h, \mathbf{u}_h + \eta \mathbf{v}_{p_h}) - b_h(p_h, \mathbf{u}_h)$$
$$= a_h(\mathbf{u}_h, \mathbf{u}_h) + a_h(\mathbf{u}_h, \eta \mathbf{v}_{p_h}) + b_h(p_h, \eta \mathbf{v}_{p_h}). \tag{3.23}$$

As for the term $a_h(\mathbf{u}_h, \eta \mathbf{v}_{p_h})$, we get

$$a_h(\mathbf{u}_h, \eta \mathbf{v}_{p_h}) = \sum_{i=1,2} \int_{\Omega_i} \mu_i \nabla \mathbf{u}_{h,i} \eta \nabla \mathbf{v}_{p_{h,i}} dx - \int_\Gamma \{\mu \eta \nabla_{\mathbf{n}} \mathbf{v}_{p_h}\} [\![\mathbf{u}_h]\!] ds$$
$$\leq \|\mathbf{u}_h\|_{1,\Omega,\mu} \|\eta \mathbf{v}_{p_h}\|_{1,\Omega,\mu} + \|\mu_{max}^{-1/2} \{\mu \eta \nabla_{\mathbf{n}} \mathbf{v}_{p_h}\}\|_{-1/2,h,\Gamma} \|\mu_{max}^{1/2} [\![\mathbf{u}_h]\!]\|_{1/2,h,\Gamma}$$
$$\leq \frac{\epsilon}{2} \|\mathbf{u}_h\|^2_{1,\Omega,\mu} + \frac{1}{2\epsilon} \|\eta \mathbf{v}_{p_h}\|^2_{1,\Omega,\mu} + \frac{1}{2\epsilon} \|\mu_{max}^{-1/2} \{\mu \eta \nabla_{\mathbf{n}} \mathbf{v}_{p_h}\}\|^2_{-1/2,h,\Gamma} + \frac{\epsilon}{2} \|\mu_{max}^{1/2} [\![\mathbf{u}_h]\!]\|^2_{1/2,h,\Gamma}$$

Exploiting the trace inequality (3.17), we get:

$$a_h(\mathbf{u}_h, \eta \mathbf{v}_{p_h}) \leq \frac{\epsilon}{2} |||\mathbf{u}_h|||^2 + \frac{1}{2\epsilon} \|\eta \mathbf{v}_{p_h}\|^2_{1,\Omega,\mu} + \frac{C_I}{2\epsilon} \|\eta \mathbf{v}_{p_h}\|^2_{1,\Omega,\mu}$$
$$\leq \frac{\epsilon}{2} |||\mathbf{u}_h|||^2 + \frac{(1 + C_I) C^2_{p1} \eta^2}{2\epsilon} \|p_h\|^2_{0,\Omega^+,\mu}. \tag{3.24}$$

Using (3.12), (3.22), (3.24) and (3.7) we obtain

$$\mathcal{B}_h[(\mathbf{u}_h, p_h), (\mathbf{v}_h, q_h)] + c_h(p_h, q_h) + s_h(p_h, q_h)$$
$$\geq C_a |||\mathbf{u}_h|||^2 - \frac{\epsilon}{2} |||\mathbf{u}_h|||^2 - \frac{(1 + C_I) C^2_{p1} \eta^2}{2\epsilon} \|p_h\|^2_{0,\Omega^+,\mu} + C_{p2} \|p_h\|^2_{0,\Omega^+,\mu}$$
$$\geq (C_a - \frac{\epsilon}{2}) |||\mathbf{u}_h|||^2 + (C_{p2} - \frac{(1 + C_I) C^2_{p1} \eta^2}{2\epsilon}) \|p_h\|^2_{0,\Omega^+,\mu} \geq C_s \|(\mathbf{u}_h, p_h)\|_{\Omega^+}{}^2,$$

and dividing by $\|(\mathbf{v}_h, q_h)\|_{\Omega^+}$ we have:

$$\frac{\mathcal{B}_h[(\mathbf{u}_h, p_h), (\mathbf{v}_h, q_h)] + c_h(p_h, q_h) + s_h(p_h, q_h)}{\|(\mathbf{v}_h, q_h)\|_{\Omega^+}} \geq \frac{\mathcal{B}_h[(\mathbf{u}_h, p_h), (\mathbf{v}_h, q_h)] + c_h(p_h, q_h) + s_h(p_h, q_h)}{\|(\mathbf{u}_h, p_h)\|_{\Omega^+}}$$
$$\geq C_s \|(\mathbf{u}_h, p_h)\|_{\Omega^+}.$$

The thesis (3.10) of the theorem holds by choosing ϵ and η such that

$$\epsilon < 2C_a \quad \text{and} \quad \eta < \sqrt{\frac{2C_{p2}\epsilon}{(1 + C_I)C_{p1}^2}}.$$

□

3.4.2 Error analysis

We start from the consistency of the scheme which will be useful for the derivation of the error estimate. For its derivation we follow [63] and [10].

Lemma 3.4.5. *Let $(\mathbf{u}_h, p_h)$ be the solution of the finite element formulation (3.2) and $(\mathbf{u}, p) \in [H^2(\Omega_1 \cup \Omega_2)]^2 \times H^1(\Omega_1 \cup \Omega_2)$ be the weak solution of (3.1). Then the finite element formulation (3.2) fulfills the following consistency relation,*

$$\mathcal{B}_h[(\mathbf{u} - \mathbf{u}_h, p - p_h), (\mathbf{v}_h, q_h)] = c_h(p_h, q_h) + s_h(p_h, q_h),\ \forall (\mathbf{v}_h, q_h) \in V_h \times Q_h. \quad (3.25)$$

Proof. The property follows by observing that the exact solution $(\mathbf{u}, p)$ satisfies

$$\mathcal{B}_h[(\mathbf{u}, p), (\mathbf{v}_h, q_h)] = (\mathbf{f}, \mathbf{v}_h)_\Omega,\ \forall (\mathbf{v}_h, q_h) \in V_h \times Q_h, \quad (3.26)$$

and then subtracting (3.2) to (3.26). □

We now analyze the approximation properties of the proposed finite element space, using the interpolation operator defined in [65]. As shown in [65], it enjoys the following approximation and stability properties:

Lemma 3.4.6. *The interpolation operator defined as in [65], namely $R_h^* : H^s(\Omega) \to V_{h,0}$, with $s = 2$ for the velocities and $s = 1$ for the pressure, is such that*

$$\|(\mathbf{v} - R_h^*\mathbf{v}, p - R_h^* p)\|_{\Omega^+}^2 \leq h^2 \left(C_u \|\mu_{max}^{1/2}\mathbf{v}\|_{2,\Omega}^2 + C_p \|p\|_{1,\Omega^+,\mu}^2 \right) \ (\textit{approximation}), \quad (3.27)$$

$$\|R_h^* w\|_{r,\Omega} \leq C \|w\|_{s,\Omega},\ 0 \leq r \leq \min(1, s),\ \forall w \in H^s(\Omega)\ (\textit{stability}). \quad (3.28)$$

Starting from these results, we prove the following theorem.

Theorem 3.4.7. *The following error estimate holds true*

$$\|(\mathbf{u} - \mathbf{u}_h, p - p_h)\|_{\Omega^+} \leq Ch \left(\|\mu_{max}^{1/2}\mathbf{u}\|_{2,\Omega} + \|p\|_{1,\Omega^+,\mu} \right). \quad (3.29)$$

Proof. . We have

$$\|(\mathbf{u}-\mathbf{u}_h, p-p_h)\|_{\Omega^+} \leq \|(\mathbf{u}-R_h^*\mathbf{u}, p-R_h^*p)\|_{\Omega^+} + \|(R_h^*\mathbf{u}-\mathbf{u}_h, R_h^*p-p_h)\|_{\Omega^+}.$$

The first term can be estimated directly using the interpolation error estimate (3.27) directly,

$$\|(\mathbf{u}-R_h^*\mathbf{u}, p-R_h^*p)\|_{\Omega^+} \leq Ch\left(\|\mu_{max}^{1/2}\mathbf{u}\|_{2,\Omega} + \|p\|_{1,\Omega^+,\mu}\right).$$

To estimate the second term we use the *inf-sup* condition (3.10), to get

$$\begin{aligned}\|(R_h^*\mathbf{u}-\mathbf{u}_h, R_h^*p-p_h)\|_{\Omega^+} \leq \sup_{\mathbf{v}_h,q_h\neq 0} C_s^{-1}(\mathcal{B}_h[(R_h^*\mathbf{u}-\mathbf{u}_h, R_h^*p-p_h),(\mathbf{v}_h,q_h)] \\ + c_h(R_h^*p-p_h,q_h) + s_h(R_h^*p-p_h,q_h))/\|(\mathbf{v}_h,q_h)\|_{\Omega^+}.\end{aligned}$$

Adding and subtracting the exact solutions $\mathbf{u}$ and p to $\mathcal{B}_h$ and using the consistency relation for the finite element formulation (3.25), we get

$$\begin{aligned}\|(R_h^*\mathbf{u}-\mathbf{u}_h, R_h^*p-p_h)\|_{\Omega^+} \leq \sup_{\mathbf{v}_h,q_h\neq 0} C_s^{-1}(\mathcal{B}_h[(\mathbf{u}-R_h^*\mathbf{u}, p-R_h^*p),(\mathbf{v}_h,q_h)] \\ + c_h(R_h^*p,q_h) + s_h(R_h^*p,q_h))/\|(\mathbf{v}_h,q_h)\|_{\Omega^+}.\end{aligned}$$

Since the stabilization terms are symmetric we can use the Cauchy-Schwarz inequality followed by the continuity property (3.14) to get

$$c_h(R_h^*p,q_h) \leq c_h(R_h^*p,R_h^*p)^{1/2}c_h(q_h,q_h)^{1/2} \leq c_h(R_h^*p,R_h^*p)^{1/2}\|(\mathbf{v}_h,q_h)\|.$$
$$s_h(R_h^*p,q_h) \leq s_h(R_h^*p,R_h^*p)^{1/2}s_h(q_h,q_h)^{1/2} \leq s_h(R_h^*p,R_h^*p)^{1/2}\|(\mathbf{v}_h,q_h)\|.$$

Finally, by using the continuity of $\mathcal{B}_h[(\cdot,\cdot),(\cdot,\cdot)]$, (3.16), it follows that

$$\begin{aligned}\|(R_h^*\mathbf{u}-\mathbf{u}_h, R_h^*p-p_h)\|_{\Omega^+} \leq C\left(\|(\mathbf{u}-R_h^*\mathbf{u}, p-R_h^*p)\|_{\Omega^+}\right. \\ \left. + c_h(R_h^*p,R_h^*p)^{1/2} + s_h(R_h^*p,R_h^*p)^{1/2}\right).\end{aligned}$$

The first term is estimated using the interpolation error estimate (3.27), then we use the definition of the stabilization terms and the stability properties of the interpolation operator (3.28) to obtain

$$c_h(R_h^*p,R_h^*p) \leq Ch^2\sum_{i=1}^{2}\|p_i\|^2_{1,\Omega_i^+,\mu}, \qquad s_h(R_h^*p,R_h^*p) \leq Ch^2\sum_{i=1}^{2}\|p_i\|^2_{1,\Omega_i^+,\mu}.$$

The thesis follows by combining the previous estimates. □

3.4.3 Conditioning of the Schur complement matrix

We are now interested in analyzing the conditioning of the system and in particular we focus on the Schur complement matrix. The forthcoming results will enable us to solve the discrete problem using the classical methods for saddle point problems like the Uzawa method [59]. Problem (3.2) can be written in algebraic form as

$$\begin{bmatrix} A & B^T \\ -B & S \end{bmatrix}\begin{bmatrix} u \\ p \end{bmatrix} = \begin{bmatrix} f_u \\ f_p \end{bmatrix}$$

where blocks are related to the bilinear forms as follows,

$$a_h(\mathbf{u}_h, \mathbf{v}_h) = (\mathbf{v}_h, A\mathbf{u}_h), \quad b_h(\mathbf{u}_h, q_h) = (q_h, B\mathbf{u}_h),$$

and for the stabilization terms we have $S = S_1 + S_2$ where,

$$c_h(p_h, q_h) = (q_h, S_1 p_h), \quad s_h(p_h, q_h) = (q_h, S_2 p_h).$$

The Schur complement $\mathcal{C}$ is defined as:

$$\mathcal{C} = BA^{-1}B^T + S$$

From (3.2), we define the following bilinear form:

$$\mathcal{L}_h\left[(\mathbf{u}_h, p_h), (\mathbf{v}_h, q_h)\right] = a_h(\mathbf{u}_h, \mathbf{v}_h) + b_h(\mathbf{v}_h, p_h) - b_h(\mathbf{u}_h, q_h) + c_h(p_h, q_h) + s_h(p_h, q_h) \tag{3.30}$$

We state the following assumptions:

Assumption 3.4.8. There exist positive numbers $C_a, C_b, C_{s1}, C_{s2}, C_B, \underline{\gamma}, \bar{\gamma}$, independent of $\mathbf{u}_h, \mathbf{v}_h, p_h, q_h$ such that

$$C_a |||\mathbf{v}_h|||^2 \leq a_h(\mathbf{v}_h, \mathbf{v}_h), \tag{3.31}$$

$$C_b(1+C)\|p_h\|_{0,\Omega^+,\mu} |||\mathbf{v}_h||| \geq b_h(\mathbf{v}_h, p_h), \tag{3.32}$$

$$C_{s1}\|p_h\|_{0,\Omega^+,\mu}\|q_h\|_{0,\Omega^+,\mu} \geq c_h(p_h, q_h), \tag{3.33}$$

$$C_{s2}\|p_h\|_{0,\Omega^+,\mu}\|q_h\|_{0,\Omega^+,\mu} \geq s_h(p_h, q_h), \tag{3.34}$$

$$C_B\|(\mathbf{u}_h, p_h)\|_{\Omega^+}\|(\mathbf{v}_h, q_h)\|_{\Omega^+} \geq \mathcal{B}_h[(\mathbf{u}_h, p_h), (\mathbf{v}_h, q_h)], \tag{3.35}$$

$$\underline{\gamma}\|(\mathbf{u}_h, p_h)\|_{\Omega^+} \leq \sup_{\mathbf{v}_h, q_h \neq 0} \frac{\mathcal{L}_h\left[(\mathbf{u}_h, p_h), (\mathbf{v}_h, q_h)\right]}{\|(\mathbf{v}_h, q_h)\|_{\Omega^+}}, \tag{3.36}$$

$$\bar{\gamma}\|(\mathbf{u}_h, p_h)\|_{\Omega^+} \geq \sup_{\mathbf{v}_h, q_h \neq 0} \frac{\mathcal{L}_h\left[(\mathbf{u}_h, p_h), (\mathbf{v}_h, q_h)\right]}{\|(\mathbf{v}_h, q_h)\|_{\Omega^+}}, \tag{3.37}$$

Analogously, there exist $\bar{\gamma}' \leq \bar{\gamma}$ such that

$$\bar{\gamma}'\|(\mathbf{u}_h, p_h)\|_{\Omega^+} \geq \sup_{\mathbf{v}_h, q_h \neq 0} \frac{b_h(\mathbf{u}_h, q_h) - c_h(p_h, q_h) - s_h(p_h, q_h)}{\|q\|_{0,\Omega^+,\mu}}. \tag{3.38}$$

We remark that the existence of $\bar{\gamma}'$ follows from (3.37) with $\bar{\gamma}' = \bar{\gamma}$. However, we can consider the case in which a better estimate of $\bar{\gamma}'$ may be available. Inequalities (3.31), (3.32), (3.33), (3.34) and (3.35) correspond to results of Lemma 3.4.2 and (3.36) is the thesis of theorem 3.4.1. All these inequalities have been previously proved. In particular, the discrete norm equivalence (3.7) has been used in (3.13) to write (3.32). Inequality (3.37) follows from the assumptions (3.33), (3.34) and (3.35).

Theorem 3.4.9. *Under the assumption 3.4.8, the eigenvalues of $\mathcal{C}$ are localized as follows:*

$$\lambda_n(\mathcal{C}) \in \left\{ z \in \mathbb{C} : \underline{\gamma} \leq |z| \leq \bar{\gamma}' \sqrt{1 + \left(\frac{C_b(1+C)}{C_a}\right)^2} \right\}. \tag{3.39}$$

Proof. To prove (3.39), we follow the general framework proposed in [35]. For each $p_h \in Q_h$, let $\tilde{\mathbf{u}}_h \in V_h$ be defined by

$$a_h(\tilde{\mathbf{u}}_h, \mathbf{v}_h) + b_h(\mathbf{v}_h, p_h) = 0 \quad \forall \mathbf{v}_h \in V, \quad \text{that is,} \quad \tilde{\mathbf{u}}_h = -A^{-1}B^T p_h. \tag{3.40}$$

Taking $\mathbf{u}_h = \tilde{\mathbf{u}}_h$ in (3.30), makes $\mathcal{L}_h\left[(\mathbf{u}_h, p_h), (\mathbf{v}_h, q_h)\right] = c_h(p_h, q_h) + s_h(p_h, q_h) - b_h(\mathbf{u}_h, q_h) = (q_h, \mathcal{C}p_h)$ independent of $\mathbf{v}_h$. Hence, using (3.36) and (3.38),

$$\underline{\gamma}\|(\tilde{\mathbf{u}}_h, p_h)\|_{\Omega^+} \leq \sup_{\mathbf{v}_h, q_h \neq 0} \frac{(q_h, \mathcal{C}p_h)}{\|(\mathbf{v}_h, q_h)\|_{\Omega^+}} \leq \sup_{q_h \neq 0} \frac{(q_h, \mathcal{C}p_h)}{\|q_h\|_{0,\Omega^+,\mu}} \leq \bar{\gamma}'\|(\tilde{\mathbf{u}}_h, p_h)\|_{\Omega^+}. \tag{3.41}$$

From (3.40), (3.31) and (3.32) we have,

$$C_a|||\tilde{\mathbf{u}}_h|||^2 \leq a_h(\tilde{\mathbf{u}}_h, \tilde{\mathbf{u}}_h) = -b_h(\tilde{\mathbf{u}}_h, p_h) \leq C_b(1+C)\|p_h\|_{0,\Omega^+,\mu}|||\tilde{\mathbf{u}}_h|||,$$

so that $|||\tilde{\mathbf{u}}_h||| \leq \dfrac{C_b}{C_a}\|p_h\|_{\Omega^+}$, yielding the following estimate,

$$\|p_h\|_{0,\Omega^+,\mu} \leq \|(\tilde{\mathbf{u}}_h, p_h)\|_{\Omega^+} \leq \sqrt{1 + \left(\frac{C_b(1+C)}{C_a}\right)^2}\|p_h\|_{0,\Omega^+,\mu},$$

and equation (3.41) becomes

$$\underline{\gamma}\|p_h\|_{0,\Omega^+,\mu} \leq \sup_{q_h \neq 0} \frac{(q_h, \mathcal{C}p_h)}{\|q_h\|_{0,\Omega^+,\mu}} \leq \bar{\gamma}'\sqrt{1 + \left(\frac{C_b(1+C)}{C_a}\right)^2}\|p_h\|_{0,\Omega^+,\mu}.$$

□

3.5 Numerical results

We analyse the order of convergence of two variants of the proposed method compared with two reference methods and we investigate how Brezzi-Pitkaranta stabilization improves the conditioning of the algebraic problem.

3.5.1 Comparison of different methods

The previous analysis is valid for those choices of finite element spaces and stabilization terms for which the *inf-sup* condition is guaranteed on the restricted sub-domains. The stabilization on the *extended cut region* makes the *inf-sup* condition to be globally satisfied. We analyze the numerical performances of the following combination:

- $\mathbb{P}^1_{bubble} - \mathbb{P}^1$ elements with Brezzi-Pitkaranta stabilization on the cut region. We notice that, since the *inf-sup* condition is satisfied because of the bubble stabilization, we do not need the additional term $c_h(p_h, q_h)$.
- $\mathbb{P}^1 - \mathbb{P}^1$ with Brezzi-Pitkaranta stabilization on all the domain, i.e. both $c_h(p_h, q_h)$ and $s_h(p_h, q_h)$ are active.

These two choices will be compared with two *reference methods*. The first one employs $\mathbb{P}^1_{bubble} - \mathbb{P}^1$ elements without any additional stabilization in the *extended cut region* ($s_h(p_h, q_h) = 0$). This is the method where we observe instabilities in the pressure

approximation, as we have shown in figure 3.1. The second one has been proposed by Burman-Becker-Hansbo [10] and it consists in choosing $\mathbb{P}^1 - \mathbb{P}^0$ elements with a stabilization based on the jump of the pressure along the edges of the mesh, so we define:

$$c_h(p_h, q_h) + s(p_h, q_h) := \sum_{F \in \mathcal{F}_1} \int_F \frac{\gamma_p}{\mu_1} h_F [\![p_{h,1}]\!][\![q_{h,1}]\!] ds + \sum_{F \in \mathcal{F}_2} \int_F \frac{\gamma_p}{\mu_2} h_F [\![p_{h,2}]\!][\![q_{h,2}]\!] ds, \tag{3.42}$$

where $\mathcal{F}_i$ denotes the set of interior faces of $\mathcal{T}_{h,i}^+$.

From the standpoint of accuracy, the considered methods are substantially equivalent. Indeed, they all satisfy the following theoretical estimate [42, 91]:

$$\|\mathbf{u} - \mathbf{u}_h\|_{1,\Omega,\mu} + \|p - p_h\|_{0,\Omega^+,\mu} \leq Ch(\|\mathbf{u}\|_{2,\Omega} + \|p\|_{1,\Omega}) \tag{3.43}$$

In what follows we will show that the performance of all methods is in agreement with the theory, but appreciable differences may appear in the magnitude of the error.

A strong point in favor of the Brezzi-Pitkaranta stabilization is that it is easy to implement, i.e. it needs a minimum effort to introduce the stabilization term in a pre-existing finite element code and, moreover, it can be easily used in a parallel context. In contrast, the assembling of a stabilization term that needs integration on the edges of the elements, such as the Burman-Becker and Hansbo stabilization, usually requires to access information about the adjacent elements to each edge, which increases the communication between processors.

3.5.2 Test cases and results

The numerical tests have been implemented in the C++ finite element library `LifeV` (`www.lifev.org`), developed by the collaboration between four institutions: École Polytechnique Fédérale de Lausanne (CMCS), Politecnico di Milano (MOX), INRIA (REO, ESTIME) and Emory University.

We solve the saddle point problems in the domain $\Omega = [0, 1]^2$ crossed by the interface $\Gamma = \{x, y | (x - x_c)^2 + (y - y_c)^2 = a^2\}$. We set $a = 0.25$ and $x_c = y_c = 0.5$. Let us define $\Omega_1 = \{x, y | (x - x_c)^2 + (y - y_c)^2 < a^2\}$ the internal part of the domain with respect to the orientation of the normal of Γ, and Ω_2 is the external part. We set $\gamma_s = 1$ and the penalty parameters $\gamma_p = \gamma_u = 10$. The determination of these parameters is fairly heuristic. This is one of the major drawbacks of using penalty methods for pressure stabilization and to enforce interface conditions. The selected values have been tuned on the simple test case 1 described below, aiming to obtain a stable numerical solution that is not prerturbed by the consistency error due to pressure stabilization. These values have been then kept constant for all the other numerical experiments. The fact that they fit to all test cases suggest that they fall in the range where stability and accuracy criteria are simultaneously satisfied.

We consider three different test cases. In the first two tests there is no variation in the parameters of the problem between the two sides of the interface. The surface Γ is then an *artificial* interface, however the additional XFEM degrees of freedom and the weak imposition of the conditions across the surface can produce extra numerical errors in the region near the interface. We discuss in details the convergence analysis for the error on the velocity and pressure solution.

Test 1: Poiseuille's flow We start from the Poiseuille's flow in the domain Ω crossed by Γ, for the verification of the numerical solver. We remind that in a Poiseuille's flow, the velocity profile is parabolic for the horizontal component and null for the vertical one. The gradient of the pressure is linear. As we can see in figure 3.5, the numerical results are coherent with the theoretical estimates (3.43). The error constant of the stabilized $\mathbb{P}^1 - \mathbb{P}^0$ scheme is slightly larger than in the other cases. This behavior can be explained observing that this method is the only one based on piecewise constant pressure elements, to approximate a linear pressure field.

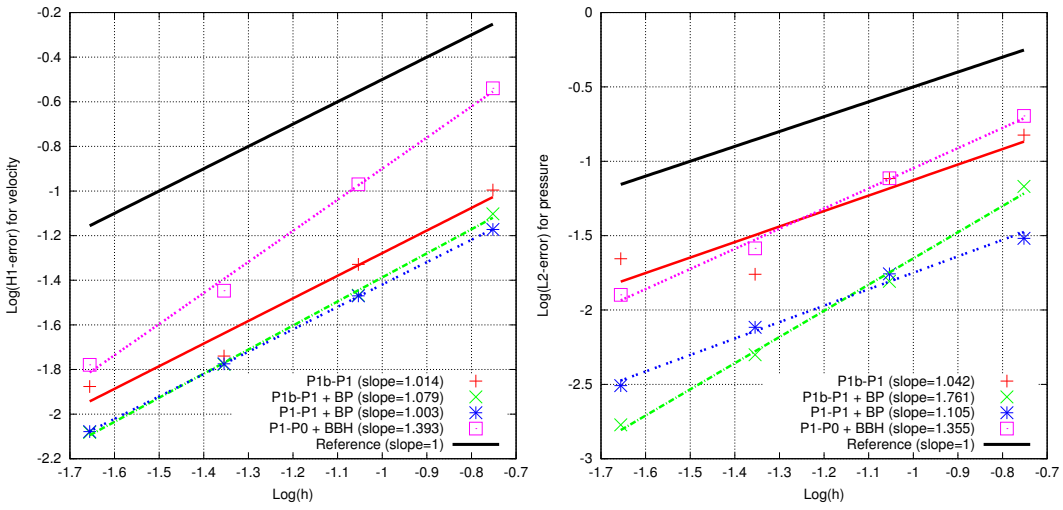

(a) H^1-norm error for velocity

(b) L^2-norm error for pressure

Figure 3.5: *Convergence analysis for test 1*

Test 2: An artificial interface in an incompressible medium We analyse the case of an artificial interface in an incompressible fluid with constant material properties over the entire domain as proposed in [10] and [65]. For problem (3.1), the following continuous analytical solution is available:

$$\mathbf{u}(x,y) = \left[20xy^3; 5x^4 - 5y^4\right], \quad p(x,y) = 60x^2y - 20y^3 - 5,$$

and is obtained by setting the right hand side $\mathbf{f} = 0$. We observe that the velocity approximation error is very similar for the four considered methods. For the approximation of the pressure, methods based on the Brezzi-Pitkaranta stabilization on the cut region perform slightly better that the others.

Test 3: An elastic interface problem After these preliminary tests, we analyze a problem with heterogeneous coefficients [10]. This is an incompressible linear elastic problem that can be reinterpreted as a Stokes flow with suitable forcing terms. Let Ω be the unit square $[0,1]^2$ and Ω_1 be the circle of radius $a = 0.25$ centered in $b = x_c = y_c = 0.5$, as defined above. We set $E_1 = E_2 = 1$, $\nu_2 = 0.25$ and $\nu_1 = 0.49$. Coefficients μ_i are defined as follows: $\mu_i = E_i/(2(1+\nu_i))$. Using polar coordinates, where $r = \sqrt{(x-x_c)^2 + (y-y_c)^2}$, $b = 0.5$, the analytical solution for velocity and pressure are

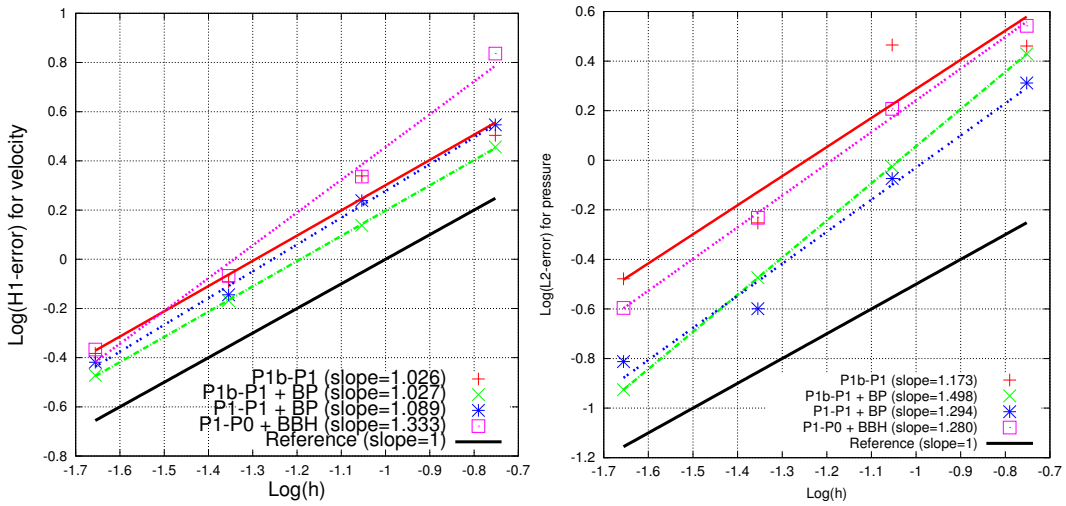

(a) H^1-norm error for velocity (b) L^2-norm error for pressure

Figure 3.6: *Convergence analysis for test 2*

given by the following expressions, for $\nu_1 \neq 0.5$:

$$u_r(r,\theta) = \begin{cases} c_1 r & \text{in } \Omega_1 \\ (r - \frac{b^2}{r})c_2 + \frac{b^2}{r} & \text{in } \Omega_2 \end{cases}$$

$$u_\theta(r,\theta) = 0$$

$$p(r,\theta) = \begin{cases} -2c_1\lambda_1 & \text{in } \Omega_1 \\ -2c_2\lambda & \text{in } \Omega_2 \end{cases}$$

$$c_1 = \left(1 - \frac{b^2}{a^2}\right) c_2 + \frac{b^2}{a^2}$$

$$c_2 = \frac{(\lambda_1 + \mu_1 + \mu_2)b^2}{(\lambda_2 + \mu_2)a^2 + (\lambda_1 + \mu_1)(b^2 - a^2) + \mu_2 b^2}.$$

which exactly satisfy the interface conditions of (3.1). The solution of this test case, calculated using $P1_{bubble} - P1$ elements, is shown in Figure 3.1. The momentum and mass conservation equation of (3.1) will be equivalently satisfied, provided that the following right hand sides, $\mathbf{f}$ and g, are chosen for the momentum and continuity equations, respectively.

$$\mathbf{f} = 0 \qquad g = -\frac{p_i}{\lambda_i} \quad \text{in} \quad \Omega_i$$

We notice that the variation on the Poisson coefficient produces a kink in the radial velocity profile and a strong discontinuity in the pressure solution. Strictly speaking, p can be interpreted as the pressure only in the incompressible case (Stokes problem), but we shall omit this distinction. Similarly to the previous results, performances of the methods are quite similar concerning the velocity approximation. When the pressure field is discontinuous, Figure 3.7 shows that resorting to a stabilization method

on the cut region is recommended. However, the best performances are obtained when pressure stabilization is adopted on the entire domain, combined with either $\mathbb{P}^1 - \mathbb{P}^0$ or $\mathbb{P}^1 - \mathbb{P}^1$ elements.

Finally, we were interested in studying the behavior of the scheme for two different choices of the weights ω_i. These results are obtained using the weights defined in (3.3). In Figure 3.8, we perform the same test using the weights defined in [63], which do not account for the heterogeneity of viscosity. Comparing the results reported in Figure 3.7 and 3.8, we do not observe a significant difference in the numerical solution. We remark that the computational cost of these weights is very similar and we conclude that both choices are suitable to solve a problem with a mild heterogeneity between coefficients.

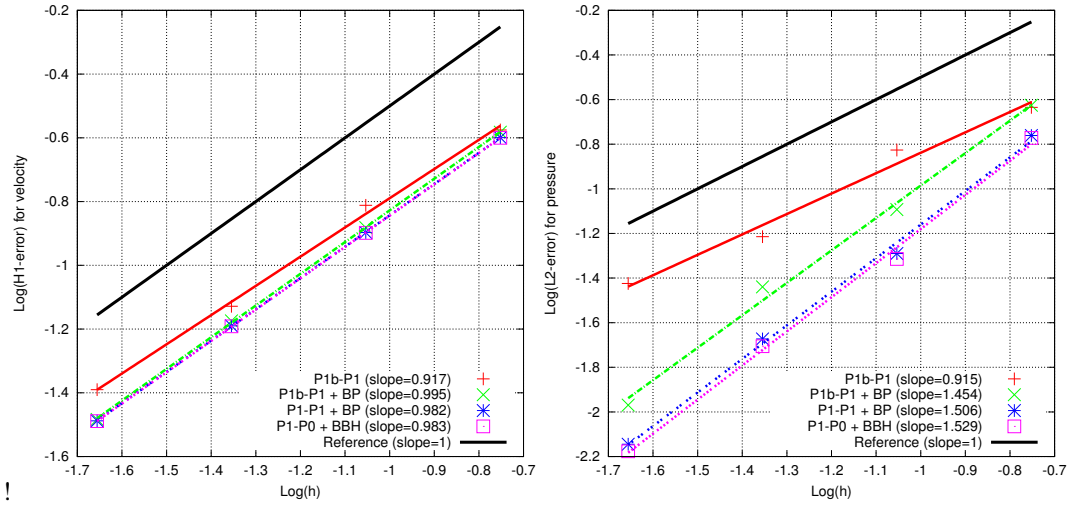

(a) H^1-norm error for velocity (b) L^2-norm error for pressure

Figure 3.7: *Convergence analysis for test 3, using the averaging weights defined in* (3.3).

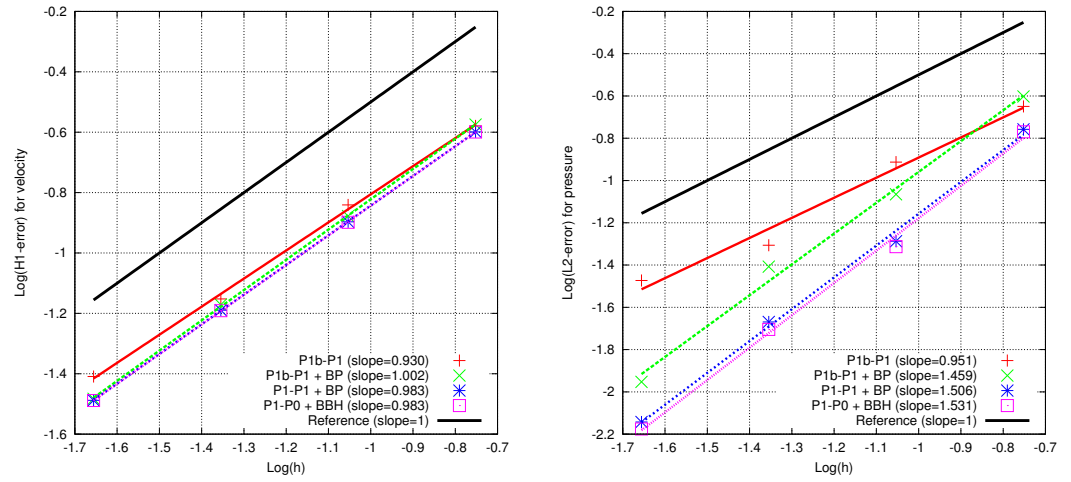

(a) H^1-norm error for velocity (b) L^2-norm error for pressure

Figure 3.8: *Convergence analysis for test 3, using the averaging weights defined in [63].*

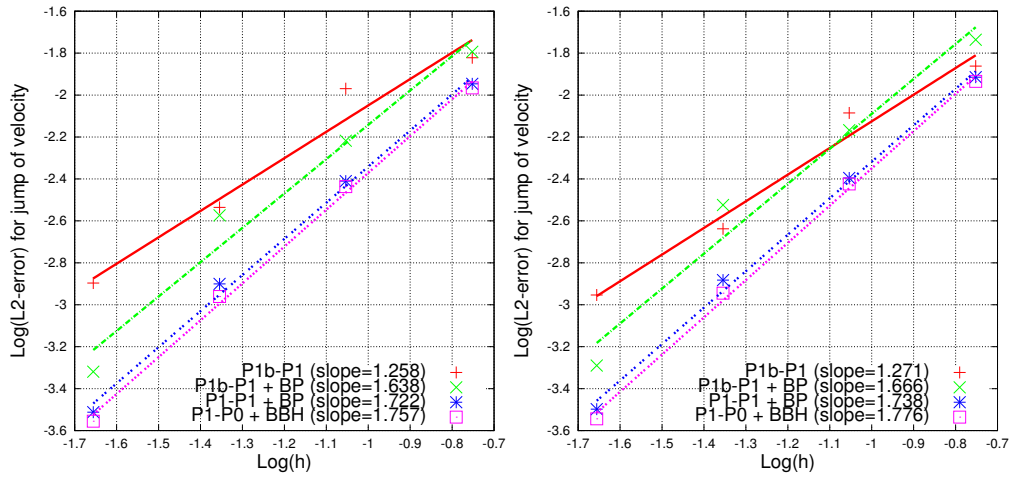

(a) Dolbow weights (b) Standard weights

Figure 3.9: *L^2-norm error for the jump of velocity across the interface.*

We finally observe that for the analysis of the numerical experiments we have used the standard H^1 and L^2 norms for velocity and pressure respectively, while the theoretical error estimate of the scheme we have analyzed is provided for $\|(\mathbf{u}-\mathbf{u}_h, p-p_h)\|_{\Omega^+}$. We claim that the norms considered for the numerical tests are the dominating terms of this more general error indicator. This is confirmed by Figure 3.9, where we show $\|[\![\mathbf{u}_h]\!]\|_{1/2,h,\Gamma}$. This term is a part of $\|(\mathbf{u}-\mathbf{u}_h, p-p_h)\|_{\Omega^+}$ and it scales as $h^{3/2}$, in agreement with the expected theoretical estimate. We notice that its magnitude is significantly smaller than the one of the velocity H^1 norm.

3.5.3 Problem conditioning

As we already pointed out, the Nitsche-XFEM method allows for using meshes independent of the position of Γ, but instabilities in the *cut region* depend on how the interface crosses the elements. For this reason, we study the conditioning of the pressure Schur complement matrix $\mathcal{C}$ for the third test case previously presented and we use the $\mathbb{P}^1 - \mathbb{P}^1$ elements with Brezzi-Pitkaranta stabilization. By increasing the radius of the circular interface Γ, see Figure 3.1, we modify the intersections between the mesh and the interface. According to the theory, we expect the method proposed is not influenced by the geometry of the problem .

In Table 3.1, we collect the obtained results. First of all, we observe that the conditioning of matrix $\mathcal{C}$ is almost constant when using $\mathbb{P}^1 - \mathbb{P}^1$ elements with Brezzi-Pitkaranta stabilization on the whole domain, as expected from (3.39). The condition number is independent of how the interface cuts the mesh.

In addition, we calculate the minimum eigenvalue of the Schur complement matrix, preconditioned with the pressure mass matrix. When the pressure stabilization on the cut region is active, we use $\mathcal{M}_p^+$ defined as,

$$\left[\mathcal{M}_p^+\right]_{mn} = \sum_{i=1}^{2} \int_{\Omega_i^+} q_h^m q_h^n dx, \qquad q_h^m, q_h^n \in Q_h,$$

where we remark that the integrals of basis functions having support in a $K \in \mathcal{G}_h$ are computed on the entire element K. For the non stabilized case, the usual definition is applied,

$$[\mathcal{M}_p]_{mn} = \sum_{i=1}^{2} \int_{\Omega_i} q_h^m q_h^n dx, \qquad q_h^m, q_h^n \in Q_h.$$

The quantities $\min\{\lambda_i((\mathcal{M}_p^+)^{-1}\mathcal{C})\}$ and $\min\{\lambda_i(\mathcal{M}_p^{-1}\mathcal{C})\}$ inform us about the *inf-sup* stability of the scheme, because they are directly proportional to the *inf-sup* constant [42]. The analysis is reported in Table 3.1. The fact that the minimum eigenvalue of $\min\{\lambda_i(\mathcal{M}_p^{-1}\mathcal{C})\}$ is nor positive, neither bounded from below when the size of cut elements decreases, confirms the lack of stability of the approximation method without pressure stabilization. Conversely, the Brezzi-Pitkaranta stabilization, applied on the cut region or on the whole domain, restores the desired positivity and boundedness property, almost uniformly with respect to the cut-element size.

r	$\min\{\frac{\lvert K\cap\Omega_1\rvert}{\lvert K\cap\Omega_2\rvert}\}$	$\kappa(\mathcal{M}_p^{-1}\mathcal{C})$ $\mathbb{P}^1_{bubble} - \mathbb{P}^1$	$\kappa((\mathcal{M}_p^+)^{-1}\mathcal{C})$ $\mathbb{P}^1 - \mathbb{P}^1$ + BP stab.	$\kappa((\mathcal{M}_p^+)^{-1}\mathcal{C})$ $\mathbb{P}^1_{bubble} - \mathbb{P}^1$ + BP stab.
0.250	0.31038	$8.15 \cdot 10^2$	$1.35 \cdot 10^3$	559.83
0.270	0.02990	$8.27 \cdot 10^3$	$1.36 \cdot 10^3$	654.35
0.280	$3.35 \cdot 10^{-4}$	$2.61 \cdot 10^7$	$1.37 \cdot 10^3$	$2.66 \cdot 10^3$
0.281	$1.34 \cdot 10^{-5}$	$2.18 \cdot 10^8$	$1.37 \cdot 10^3$	$9.14 \cdot 10^3$

Table 3.1: *Conditioning of the preconditioned Schur complement $\mathcal{C}$ for small perturbations of the radius r of Ω_1.*

r	$\min\{\frac{\lvert K\cap\Omega_1\rvert}{\lvert K\cap\Omega_2\rvert}\}$	$\min\{\lambda_i(\mathcal{M}_p^{-1}\mathcal{C})\}$ $\mathbb{P}^1_{bubble} - \mathbb{P}^1$	$\min\{\lambda_i((\mathcal{M}_p^+)^{-1}\mathcal{C})\}$ $\mathbb{P}^1 - \mathbb{P}^1$ + BP stab.	$\min\{\lambda_i((\mathcal{M}_p^+)^{-1}\mathcal{C})\}$ $\mathbb{P}^1_{bubble} - \mathbb{P}^1$ + BP stab.
0.250	0.31038	-1.6434	0.486	0.2318
0.270	0.02990	-2.6736	0.4945	0.2316
0.280	$3.35 \cdot 10^{-4}$	-4.3228	0.4939	0.1359
0.281	$1.34 \cdot 10^{-5}$	-22.1581	0.4936	0.1235

Table 3.2: *Minumun eigenvalue of the preconditioned Schur complement $\mathcal{C}$ for small perturbations of the radius of Ω_1.*

3.6 Conclusions

The work developed in this chapter arises from the observation that the approximation of saddle point problems with extended finite elements poses some stability issues. In particular, for the Stokes problem the approximation of the pressure may be locally unstable. Standard mixed finite element spaces combined with simple enrichment strategies lead to a satisfactory approximation method, provided that pressure stabilization is introduced into the scheme. The general framework of symmetric stabilization techniques is suitable to cure this kind of issues. In particular, we have shown that the

Brezzi-Pitkaranta stabilization scheme is effective also in this new approximation context. The algebraic properties of the scheme are also analyzed, enabling the application of standard solvers, such as the Uzawa method.

Part II

Multidomain problems with heterogeneous dimensionality

CHAPTER 4

Tissue perfusion in vascularized tissue

4.1 Introduction

In the following two chapters we will analyze multidomain problems with heterogenous dimension. In particular, we are interested in studing problems where a complex 3D structure is embedded into another 3D domain. In this chapter we start with the analysis of tissue perfusion in vascularized tissue.
Small vessels, such as arterioles and capillaries, are the main actors of the microcirculation mechanisms and they are involved in transfer processes between blood and tissue. Blood circulation is responsible for a quite large number of exchange processes with the external tissue, such as oxygen transport, carbon dioxide removal and thermal regulation, and all these functions strongly affected the body vital processes. The simulation of these biological transfer mechanism is a challenging field of investigation, since mathematical modeling could provide new insights to medicine and biomedical engineer. There exist many applications in which is important to understand the connection between vessels and tissue, for example pharmacokinetics treatments or design of particular biomedical devices.

The big aim of this chapter is to study tissue perfusion in vascularized *tumor* tissues. Blood vessels in tumors are substantially leakier than in healthy tissue and they are tortuous, causing spatial and temporal heterogeneity in tumor blood flow. Further, the pressure generated by proliferating cells reduces tumor blood and lymphatic flow. These vascular abnormalities lead to an impaired blood supply and abnormal tumor microenvironment characterized by hypoxia and elevated interstitial fluid pressure that reduces the distribution of macromolecules through advection. Drug treatments have been developed specifically to target the abnormal vasculature in tumors; however, their impact is hard to predict as the relationship between network structure and the func-

tional parameters that determine mass transport is subtle [29].
Even if many recent works are focused on the investigation of these transport processes at the level of quite large vessels, such as arteries or arterioles, [69], [70], in this thesis we will just focus on the level of capillaries, as it has been already done in some works by Dr. T. Secomb, [50, 51, 102, 103]. These vessels have particular characteristics that allow us to make some assumptions in order to implement model reduction, as we will see in the next section.
We start now introducing the model for the perfusion problem.

4.2 Model set up

We define a mathematical model for fluid transport in a permeable biological tissue perfused by a capillary network. We consider a domain Ω that is composed by two parts, Ω_v and Ω_t, the capillary bed and the tumor interstitium, respectively. Assuming that the capillaries can be described as cylindrical vessels, we denote with Γ the outer surface of Ω_v, with R its radius and with Λ the centerline of the capillary network. Figure 4.1 (panels (a, b)) shows a description of the geometrical model. The radius of the vessels could be in general a function of the arc length along Λ.
At this stage, any physical quantity of interest, such as the blood pressure p and the blood velocity $\mathbf{u}$, is a function of space (being $\mathbf{x} \in \Omega$ the spatial coordinates) and time t. These quantities obey different balance laws, depending on the portion of the domain of interest and, in general, they are not continuous at the interface between subdomains. We first address the fluid transport in each portion of Ω, then we discuss the proper interface conditions in order to close the resulting coupled differential problem.
We consider the tumor interstitium Ω_t as an isotropic porous medium, such as the Darcy's law applies, while we start assuming a Newtonian model for the blood flow in the capillaries. The rheology of blood is analyzed in detail in [97], where it is pointed out that non-Newtonian models may be more appropriate to describe blood behavior in particular conditions. Microcirculation is an extreme case where the size of vessels is the smallest and the effect of blood pulsation is almost negligible. We will discuss in the next sections how the blood flow model could be adapted to these special conditions.

An essential effect for the applications we have in mind, i.e. tissue perfusion in tumor tissue, is the lymphatic drainage. The lymphatic vessels consist of one way endothelium conduits from the peripheral tissues to the blood circulation. Excess of fluid extravasated from the blood circulation is drained by lymphatic vessels and returned to the blood stream: a functional lymphatic network rapidly removes fluid and this results in lower interstitial fluid pressure and biochemical concentration levels. The lymphatic vessels are important in modeling tumor microenvironment since they transport tumor cells. It has been estimated that 80% of metastasis of solid cancers, such as breast cancer and melanoma, disseminate through the lymphatic system, while 20% of metastases may occur through the blood vasculature or by direct seeding, [7]. For this reason, interstitial flow and lymphatic drainage should be considered together. Unlike the capillary network, we do not have a geometrical description of the lymphatic vessels, so we cannot directly define the geometrical interaction between the lymphatics and the tissue. Following the work by Soltani and Chen, [106], we decide to model the lymphatic drainage as a sink term in the equation for the interstitial flow. More

precisely, we assume that the volumetric flow rate due to lymphatic vessels, Φ^{LF}, is proportional to the pressure difference between the interstitium and the lymphatics, namely $\Phi_{LF}(p_t) = L_p^{LF}\frac{S}{V}(p_t - p_L)$, where L_p^{LF} is the hydraulic conductivity of the lymphatic wall, S/V is the surface area of lymphatic vessels per unit volume of tissue and p_L is the hydrostatic pressure within the lymphatic channels.

As a consequence of all the modelling assumptions described above, the fluid problem in the entire domain Ω reads as follows:

$$\begin{cases} \nabla \cdot \mathbf{u}_t + L_p^{LF}\frac{S}{V}(p_t - p_L) = 0 & \text{in } \Omega_t \\ \mathbf{u}_t = -\dfrac{k}{\mu}\nabla p_t & \text{in } \Omega_t \\ \rho\dfrac{\partial \mathbf{u}_v}{\partial t} + \rho(\mathbf{u}_v \cdot \nabla)\mathbf{u}_v = -\nabla p_v + \mu\Delta \mathbf{u}_v & \text{in } \Omega_v \\ \nabla \cdot \mathbf{u}_v = 0 & \text{in } \Omega_v \end{cases} \tag{4.1}$$

where μ and k denote the dynamic blood viscosity and the constant tumor permeability, respectively, and ρ is the blood density. At the interface $\Gamma = \partial\Omega_v \cap \partial\Omega_t$ we impose continuity of the flow:

$$\mathbf{u}_v \cdot \mathbf{n} = \mathbf{u}_t \cdot \mathbf{n} = L_p((p_v - p_t) - \sum_k \sigma_k(\pi_{v,k} - \pi_{t,k})) \quad \mathbf{u}_t \cdot \boldsymbol{\tau} = 0, \quad \text{on } \Gamma \tag{4.2}$$

where $\mathbf{n}$ is the outward unit vector normal to the capillary surface. The fluid flux across the capillary wall can be obtained on the basis of linear non-equilibrium thermodynamic arguments, originally developed by Kedem and Katchalsky. In particular L_p is the hydraulic conductivity of the vessel wall, $\pi_v - \pi_t$ is the difference in oncotic pressure where $\pi = R_g T c$ is the oncotic pressure given by a concentration c of a given solvent, R_g is the universal gas constant and T is the absolute temperature. Because of osmosis, the pressure drop across the capillary wall is affected by the difference in the concentration of chemicals, namely $c_v - c_t$, where c_v and c_t denote the concentration in the capillaries and in the interstitium, respectively. The osmotic pressure is modulated by the reflection coefficient σ that quantifies the departure of a semi-permeable membrane from the ideal permeability (where any molecule is able to travel across the membrane without resistance). The index k spans over all solutes that are dissolved in blood. However, not all of them will affect the oncotic pressure. Only the large molecules, such as proteins, can induce a significant oncotic pressure gradient. Indeed, the oncotic pressure gradient is mainly due to the significant presence of albumin in blood [31, 55, 89], whose concentration can be reasonably considered to be constant. For this reason, we assume that solutes such as oxygen or low concentrated drugs can not significantly affect the oncotic pressure gradient. Then, for our model, the capillary leakage only depends on the hydrostatic pressure according to the following expression,

$$J_v(p_t, p_v) := L_p((p_v - p_t) - \sigma_p R_g T(c_{v,p} - c_{t,p})) \tag{4.3}$$

where, in agreement with the definition of π, $c_{v,p}$ and $c_{t,p}$ denote the constant protein concentration in the capillaries and the interstitial tissue respectively.

Finally, to be uniquely solvable, problem (4.1) must be complemented by boundary conditions on $\partial\Omega_t$ and $\partial\Omega_v$. The prescription of these conditions significantly depends

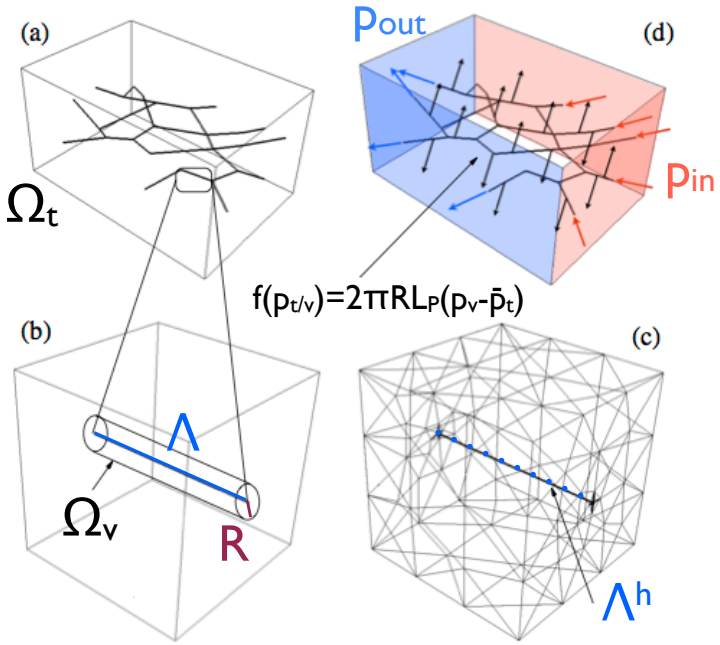

Figure 4.1: *Panel* (a)*: the reduction from three-dimensional to one-dimensional description of capillary vessels. The vessels network is available thanks to the courtesy of Dr. T. Secomb, [101]. Panel* (b)*: a descrip tion of the interstitial tissue with embedded capillary network (single vessel of radius R). Panel* (c)*: discretization with the finite element method. Panel* (d)*: a sketch of the fluid exchange between the capillary bed and the tissue interstitium. We highlight the inflow and outflow sections of the network.*

on the particular features of the problem at hand, as well as on the available data. For this reason, we postpone any further consideration on boundary conditions to Section 4.5, where we will discuss the numerical simulations and the related results.

4.3 Coupling microcirculation with interstitial flow

The previous fully three-dimensional model is able to capture the phenomena we are interested in. However, two relevant simplifications may be applied without significant loss of accuracy. At the modelling level, a quasi-static flow model can be replaced to the Navier-Stokes equations in deformable domains. More importantly, we aim to override the technical difficulties that arise in the numerical approximation of the coupling between a complex network with the surrounding volume. To this purpose, as we have already seen in the first chapter, 1, we adopt the multiscale approach developed in [32–34], which is inspired to the immersed boundary method.

4.3.1 An immersed boundary method to model networks

As we have already seen in the first chapter, the immersed boundary (IB) method has been developed to study fluid-structure interaction by Charles S. Peskin [90]. The original idea of representing immersed structures with Dirac delta functions was then taken

by Carlo D'Angelo to study elliptic problems in fractured domains, [32–34].
The concept of the immersed boundary method applied to this case can be outlined as follows. To avoid resolving the complex three-dimensional (3D) geometry of the capillary network, we exploit the IB method combined with the assumption of large aspect ratio between vessel radius and capillary axial length. This approach is represented in Figure 4.1, panels (a, b). More precisely, we apply a suitable rescaling of the equations and let the capillary radius go to zero ($R \to 0$). By this way, we replace the immersed interface and the related interface conditions with an equivalent mass source.

We denote with f the flux released by the surface Γ, which is a flux per unit area. The definition of f comes from the interface conditions (4.3), that we have prescribed above. At the interface between the capillary network and the tissue we require the flux continuity, i.e.

$$\mathbf{u}_t(t, \mathbf{x}) \cdot \mathbf{n} = f(p_{t/v}(t, \mathbf{x})) \qquad \text{on } \Gamma,$$

where $\mathbf{u}_t(t, \mathbf{x})$ with $\mathbf{x} \in \Gamma$ is the volume averaged interstitial filtration velocity in the tissue and $f(p_{t/v}(t, \mathbf{x}))$ is a point-wise constitutive law for the capillary leakage in terms of the fluid pressure, denoted here with the shorthand symbol $p_{t/v}(t, \mathbf{x})$. The immersed boundary method is able to represent the action of f on Γ as an equivalent source term, F, that is actually distributed on the entire domain Ω. More precisely, $F = F(p_{t/v}(t, \mathbf{x}))$ is a measure defined by

$$\int_\Omega F(p_{t/v}(t, \mathbf{x}))v = \int_\Gamma f(p_{t/v}(t, \mathbf{x}))v \qquad \forall v \in C^\infty(\Omega), \tag{4.4}$$

where v plays the role of a test function in the variational formulation that will be defined with more details later on. Hence, we use the notation $F(p_{t/v}(t, \mathbf{x})) = f(p_{t/v}(t, \mathbf{x}))\delta_\Gamma$, meaning that F is the Dirac measure concentrated on Γ, having density f.

Proceeding along the lines of [32], when $R \to 0$ we aim to replace the mass flux per unit area by an equivalent mass flux per unit length, distributed on the centerline Λ of the capillary network. To start with, we recall the assumption that the vessels can be represented as cylinders originated by a given mean line Λ. Let $\gamma(s)$ be the intersection of Γ with a plane orthogonal to Λ, located at s and let (s, θ) be the local axial and angular coordinates on the cylindrical surface generated by Λ with radius R. We apply the mean value theorem to represent the action of F on v in (4.4) by means of an integral with respect to the arc length on Λ. More precisely, there exists $\tilde{\theta} \in [0, 2\pi]$ such that

$$\begin{aligned}\int_\Omega F(p_{t/v})v &= \int_\Lambda \int_{\gamma(s)} f(p_{t/v}(t, s, \theta))v(s, \theta)Rd\theta ds \\ &= \int_\Lambda |\gamma(s)| f(p_{t/v}(t, s, \tilde{\theta}))v(s, \tilde{\theta})ds, \quad \forall v \in C^\infty(\Omega)\,. \end{aligned} \tag{4.5}$$

Then, we exploit the fact that capillaries are narrow with respect to the characteristic dimension of the surrounding volume. Namely, we assume that $R \ll |\Omega_t|^{1/d}$ where $d = 2, 3$ is the number of space dimensions of the model. Provided that f is a linear

function or operator, we conclude that

$$\begin{aligned}
&\lim_{R\to 0} v(s,\tilde{\theta})|_{\gamma(s)} = v(s)|_{\Lambda}, \quad \forall v \in C^{\infty}(\Omega),\\
&\lim_{R\to 0} f(p_{t/v}(t,s,\tilde{\theta})|_{\gamma(s)} = f(\overline{p}_{t/v}(t,s)),\\
&\overline{p}_{t/v}(t,s) := \frac{1}{|\gamma(s)|}\int_{\gamma(s)} p_{t/v}(t,s,\theta)Rd\theta.
\end{aligned} \tag{4.6}$$

We observe that, while $v(s,\theta)$ is a smooth function that can be evaluated on Λ, the solution of the problem may not be regular enough to define the point-wise value of $p_{t/v}|_{\Lambda}$. For this reason, the average operator on $\gamma(s)$ is still applied to $p_{t/v}$, even in the limit case when $R \to 0$. In conclusion, substituting the previous formula to equation (4.5) we recover

$$\int_{\Omega} F(p_{t/v})v = \int_{\Lambda} |\gamma(s)| f(\overline{p}_{t/v}(t,s))v(s)ds. \tag{4.7}$$

4.3.2 Models for microvascular flow

The IB method described above is naturally combined with a one-dimensional (1D) model for blood flow and transport in the cardiovascular system. The derivation of such model from the full Navier-Stokes equations is a vivid field of research. We refer the interested reader to [53, 88] for an introduction and for instance to [24, 52, 96] for more advanced studies. For microcirculation, however, the derivation of a reduced flow model is significantly simpler than in the general case. To develop the model we rely on the following assumptions: (i) the displacement of the capillary walls can be neglected, because the pressure pulsation at the level of capillaries is small; (ii) the convective effects can be neglected, because the flow in each capillary is slow; (iii) the flow almost instantaneously adapts to the changes in pressure at the network boundaries, because the resistance of the network is large with respect to its inductance. This means that the quasi-static approximation is acceptable. As a result of that, the blood flow along each branch of the capillary network can be described by means of Poiseuille's law for laminar stationary flow of incompressible viscous fluid through a cylindrical tube with radius R.

Let us decompose the network Λ into individual branches Λ_i, $i = 1, \dots, N$. We denote with $\boldsymbol{\lambda}_i$ an arbitrary orientation of each branch that defines the increasing direction of the arc length s_i. Let $\boldsymbol{\lambda}$, s be the same quantities referring to the entire network Λ. According to Poiseuille's flow, conservation of mass and momentum become,

$$\mathbf{u}_{v,i} = -\frac{R^2}{8\mu}\frac{\partial p_{v,i}}{\partial s_i}\boldsymbol{\lambda}_i, \quad -\pi R^2 \frac{\partial \mathbf{u}_{v,i}}{\partial s_i} = g_i, \tag{4.8}$$

$$\frac{\pi R^4}{8\mu}\frac{\partial^2 p_{v,i}}{\partial s_i^2} = g_i,$$

where g_i is a generic source term. The governing flow equation on Λ is obtained by summing (4.8) over the index i. In conclusion, we now represent the blood flow in the capillary bed on its centerline Λ. The coupled problem for microcirculation and

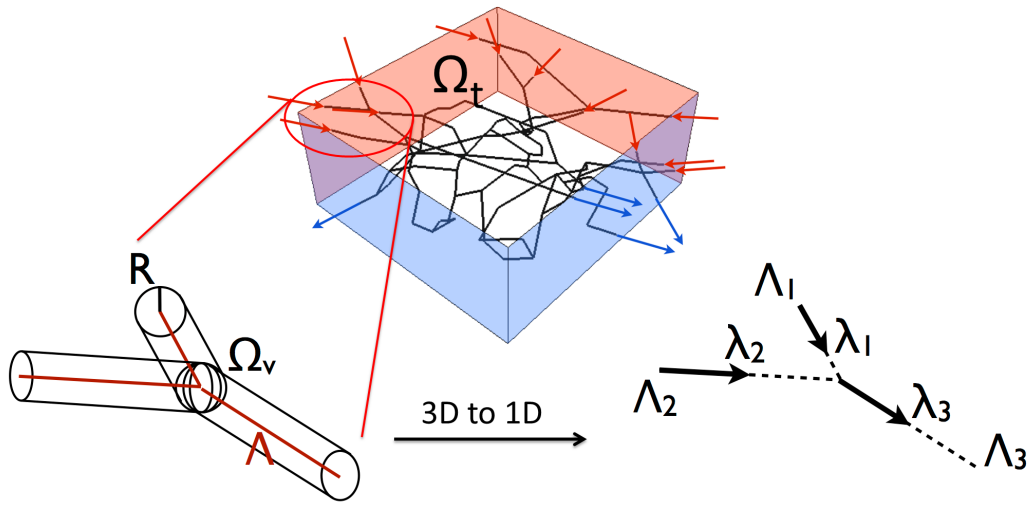

Figure 4.2: *Visualization of a realistic vascular network that is used in the simulations, courtesy of Dr. T. Secomb, available online at [101]. The transition from a three-dimensional to a one-dimensional description of the vessels is depicted below. We represent the branches decomposition of the network and the branches orientation.*

interstitial flow consists to find the pressure fields p_t, p_v and the velocity fields $\mathbf{u}_t$, $\mathbf{u}_v$ such that

$$\begin{cases} -\nabla \cdot \left(\dfrac{k}{\mu}\nabla p_t\right) + L_p^{LF}\dfrac{S}{V}(p_t - p_L) - f(p_{t/v})\delta_\Lambda = 0 & \text{in } \Omega \\ \mathbf{u}_t = -\dfrac{k}{\mu}\nabla p_t & \text{in } \Omega \\ -\dfrac{\pi R^4}{8\mu}\dfrac{\partial^2 p_v}{\partial s^2} + f(p_{t/v}) = 0 & s \in \Lambda \\ \mathbf{u}_v = -\dfrac{R^2}{8\mu}\dfrac{\partial p_v}{\partial s}\boldsymbol{\lambda} & s \in \Lambda \end{cases} \tag{4.9}$$

where the term $f(p_{t/v})$ accounts for the blood flow leakage from vessels to tissue and it has to be understood as the Dirac measure concentrated on Λ and having line density f. A schematic visualization of this flow is reported in Figure 4.1, panel (d), where black arrows depict the fluid exchange between the capillaries and the interstitial tissue. The expression of $f(p_{t/v})$ is provided by the Kedem-Katchalsky equation (4.2). Since in this chapter we focus on flow, we decide to drop the effects of the concentration gradients across the capillary walls. In this case, the constitutive law for the leakage of the capillary walls reduces to the Starling's law of filtration,

$$f(p_{t/v}) = 2\pi R L_p(p_v - \overline{p}_t) \quad \text{with} \quad \overline{p}_t(s) = \frac{1}{2\pi R}\int_0^{2\pi} p_t(s,\theta) R d\theta. \tag{4.10}$$

We notice that f is not a simple function, but rather an integral operator, as it includes the computation of the mean value of the interstitial pressure p_t. Since the capillary bed

is now approximated with its centerline, the average $\overline{p}_v(s)$ coincides with the pointwise value $p_v(s)$. We will discuss later on how to approximate $\overline{p}_t(t,s)$ by means of quadrature rule. We finally observe that in problem (4.9) the distinction between the subregion Ω_t and the entire domain Ω is no longer meaningful, because Λ has null measure in $\mathbb{R}^d$. For notational convenience, in what follows we will then identify Ω_t with Ω and Ω_v with Λ.

4.3.3 Dimensional analysis

Writing the equations in dimensionless form is essential to put into evidence the most significant mechanisms governing the flow through healthy and tumor tissue. We first identify the characteristic dimensions of our problem. We choose length, velocity and pressure as primary variables for the analysis. The characteristic length, d, is the average spacing between capillary vessels, the characteristic velocity, U, is the average velocity in the capillary bed and the characteristic pressure, P, is the average pressure in the interstitial space. Estimates of these values are reported in [7] for healthy tissue. The dimensionless form of (4.9) is then,

$$\begin{cases} -\kappa_t \Delta p_t + Q^{LF}(p_t - p_L) = Q(p_v - \overline{p}_t)\delta_\Lambda & \text{in } \Omega \\ \mathbf{u}_t = -\kappa_t \nabla p_t & \text{in } \Omega \\ -\kappa_v \dfrac{\partial^2 p_v}{\partial s^2} + Q(p_v - \overline{p}_t) = 0 & s \in \Lambda \\ \mathbf{u}_v = -\dfrac{\kappa_v}{\pi R'^2}\dfrac{\partial p_v}{\partial s}\boldsymbol{\lambda} & s \in \Lambda \end{cases} \tag{4.11}$$

In the Poiseuille's equation we use the non dimensional radius $R' = R/d$. The dimensionless groups affecting our equations are the following,

$$\kappa_t = \frac{k}{\mu}\frac{P}{Ud}, \quad Q^{LF} = L_p^{LF}\frac{S}{V}\frac{Pd}{U}, \quad Q = 2\pi R' L_p \frac{P}{U}, \quad \kappa_v = \frac{\pi R'^4}{8\mu}\frac{Pd}{U}, \tag{4.12}$$

which represent the hydraulic conductivity of the tissue, the non dimensional lymphatic drainage, the hydraulic conductivity of the capillary walls and the hydraulic conductivity of the capillary bed, respectively. We refer to section 4.5 for an estimate of these dimensionless groups magnitude and the related discussion.

4.4 Numerical approximation

For complex geometrical configurations explicit solutions of problem (4.11) are not available. Numerical simulations are the only way of applying the model to real cases. Besides applications, the study of numerical approximation methods for problem (4.11) requires first to address existence, uniqueness and regularity of the exact solutions and then to analyse the accuracy of the proposed scheme. These topics, already addressed for a similar problem setting in [33, 34], are particularly relevant in this case because they inform us about the ability of the scheme to approximate the quantities of interest for applications.

The solution of problem (4.11) does not satisfy standard regularity estimates, because the forcing term of equation (4.11)(a) is a Dirac measure. To characterize the regularity of the trial and test spaces we do not resort to weighted Sobolev spaces, as proposed in [33]. Indeed, that approach to analyze and discretize the problem naturally ends up with error estimates requiring finite element approximation on graded meshes, a necessary condition to capture the solution gradients in the neighborhood of the singularity. In this section we investigate the validity of weaker error estimates, which provide control on the approximation error under less restrictive requirements on the scheme. This objective is achieved by following [73], where the error analysis is based on the fact that p_t does not belong to H^1 but $p_t \in W_0^{1,p}, p \in [1, 3 - d/2)$ holds instead. Then, we consider the solution p_t of (4.9) as an element of $W_0^{1,p}, p \in [1, 3 - d/2)$ and we define our test space $W_0^{1,q}$ as:

$$W_0^{1,q} = \{v \in W^{1,q} : v = 0 \text{ on } \partial\Omega\}, \qquad \frac{1}{p} + \frac{1}{q} = 1$$

The discretization of problem (4.11) is achieved by means of the finite element method that arises from the variational formulation of the problem combined with a partition of the domain into small elements, as shown in Figure 4.1, panel (c). We multiply the first equation by a test function $q_t \in W_0^{1,q}$ and integrate over Ω. The Laplace operator is treated using integration by parts combined, for the sake of simplicity, with homogeneous Neumann conditions on $\partial\Omega$, while we use (4.7) to write

$$\big((p_v - \overline{p}_t)\delta_\Lambda, q_t^h\big)_\Omega = \big(p_v - \overline{p}_t, q_t^h\big)_\Lambda.$$

We proceed similarly for the governing equation on the capillary bed. We denote with m_i^-, m_i^+ the extrema of Λ_i oriented along the arc length and with $\boldsymbol{\lambda}_i^{\pm}(m_i)$ the reference outgoing unit vectors of Λ_i at those points. We choose test functions for the pressure field on the capillary bed $q_v \in V_{v,0}$, where $V_{v,0}$ is the subspace of $H^1(\Lambda)$ of functions which vanish on the boundaries of Λ. After integration by parts on each branch Λ_i separately, we obtain the following equation, for any $i = 1, \dots, N$

$$\kappa_v\big(\partial_s p_v, \partial_s q_v\big)_{\Lambda_i} + \kappa_v \partial_s p_v q_v|_{m_i^-} - \kappa_v \partial_s p_v q_v|_{m_i^+} + Q\big(p_v - \overline{p}_t, q_v\big)_{\Lambda_i} = \big(p_{v,0}, q_v\big)_{\Lambda_i},$$

where $p_{v,0}$ denotes the lifting of nonhomogeneous Dirichlet boundary data for the capillary network. Let $i \in \mathcal{J}$ be the indices that identify the branches with the common node m_j. The flow balance at m_j implies that

$$\sum_{i=\mathcal{J}} -\kappa_v \partial_s p_{v,i}|_{m_j}\, q_{v,i}|_{m_j} \boldsymbol{\lambda}_i \cdot \boldsymbol{\lambda}_i^{\pm}(m_j) = 0.$$

Reminding that the test functions for the pressure field on the capillary bed are continuous on the entire network, namely $q_v \in C^0(\Lambda)$ because $V_{v,0} \subset C^0(\Lambda)$ on 1D manifolds, summing up the previous equations with respect to the number of branches, we obtain

$$\kappa_v\big(\partial_s p_v, \partial_s q_v\big)_\Lambda + Q\big(p_v - \overline{p}_t, q_v\big)_\Lambda = \big(p_{v,0}, q_v\big)_\Lambda, \ \forall q_v \in V_{v,0}.$$

Then the weak formulation of (4.11) requires to find $p_t \in V_t := W_0^{1,p}$ and $p_v \in V_{v,0}$ such that,

$$\begin{cases} a_t(p_t, q_t) + b_\Lambda(\overline{p}_t, q_t) = F_t(q_t) + b_\Lambda(p_v, q_t), \ \forall q_t \in W_0^{1,q}, \\ a_v(p_v, q_v) + b_\Lambda(p_v, q_v) = F_v(q_v) + b_\Lambda(\overline{p}_t, q_v), \ \forall q_v \in V_{v,0}, \end{cases} \tag{4.13}$$

with the following bilinear forms and right hand sides,

$$\begin{aligned} a_t(p_t, q_t) &:= \kappa_t \big(\nabla p_t, \nabla q_t\big)_\Omega + Q^{LF}\big(p_t, q_t\big)_\Omega, \\ a_v(p_v, q_v) &:= \kappa_v \big(\partial_s p_v, \partial_s q_v\big)_\Lambda, \\ b_\Lambda(p_v, q_v) &:= Q\big(p_v, q_v\big)_\Lambda, \\ F_t(q_t) &:= Q^{LF}\big(p_L, q_t\big)_\Omega, \\ F_v(q_v) &:= \big(p_{v,0}, q_v\big)_\Lambda. \end{aligned}$$

At the discrete level, one of the advantages of our problem formulation is that the partition of the domains Ω and Λ into elements are completely independent. We denote with $\mathcal{T}_t^h$ an admissible family of partitions of Ω into tetrahedrons $K \in \mathcal{T}_t^h$, where the apex h denotes the mesh characteristic size. We also assume that Ω has a simple shape, such that it can be exactly represented by a collection of elements. Let $V_t^h := \{v \in C^0(\Omega) : \ v|_K \in \mathbb{P}^1(K), \ \forall K \in \mathcal{T}_t^h\}$ be the space of piecewise linear continuous finite elements on $\mathcal{T}_t^h$. Since natural boundary conditions will be applied on $\partial\Omega$, we do not enforce any constraint on the degrees of freedom of V_t^h located at the boundary, but the definition of $a_t(\cdot,\cdot)$ may be subject to some modifications.

For the discretization of the capillary bed, each branch Λ_i is partitioned into a sufficiently large number of linear segments E, whose collection is Λ_i^h, which represents a finite element mesh on a one-dimensional manifold. Then, we will solve our equations on $\Lambda^h := \cup_{i=1}^N \Lambda_i^h$ that is a discrete model of the true capillary bed. Let $V_{v,i}^h := \{v \in C^0(\Lambda_i) : \ v|_E \in \mathbb{P}^1(E), \ \forall E \in \Lambda_i^h\}$ be the piecewise linear and continuous finite element space on Λ_i. The numerical approximation of the equation posed on the capillary bed is then achieved using the space $V_v^h := \big(\cup_{i=1}^N V_{v,i}^h\big) \cap C^0(\Lambda)$. We observe that the continuity of the discrete pressure at the junctions of the network is enforced by construction, by means of the approximation space. More precisely, we will use $V_{v,0}^h$, that is the restriction of V_v^h to functions that vanish on the boundary of Λ, to enforce essential boundary conditions on the pressure, at the inflow and outflow sections of the capillary bed. The mesh characteristic size is denoted with a single parameter h, because we will proportionally refine both finite element spaces V_t^h, V_v^h. The discrete problem arising from (4.11) requires to find $p_t^h \in V_t^h$ and $p_v^h \in V_{v,0}^h$ such that

$$\begin{cases} a_t(p_t^h, q_t^h) + b_{\Lambda^h}(\overline{p}_t^h, q_t^h) = F_t(q_t^h) + b_{\Lambda^h}(p_v^h, q_t^h), \ \forall q_t^h \in V_t^h, \\ a_v(p_v^h, q_v^h) + b_{\Lambda^h}(p_v^h, q_v^h) = F_v(q_v^h) + b_{\Lambda^h}(\overline{p}_t^h, q_v^h), \ \forall q_v^h \in V_{v,0}^h, \end{cases} \tag{4.14}$$

where the bilinear forms $a_t(\cdot,\cdot)$, $a_v(\cdot,\cdot)$, $b_\Lambda(\cdot,\cdot)$ are the same as before, with the only difference that $b_{\Lambda^h}(\cdot,\cdot)$ is now defined over the discrete representation of the network Λ_h.

The solution of the problem (4.13) is characterized by a low regularity, in other words, $V_t \notin H^1(\Omega)$. For this reason, studying the convergence properties of (4.13) to (4.14) is a challenging task. A novel approach for the a priori error analysis of an elliptic problem with a Dirac measure source term has recently been developed in [73], where the authors derive a quasi-optimal a priori estimate for first order finite elements approximation and optimal error bounds for higher order approximations, on a family of quasi-uniform meshes in a L^2-seminorm. Graded meshes are no longer needed to achieve optimality in this new theoretical context. We remark the fact that, in their

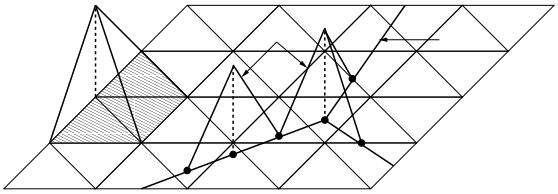

Figure 4.3: *A basis function of the finite element space for the interstitium, ψ_t^i, is depicted on the left. This is a classical piecewise linear and continuous* hat *function. On the right, we show the basis functions ψ_v^i used for the approximation on the capillary network. Note that, by construction, those functions are continuous at the junctions of network branches.*

work, the authors analyze a two-dimensional (2D) elliptic problem with Dirac source terms, while our model turns out to be a 3D-1D coupled system of elliptic equations. For this reason we are interested to investigate whether the convergence properties proved in [73] are valid in a more general case, where the Dirac measure term is in turn coupled to the solution in the surrounding volume through a partial differential equation. For the sake of clarity, we report below the main convergence results of [73], adapted to our particular case.

Let $p_t \in W_0^{1,p}$ the weak solution of (4.13) and let $p_t^h \in V_t^h$ be the finite element approximation given by (4.14). Then, the following upper bound for the L^2-error holds:

$$\|p_t - p_t^h\|_{L^2(\Omega\setminus\Omega_v)} \lesssim h^2 |\log h|. \tag{4.15}$$

The numerical experiments performed to investigate whether the same a priori estimates are still valid for coupled problems such as (4.9) is reported in Section 4.4.3.

4.4.1 Algebraic formulation

We aim to study the matrix form of the variational problem (4.14). Let us denote with $\{\psi_t^i\}$, $i = 1, \dots, N_t^h$ the piecewise linear and continuous Lagrangian finite element basis for V_t^h and with $\{\psi_v^i\}$, $i = 1, \dots, N_v^h$ the one for V_v^h. These two sets of bases are completely independent, since the 3D and 1D meshes do not conform. A sketch of the approximation functions used on the interstitium and on the capillary bed is provided in Figure 4.3. Let $\mathbf{U}_t = \{U_t^1, \dots U_t^{N_t^h}\}$ and $\mathbf{U}_v = \{U_v^1, \dots U_v^{N_v^h}\}$ be the degrees of freedom corresponding to $\{\psi_t^i\}$ and $\{\psi_v^i\}$, respectively. Equations (4.14) are equivalent to,

$$\sum_{j=1}^{N_t^h} U_t^j [\kappa_t (\nabla \psi_t^j, \nabla \psi_t^i)_\Omega + Q^{LF}(\psi_t^j, \psi_t^i)_\Omega + Q(\overline{\psi}_t^j, \psi_t^i)_{\Lambda^h}]$$

$$= Q^{LF}(p_L, \psi_t^i)_\Omega + \sum_{j=1}^{N_v^h} U_v^j (\psi_v^j, \psi_t^i)_{\Lambda^h} \quad i = 1, \dots N_t^h$$

$$\sum_{j=1}^{N_v^h} U_v^j[\kappa_v(\partial_s\psi_v^j, \partial_s\psi_v^i)_{\Lambda^h} + Q(\psi_v^j, \psi_v^i)_{\Lambda^h}]$$

$$= (U_{v,0}, \psi_v^i)_{\Lambda^h} + \sum_{j=1}^{N_t^h} U_t^j(\overline{\psi}_t^j, \psi_v^i)_{\Lambda^h} \quad i = 1, \dots N_v^h$$

where $\overline{\psi}_t^j$ is the average of ψ_t^j, according to (4.6). The above equations form the following linear system,

$$\begin{bmatrix} A_{tt} + M_{tt} + B_{tt} & B_{tv} \\ B_{vt} & A_{vv} + B_{vv} \end{bmatrix} \begin{bmatrix} \mathbf{U}_t \\ \mathbf{U}_v \end{bmatrix} = \begin{bmatrix} \mathbf{F}_t \\ \mathbf{F}_v \end{bmatrix} \Leftrightarrow A\mathbf{U} = \mathbf{F} \tag{4.16}$$

where the components of the right hand side vectors are respectively

$$F_t^i = Q^{LF}(p_L, \psi_t^i)_\Omega, \quad \text{and} \quad F_v^i = (U_{v,0}, \psi_v^i)_{\Lambda^h}.$$

Since the two meshes are completely independent, matrices B_{tt}, B_{tv}, B_{vt} and B_{vv} are built using interpolation and average operators. In particular, we define a discrete operator able to extract the mean value of ψ_t^i and another one able to interpolate between V_t^h and V_v^h. For every node $s_k \in \Lambda^h$ we define $\mathcal{T}_\gamma^h(s_k)$ as the discretization of the perimeter of the vessel $\gamma(s_k)$. For simplicity, we assume that $\gamma(s_k)$ is a circle of radius R defined on the orthogonal plane to Λ^h at point s_k. This set of points is used to interpolate the basis functions ψ_t^i. Let us introduce a local discrete interpolation matrix $\Pi_\gamma(s_k)$ which returns the values of each test function ψ_t^i on the set of points belonging to $\mathcal{T}_\gamma^h(s_k)$. Then, we consider the average operator $\overline{\pi}_{vt} : V_t^h \to V_v^h$ such that $\overline{q}_t = \overline{\pi}_{vt} q_t$. The matrix that corresponds to this operator belongs to $\mathbb{R}^{N_v^h \times N_t^h}$ and it is constructed such that each row is defined as,

$$\overline{\Pi}_{vt}|_k = \mathbf{w}^T(s_k)\Pi_\gamma(s_k) \qquad k = 1, \dots N_v^h$$

where $\mathbf{w}$ are the weights of the quadrature formula used to approximate $\overline{q}_t = \dfrac{1}{2\pi R}\displaystyle\int_0^{2\pi} q_t(s) R d\theta$ on the nodes belonging to $\mathcal{T}_\gamma^h(s_k)$. The discrete interpolation operator $\pi_{vt} : V_t^h \to V_v^h$ returns the value of each basis function belonging to V_t^h in correspondence of nodes of V_v^h. In algebraic form it corresponds to an interpolation matrix $\Pi_{vt} \in \mathbb{R}^{N_v^h \times N_t^h}$. Using these tools we obtain,

$$\begin{aligned} B_{tt} &= \mathbf{V}_t^T \Pi_{vt}^T M_{vv} \overline{\Pi}_{vt} \mathbf{U}_t, \\ B_{tv} &= \mathbf{V}_t^T \Pi_{vt}^T M_{vv} \mathbf{V}_v, \\ B_{vt} &= \mathbf{V}_v^T M_{vv} \overline{\Pi}_{vt} \mathbf{U}_t, \\ B_{vv} &= M_{vv} \mathbf{U}_v, \end{aligned}$$

where M_{vv} is the mass matrix on V_v^h, $[M_{vv}]_{i,j} = (\psi_v^j, \psi_v^i)_{\Lambda^h}$.

For the assembly of (4.16) we use a code developed in GetFem++, a general purpose C++ finite element library [93]. To solve system (4.16) we apply the GMRES method with incomplete-LU preconditioning. We perform an analysis of the computational cost of the different parts of the algorithm when the characteristic size of both the

3D and the 1D computational meshes is proportionally decreased, obtaining the data reported in Figure 4.4. It shows that, when the size h becomes small, the major computational time is taken from the construction of the interpolation matrices Π_{vt} and $\overline{\Pi}_{vt}$. This is a very interesting observation, because it reveals that computational issues may arise when dealing with the interaction of two geometrical structures, such as the mesh for the network and the bulk volume. Although this is not a severe limitation in our case, because we use moderately small domains and meshes, it may become a problem of paramount importance for larger computations. To override these drawbacks, the development of the finite element solver should be complemented by expertise in the field of computational geometry, in particular for the application of efficient search algorithms and data structures to build the interpolation matrices defined above.

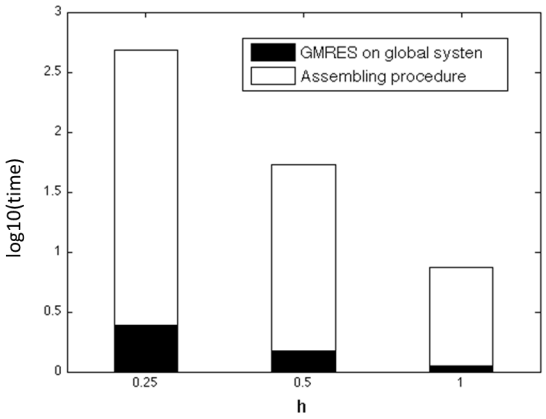

Figure 4.4: *Computational time for matrix assembly (white) compared with the one required to solve the algebraic system (black). The bars quantify the logarithm of the CPU time ($\log_{10}$) measured in seconds. The results refer to the geometrical model* `rat98` *to be introduced in the next section.*

4.4.2 Preliminary validation

Let us consider Darcy's equation for the interstitium in a slightly simpler setting than problem (4.1), where in particular the lymphatic term is neglected. An alternative way to set up and solve the problem has been been studied in [29,103,109], starting from the Green's representation of the Laplace equation. In this case it is possible to define the pressure solution by means of boundary potentials, using the representation formula:

$$G(\mathbf{x}-\mathbf{y}) = \frac{1}{4\pi}\frac{1}{|\mathbf{x}-\mathbf{y}|}$$

$$p_t = p_0 - \int_\Gamma G(\mathbf{x}-\mathbf{y})\mathbf{n}\cdot\nabla p_t d\sigma + \int_\Gamma (p_t - p_0)\mathbf{n}\cdot\nabla G(\mathbf{x}-\mathbf{y})d\sigma \qquad (4.17)$$

where $G(\mathbf{x}-\mathbf{y})$ is the fundamental solution of the Laplace equation, p_0 is a far-field interstitial pressure, in particular $p_t \to p_0$ as $|\mathbf{x}| \to \infty$, and Γ is the external capillary surface. The two boundary integrals are called single and double layer potential, respectively. Substituting the boundary condition on the flux (4.2) into the single layer potential and manipulating the double layer potential, we obtain an integro-differential

representation formula for the exact solution,

$$\begin{cases} \dfrac{d^2 p_v}{ds^2} = \dfrac{8\mu L_p}{\pi R^4} \displaystyle\int_{\gamma(s)} (p_v - p_t) d\sigma, \\ \dfrac{1}{2}(p_t(\mathbf{x}) - p_0) = \dfrac{\mu}{\kappa} \displaystyle\int_\Gamma L_p (p_v - p_t) G(\mathbf{x} - \mathbf{y}) d\sigma \\ \qquad\qquad + \displaystyle\int_\Gamma (p_t - p_0)\mathbf{n} \cdot \nabla G(\mathbf{x} - \mathbf{y}) d\sigma. \end{cases} \tag{4.18}$$

The solution of this model in a simple configuration featuring the flow along a single linear capillary with prescribed boundary conditions is studied in [29]. Our goal is to compare that solution, reported in [29], with the one obtained with our numerical method using the same geometry and parameters of [29]. Prescribed boundary conditions are a pressure drop along the capillary and an imposed pressure value on the outer tissue domain, that is, $p_v(s = in) = 1$, $p_v(s = out) = 0.5$ and $p_t = p_0 = 0$ on $\partial\Omega$. We solve problem (4.11) neglecting the lymphatic term and we represent the capillary pressure as a function of the arclength s, for different values of the vascular conductivity $\hat{L}_p$, where $\hat{L}_p = \dfrac{\mu L_p}{L}$ and L is the domain dimension. The results, shown in Figure 4.5, are in excellent agreement with what is reported in Fig.7 of [29]. This allows us to conclude that our numerical solver is correct and it represents a valid alternative to other solution strategies.

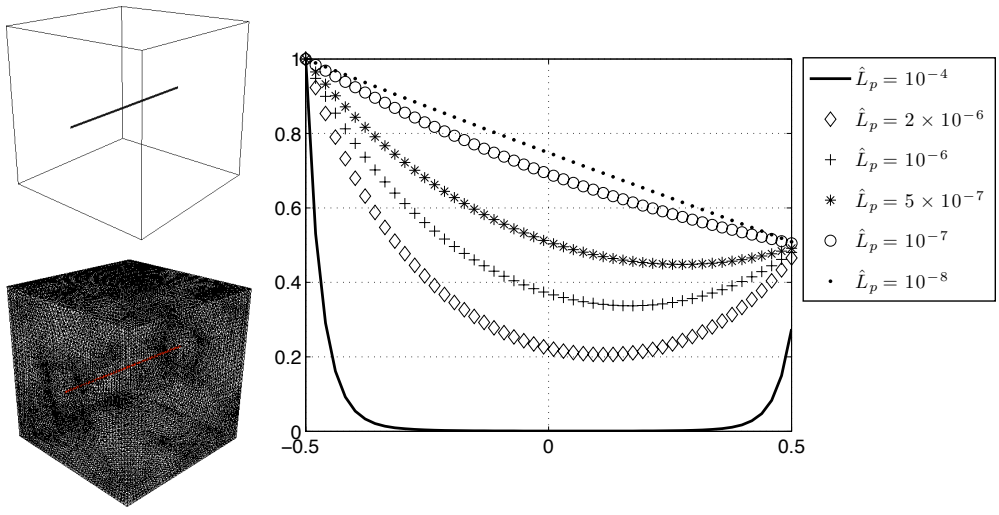

Figure 4.5: *Top left: geometry representing an isolated capillary immersed in a tumor tissue. Bottom left: computational mesh used to define the reference solution p_t^h used to compute the numerical error. Right: capillary pressure as a function of arclenght for vascular conductivities $\hat{L}_p = 10^{-4}$ (black line), 2×10^{-6}, 10^{-6}, 5×10^{-7}, 10^{-7} and 10^{-8} (black dotted line).*

4.4.3 Error analysis

We use the same model problem introduced in section 4.4.2, also to perform the numerical error analysis. In particular we want to test if the convergence error estimate,

proposed in [73], is again valid in the more general case of 3D-1D coupled problems, where the 1D problem acts as a concentrated source embedded in the surrounding volume.
Since we do not know an analytic expression for the exact solution p_t of the considered problem, (4.9), in order to evaluate the norm of the error (4.15), we construct a reference solution on a very fine mesh, reported in Figure 4.5. We fix in this case $h = 1/40$. From now on, we will approximate the exact solution p_t with the numerical solution p_t^h obtained on this fine mesh. Then we compute the numerical solution p_t^h on coarser meshes, fixing $h = 1/20$, $h = 1/10$ and $h = 1/5$ respectively. We compute the L^2-seminorm of the error, $\|p_t - p_t^h\|_{L^2(\Omega\setminus\Omega_v)}$, fixing Ω_v as the cylinder of radius R surrounding the vessel. For the sake of completeness we also assess the error using the H^1-seminorm. The numerical results are reported in Figure 4.6.

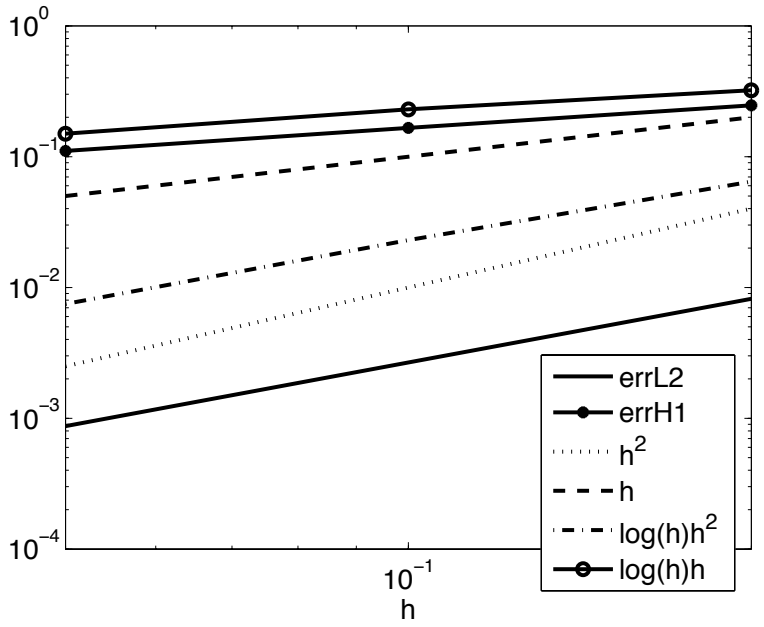

Figure 4.6: *L^2 and H^1 seminorm error decay.*

The numerical tests confirm that error bound (4.15) is still valid for (4.13). Furthermore, the following behavior of the H^1-seminorm error is observed:

$$\|p_t - p_t^h\|_{H^1(\Omega\setminus\Omega_v)} \lesssim h|\log h|. \tag{4.19}$$

Although still preliminary, these findings are encouraging at multiple levels. From the standpoint of applications, they confirm that graded meshes are not required to accurately approximate the pressure field in the volume outside Ω_v, where it has a precise physical meaning according to problem (4.1). A standard finite element formulation, as in (4.14), combined with suitably refined quasi-uniform partition, $\mathcal{T}_t^h$, will capture the main features of the pressure field, as prescribed by (4.15). As a result, the 3D to 1D model reduction technique discussed here turns out to be a very effective approach, which brings significant simplifications to handle the complex network of capillaries at the computational level, without severely compromising the accuracy of the discretization method.

From the theoretical standpoint, we believe that these results shed light on possible directions to extend the analysis of [73]. The results of [73] apply to elliptic problems with a Dirac measure as forcing term and the numerical evidence in support of the analysis is limited to the case of point sources distributed in a bi-dimensional domain. Here we are studing a more challenging problem, in which a 1D manifold is embedded into a 3D domain. Furthermore, we have to solve a coupled problem, namely a problem in which the solutions on the 3D domain and 1D manifold depend on each other. Also, an H^1 error estimate seems to be satisfied by the same theoretical framework. Ongoing work is therefore oriented to extend the analysis of [73] to a problem setting equivalent to (4.13).

4.5 Application to microcirculation and interstitial flow

Fluid and mass transport within a tumor are governed by a subtle interplay of sinks and sources, such as the leakage of the capillary bed, the lymphatic drainage and the exchange of fluid with the exterior volume. The aim of this section is to apply the computational model (4.11) to investigate how these effects influence significant and measurable quantities characterizing the flow into a vascularized tumor mass.

4.5.1 Available data

We aim to analyse fluid transport through tumor tissue *in-vivo*. For the reconstruction of the geometrical model of the capillary bed, we use the available data for a R3230AC mammary carcinoma in rat dorsal skin flap preparation, available in [101]. We consider two datasets, obtained with two independent experiments. The first one, labelled as `rat93` shows the microvascular structure over a region with overall dimensions $250 \times 370 \times 200\mu$m. We refer the interested reader to [102] for more details about this experiment. The average radius of the capillary vessels is assumed to be constant and set to $R = 7.64\,\mu$m. The characteristic length of the problem is chosen as the average spacing between the capillaries, $d = 50\mu$m, according to what reported in [76]. The second case consists of the vascular network on a wider sample of dimensions $550 \times 520 \times 230\mu$m and it is labelled as `rat98`. The characteristic size D of the considered tissue samples is thus in the range of 500μm. The details of the preparation are reported in [103], while the geometries are represented in figure 4.7.

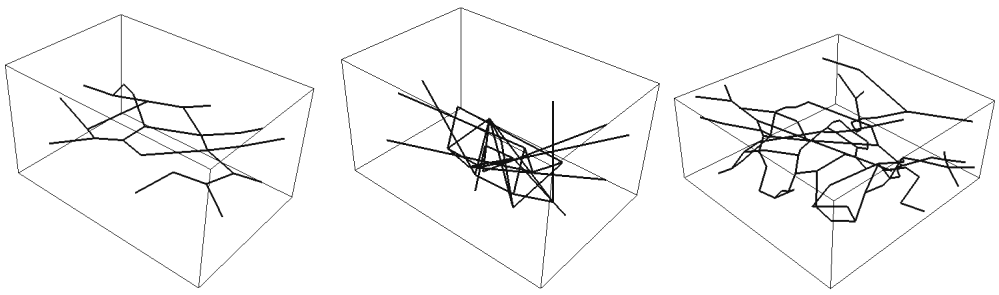

Figure 4.7: *From left to right,* `rat93` *geometry, its random perturbation and* `rat98` *geometry.*

According to [7] and [71], a vascularized healthy tissue is characterized by an average interstitial pressure $P = 1$mmHg and by a characteristic flow speed in the capillary

bed of $U = 100\mu\text{m}/s$. In the healthy case, the parameters that characterize the transport properties of the tissue are the hydraulic conductivity of the interstitium, $k = 10^{-18}\,\text{m}^2$, the hydraulic conductivity of the capillary walls, $L_p = 10^{-12}\,\text{m}^2\text{s/kg}$ and the plasma viscosity $\mu = 4 \times 10^{-3}\,\text{kg}/(\text{ms})$. The magnitude of the lymphatic drainage, modeled as a distributed sink term, is estimated in [7] to be $L_p^{LF}\frac{S}{V} = 0.5\,(\text{mmHg h})^{-1}$.

Given these data, we quantify the magnitude of the dimensionless groups reported in (4.12). We obtain the following values,

$$\kappa_t = 2\times10^{-5}, \quad Q^{LF} = 5.2088\times10^{-5}, \quad Q = 9.6007\times10^{-7}, \quad \kappa_v = 2.6759. \tag{4.20}$$

Since κ_v, the dimensionless conductivity of the capillary bed, is significantly larger than the other quantities, we infer that, as expected, the transport in the coupled capillary/interstitial medium is dominated by the flow in the vascular network. More interestingly, we observe that the other dimensionless numbers lay in a similar range, namely $10^{-6} \lesssim Q,\, \kappa_t,\, Q^{LF} \lesssim 10^{-5}$. This suggests that the interstitial flow, the leakage of the capillary bed and the lymphatic drainage have comparable effects on the interstitial flow and pressure. The significance of model (4.11) is the ability to capture the interplay between these phenomena. The aim of the forthcoming sections is indeed to use the model to analyze these effects in different conditions, representing for instance healthy and tumor tissue.

4.5.2 Influence of the boundary conditions

The samples `rat93` and `rat98` represent microscopic regions separated from the surrounding tumor mass by artificial planar sections. An appropriate modelling of boundary conditions is required.

For the capillary flow, we aim to enforce a suitable pressure gradient along the network. Observing that the inflow and outflow sections of the network lay on the lateral side of the tissue slab, see Figure 4.1 (d), we enforce a given pressure p_{in} on two adjacent faces and a pressure p_{out} on the opposite ones. By this way, the pressure drop $p_{in} - p_{out}$ is enforced at the tips of the network. To estimate the magnitude of the pressure drop, we use Poiseuille's law to fit a given value of the average blood velocity through healthy microvascular network, namely $\bar{u}_v = 0.2$ mm/s. More precisely, using equation $(4.9)_d$, we obtain

$$\frac{p_{in} - p_{out}}{|\Lambda|} = -\frac{8\mu}{R^2}\bar{u}_v,$$

which provides a pressure drop equal to $p_{in} - p_{out} = 0.4056$ mmHg for `rat93` and $p_{in} - p_{out} = 1.2522$ mmHg for `rat98`.

For the interstitial flow, we aim to model the *in-vivo* configuration, where the available tumor sample is embedded into a similar environment. To represent this case, we believe that the most flexible option is to use Robin-type boundary conditions for the interstitial pressure,

$$-\kappa_t \nabla p_t \cdot \mathbf{n} = \beta(p_t - p_0). \tag{4.21}$$

In equation (4.21), p_0 represents the far field pressure value, while β can be interpreted as an effective conductivity accounting for layers of tissue surrounding the considered sample. Assuming that the interstitial pressure decays from p_t to p_0 over a distance comparable to the sample characteristic size, D, dimensional analysis shows that a

rough estimate of the conductivity is $\beta = \kappa_t/D$. The specific aim of this section is to test the sensitivity of the model to variations of the parameter β over a few orders of magnitude around the reference value κ_t/D, which is equivalent to 10^{-6} in dimensionless form.

The results of the simulations obtained using the values $\beta = \{0, 10^{-2}, 1, 10^2\} \times (\kappa_t/D)$ and the `rat98` geometry are reported in Figure 4.8. The analysis of the interstitial pressure field p_t shows that the results obtained using $\beta = 0$, that is homogeneous Neumann boundary conditions, or $\beta = 10^{-2}\kappa_t/D$ are almost equivalent (not shown). As confirmed by the top panel of Figure 4.8, more significant differences are observed when β is further increased. In those cases, the boundary of the domain clearly feels the influence of the reference pressure p_0, which is weakly enforced in proximity of the boundary. Anyway, this analysis leads us to conclude that, in the case of healthy tissue, boundary conditions mildly affect the interstitial pressure distribution. We claim that the sensitivity with respect to boundary conditions is mitigated by the presence of the uniformly distributed lymphatic drainage effect, which removes the fluid in excess released by the leaky capillary network. To confirm this hypothesis, the same set of numerical experiments has been performed for a modified model where the lymphatic drainage has been switched off. This is, in fact, the assumption that is usually adopted to model tumors. The results are reported on the bottom panel of Figure 4.8. A remarkable difference is observed with respect to the previous case. Now, the physiological capillary leakage can only be balanced by the flow exchanged through the external boundary. As a consequence of that, the interstitial pressure field is completely saturated when homogeneous Neumann conditions are enforced on the boundary, see Figure 4.8 (bottom-left). For this reason, it is essential to correctly capture the fluid flow through the artificial boundaries of the domain. According to the results reported here and in the forthcoming section, we believe that the range $\beta \in (1, 10^2) \times (\kappa_t/D)$ is the most adequate for this purpose.

4.5.3 Comparison of flow in healthy and tumor tissue models

The natural application of the model is a comparison of flow in the healthy and pathological conditions. To pursue this aim, we compare the following cases:

A, healthy tissue. With respect to our model, this case is defined by:

- a normal capillary network configuration. To match this condition, we use the network `rat93` available from [101], which shows a smooth and regular ramification of capillaries.
- a normal capillary phenotype, represented by the physiological value of the capillary conductivity $L_p = 10^{-12}\,\mathrm{m^2 s/kg}$.
- a normal lymphatic drainage function. This effect is accounted by the term $L_p^{LF}\frac{S}{V} = 0.5\,(\mathrm{mmHg\,h})^{-1}$.

B, tumor tissue. With respect to our model, this case is defined by:

- a tortuous capillary network configuration that is obtained in our case by means of a random perturbation of the points between the segments of the

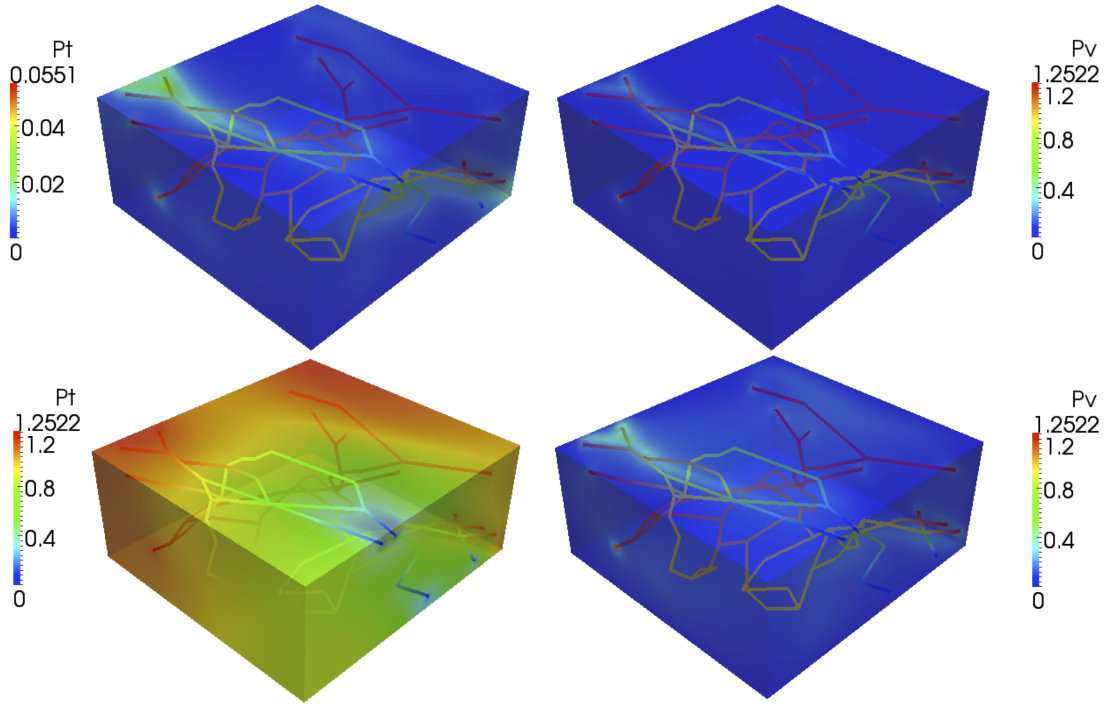

Figure 4.8: *Results of tissue and vessels fluid pressures, p_t and p_v, computed fixing $\beta = 0$ (top-left) and $\beta = 10^2 \kappa_t / D$ (top-right). The other transport parameters are set to represent healthy tissue. On the bottom panel we perform the same comparison when the lymphatic drainage has been switched off.*

`rat93` geometry, shown in Figure 4.7 (central geometry). To obtain a significant difference, the amplitude of the perturbations is adjusted such that the total length of the network almost doubles with respect to the healthy case.

- an increased leakage due to the tumor capillary phenotype. This effect is obtained by increasing the capillary conductivity up to $L_p = 10^{-10}\,\mathrm{m^2 s/kg}$.
- absence of lymphatic drainage function, namely $L_p^{LF}\frac{S}{V} = 0\,(\mathrm{mmHg\,h})^{-1}$.

In addition to these cases, we consider some intermediate configurations that will help us to highlight the competing effects of enhanced permeability and lymphatic drainage. The first one, labelled as case C below, represents the properties of the tumor treated with a vascular re-normalization therapy:

C, tumor after vascular re-normalization therapy. The main characteristic of the model are reported from [72]:

- for the re-normalized capillary bed geometry we use the `rat93` data.
- a tumor capillary phenotype is assumed to be normal after the therapy.
- absence of lymphatic drainage function.

Keeping in mind that it does not correspond to an observed physiological state, it will be interesting to compare Case C with the dual one, which arises from the tumor model, where only the lymphatic drainage is restored to the healthy state. Furthermore, to achieve a more direct comparison with case C, we use the smooth vascular geometry in this case too. More precisely, the configuration, labelled as D, is defined as follows:

D, tumor with active lymphatic drainage. This idealized case is obtained by:

- the same capillary network used for the healthy case.
- a tumor capillary phenotype and corresponding wall conductivity.
- presence of healthy lymphatic drainage function.

An extensive comparison of the flow indicators for the test cases A, B, C and D, is reported in Table 4.1 below. The numerical experiments are also repeated for different types of boundary conditions on the artificial sections $\partial\Omega$, namely, we vary the parameter β as $\beta \in \{0, 1, 10^2\}\kappa_t/D$.

Analysis of blood flow in the capillary bed.

Blood flow in the capillary bed is basically represented by the average value of the velocity in the network, that is directly computed from the pressure field in the network as follows,

$$\overline{u}_v = \frac{1}{|\Lambda|}\int_\Lambda \mathbf{u}_v \cdot \boldsymbol{\lambda} ds = -\frac{1}{|\Lambda|}\int_\Lambda \frac{R^2}{8\mu}\frac{\partial p_v}{\partial s}\boldsymbol{\lambda}\cdot\boldsymbol{\lambda} ds\,.$$

With respect to this quantity, from Table 4.1 we observe that cases A, C and D, which are characterized by the same network geometry, are almost equivalent for all numerical experiments, while the same quantity for case B is basically halved. These results provide a strong evidence that blood filtration in the capillary network is inversely proportional to the total length of the network, as shown by the expression above, while it is almost insensitive to all the other variables of the problem. This conclusion is confirmed by the analysis of the dimensionless groups characterizing the problem, namely (4.20). Since $\kappa_v \gg \kappa_t, Q, Q^{LF}$, the flow problem in the capillary bed is decoupled from the one in the interstitial tissue. In other words, the feedback of the interstitial fluid pressure on the capillary network is almost negligible. Because of leakage, the network substantially acts as a source term on the tissue.

Looking at the spatial variation of the blood velocity on Λ, we observe that it is almost constant over the network, as a consequence of the fact that the pressure p_v is linearly decreasing from p_{in} to p_{out}. This behavior is due to the fact that equation $(4.9)_c$ is linear and the leakage effect is small. Although this model is very popular for microcirculation, see for instance [6, 29, 33, 100, 105, 109], it is affected by some limitations. Using a linear model implies that the capillary flow is not sensitive to the tortuosity of the network, which could be quantified in our case by the magnitude of the angles between the individual branches. Another limitation is that the presence of red blood cells is only indirectly accounted for, by suitably tuning the viscosity of the fluid. Although the full three-dimensional resolution of the fluid particle interaction, addressed for instance in [45, 79, 80], would be too demanding for our purposes, other reduced microcirculation models, such as [44, 74], should be in future compared to the present approach.

Quantitative indicators of interstitial flow.

Interstitial flow directly affects how efficiently nutrients, drugs and wastes are transported to and from cells among the interstitial tissue. To analyze these effects we introduce two quantitative indicators: the net fluid flux from the capillary network to the interstitial volume and the equivalent conductivity of the tissue construct.

The local fluid exchange rate is defined as $f(p_{t/v})$ in equation (4.10). In Table 4.1 we report its mean value over the network,

$$\overline{f}(p_{t/v}) = \frac{2\pi R L_p}{|\Lambda|} \int_\Lambda (p_v - \overline{p}_t) ds \,.$$

This expression shows that $\overline{f}$ is affected by the hydraulic conductivity of the capillary walls, L_p, as well as by the interstitial fluid pressure $\overline{p}_t$ and because of the negative sign these quantities have a competitive role in determining the flux.

The other indicator is the norm of the diagonal hydraulic tensor K, defined according to Darcy's law for an isotropic porous construct,

$$\overline{\mathbf{u}} = -K\overline{\delta \mathbf{p}} \tag{4.22}$$

where $\overline{\mathbf{u}}$ and $\overline{\delta \mathbf{p}}$ are mean quantities computed over the entire tissue construct,

$$\overline{\mathbf{u}} = \frac{1}{|\Omega|} \int_\Omega \mathbf{u} \, d\Omega, \qquad \overline{\delta \mathbf{p}} = \frac{1}{|\Omega|} \int_\Omega \delta \mathbf{p} \, d\Omega$$

where δp is defined as the difference from the local pressure and the basal pressure, namely $\delta p(t, \boldsymbol{x}) = p(t, \boldsymbol{x}) - p_0$. The hydraulic conductivity tensor represents the ease with which a fluid can move through the medium and, according to equations (4.22), it is determined by the pressure drop in the construct, which in turn is affected by the conductivity of the capillaries as well as by the lymphatic drainage into the tissue. Since we are actually dealing with two different subregions, namely Ω_v and Ω_t, to compute proper values of $\overline{\mathbf{u}}$ and $\overline{\delta \mathbf{p}}$ we use the following definitions:

$$\begin{aligned}
\overline{\mathbf{u}}_v &= \frac{1}{|\Lambda|} \int_\Lambda \mathbf{u}_v ds, \quad \overline{\mathbf{u}}_t &&= \frac{1}{|\Omega_t|} \int_{\Omega_t} \mathbf{u}_t d\sigma, \\
\overline{\delta \mathbf{p}_\mathbf{v}} &= \frac{1}{|\Lambda|} \int_\Lambda \delta \mathbf{p}_\mathbf{v} ds, \quad \overline{\delta \mathbf{p}_\mathbf{t}} &&= \frac{1}{|\Omega_t|} \int_{\Omega_t} \delta \mathbf{p}_\mathbf{t} d\sigma, \\
\overline{\mathbf{u}} &= \frac{\overline{\mathbf{u}}_v \pi R^2 |\Lambda| + \overline{\mathbf{u}}_t |\Omega_t|}{\pi R^2 |\Lambda| + |\Omega_t|}, \qquad \overline{\delta \mathbf{p}} &&= \frac{\overline{\delta \mathbf{p}_\mathbf{v}} \pi R^2 |\Lambda| + \overline{\delta \mathbf{p}_\mathbf{t}} |\Omega_t|}{\pi R^2 |\Lambda| + |\Omega_t|} \,.
\end{aligned}$$

Furthermore, observing that the sample `rat93` features an almost planar network in x and y directions, the final form of equation (4.22) results in:

$$\begin{bmatrix} \overline{u}_x \\ \overline{u}_y \end{bmatrix} = - \begin{bmatrix} K_{xx} & 0 \\ 0 & K_{yy} \end{bmatrix} \begin{bmatrix} \overline{\delta p}_x \\ \overline{\delta p}_y \end{bmatrix} \,.$$

Given K_{xx} and K_{yy} from the equations above, we compute a representative value of the tensor K using the Frobenius norm:

$$\|K\|_F = \sqrt{tr(KK^T)}.$$

The computed values for $\|K\|_F$ are reported in Table 4.1. High values of $\|K\|_F$ indicate that the construct could be well perfused, conversely low values of $\|K\|_F$ mean that the construct is impervious. The net fluid flux $\overline{f}$ and the hydraulic conductivity indicator $\|K\|_F$ are affected by both the capillary leakage and the interstitial fluid pressure. Understanding which of these two factors dominates in different conditions will be the objective of the forthcoming section.

Analysis of capillary leakage and interstitial pressure. The effect of enhanced permeability and retention.

We discuss the results of the simulations case by case, for the test cases A, B, C and D defined before.

Case A Table 4.1 and Figure 4.9 show that $\overline{f}$ is rather insensitive to the outer boundary conditions on the interstitial volume for the healthy tissue model. This is due to the lymphatic drainage effect, which removes the excess of fluid in the interstitial volume no matter of how much fluid is exchanged across the artificial sections $\partial\Omega$. In other words, the retention effect is absent for the healthy tissue. This allows the capillary leakage to reach its physiological range. The presence of lymphatic drainage causes the pressure field in the tissue to be very low, since the interstitial pressure nearly approaches the minimum value in all the domain, as shown in Figure 4.10 (top-left). The value of the $\|K\|_F$ indicator is higher than all other cases for the entire range of β and it slightly increases with β, due to the fact that the artificial boundaries become more permeable to flow.

Case B The situation is radically different for the tumor case, because the interstitial fluid pressure is highly sensitive to the conditions that regulate the fluid exchange with the external volume. We analyze the variation of $\overline{f}$ by progressively increasing the values of β. The first dataset of Table 4.1 corresponds to homogeneous Neumann boundary conditions for the external boundary $\partial\Omega$. In absence of lymphatic drainage and fluid exchange with the exterior, the interstitial fluid pressure becomes completely saturated. More precisely, we observe that the average interstitial fluid pressure on Ω, denoted as $\overline{p}_t$, reaches the average capillary pressure over the network, which is not reported but could easily be quantified as $(p_{in}+p_{out})/2 \simeq 0.2$ mmHg, since we know that p_v linearly varies over Λ. As a result of that, the pressure gradient $p_v - \overline{p}_t$ is significantly lower than the physiological value and the corresponding net flux practically vanishes, namely $\overline{f} = 1.0004 \times 10^{-25}$ cm^3/s. At the same time, the local fluid exchange is not completely negligible, owing to the variations of the pressure in the capillary bed. In the worst case $\beta = 0$, the maximal flow rate is indeed equal to $\max_\Lambda f(p_{t/v}) = 8.7531 \times 10^{-14}$ cm^3/s.

In conclusion, the fluid retention effect combined with the increased conductivity of the tumor capillary phenotype leads to interstitial fluid pressure saturation and significant reduction of the interstitial flow. As confirmed by Table 4.1 and Figure 4.9, the situation progressively improves when β increases, because the exchange of fluid with the exterior region decreases $\overline{p}_t$ and restores more natural values of the capillary transmural pressure gradient $p_v - \overline{p}_t$. As a consequence of that, the transmural capillary flux increases with β and attains values larger than in Case A. This suggests that the augmented capillary hydraulic conductivity becomes the dominant factor for extravasation. Regarding the value of $\|K\|_F$, we observe that it is lower than all the other cases, confirming that the overall interstitial flow is less than in the case of healthy tissue.

Case C The interstitial fluid pressure is again highly sensitive to the boundary condition that regulates the fluid exchange with the external volume, since the lymphatic system is absent. When $\beta = 0$ the value of $\overline{f}$ is similar to the value reached in Case B, $\overline{f} = 4.3887 \times 10^{-26}$ and the mean interstitial fluid pressure becomes completely saturated

reaching the mean value $\overline{p}_t = 0.222084$. On the contrary, the behavior becomes more similar to Case A when the value of β increases, namely $\beta \in \{1, 10^2\}\kappa_t/D$, because the boundary conditions contrast the absence of the lymphatic drainage.
Figure 4.9 (top) shows that the fluid flux $\overline{f}$ reaches values similar to Case A, because the conductivity of the capillary walls is equal to the one of healthy tissue. The two cases are comparable also with respect to the value of $\|K\|_F$, although the healthy tissue model is slightly more permeable. Figure 4.9 (bottom) shows that $\|K\|_F$ increases together with the exchange of fluid with the exterior region, namely the parameter β, because it induces a low pressure field within the tissue, as we observe in Figure 4.10 (bottom-left).

Case D This last case is characterized by all the factors that increase the leakage from capillaries to tissue. Indeed we are considering the presence of the lymphatic network and we choose the high value of the vessels conductivity, equal to the tumor case. On one hand, thanks to the first effect, the interstitial fluid pressure is insensitive to the boundary conditions on the interstitial volume and there is no retention effect, as it happens for Case A. On the other hand, the high value of the hydraulic conductivity leads to a considerable interstitial fluid flux for each values of β. The inspection of the interstitial pressure field, shown in Figure 4.10 (bottom-right), suggests that high conductivity and lymphatics drainage play against each other, causing a significant transversal pressure gradient in the neighbourhood of the capillary bed. As a result of that, the equivalent conductivity indicator $\|K\|_F$ is rather small if compared to the previous cases, see in particular Figure 4.9 (bottom).

In conclusion, these results highlight the importance of avoiding fluid retention in order to facilitate interstitial flow. In absence of lymphatic drainage, an appropriate fluid exchange from the tumor mass to the exterior could increase the ability of releasing therapeutic agents from the capillary network. In conditions where the drainage is limited, but not completely absent, the vascular renormalization therapy [72] has the potential to restore the physiological flow conditions.

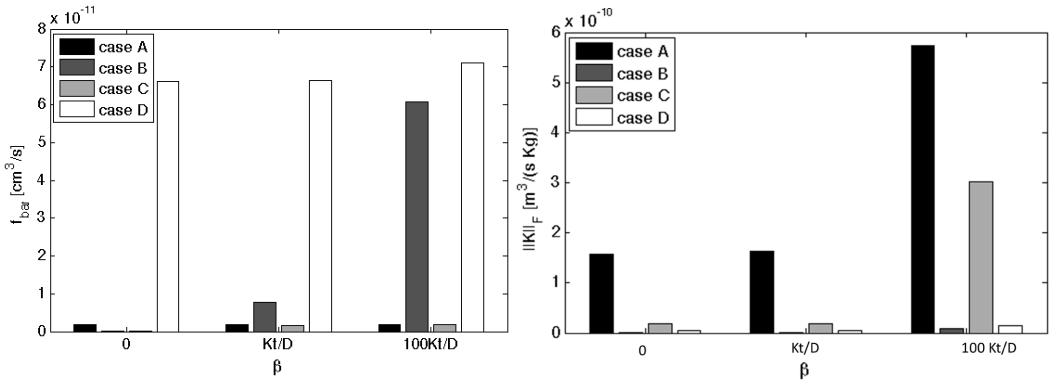

Figure 4.9: *Total fluid flux $\overline{f}$ (left) and hydraulic conductivity indicator $\|K\|_F$ (right) for the different cases A, B, C and D (left to right on each group of bars).*

Neumann boundary conditions $\beta = 0$

	case **A**	case **B**	case **C**	case **D**
$\overline{p}_t$ [mmHg]	0.000933564	0.215985	0.222084	0.0343636
$\overline{u}_v$ [mm/s]	0.19999	0.090445	0.19999	0.19999
$\overline{f}$ [cm^3/s]	1.7992×10^{-12}	1.0004×10^{-25}	4.3887×10^{-26}	6.6227×10^{-11}
$\|$ Keq $\|_F$ [m^3/(s Kg)]	1.5718×10^{-10}	1.0524×10^{-12}	1.9409×10^{-11}	4.1082×10^{-12}

Robin boundary conditions $\beta = \kappa_t/D$

	case **A**	case **B**	case **C**	case **D**
$\overline{p}_t$ [mmHg]	0.000923907	0.189832	0.036731	0.0340585
$\overline{u}_v$ [mm/s]	0.19999	0.090445	0.19999	0.19999
$\overline{f}$ [cm^3/s]	1.7993×10^{-12}	7.8066×10^{-12}	1.4868×10^{-12}	6.6364×10^{-11}
$\|$ Keq $\|_F$ [m^3/(s Kg)]	1.6264×10^{-10}	1.1715×10^{-12}	1.9238×10^{-11}	4.2386×10^{-12}

Robin boundary conditions $\beta = 10^2\kappa_t/D$

	case **A**	case **B**	case **C**	case **D**
$\overline{p}_t$ [mmHg]	0.000723531	0.0709247	0.00260011	0.0274557
$\overline{u}_v$ [mm/s]	0.19999	0.090445	0.19999	0.19999
$\overline{f}$ [cm^3/s]	1.8017×10^{-12}	6.0667×10^{-11}	1.7693×10^{-12}	7.0980×10^{-11}
$\|$ Keq $\|_F$ [m^3/(s Kg)]	5.7370×10^{-10}	9.2741×10^{-12}	3.0191×10^{-10}	1.5504×10^{-11}

Table 4.1: *Characteristic indicators of capillary and interstitial flow for different test cases and boundary conditions.*

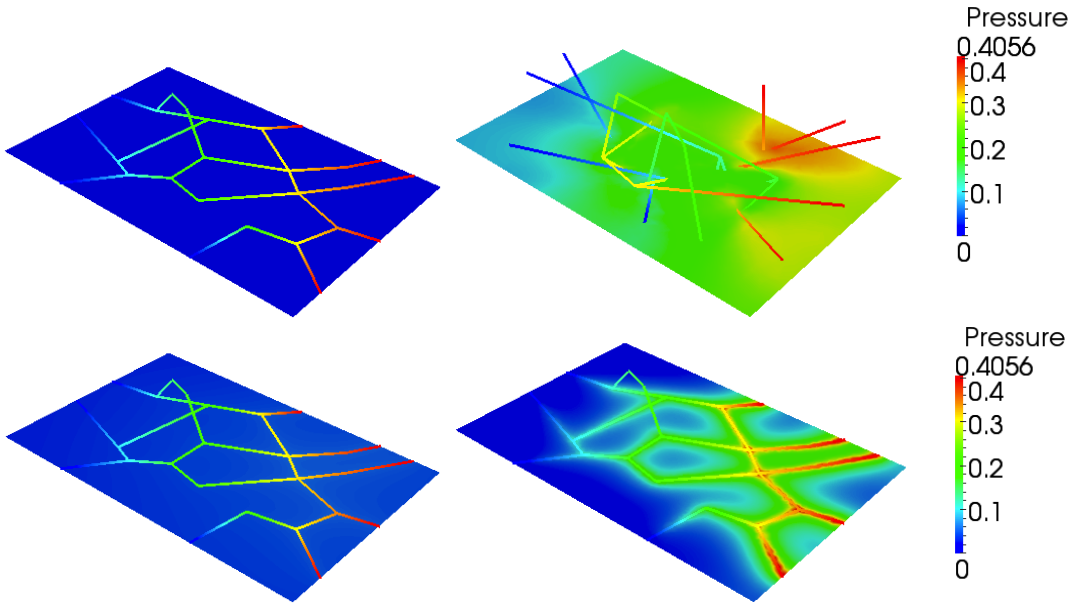

Figure 4.10: *Results of tissue and vessels fluid pressures, p_t and p_v, computed fixing $\beta = \kappa_t/D$. Cases A, B, C and D are listed from top-left to bottom-right. We represent a slice of the 3D tissue domain Ω in z = 100 μm.*

4.6 Conclusions

In this chapter we have developed a computational model able to capture the flow through a heterogeneous system characterized by a network of leaky channels embedded into a porous medium. A model reduction technique, inspired to the immersed boundary method, allows us to achieve simulations of non trivial network geometries with a moderate computational cost. The application of the model to the flow through vascularized solid tumors has been extensively discussed. The efficiency of the method is tested by using the realistic vascular geometries reported in [102, 103]. This feature suggests that the model may be successfully coupled with a dynamic model for angiogenesis, such as the one recently appeared in [113].

The extension of this first part will be developed in the next chapter, where flow models will be combined with mass transport, in order to analyze the distribution of nutrients or therapeutic agents such as drugs or pharmacologically active nanoparticles. The application of this modelling framework to the transport of small molecules, such as oxygen, has already been addressed in [102]. The treatment of vascular diseases using locally delivered nanoparticles is on the edge of biomedical research [46]. Theoretical models describing these phenomena into small arteries are currently being developed from both computational and analytical standpoints, see for example [70] and [112], respectively.

CHAPTER 5

A computational model of drug delivery through microcirculation to compare different tumor treatment options

5.1 Introduction

We complete the study developed in the previous chapter, analyzing mass transport in vascularized tumor tissues. Also in this case we deal with multidomain problems with heterogenous dimension. Mass transport plays a fundamental role in the development of cancer [46]. At different phases of cancer disease, such as the propagation of growth signals, the invasion of other tissue and the activation angiogenesis, tumors use mass transport phenomena to interact with the surrounding environment [62]. Mass transport is also at the basis of cancer pharmacological treatment. Targeting vascularized tumors using the vascular network is a natural therapeutic option. Nevertheless, the success of anticancer therapies in treating cancer cells is limited by their inability to reach their target *in vivo* in adequate quantities [68]. An agent that is delivered intravenously reaches cancer cells via distribution through the vasculature, transport across the wall of the vessels and transport through the tissue interstitium. Each of these steps can be seen as a barrier to delivery. In addition, delivered molecules may bind to constituents of the extracellular matrix and be metabolised by cells.

The characteristic traits of cancer can be seen as the emergent effects of a cascade of phenomena that propagate from the molecular scale, through the cell and the tissue microenvironment, up to the systemic level. Transport phenomena at the level of the capillary network (the microenvironment or microscale) play a key role in this sequence of effects. In particular, the capillary phenotype of a tumor is an important factor for the drug delivery process [25]. As we have already seen, blood vessels in tumors are

leakier and more tortuous than the normal vasculature and the pressure generated by the proliferating cells reduces tumor blood and lymphatic flow. These abnormalities lead to an impaired blood supply and abnormal tumor microenvironment characterized by hypoxia and elevated interstitial fluid pressure. These effects reduce the ability to deliver drugs.

The objective of the work developed in this chapter is to perform a comparative study of different modalities to deliver drug into a vascularized tumor mass. This is achieved by developing a new pharmacokinetic model able to capture the absorption of a drug through the vascular network as well as its distribution and metabolization in the tumor. Following the seminal sequence of works by Baxter and Jain [6–9], we believe that the interplay between blood perfusion, fluid exchange with the interstitial volume, mass transport in the capillary bed, through the capillary walls and into the surrounding tissue, are important effects to understand the delivery process at the microscale. Temporal and spatial dependence will be fully accounted in our governing equations, in contrast to the approach based on compartment models. Since we consider these phenomena at the level of capillaries, it is possible to derive the governing equations from a mechanistic standpoint based on the fundamental laws of flow and mass transport. The model is also prone to be adapted to different delivery methods, because it descends form a general theoretical framework. Besides studying the case of bolus injection, which consists in delivering a solution containing the active drug into the systemic circulation, we will apply the model to analyze the delivery of drug from nanoparticles, which are in turn injected into the blood stream and interact with the capillary walls.

To reduce the geometrical complexity of the model, we exploit the immersed finite element method [78, 115]. The capillary bed is modelled as a network of one-dimensional channels. Due to the natural leakage of capillaries, it acts as a concentrated source of flow immersed into the interstitial volume. This modelling approach significantly reduces the issues related to the simulation of the flow in the microvessels. The main methodological and theoretical aspects of the method have already been addressed in the previous chapter 4. In particular, the model ends up to be a system of partial differential equations, which are hard to solve with analytical tools. For this reason, the model is complemented with the numerical solver developed in the previous chapter, based on the finite element method.

The comparison results suggest that using nanoparticles as intermediate vectors for chemotherapy improves the treatment. For the same amount of injected dosage, drug charged nanoparticles provide higher concentration levels in the interstitial tissue of the tumor and more persistent delivery over time with respect to bolus injection. Owing to the computational approach, these conclusions are based on the analysis of specific performance indicators, such as the interstitial drug concentration levels, the drug metabolization rates, the cell surviving fractions and the corresponding timecourses.

5.2 Model set up

We start the derivation of the model by presenting the governing equations for microcirculation, tissue perfusion and mass transport. In a second phase, we will adapt these general equations to the specific cases. The first case is the study of the coupled trans-

port of oxygen and tirapazamine, a drug specifically designed to target hypoxic cells. In the second one we apply the theory to analyze the delivery of drugs consequent to the injection of nanoparticles into the tumor region.

5.2.1 A general framework

We aim to model fluid and mass transport in a permeable biological tissue perfused by a capillary network. We start recalling the principal components of the model, introduced in section 4.2. We consider a domain Ω that is composed by two parts, Ω_v and Ω_t, the capillary bed and the tumor interstitium, respectively. To account for the microvascular network, we model the capillaries as cylindrical vessels. We denote with Γ the outer surface of Ω_v, with R its radius and with Λ the centerline of the capillary network. A characteristic feature of the computational model is that the capillaries are actually represented as one-dimensional channels. As shown in [12,50,51,103] this approximation significantly simplifies the problem at the computational level. This is done by taking the limit $R \to 0$ and shrinking the capillary bed to its centerline Λ. We denote with s the arc length coordinate along this line. A sketch of the domains before and after adopting the one-dimensional representation of the capillary network is visualized in Figure 4.2. After this step, we observe that the distinction between the subregion Ω_t and the entire domain Ω is no longer meaningful, because Λ has null measure in $\mathbb{R}^d$. For notational convenience, in what follows we will then identify Ω_t with Ω and Ω_v with Λ.

The physical quantities of interest are the flow pressure p, the velocity $\mathbf{u}$ and the concentration of transported solutes c. They are all defined as fields depending on time t and space, being $\mathbf{x} \in \Omega$ the spatial coordinates. Furthermore, we will denote with the subscript v their restriction to the capillary bed (vessels), and with t the restriction to the interstitial tissue. The derivation of our model stems from fundamental balance laws regulating the flow in the capillary bed, the extravasation of plasma and solutes and their transport in the interstitial tissue.

Flow equations

The flow model consists in two parts, the microcirculation and the flow in the interstitial volume, which interact through suitable interface conditions. We refer the reader to the previous section 4.3.2, where the model has been derived.
We remind that one of the functions of the capillary network is to transport and distribute fluid and chemicals to the interstitial volume. This is achieved by means of the leakage of the capillary walls. We model this effect using the Kedem-Katchalsky equation, that is

$$J_v := L_p((p_v - p_t) - \sum_k \sigma_k(\pi_{v,k} - \pi_{t,k}))$$

The meanings of all the different parameters are reported in section 4.3.2. We highlight that although the index k spans over all solutes that are dissolved in blood, not all of them significantly affect the oncotic pressure. Only the large molecules, such as proteins, can induce a significant oncotic pressure gradient. Indeed, the oncotic pressure gradient is mainly due to the significant presence of albumin in blood [31,55,89], whose concentration can be reasonably considered to be constant. According to data provided

there, the oncotic pressure gradient due primarily to albumin in arterioles and capillaries is about 25 mmHg, which is comparable to the hydrostatic pressure in the vessel. In contrast, we assume that solutes such as oxygen or low concentrated drugs can not significantly contribute. This assumption will be further discussed in what follows, on the basis of the physical parameters characterizing the transport of the considered solutes. As a result, for our purposes, the capillary leakage only depends on the hydrostatic pressure according to the following expression,

$$J_b(p_t, p_v) := L_p((p_v - p_t) - \sigma(\pi_v - \pi_t)) = L_p((p_v - p_t) - \sigma_p R_g T(c_{v,p} - c_{t,p}))$$

where, in agreement with the definition of π, $c_{v,p}$ and $c_{t,p}$ denote the constant protein concentration in the capillaries and the interstitial tissue respectively. As a consequence, the flow equations will not depend on the mass transport model that will be developed in the next section. In contrast to what we have done in the previous chapter, we do not drop the effects of the proteins concentration gradient across the capillary walls. We are no more focused only on the flow equations, but also on the mass transport, therefore we want to investigate what is the effect of the oncotic pressure term on the system.

As a consequence of all the modelling assumptions and the application of the immersed boundary method, the coupled problem for microcirculation and perfusion consists to find the pressure fields p_t, p_v and the velocity fields $\mathbf{u}_t$, $\mathbf{u}_v$ such that

$$\begin{cases} -\nabla \cdot \left(\dfrac{k}{\mu}\nabla p_t\right) + L_p^{LF}\dfrac{S}{V}(p_t - p_L) - f_b(\overline{p}_t, p_v)\delta_\Lambda = 0 & \text{in } \Omega \\ \mathbf{u}_t = -\dfrac{k}{\mu}\nabla p_t & \text{in } \Omega \\ -\dfrac{\pi R^4}{8\mu}\dfrac{\partial^2 p_v}{\partial s^2} + f_b(\overline{p}_t, p_v) = 0 & s \in \Lambda \\ \mathbf{u}_v = -\dfrac{R^2}{8\mu}\dfrac{\partial p_v}{\partial s}\boldsymbol{\lambda} & s \in \Lambda \end{cases} \tag{5.1}$$

$$f_b(\overline{p}_t, p_v) := 2\pi R L_p((p_v - \overline{p}_t) - \sigma(\pi_v - \overline{\pi}_t))$$

where the term $f_b(\overline{p}_t, p_v)\delta_\Lambda$ accounts for the blood flow leakage from vessels to tissue and it has to be understood as the Dirac measure concentrated on Λ, denoted with δ_Λ, and having line density f_b. Since the capillary bed is represented by a one-dimensional network embedded into the interstitial volume, the equations would result to be ill posed if the coupling between the two subregions was considered pointwise [33, 34]. For this reason, the function $f_b(\overline{p}_t, p_v)$ is such that the capillary bed is affected by the average of quantities in the interstitial tissue, calculated on a cylindrical surface that represents the actual size of capillaries. The average value of pressure, velocity or concentration fields over the real surface of the capillary bed is denoted by

$$\overline{g}(s) := \frac{1}{2\pi R}\int_0^{2\pi} g(s, \theta) R d\theta.$$

Mass transport

To model drug transport in the interstitial tissue we assume that molecules are advected by the fluid and diffuse in all Ω. In addition chemical species may be metabolised by the

cells in the interstitial tissue. The distribution of solutes in the interstitial tissue is also affected by the lymphatic drainage, which is described as a distributed sink proportional to $L_p^{LF}\frac{S}{V}(p_t - p_L)c_t$, similarly to the flow model.

Mass transport in the capillary bed is modelled by means of advection-diffusion equations. More precisely, the one dimensional model for mass transport in the capillaries network is derived, as in [32], starting from the actual 3D advection-diffusion problem. The coupled problem, accounting for transport of chemicals from the microvasculature to the interstitium, consists to find the concentrations c_v and c_t respectively, such that

$$\begin{cases} \dfrac{\partial c_v}{\partial t} + \dfrac{\partial}{\partial s}(|\mathbf{u}_v|c_v - D_v\dfrac{\partial}{\partial s}c_v) = -\dfrac{1}{\pi R^2}f_c(\overline{p}_t, p_v, \overline{c}_t, c_v) & \text{in } \Lambda \\ \dfrac{\partial c_t}{\partial t} + \nabla\cdot(c_t\mathbf{u}_t - D_t\nabla c_t) + mc_t + L_p^{LF}\dfrac{S}{V}(p_t - p_L)c_t = f_c(\overline{p}_t, p_v, \overline{c}_t, c_v)\delta_\Lambda & \text{in } \Omega \end{cases}$$

where D_v and D_t are the molecular diffusivities, in the capillaries and the interstitium, respectively, assumed to be constant in each region. The rate of metabolization in the interstitium is denoted by m. This parameter may be in turn a function of the concentrations, as it will be pointed out later on. The function $f_c(\overline{p}_t, p_v, \overline{c}_t, c_v)$ accounts for the mass transfer from the capillary bed to the interstitial tissue and it is proportional to the mass flux per unit length of the capillary vessels. Since the concentration in the vascular network, c_v, is defined as mass per unit volume, $f_c(p_t, p_v, c_t, c_v)$ is scaled by the vessel cross section πR^2 when it is evaluated on Λ. We describe the capillary walls as *semipermeable membranes* allowing not only for the leakage of fluid, but also for the selective filtration of molecules. Again, the Kedem-Katchalsky equations represent a good model for these phenomena. According to these equations, the flux of chemicals per unit surface across the capillary walls is:

$$J_c(p_t, p_v, c_t, c_v) := (1-\sigma)J_b(p_t, p_v)c_{t/v} + P(c_v - c_t) \quad \text{on } \Gamma,$$

where P is the permeability of the vessel wall with respect to solutes and σ is the osmotic reflection coefficient. It quantifies the departure of the membrane behavior from the case of ideal permeability. The symbol $c_{t/v}$ denotes the average concentration within the capillary walls. It is defined as a suitable combination of the concentrations on the two sides of the walls [89]. In particular, we set $c_{t/v} := w\overline{c}_t + (1-w)c_v$ where $0 < w < 1$ is a weight that depends on the Péclét number of the solute transport through the wall. Then, under the assumption that capillaries can be modeled as cylindrical channels, the magnitude of the mass flux exchanged per unit length between the network of capillaries and the interstitial volume at each point of the capillary vessels is the following,

$$f_c(\overline{p}_t, p_v, \overline{c}_t, c_v) = 2\pi R\big[(1-\sigma)J_b(\overline{p}_t, p_v)c_{t/v} + P(c_v - \overline{c}_t)\big].$$

Boundary and initial conditions

The fluid dynamics and mass transport equations are not complete yet. Before being solved, they must be complemented with boundary conditions on the artificial sections that separate the domains Ω and Λ from the surrounding tissue. As before, we model a

sample of tissue that is able to exchange fluid and mass with the exterior. As a result, for the prescription of boundary conditions we have to define what are the *inflow* and *outflow* boundaries. In addition, for the governing equations that depend on time, we need to prescribe the initial conditions of the system. Only the drug transport equations depend on time. The initial drug concentrations will be set to the basal values, equal to zero.

For the capillary network, we denote by $\partial\Lambda_{in}$ and $\partial\Lambda_{out}$ the inflow and outflow sections of $\partial\Lambda$ respectively (as shown in Figure 4.2 using different colors and arrows). We regulate the flow by enforcing the values of the blood pressure at the extrema of the capillaries. As a result, we prescribe the following conditions:

$$p_v = p_0 + \Delta p \text{ on } \partial\Lambda_{in} \quad \text{and} \quad p_v = p_0 \text{ on } \partial\Lambda_{out},$$

where the total pressure drop Δp is computed to ensure that the average blood velocity in the network fits with the measured values in healthy human microvasculature, as we have done in section 4.5.2. We proceed similarly for the mass transport equations, to model the administration of the drug through the vascular system. Given the maximal drug concentration injected in the blood stream, $c_{v,max}$, we then enforce

$$c_v = c_{v,max} \text{ on } \partial\Lambda_{in} \quad \text{and} \quad \partial_s c_v = 0 \text{ on } \partial\Lambda_{out}.$$

On the outflow boundary of the network we constrain the derivatives of the drug concentration, rather than the value itself. As a consequence, the concentration value is determined by the model, on the basis of the convection and reaction mechanisms.

The interstitial tissue, Ω, is assumed to be an isotropic material. To comply with this property, we enforce on all the artificial interfaces of the tissue, $\partial\Omega$, boundary conditions that mimic the resistance of the surrounding material. For the fluid dynamics equations, these conditions are discussed in detail in section 4.5.2 and read as follows:

$$-\kappa_t \nabla p_t \cdot \mathbf{n} = \beta_b (p_t - p_0)$$

where $\mathbf{n}$ is the outer unit normal vector of the interstitial boundary, p_0 is the basal (atmospheric) pressure and β_b is a parameter inversely proportional to the resistance of the surrounding tissue. More precisely, $\beta_b \to 0$ corresponds to the case of infinite resistance. In this case the fluid flow can not cross the boundaries of Ω. The sensitivity of the solution with respect to β_b and suitable expressions to calculate it on the basis of the other model parameters are provided in section 4.5.2. We proceed analogously for the transport of solutes by setting,

$$-D_t \nabla c_t \cdot \mathbf{n} = \beta_c c_t$$

where β_c quantifies the conductivity of the outer tissue with respect to solute transport. Here, we have implicitly assumed that the basal solute concentration is equal to zero. The values of β_b, β_c used in the simulations are reported in Tables 5.1, 5.2, respectively.

5.2.2 Coupled system of O_2 and tirapazamine

Hypoxia targeted drugs, such as *tirapazamine* (TPZ), are designed to be metabolised more quickly by hypoxic cells. The distribution of such drugs in the interstitial tissue then depends on the local availability of oxygen. To model these effects, we adapt the

single-specie mass transport model developed above to the case of multiple solutes. As a result, this approach ends up with a system of reaction diffusion equations.

We study the distribution of the oxygen partial pressure, denoted by c^{ox}. Since oxygen is persistently supplied by the capillary bed, we rely in this case on the steady problem formulation. Oxygen distributes into the interstitial volume thanks to diffusion and transport. The rate of oxygen absorption depends in turn on the oxygen partial pressure profile itself. This dependence is represented by a Michaelis-Menten formula,

$$m^{ox}(c_t^{ox}) = \frac{m_0^{ox}}{c_t^{ox} + c_0^{ox}}$$

where m_0^{ox} represents the maximal oxygen demand, i.e. the rate of oxygen consumption when oxygen is not limited, and c_0^{ox} is the oxygen concentration at which the reaction rate is half of m_0^{ox}.

Let us now denote by c^{tpz} the concentration of TPZ. This is a relatively small molecule that obeys to the governing equations of mass transport described above. Following [68] the consumption rate of TPZ depends on the oxygen concentration through the following expression

$$m^{tpz}(c_t^{ox}) = m_0^{tpz} \frac{c_0^{tpz}}{c_0^{tpz} + c_t^{ox}},$$

where m_0^{tpz} is the metabolization rate when TPZ metabolism is not limited by the oxygen concentration, and c_0^{tpz} is the oxygen concentration at which the consumption rate for TPZ is halved compared to that under anoxia.

The general mass transport model (**??**), adapted to the previous assumptions, ends up with the following equations,

$$\begin{cases} \dfrac{\partial c_t^{ox}}{\partial t} + \nabla \cdot (c_t^{ox}\mathbf{u}_t - D_t^{ox}\nabla c_t^{ox}) + m^{ox}(c_t^{ox})c_t^{ox} + L_p^{LF}\frac{S}{V}(p_t - p_L)c_t^{ox} \\ \qquad = f_s^{ox}(\overline{p}_t, p_v, \overline{c}_t^{ox}, c_v^{ox})\delta_\Lambda & \text{in } \Omega \\ \dfrac{\partial c_t^{tpz}}{\partial t} + \nabla \cdot (c_t^{tpz}\mathbf{u}_t - D_t^{tpz}\nabla c_t^{tpz}) + m^{tpz}(c_t^{ox})c_t^{tpz} + L_p^{LF}\frac{S}{V}(p_t - p_L)c_t^{tpz} \\ \qquad = f_s^{tpz}(\overline{p}_t, p_v, \overline{c}_t^{tpz}, c_v^{tpz})\delta_\Lambda & \text{in } \Omega \\ \dfrac{\partial c_v^{ox}}{\partial t} + \dfrac{\partial}{\partial s}(u_v c_v^{ox} - D_v^{ox}\dfrac{\partial}{\partial s}c_v^{ox}) = -\dfrac{1}{\pi R^2} f_s^{ox}(\overline{p}_t, p_v, \overline{c}_t^{ox}, c_v^{ox}) & \text{on } \Lambda \\ \dfrac{\partial c_v^{tpz}}{\partial t} + \dfrac{\partial}{\partial s}(u_v c_v^{tpz} - D_v^{tpz}\dfrac{\partial}{\partial s}c_v^{tpz}) = -\dfrac{1}{\pi R^2} f_s^{tpz}(\overline{p}_t, p_v, \overline{c}_t^{tpz}, c_v^{tpz}) & \text{in } \Lambda \end{cases} \tag{5.2}$$

$$f_c^*(\overline{p}_t, p_v, \overline{c}_t^*, c_v^*) = 2\pi R\big[(1-\sigma^*)L_p\big((p_v - \overline{p}_t) - \sigma(\pi_v^* - \overline{\pi}_t^*)\big)c_{t/v} + P^*(c_v^* - \overline{c}_t^*)\big]$$

where $* = $ ox, tpz.

Parameters of the model and dimensional analysis

We apply the coupled oxygen-TPZ model, namely equation (5.2) to calculate the time and space dependent concentration profiles of TPZ in the interstitial volume, after a bolus injection of TPZ equal to C_{max}^{tpz} for a duration of $T_{max} = 20$ minutes. More precisely, we enforce the boundary condition $c_v^{tpz} = C_{max}^{tpz}$ on $\partial\Lambda_{in}$ for $t \in (0, T_{max})$. The numerical simulation is however extended for a longer time interval. The parameters needed to feed the fluid dynamics and the mass transport equations are taken from different sources. For the fluid equations we refer to section 4.5.1 and references therein. For the transport of oxygen and TPZ we use the dataset provided in [68]. The parameters that will be used in the numerical simulations (and the corresponding sources) are reported in Table 5.1.

Before proceeding, we aim to use the available data to verify the assumption that the contribution of oxygen and TPZ to the oncotic pressure is negligible. This hypothesis has already been widely investigated for oxygen, [85,89], and it results to be accurately satisfied, because oxygen is a very small molecule. For TPZ the question remains open. An upper bound for the oncotic pressure generated by TPZ dissolved in blood is $\pi_{max}^{TPZ} = \sigma^{TPZ} R_g T C_{max}^{TPZ}$. The main issue is the quantification of the reflection coefficient σ^{TPZ}. Using the *pore theory*, this parameter can be estimated as

$$\sigma^{TPZ} = \left(1 - \left(1 - \frac{r^{TPZ}}{r^{pores}}\right)^2\right)^2 \quad \text{and} \quad r^{TPZ} = \frac{k_B T}{6\pi\mu D^{TPZ}}$$

where r^{TPZ} is an estimate of the TPZ molecular radius and r^{pores} quantifies the average dimension of the endothelial fenestrations in the capillary walls. For the latter, following [89] and references therein, we take $r^{pores} = 5 \times 10^{-9}$ m. For the former, we use the Stokes-Einstein equation (reported above, where $k_B T$ is the Boltzmann thermal energy and μ is the viscosity of blood plasma) to approximate the TPZ radius using the molecule diffusivities, provided in Table 5.1. This results in the following upper bound for the TPZ radius $r^{TPZ} < 3 \times 10^{-10}$ m. When we compare this estimate with the Bohr radius (the most probable distance between the proton and electron in a hydrogen atom), it turns out that one TPZ molecule should span approximately over 5 radii, which seems to be appropriate for the molecule, whose chemical formula is $C_7H_6N_4O_2$. Using the available estimate for r^{TPZ} we obtain $\sigma^{TPZ} < 0.013$, which completely justifies our assumption. Indeed, the corresponding oncotic pressure is $\pi_{max}^{TPZ} = \sigma^{TPZ} R_g T C_{max}^{TPZ} < 0.08$ mmHg. This value is almost negligible with respect to the oncotic pressure gradient induced by the blood proteins that amounts to 25 mmHg.

Given the set of parameters, our first step towards the application of the models is to perform a dimensional analysis of the corresponding equations. The results will inform us on the relative magnitude of the concurrent phenomena that affect mass transport, such as molecular diffusion, convection and ligand-receptor interactions. We choose length, velocity and concentration as primary variables for the analysis. We use the characteristic dimensions introduced int the previous chapter, section 4.5.1. The characteristic length, $d = 50\mu m$, is the average spacing between capillary vessels, the characteristic velocity, $U = 100\mu m/s$, is the average velocity in the capillary bed and $\delta P = 1$ mmHg is the characteristic hydrostatic pressure drop along the extrema of the capillary network that will be considered in the simulations. The characteristic concen-

parameter	units	value	source
$p_0 + \Delta p$	mmHg	35	[55]
Δp	mmHg	1.25	[28]
$\sigma\pi_v$	mmHg	28	[55]
$\sigma\pi_t$	mmHg	0.1	[55]
L_p	m^2s/kg	10^{-10}	[72]
$L_p^{LF}\frac{S}{V}$	mmHg^{-1} hours^{-1}	0.5	[7]
β_b	–	10^{-6}	[28]
R	μm	7.64	[101]

Table 5.1: *Physical parameters characterizing the perfusion problem.*

parameter	units	oxygen		TPZ	
D_t	cm^2/s	1.35×10^{-5}	[68]	1.87×10^{-6}	[68]
D_v	cm^2/s	5×10^{-3}	$--$	6.9259×10^{-4}	$--$
P	cm/s	3.5×10^{-3}	[103]	5×10^{-3}	$--$
m_0^{tpz}	$1/s$			0.0317	[68]
m_0^{ox}	$mmHg/s$	8.0645	[68]		
C_{max}^{tpz}	g/m^3			48	[68]
C_{max}^{ox}	$mmHg$	100	[102]		
β_c	–	10^{-3}	[28]	10^{-3}	[28]

Table 5.2: *Physical parameters for oxygen and TPZ delivery, transport and metabolization.*

tration, C_{max} (Table 5.1), is defined as the maximal admissible value at the systemic level for each considered chemical specie. The dimensionless form of the mass transport problem is then,

$$\begin{cases} \dfrac{\partial c_t^*}{\partial t} + \nabla \cdot (c_t^* \mathbf{u}_t - A_t^* \nabla c_t^*) + Da_t^*(c_t^{ox}) c_t^* + Q_{PL}(p_t - p_L) c_t^* \\ \qquad\qquad = f_c^*(p_t, p_v, c_t^*, c_v^*)\delta_\Lambda \qquad \text{in } \Omega \\ \dfrac{\partial c_v^*}{\partial t} + \dfrac{\partial}{\partial s}(|\mathbf{u}_v| c_v^* - A_v^* \dfrac{\partial}{\partial s} c_v^*) = -\dfrac{d^2}{\pi R^2} f_c^*(p_t, p_v, c_t^*, c_v^*) \qquad \text{in } \Lambda \end{cases}$$

$$f_c^*(p_t, p_v, c_t^*, c_v^*) = 2\pi(R/d)\big[(1-\sigma^*)Q\big((p_v - \overline{p}_t) - \sigma(\pi_v - \overline{\pi}_t)\big)c_{t/v}^* + \Upsilon^*(c_v^* - \overline{c}_t^*)\big]$$

where all the symbols now refer to dimensionless quantities and the superscript $*$ stands for either oxygen (ox) or tirapazamine (tpz). For convenience, we do not distinguish the notation from the dimensional setting. The dimensionless groups that characterize the flow are

$$u_t = \frac{|\mathbf{u}_t|}{U}, \quad u_v = \frac{|\mathbf{u}_v|}{U}, \quad Q = \frac{L_p \delta P}{U}, \quad Q_{PL} = L_p^{LF}\frac{S}{V}\frac{\delta P d}{U}.$$

We refer to the previous chapter, section 4.5.1, for a detailed discussion of their interplay. Here, we are particularly interested in the analysis of mass transport, which is described by the following quantities:

$$A_v^* = \frac{D_v^*}{dU}, \quad A_t^* = \frac{D_t^*}{dU}, \quad Da_t^* = m^* \frac{d}{U}, \quad \Upsilon^* = \frac{P^*}{U}$$

The groups A_t^*, A_v^* are the inverse of the Péclét numbers in the interstitium and the blood stream, respectively. They quantify the ratio of diffusion and transport phenomena. The Damkohler number, Da_t^*, represents the magnitude of metabolism with respect to diffusion. Finally, Υ^* characterizes the magnitude of leakage from the capillary bed. Using the parameters reported in Table 5.2, the magnitude of the dimensionless groups for oxygen and TPZ, respectively, is

$$A_v^{ox} = 100, \;\; A_t^{ox} = 0.27, \;\; Da_t^{ox} = 4.0323, \;\; \Upsilon^{ox} = 0.35$$

$$A_v^{tpz} = 13.85, \;\; A_t^{tpz} = 0.0374, \;\; Da_t^{tpz} = 0.0159, \;\; \Upsilon^{tpz} = 0.5$$

where to quantify the reaction coefficients Da_t^{ox} and Da_t^{tpz}, we take maximal oxygen concentration, i.e. $C^{ox} = 100$ mmHg.

We observe that $A_v^{ox} > A_v^{tpz} > 1 > A_t^{ox} > A_t^{tpz}$. Since the molecular diffusivity of oxygen and TPZ in the interstitial tissue is rather low, the dynamics of these molecules in the interstitium is moderately transport dominated. We notice, however, that this conclusion is based on the mean blood velocity in the capillaries, U, used to quantify transport. It could thus lead to a slight overestimation of the transport phenomena in the tissue.

Concerning the Damkohler numbers, we notice that $Da_t^{ox} > A_t^{ox}$, which means that the distribution of oxygen in the tissue is reaction dominated, while for TPZ these two mechanisms are almost in equilibrium, i.e. $Da_t^{tpz} \simeq A_t^{tpz}$.

5.2.3 Transport of nanoparticles and drug delivery

We will apply now the developed theory to analyze the transport of nanoparticles into the tumor region. Nanoparticles are used as vectors for the delivery of drugs to the tissue. The advantage of this technology with respect to systemic delivery is that chemoterapic agents are released selectively to the tumor mass. The side effects of these drugs on patients are thus reduced. We aim at modeling the transport of nanoparticles in the capillary network and the consequent delivery of a drug, which in our case is again TPZ, to enable comparisons with the bolus injection delivery method. The model arises from the general equations of blood flow and mass transport, with some modifications. In particular, it has to be adapted to account for three different stages of the delivery process: (*i*) the transport of nanoparticles in the capillary network; (*ii*) the adhesion of the particles to the capillary wall; (*iii*) the delivery of the encapsulated drug in the surrounding tissue.

Steps (i) & (ii): nanoparticle transport and adhesion. The model accounting for nanoparticle transport in the blood stream and their adhesion to the wall results in the following equations:

$$\frac{\partial c_v}{\partial t} + \frac{\partial}{\partial s}(|\mathbf{u}_v| c_v - D_v \frac{\partial c_v}{\partial s}) + \frac{2\pi R}{\pi R^2} \Pi c_v = 0 \quad \text{in } \Lambda \times (0, T)$$

where $c_v(\mathbf{x}, t)$ is the nanoparticle concentration inside the vessels and it is measured as number of particles per unit volume [♯/m^3]. The adhesion of particles to the wall, that was not accounted in the general model, is described as a sink term distributed along the length of the capillary network, namely Πc_v on Λ. The new term Πc_v is a

flux of particles sequestrated to the flow per unit surface of capillary wall. Since we consider a one-dimensional model along the capillary axis, we use the corresponding flux per unit length $2\pi R\Pi c_v$. The sink term, per unit volume, equivalent to this flux is then obtained by scaling the flux per unit length with the vessel cross section, that is πR^2. The vascular deposition parameter, Π, is estimated using a ligand-receptor model for the interaction of particles with the endothelial layer, which is based on previous works [37, 69, 70]. We report here the main components of the model. The vascular deposition parameter is defined as

$$\Pi(s) = P_a|S(s)|\frac{d_p}{2}$$

where P_a is the probability of particle adhesion, $S(s)$ is the the wall shear rate and d_p is the diameter of the considered nanoparticle. Given the plasma viscosity μ, the wall shear stress at the axial coordinate s along the capillary network is $\mu S(s)$. As a result, we compute the wall shear rate using the Poiseuille's flow equation. To this aim, we remind that the network Λ has been decomposed into individual branches Λ_i, $i = 1, \dots, N$. Then, the shear rate assumes a constant value on each branch given by

$$|S_i| = \frac{R}{2\mu}\frac{|\Delta_i p_v|}{L_i}$$

where $|\Delta_i p_v|$ is the absolute value of the pressure drop along each branch of the network and L_i is the branch length. The probability of adhesion, P_a, is in turn defined as a function of particle size, shape and surface properties,

$$P_a(s) = m_l K_a^0 \alpha_2 \pi r_0^2 exp\bigg(-\beta\frac{\mu|S(s)|}{\alpha_2}\bigg).$$

In the above expression m_l is the surface density of the ligand molecules that decorate the nanoparticle surface and K_a^0 is the affinity constant of the interaction between ligands and receptors. The parameter α_2, defined as

$$\alpha_2 = m_r\left[1 - \left(1 - \frac{\Delta}{d_p/2}\right)^2\right]$$

is a function of the density of receptors on the endothelial surface, m_r, and of the separation distance between the particle and the substrate at the equilibrium, Δ. The parameter r_0 represents the radius of the adhesion point and $\beta = \dfrac{\lambda 6F}{k_B T}$ is a constant, where F is the coefficient of hydrodynamic drug force on the spherical particle and $k_B T$ is the Boltzmann thermal energy.

The model must be complemented by suitable initial and boundary conditions. At the inlet $\partial\Lambda_{in}$ we prescribe a Dirichlet boundary condition c_v^0, which represents the amount of injected particles. At the outflow $\partial\Lambda_{out}$ we specify a homogeneous Neumann boundary condition. We assume that the blood stream does not contain any particle at the initial time.

Once the problem for particle transport and adhesion is solved, we compute the density of nanoparticles adhering per unit surface to the wall as

$$\Psi(s,t) := \int_0^t \Pi(s)c_v(s,\tau)d\tau.$$

Step (iii): drug release from nanoparticles. We assume that the particles decorating the arterial wall are loaded with drug and they are able to release it to the surrounding tissue. The model directly descends from the general formulation of mass transport in the interstitial tissue. However, the Kedem-Katchalsky equations do not seem to be the most appropriate model to calculate the drug release rate from the surface of the capillary walls. This is motivated by the following observations. On one hand, due to the complex interaction of the nanoparticles with the endothelial layer, involving phenomena such as intracellular trafficking and particle extravasation [46–48, 104], we assume that the endothelium is no longer a significant barrier to deliver nanoparticle-carried drugs to the interstitial volume. On the other hand, the drug delivery rate mostly depends on the release profile of a single particle. The drug release rate per unit surface will be then determined by combining the flux delivered by a single particle with the density of particles per unit surface.

Determining the release profile of a single (spherical) loaded particle is a well studied problem in pharmacology [81]. Here, following [5, 81, 86] we define it using a power law model,

$$\frac{q(t)}{q_\infty} = \frac{t^b}{t^b + m}, \quad q_\infty = c^*_{np} V_{np}, \quad \text{then} \quad q(t) = \frac{t^b}{t^b + m} c^*_{np} V_{np},$$

where $q(t)$ is the amount of drug released and q_∞ is the total drug load of a nanoparticle, given by the total drug concentration inside the nanoparticle, c^*_{np} (where $*$ denotes an unspecified drug loaded on the particles), multiplied by the nanoparticle volume V_{np}. The parameter m is expressed in dimensions of time to the power of b. The two parameters m and b reflect the structural and geometric properties of the delivery system. The drug release rate from a single nanoparticle is therefore obtained as

$$J_{np}(t) = \frac{dq(t)}{dt} = \frac{mbt^{b-1}}{(t^b + m)^2} c^*_{np} V_{np},$$

and the total drug release rate per unit surface is computed as,

$$J(s,t) = J_{np}(t)\Psi(s,t).$$

To conclude, we apply the immersed boundary method to describe the capillary bed as a source term concentrated on the centerline Λ. More precisely, the action of drug loaded nanoparticles on the interstitial tissue is described by the source term $2\pi R J(s,t)$, assuming that the capillaries are cylindrical channels of radius R. To compare the nanoparticle delivery approach with the bolus delivery strategy previously considered, we load the particles with TPZ. The drug concentration into the tissue is modeled by the following equations:

$$\begin{cases} \dfrac{\partial c_t^{tpz}}{\partial t} + \nabla \cdot (c_t^{tpz}\mathbf{u}_t - D_t^{tpz}\nabla c_t^{tpz}) + m^{tpz}(c_t^{ox}, c_t^{tpz}) \\ \qquad\qquad + L_p^{LF}\frac{S}{V}(p_t - p_L)c_t^{tpz} = 2\pi R J(s,t)\delta_\Lambda \quad \text{in } \Omega \times (0,T] \\ \\ D_t^{tpz}\nabla c_t^{tpz} \cdot \mathbf{n} = \beta_c(c_t^{tpz} - c_0^{tpz}) \qquad\qquad \text{on } \partial\Omega \times (0,T] \end{cases} \tag{5.3}$$

parameter	units	value
β	N^{-1}	2.39×10^{11}
μ	Ns/m^2	0.001
d_p	m	2×10^{-6}
α_2	$\sharp/m^2$	3.4×10^{9}
$m_l K_a^0 r_0^2$	m^2	1.2585×10^{-9}
b	–	0.8
m	$hours^b$	1
C_{max}^{np}	$\sharp/m^3$	1.4354×10^{12}
D_v	cm^2/s	6.98×10^{-9}

Table 5.3: *Physical parameters used to model nanoparticle injection and adhesion [69].*

Parameters of the model

The nanoparticle transport and adhesion model requires to characterize several parameters, for which we refer to [37, 69, 70]. For the sake of clarity, in Table 5.3 we report the values summarized in [69] Table 1.

It is possible to calibrate the power law model in order to describe different scenarios, for example a fast release mechanism or a slow release rate. We fix the parameters of the model, m and b, such that 90% of the total drug is released within one day. The corresponding parameter values are reported in Table 5.3.

Another important quantity is the concentration of nanoparticles injected at the inflow of capillary network. Since we are interested in comparing the amount of TPZ delivered from bolus and nanoparticle injection, we aim at determining the concentration of injected nanoparticles that match the TPZ bolus concentration, previously defined as C_{max}^{tpz}. Similarly, the concentration of injected nanoparticles will be denoted by C_{max}^{np} and its value is determined according to the following balance equation,

$$C_{max}^{np} c_{np}^{tpz} V_{np} = C_{max}^{tpz}.$$

To determine the value of C_{max}^{np} we need an estimate of the amount of drug cast in each particle, namely c_{np}^{tpz}. To determine this value we rely on two assumptions: (i) the drug mass fraction in each particle, denoted as f^{tpz}, is equal to the unity; (ii) the density of the particles is comparable to the density of water, ρ_w. As a result, we conclude that

$$c_{np}^{tpz} = \rho_w f^{tpz}.$$

and we compute the value of C_{max}^{np} that is reported in Table 5.3.

5.2.4 Numerical approximation

For complex geometrical configurations explicit solutions of problems (5.1), (5.2) and (5.3) are not available. We have already seen in the previous chapter that numerical simulations are the only way of applying the model to real cases. Besides applications, the study of numerical approximation methods for such problems requires first to address existence, uniqueness and regularity of the exact solutions and then to analyze the accuracy of the proposed scheme. The solution of these problems do not satisfy standard regularity estimates, because all the forcing terms are Dirac measures. Also in this case, to characterize the regularity of the trial and test spaces we do not resort to

weighted Sobolev spaces, as proposed in [33]. Indeed, we have discussed in sections 4.4 and 4.4.3 that we do not need graded meshes to capture the solution gradients in the neighborhood of the singularity. Therefore we will choose trial and test functions belonging to spaces defined in [73].
The discretization of the flow problem (5.1) is described in section 4.4 and is achieved by means of the finite element method that arises from the variational formulation of the problem combined with a partition of the domain into small elements. We follow the same method also to discretize problems (5.2) and (5.3).
Starting from the problems of oxygen and TPZ mass transport, we multiply each tissue equations in (5.2) by a test function $q_t \in W_0^{1,q}$, that is the natural trial space for the problem in the interstitium, as we have already shown in section 4.4. We integrate over Ω and the transport operator is treated using integration by parts combined, for the sake of simplicity, with homogeneous Neumann conditions on $\partial\Omega$. Regarding the interface flux term we write

$$\big(f_c^*(p_t, p_v, c_t^*, c_v^*)\delta_\Lambda, q_t\big)_\Omega = \big(f_c^*(p_t, p_v, c_t^*, c_v^*), q_t\big)_\Lambda.$$

We proceed similarly for the governing equation on the capillary bed and, following what already explained in section 4.4, we integrate by parts on each branch Λ_i separately and we impose mass conservation at each index that identifies a branch of the network. We highlight that the test functions for the pressure field on the capillary bed are continuous on the entire network, namely $q_v \in C^0(\Lambda)$ since we choose $V_{v,0}$ as the subspace of $H^1(\Lambda)$ of functions which vanish on the boundaries of Λ and therefore $V_{v,0} \subset C^0(\Lambda)$ on 1D manifolds. This allows us to obtain

$$\big(\frac{\partial c_v^*}{\partial t}, q_v\big)_\Lambda + \big(|\mathbf{u}_v|c_v^* - D_v^*\frac{\partial}{\partial s}c_v^*, \frac{\partial}{\partial s}q_v\big)_\Lambda = \big(-\frac{1}{\pi R^2}f_c^*(p_t, p_v, c_t^*, c_v^*), q_v\big)_\Lambda,\ \forall q_v \in V_{v,0}.$$

Then the weak formulation of (5.2) requires to find $c_t^* \in W_0^{1,p}$ and $c_v^* \in V_{v,0}$ such that,

$$\begin{cases} \big(\frac{\partial c_t^*}{\partial t}, q_t\big)_\Omega + a_t(c_t^*, q_t) + b_\Lambda^t(\overline{c}_t^*, q_t) = b_\Lambda^t(c_v^*, q_t),\ \forall q_t \in W_0^{1,q}, \\ \\ \big(\frac{\partial c_v^*}{\partial t}, q_v\big)_\Lambda + a_v(c_v^*, q_v) + b_\Lambda^v(c_v^*, q_v) = b_\Lambda^v(\overline{c}_t^*, q_v),\ \forall q_v \in V_{v,0}, \end{cases} \tag{5.4}$$

with the following bilinear forms,

$$\begin{aligned}
a_t(c_t^*, q_t) &:= \big(c_t^*\mathbf{u}_t - D_t^*\nabla c_t^*, \nabla q_t\big)_\Omega + \big(m^*(c_t^{ox})c_t^*, q_t\big)_\Omega + L_p^{LF}\tfrac{S}{V}\big((p_t - p_L)c_t^*, q_t\big)_\Omega, \\
a_v(c_v^*, q_v) &:= \big(|\mathbf{u}_v|c_v^* - D_v^*\frac{\partial}{\partial s}c_v^*, \frac{\partial}{\partial s}q_v\big)_\Lambda, \\
b_\Lambda^t(c_v^*, q_v) &:= \big(2\pi R\big[(1-\sigma^*)L_p\big((p_v - \overline{p}_t) - \sigma(\pi_v - \overline{\pi}_t)\big)(1-w)c_v^* + P^*c_v^*\big], q_v\big)_\Lambda, \\
b_\Lambda^t(\overline{c}_t^*, q_t) &:= \big(2\pi R\big[(1-\sigma^*)L_p\big((p_v - \overline{p}_t) - \sigma(\pi_v - \overline{\pi}_t)\big)w\overline{c}_t^* - P^*\overline{c}_t^*\big], q_t\big)_\Lambda, \\
b_\Lambda^v(c_v^*, q_v) &:= \big(2/R\big[(1-\sigma^*)L_p\big((p_v - \overline{p}_t) - \sigma(\pi_v - \overline{\pi}_t)\big)(1-w)c_v^* + P^*c_v^*\big], q_v\big)_\Lambda, \\
b_\Lambda^v(\overline{c}_t^*, q_t) &:= \big(2/R\big[(1-\sigma^*)L_p\big((p_v - \overline{p}_t) - \sigma(\pi_v - \overline{\pi}_t)\big)w\overline{c}_t^* - P^*\overline{c}_t^*\big], q_t\big)_\Lambda.
\end{aligned}$$

We proceed in a similar way also for equations (5.3), obtaining the following variational form, where we have to find $c_t^{tpz} \in W_0^{1,p}$ and $c_v \in V_{v,0}$ such that

$$\begin{cases} \left(\frac{\partial c_t^{tpz}}{\partial t}, q_t\right)_\Omega + a_t^{tpz}(c_t^{tpz}, q_t) = F(t), \ \forall q_t \in W_0^{1,q}, \\ \\ \left(\frac{\partial c_v}{\partial t}, q_v\right)_\Lambda + a_v^{tpz}(c_v, q_v) = 0, \ \forall q_v \in V_{v,0}, \end{cases} \tag{5.5}$$

and the bilinear forms are,

$$\begin{aligned} a_t^{tpz}(c_t^{tpz}, q_t) &:= \left(c_t^{tpz}\mathbf{u}_t - D_t \nabla c_t^{tpz}, \nabla q_t\right)_\Omega + \left(m^{tpz}(c_t^{ox}) c_t^{tpz}, q_t\right)_\Omega + \left(L_p^{LF} \tfrac{S}{V}(p_t - p_L) c_t^{tpz}, q_t\right)_\Omega, \\ a_v^{tpz}(c_v, q_v) &:= \left(|\mathbf{u}_v| c_v - D_v \frac{\partial c_v}{\partial s}, \frac{\partial}{\partial s} q_v\right)_\Lambda + \left(\frac{2\pi R}{\pi R^2} \Pi c_v, q_v\right)_\Lambda \\ F(t) &:= \left(2\pi R J(t), q_t\right)_\Lambda \end{aligned}$$

For the numerical approximation of the variational problems (5.4) and (5.5), we consider a standard backward Euler time advancing scheme together with piecewise linear finite element space discretization.
For the space approximation we have to introduce an admissible family of partitions of Ω into tetrahedrons $K \in \mathcal{T}_t^h$, where the apex h denotes the mesh characteristic size. We recall that, at the discrete level, one of the advantages of our problem formulation is that the partition of the domains Ω and Λ into elements are completely independent. The computational meshes used to solve the transport problems are reported in Figure 5.1.

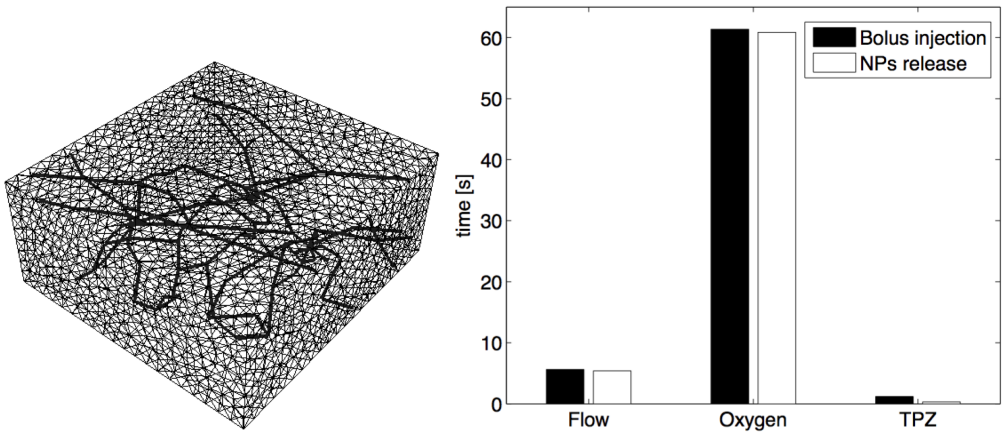

Figure 5.1: *On the left: meshes used to solve problems (5.7), (5.8) and (5.9). The partition of the domains Ω and Λ into elements are completely independent. In particular the partition of Ω is composed by 32624 elements, while the partition of Λ is composed by 8400 nodes, 80 nodes for each branch. On the right: computational time for solving the algebraic systems of the flow equations, the oxygen transport problem and the TPZ mass transport problem for the two different modalities of transport. We represent one single time step for the solution of the TPZ transport problem. The bars quantify the CPU time measured in seconds.*

Following section 4.4, let $V_t^h := \{v \in C^0(\Omega) : \ v|_K \in \mathbb{P}^1(K), \ \forall K \in \mathcal{T}_t^h\}$ be the space of piecewise linear continuous finite elements on $\mathcal{T}_t^h$. Again, for the discretization of the capillary bed, each branch Λ_i is partitioned into a sufficiently large number of

linear segments E, whose collection is Λ_i^h, which represents a finite element mesh on a one-dimensional manifold. Then, we will solve our equations on $\Lambda^h := \cup_{i=1}^N \Lambda_i^h$ that is a discrete model of the true capillary bed. Let $V_{v,i}^h := \{v \in C^0(\Lambda_i) : v|_E \in \mathbb{P}^1(E),\ \forall E \in \Lambda_i^h\}$ be the piecewise linear and continuous finite element space on Λ_i. The numerical approximation of the equation posed on the capillary bed is then achieved using the space $V_v^h := \left(\cup_{i=1}^N V_{v,i}^h\right) \cap C^0(\Lambda)$. The discrete problems arising from (5.4) and (5.5) requires to find $c_t^{*h} \in V_t^h$, $c_v^{*h} \in V_{v,0}^h$, $c_t^{tpz,h} \in V_t^h$ and $c_v^h \in V_{v,0}^h$ such that

$$\begin{cases} \left(\frac{\partial c_t^{*h}}{\partial t}, q_t^h\right)_\Omega + a_t(c_t^{*h}, q_t^h) + b_{\Lambda^h}^t(\overline{c}_t^{*h}, q_t^h) = b_{\Lambda^h}^t(c_v^{*h}, q_t^h),\ \forall q_t^h \in V_t^h, \\ \\ \left(\frac{\partial c_v^{*h}}{\partial t}, q_v^h\right)_\Lambda + a_v(c_v^{*h}, q_v^h) + b_{\Lambda^h}^v(c_v^{*h}, q_v^h) = b_{\Lambda^h}^v(\overline{c}_t^{*h}, q_v^h),\ \forall q_v^h \in V_{v,0}^h, \end{cases} \tag{5.6}$$

$$\begin{cases} \left(\frac{\partial c_t^{tpz,h}}{\partial t}, q_t^h\right)_\Omega + a_t^{tpz}(c_t^{tpz,h}, q_t^h) = F(t),\ \forall q_t^h \in V_t^h, \\ \\ \left(\frac{\partial c_v^h}{\partial t}, q_v^h\right)_\Lambda + a_v^{tpz}(c_v^h, q_v^h) = 0,\ \forall q_v^h \in V_{v,0}^h, \end{cases} \tag{5.7}$$

where the bilinear forms $a_t(\cdot,\cdot)$, $a_v(\cdot,\cdot)$, $b_{\Lambda^h}(\cdot,\cdot)$, $a_t^{tpz}(\cdot,\cdot)$, $a_v^{tpz}(\cdot,\cdot)$ are the same as before, with the only difference that $b_{\Lambda^h}(\cdot,\cdot)$ is now defined over the discrete representation of the network Λ_h. The interpolation and average operators, that are need to evaluate the bilinear form $b_{\Lambda^h}(\cdot,\cdot)$, are described in section 4.4.

The space discretization must be complemented with the time advancing scheme. Let $t > 0$ be the time step, $t_n = nt$ the n-th time step, and $c_t^{*h,n} \in V_t^h$, $c_v^{*h,n} \in V_{v,0}^h$, the numerical approximations of $c_t^{*h}(t_n)$ and $c_v^{*h}(t_n)$. The time advancing scheme for the problem (5.6) reads as follows: given $c_t^{*h,n} \in V_t^h$ and $c_v^{*h,n} \in V_{v,0}^h$ find $c_t^{*h,n+1} \in V^h$ and $c_v^{*h,n+1} \in V_{v,0}^h$, such that

$$\begin{cases} \left(\frac{1}{\Delta t} c_t^{*h,n+1}, q_t^h\right)_\Omega + a_t(c_t^{*h,n+1}, q_t^h) + b_{\Lambda^h}^t(\overline{c}_t^{*h,n+1}, q_t^h) = \\ \qquad\qquad \left(\frac{1}{\Delta t} c_t^{*h,n}, q_t^h\right)_\Omega + b_{\Lambda^h}^t(c_v^{*h,n+1}, q_t^h),\ \forall q_t^h \in V^h, \\ \left(\frac{1}{\Delta t} c_v^{*h,n+1}, q_v^h\right)_\Lambda + a_v(c_v^{*h,n+1}, q_v^h) + b_{\Lambda^h}^v(c_v^{*h,n+1}, q_v^h) = \\ \qquad\qquad \left(\frac{1}{\Delta t} c_v^{*h,n}, q_v^h\right)_\Lambda + b_{\Lambda^h}^v(\overline{c}_t^{*h,n+1}, q_v^h),\ \forall q_v^h \in V_{v,0}^h, \end{cases} \tag{5.8}$$

We apply the same time advance scheme also to equations (5.7).

Finally, we observe that the oxygen concentration transport equations, (5.2), involve a non linear term, represented by the Michelis-Menten reaction formula. To solve this non linearity, we apply an iterative scheme strategy, where the oxygen concentration that appears in the reaction coefficient, is evalutated at the previous iterative step. To describe properly this iterative scheme we simplify the notation and from now on we drop the time index $n+1$. The index will be explicitly indicated only when referring to a time step different from t_{n+1}. For the same reason, we drop the index h everywhere.

The iterative strategy results to be the following: for all $n = 1, \dots, N$ given an initial guess $c_t^{ox,0}$, $c_v^{ox,0}$ and a given tolerance ε, for $k = 1, 2, \dots$ find a sequence $c_t^{ox,k}$, $c_v^{ox,k}$ such that,

$$\begin{cases} \big(\frac{1}{\Delta t} c_t^{ox,k}, q_t\big)_\Omega + \big(c_t^{ox,k}\mathbf{u}_t - D_t^{ox}\nabla c_t^{ox,k}, \nabla q_t\big)_\Omega + \big(m^{ox}(c_t^{ox,k-1})c_t^{ox,k}, q_t\big)_\Omega + \\ \qquad L_p^{LF}\tfrac{S}{V}\big((p_t - p_L)c_t^{ox,k}, q_t\big)_\Omega = \big(\frac{1}{\Delta t} c_t^{ox,k,n}, q_t\big)_\Omega - b^t_{\Lambda^h}(\overline{c}_t^{ox,k}, q_t) + b^t_{\Lambda^h}(c_v^{ox,k}, q_t),\ \forall q_t \in V^h, \\ \big(\frac{1}{\Delta t} c_v^{ox,k}, q_v\big)_\Lambda + a_v(c_v^{ox,k}, q_v) + b^v_{\Lambda^h}(c_v^{ox,k}, q_v) = \big(\frac{1}{\Delta t} c_{v,n}^{ox,k}, q_v\big)_\Lambda + b^v_{\Lambda^h}(\overline{c}_t^{ox,k}, q_v),\ \forall q_v \in V^h_{v,0}, \end{cases} \tag{5.9}$$

until the following stopping criterion is satisfied:

$$\frac{\|c_t^{ox,k} - c_t^{ox,k-1}\|_0}{\|c_t^{ox,k}\|_0} + \frac{\|c_v^{ox,k} - c_v^{ox,k-1}\|_0}{\|c_v^{ox,k}\|_0} < \varepsilon. \tag{5.10}$$

where $\|\cdot\|_0$ is the Euclidean norm of the vector of nodal values.
Regarding the coupling between the oxygen and the TPZ concentration, we actually solve the steady counterpart of (5.8) for the oxygen transport, because oxygen is persistently supplied by the capillary bed. Therefore, once computed the oxygen concentration profile, we use it to determine once for all the reaction term that appears in the TPZ transport equation. This choice seems to be reasonable also because there isn't any feedback of the TPZ concentration on the oxygen consumption.

For the numerical solution of problems (5.9), (5.8) and (5.7) we use GetFem++, a general purpose C++ finite element library [93]. The discretization of flow problem (5.1), already described in Chapter 4, is solved applying the GMRES method with incomplete-LU preconditioning. The tolerance for the stopping criterion for the iterative method to solve the oxygen transport equations (5.9) is fixed to $\varepsilon = 10^{-8}$. We reach the convergence in 61 iterations. At each iteration, we apply the GMRES method to solve the corresponding linear systems. Regarding the TPZ transport, the monolithic algebraic system constructed from (5.8) is again solved using the GMRES method with incomplete-LU preconditioning. Conversely, the two equations composing system (5.7) are actually decoupled, therefore they are addressed in sequence: we solve the vessel equation (5.7)b first, in order to compute the flux $J(t)$, which is the forcing term of the tissue equation (5.7)a. Since these equations are independent, their numerical solution turns out to be faster than the one of system (5.8), as we observe from the results reported in Figure 5.1 and in Table 5.4.

Referring to the dimensional analysis performed in Section 5.2.2, we notice that the Damkohler number for the oxygen transport equation is bigger than the molecular diffusivity in the tissue, namely $Da_t^{ox} > A_t^{ox}$, which means that the distribution of oxygen in the tissue is reaction dominated, while for TPZ these two mechanisms are almost in equilibrium, i.e. $Da_t^{tpz} \simeq A_t^{tpz}$. We also observe that the magnitude of leakage, Υ^*, is always bigger than that of diffusivity in the interstitium, A_t^*. To cope with the reaction dominated nature of these mass transport equations, we adopt the mass lumping stabilization techniques addressed in [92] for the reaction terms corresponding to the coefficients Da_t^{ox} and Υ^*. Although the dimensional analysis addressed in Section 5.2.2 suggests that the mass transport problems in the interstitial tissue may be moderately transport dominated, numerical experiments confirm that resorting to stabi-

	Bolus injection	Nanoparticle release
problems initialization	301.7	301.59
assembling fluid system	1.02	1.04
solving fluid system	5.62	5.39
assembling O_2 system	1.32	1.35
solving O_2 system	61.36	60.86
assembling drug system	1.37	1.48
solving drug system (one single step)	1.2	0.21
solving drug system (T=20 min)	3374.04	1231.24

Table 5.4: *Computational time for solving different parts of problems* (5.7)*,* (5.8) *and* (5.9)*. Computational time is measured in seconds.*

lization methods for the convective terms is not required for the applications that will be addressed.

5.3 Results and discussion

The delivery of anticancer agents mediated through nanoparticle injection in the blood stream and subsequent adhesion to the vascular walls may feature significant advantages with respect to the traditional drug bolus delivery. We are interested to compare these two delivery modalities for TPZ.

5.3.1 Indicators of drug delivery performance

The natural output of the mass transport models described before are concentration profiles in the vessels, $c_v(t,s)$, and in the tissue, $c_t(t,x)$. From the clinical standpoint, these may not be the most significant indicators of the treatment performance. For this reason, we also study the amount of TPZ metabolised by cells up to a given reference time. We denote this quantity as $M^{tpz}(t,x)$. In addition, for more quantitative comparisons, we look at the total amount of TPZ metabolised in the considered portion of tissue, that is $\overline{M}^{tpz}(t)$. On the basis of equations (5.2), these indicators are defined as

$$M^{tpz}(t,\boldsymbol{x}) = \int_0^t m^{tpz}\big(c_t^{ox}(\tau,\boldsymbol{x}), c_t^{tpz}(\tau,\boldsymbol{x})\big)d\tau, \quad \overline{M}^{tpz}(t) = \int_\Omega M^{tpz}(t,\boldsymbol{x})d\boldsymbol{x}.$$

Following [68], the amount of drug metabolised in the tissue can be related to the cell survival. In particular, the cell *surviving fraction* (SF) represents the complement of the fraction of cells treated (killed) by TPZ with respect to the number of control cells (the total number of cells in the tissue, before treatment started). Several models are available to quantify the surviving fraction [68]. In particular, we use

$$SF(t,\boldsymbol{x}) = \exp\big(-\alpha M^{tpz}(t,\boldsymbol{x})\big), \quad \overline{SF}(t) = \exp\big(-\alpha\overline{M}^{tpz}(t)\big)$$

where α is a phenomenological coefficient. For the following calculations we assume $\alpha = 2.52\times10^{-4}\ \mu\text{M}^{-1}$ (0.0014 g/m^3) as in [68].

5.3.2 Oxygen transport and TPZ delivery from bolus injection

We discuss the simulations of TPZ delivery obtained with model (5.2). In Figure 5.2 we compare the oxygen and the TPZ concentrations 20 minutes after that the delivery

of TPZ into the systemic circulation has started. As expected, the TPZ concentration is significantly influenced by the distribution of oxygen concentration. From the inspection of the concentration maps, also the pattern of the microvascular network plays a role. Although this is a coupled system, the following dominant interactions seem to emerge from the analysis of the results.

Oxygen concentration patterns substantially depend on the density of capillaries per unit volume. Regions of the sample tissue not well perfused by the capillary network show low oxygen concentrations, justifying the risk of hypoxic conditions for an irregular configuration of the microvessels. This conclusion is also supported by the dimensional analysis of the governing equations. Since oxygen transport in the interstitial volume is reaction dominated, regions free of oxygen sources will easily experience low oxygen supply. The visualization of oxygen concentration maps of Figure 5.2 can be directly compared with the results of [103], see in particular Figure 3A, obtained using an equivalent model for oxygen transport. As a preliminary and qualitative validation of our results, we observe that the contour plots of the calculated oxygen concentration look remarkably similar in the two cases. As expected, the TPZ concentration is significantly influenced by the distribution of oxygen concentration. The distribution of TPZ in the considered tissue sample seems to be more uniform than in the case of oxygen. Again, dimensional analysis supports this conclusion, because it shows that diffusion and reaction equivalently contribute to TPZ transport.

In spite of the difference between the governing mechanisms at the basis of oxygen and TPZ transport, the simulated concentration maps of these species share common traits. This may be explained by two concurrent factors. On one hand, both solutes are affected by the distribution of capillaries. On the other hand, the metabolization of TPZ increases in hypoxic regions. This effect sustains TPZ concentration gradients similar to the ones of oxygen, by turning off TPZ absorption where oxygen concentration is elevated, and promoting TPZ metabolization where oxygen is low. Finally, the inspection of metabolized TPZ, namely $M^{tpz}(t,x)$, shows that the objective of reaching the hypoxic regions with a chemotherapy agent is substantially achieved. More precisely, oxygen and $M^{tpz}(t,x)$ maps show a complementary pattern. It means that most of TPZ is metabolized in hypoxic regions.

Before proceeding, we study the sensitivity of these results with respect to the boundary conditions applied on the artificial sections separating the interstitial volume from the exterior. Indeed, in the previous chapter 4, we have highlighted the importance of the boundary conditions to determine the interstitial pressure. Figure 5.2 (bottom row) shows the results when homogeneous Neumann conditions (no flux) are prescribed for the concentrations on the boundary of Ω. This is equivalent to setting $\beta_c = 0$ in the general boundary conditions used above, namely $-D_t \nabla c_t \cdot \mathbf{n} = \beta_c c_t$ (where the value of β_c is provided in Table 5.2). A slight increase in the TPZ concentration field is observed, in agreement with the fact that the outgoing diffusive flux is set to zero with the choice $\beta_c = 0$. For a more quantitative comparison, we study the sensitivity of the total amount of metabolized TPZ, $\overline{M}^{tpz}(t)$. After injecting TPZ for 20 minutes, we calculate $\overline{M}^{tpz}(t) = 7.76838 \times 10^{-9}$ g/m^3 when using Robin boundary conditions and $\overline{M}^{tpz}(t) = 8.6685 \times 10^{-9}$ g/m^3 in the case of Neumann conditions. Owing to these results, we conclude that the parameter β_c is not a factor of primary importance to determine the concentrations of oxygen and TPZ. As a result, we will

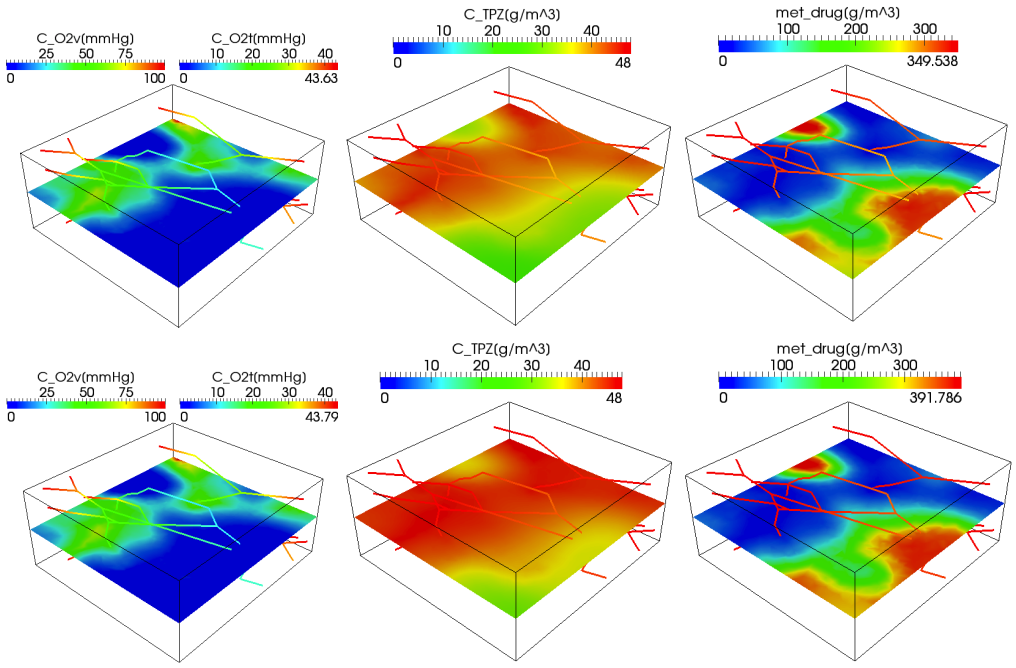

Figure 5.2: *Oxygen concentration profile, TPZ concentration profile and metabolized drug profile are visualized from left to right. On the top row, simulations are performed using Robin boundary conditions for the concentrations of oxygen and TPZ at the boundary of the interstitial volume with the exterior. The results obtained using homogeneous Neumann conditions are depicted at the bottom.*

use Robin conditions for all the forthcoming simulations.

5.3.3 Nanoparticle adhesion patterns and delivery of TPZ from nanoparticle injection

We split the analysis of the TPZ delivery from nanoparticles in two parts. First we focus on the nanoparticle adhesion model, with the aim to validate our results with respect to the ones reported in [69, 70]. In a second phase, we analyze the concentration of TPZ delivered from the nanoparticles that decorate the capillary walls.

Nanoparticle adhesion is regulated by the vascular adhesion parameter Π, which in turn depends on the shear rate induced by the interaction of blood flow with the capillary walls. These two quantities are depicted in Figure 5.3. We observe that the wall shear rate features a significant spatial variation, although the capillary radius is considered to be constant along the network. This effect is due to the variable pressure, and consequently flow rate, along the network. We observe that the calculated values of wall shear rate fall in the physiological range. According to the adopted adhesion model, the variability of wall shear rate is conveyed to the adhesion parameter, reported on Figure 5.3 (left). As a result, we expect that the concentration of nanoparticles will not be uniform along the network.

The nanoparticle concentration, namely $\Psi(s,t)$, depends on the adhesion parameter and on the particle concentration traveling through the vascular network. To compare the delivery of TPZ from nanoparticle with the case of bolus injection, we consider a constant concentration of injected particles for 20 minutes. A preliminary validation of

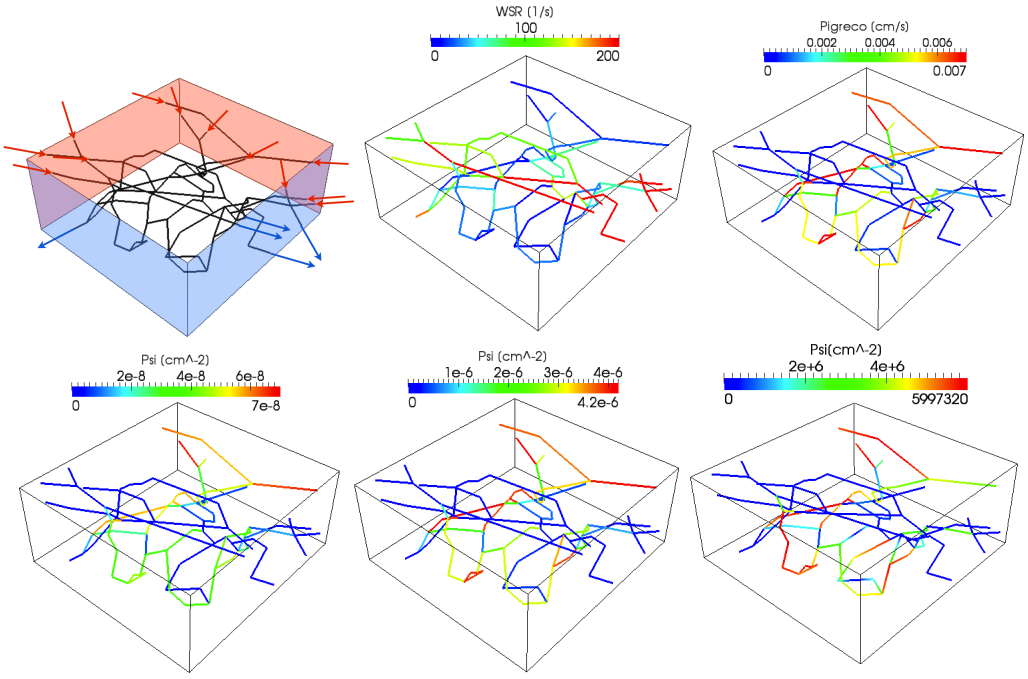

t=20 s
normalized C^{np}_{max}

t=20 min
normalized C^{np}_{max}

t=20 min
absolute C^{np}_{max}

Figure 5.3: *Top panel: profiles of wall shear rate and vascular deposition parameter $\Pi(s)$ along the capillary network. Bottom, starting from the left: the density of nanoparticles decorating the wall, Ψ, at 20 seconds and at 20 minutes after nanoparticle injection has started. These values refer to a nominal unit concentration of injected particles ($\sharp/m^3$). Bottom right: Ψ at 20 minutes after injection for an inlet nanoparticles concentration equal to C^{np}_{max}.*

our simulations arises observing that the nanoparticle density per unit capillary surface, calculated for an injection phase lasting 20 seconds, is comparable to that reported in [69, 70]. The analysis of adhered particles at 20 minutes after the initial time, shows that adhesion progressively increases. According to the model, saturation of particle receptors is not likely to be observed under the considered conditions. The results of Figure 5.3 (left and middle panels, bottom row) refer to the concentration of adhered nanoparticles normalized with respect to the injected value. On the right, we show the density of adhering particles when we consider the initial particle concentration C^{np}_{max}, which is calculated in order to match the the total flow of TPZ relative to the systemic bolus injection, as we have explained in section 5.2.3.

Figure 5.4 shows the TPZ concentration delivered from nanoparticles at 20 seconds and 20 minutes after particle injection has started. Although the concentration levels are significantly different in the two cases, because of the time scales, the concentration maps share some similarities. In both cases, however, the geometry of the network can not be immediately related to the TPZ concentration map. Indeed, it is rather the distribution of the adhesion factor along the network, Π, and accordingly the nanoparticles concentration the Ψ, that affect the calculated concentration field. Finally, the amount of metabolized TPZ behaves again as the complementary of the oxygen concentration field.

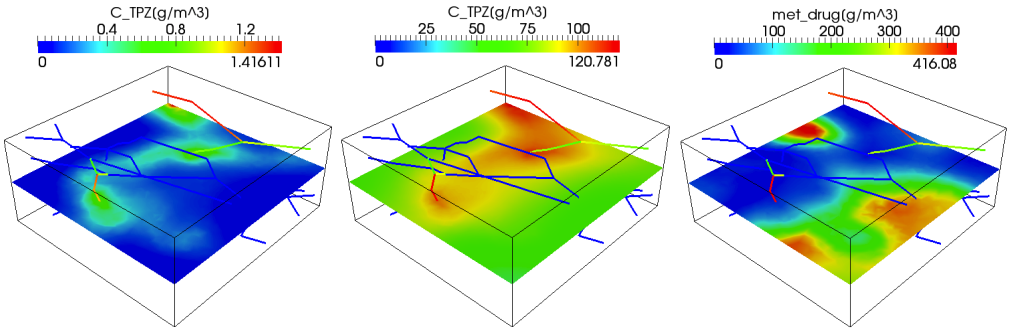

Figure 5.4: *TPZ concentration maps at 20 seconds and 20 minutes after starting nanoparticle release (left and central panels). On the right we show the metabolized drug after 20 minutes. Robin boundary conditions are used in all cases.*

5.3.4 Comparison of TPZ delivery from bolus and nanoparticle injection

Our main objective is the comparison of these two modalities to deliver drug to a tumor. In particular, the proposed model will enable us to compare how the concentration of delivered drug varies in space and time for the two cases. We also point out that, although the delivery pathway is different, the comparisons refer to the same amount of drug injected into the system.

In Figure 5.5 we visualize the TPZ concentration maps in the two cases, reported at 20 minutes, 40 minutes and at a final points comparable to the time at which there will be no longer drug to be delivered to the tissue. The magnitude of the end time point may differ in bolus or nanoparticle injection. The first time point (20 minutes) corresponds to the instant when the injection of drug or particles into the vessels is turned off. The analysis of the results reveals some differences since the beginning of the delivery process. The drug concentration in the case of nanoparticle delivery is larger than the one of bolus delivery at all time points and the discrepancy increases with time.

Figure 5.5 also shows that the concentration of TPZ delivered from bolus injection rapidly vanishes after the injection is switched off. At 40 minutes after the injection has started, there is only a negligible trace of TPZ in the tissue, while after 3 hours the drug has completely vanished. This is clearly due to drug metabolization. Surprisingly, TPZ drug concentration from bolus delivery is also lower at the first time point. The superior performance of the nanoparticle delivery system on the short time scale can be justified by the role of nanoparticle adhesion. This effect helps to harvest drug from the blood stream and to store it on the arterial walls. As a result drug may be delivered in higher concentrations to the interstitial volume and at the same time a lower fraction of the injected drug is washed away by the blood stream leaving the tissue sample.

In addition, the release rate from nanoparticles is more persistent. Drug will be delivered to the tissue over a period of time that is significantly longer than 20 minutes. This is due to the nanoparticle matrix, which represents a diffusional barrier to the release of drug into the tissue. In this case, drug delivery and metabolization nearly balance, because the TPZ concentration in the interstitial volume slowly decreases for a period of almost one day. This interpretation is strengthened by visualizing the time-

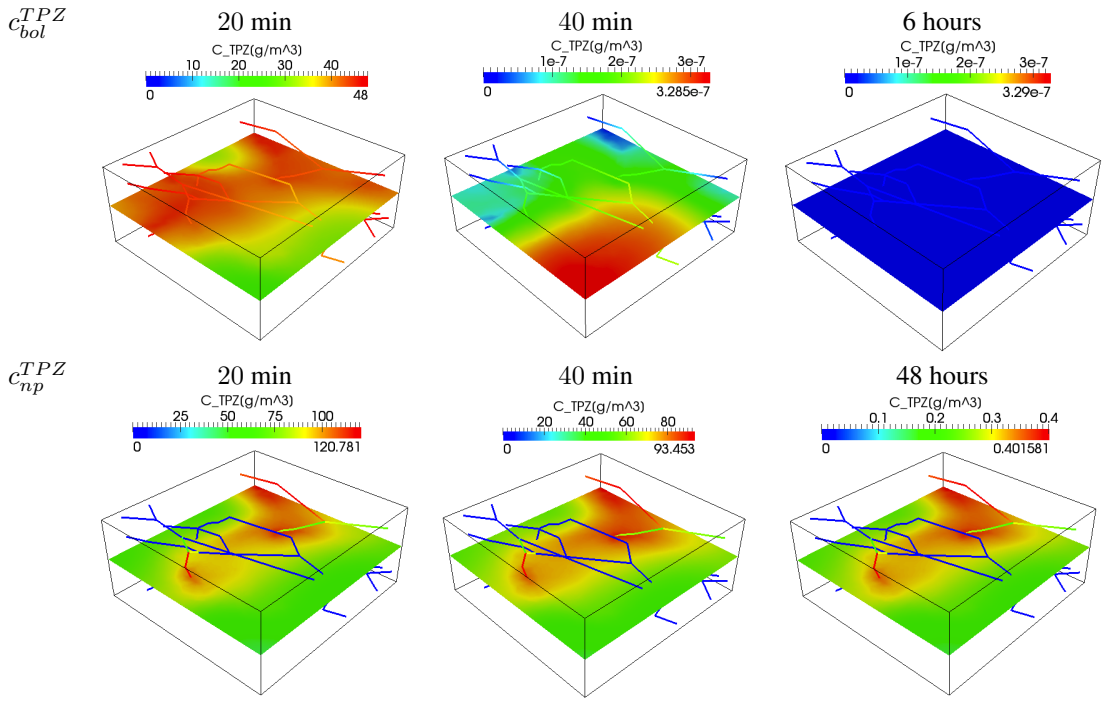

Figure 5.5: *Comparison of TPZ concentrations released from bolus injection (subscript bol) and nanoparticle injection (subscript np).*

course of the total amount of drug available in the tissue, namely the volumetric integral of the TPZ concentration. The results, shown in Figure 5.6, further highlight the inefficiency of drug bolus delivery when compared to drug delivery from nanoparticles.

Bolus injection turns out to be a sub-optimal delivery strategies for two reasons. On one hand, tissue drug concentration rapidly reaches a plateau, much before the final injection time. The drug injected during this plateau phase is more likely to be washed out by the blood stream. On the other hand, bolus injection system lacks any buffer mechanism. Once injection is switched off, drug levels rapidly decrease. In comparison, the nanoparticle delivery system features two significant advantages. First of all, the particle adhesion mechanism allows for the accumulation of drug on the capillary walls. Secondly, the presence of particles decorating the capillary walls ensures a persistent drug release rate after that particle injection has stopped.

The profiles of TPZ concentration have a direct impact on the quantity of metabolized drug. The maps of metabolized drug are shown in Figure 5.7. We observe that these maps look alike in all reported cases. This similarity confirms the dominant role of oxygen concentration to selectively activate the drug metabolization. However, the magnitude changes drastically from case to case. Since for the bolus delivery mode the drug supply to the tissue stops at 20 minutes, the amount of metabolized drug remains almost constant after this time. In contrast, the buffer effect provided by the adhered nanoparticles allows to achieve a significant increase of metabolized drug over time. After 48 hours, the magnitude of metabolized TPZ from nanoparticle injection is almost 20 fold larger than in the case of bolus injection.

Finally, we compare the cell surviving fractions (SF) calculated from bolus and

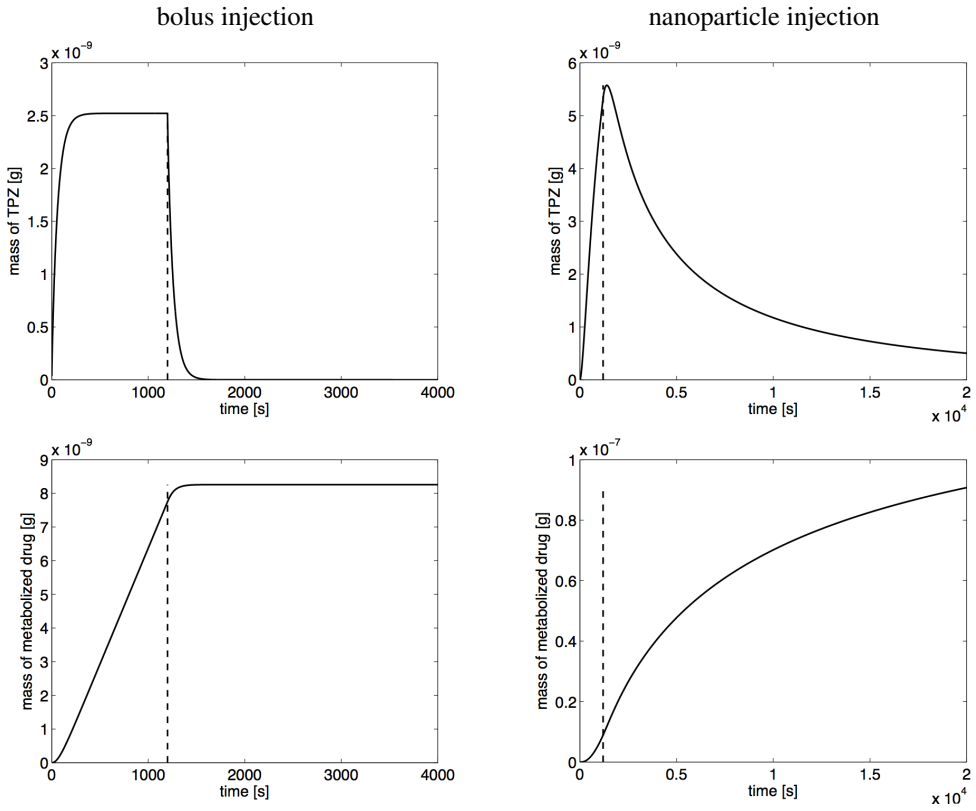

Figure 5.6: *Comparison of systemic and nanoparticle release timecourses. The variation of* $\int_\Omega c_t^{tpz}$ *and* $\overline{M}^{tpz}$ *over time is visualized. The red line marks the time at which the injection of drug or particles into the vessels is stopped.*

nanoparticle injection. The cell surviving fraction depends on space and time, but also on the oxygen availability. To selectively attack tumor mass, TPZ it targeted to treat hypoxic tissue. For this reason, it is convenient to plot the dependence of SF on oxygen partial pressure. This visualization is shown in Figure 5.8. The points of this diagram correspond to the nodes of the computational grid in the interstitial volume, denoted with $\boldsymbol{x}_i$. For each node, we extract the value of oxygen concentration and surviving fraction, at the final time,

$$(t = T, \boldsymbol{x}_i) \rightarrow c_t^{ox}(t = T, \boldsymbol{x}_i),\ SF(t = T, \boldsymbol{x}_i).$$

Then, in the diagrams of Figure 5.8 the surviving fraction is plotted with respect to the corresponding oxygen concentration, while the spatial information is lost. As expected, SF sharply decreases for low oxygen concentrations, confirming that TPZ is able to selectively target hypoxic regions. The nanoparticle delivery mode results to be more effective also with respect to this indicator. On a short time scale, equivalent to the injection time, the efficacy of the two treatments is comparable and not particularly satisfactory because more than 50% of the cells still survive in hypoxic regions. While the situation is almost unchanged for longer time scales in the case of bolus delivery, the performance significantly improves for nanoparticles on the time scale of 48 hours. In fact, we observe that in the regions of tissue exposed to oxygen partial pressure lower

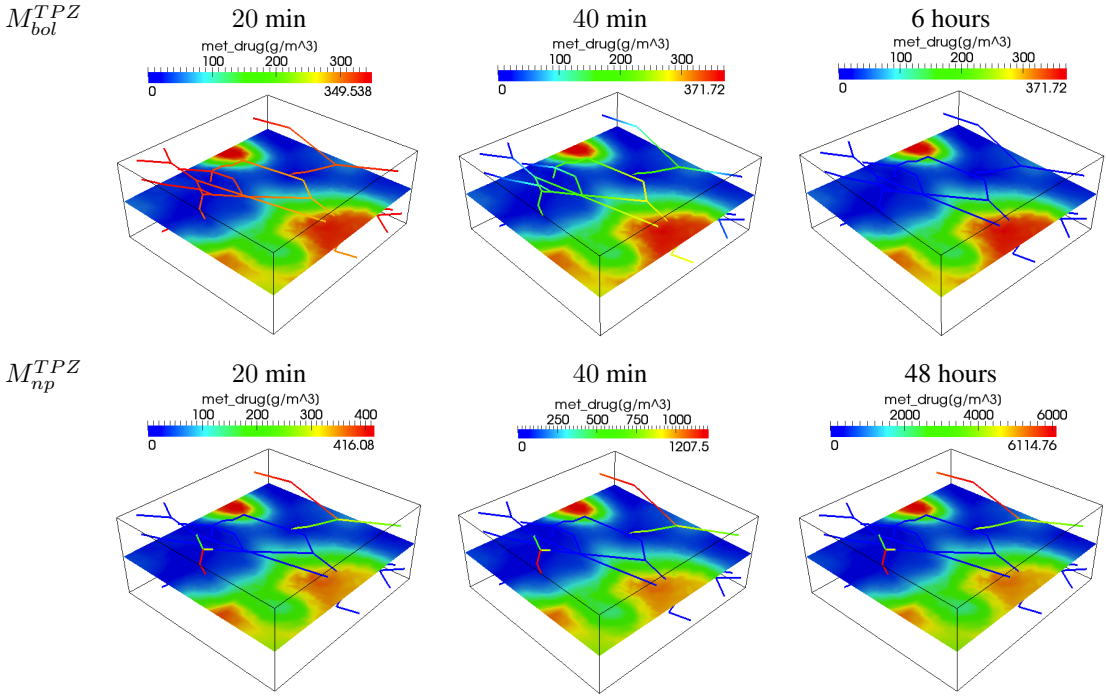

Figure 5.7: *Comparison of metabolized TPZ released from bolus injection (subscript bol) and nanoparticle injection (subscript np).*

than 10 mmHg, more than 70% of cells are killed by the drug. A slight drawback of this type of treatment can be detected looking at the distribution of the points. The dispersion of the point cloud increases and the slope of the underlying curve decreases with respect to the other plots. This suggests that the action of TPZ becomes less selective to target cells exposed to low oxygen concentration.

5.4 Conclusions

In this chapter we have developed a model capable to simulate the spatio-temporal evolution of drugs delivered to a tumor mass. The analysis is performed at the microscale, where the fundamental physics at the basis of flow and transport can be directly applied. We have used the model to compare bolus and nanoparticle injection for delivering chemotherapy agents. The model provides different insights on treatment performance, based on the analysis of specific quantitative indicators, such as the cell surviving fraction. On one hand, we show that bolus injection does not ensure an optimal delivery. Drug washout by the blood stream and saturation of the concentration level in the interstitial tissue limit the amount of drug that reaches the malignant cells. On the other hand, we observe that a more controlled drug delivery process, achieved by means of nanoparticle injection, helps to override the previous limitations. The model captures an expected trend that is confirmed by several studies [2, 16].

Besides these encouraging results, the model is prone to several improvements. One of the main limitations of the study consists to consider a tumor as a static environment. This assumption may be questionable, especially over the characteristic time scales of

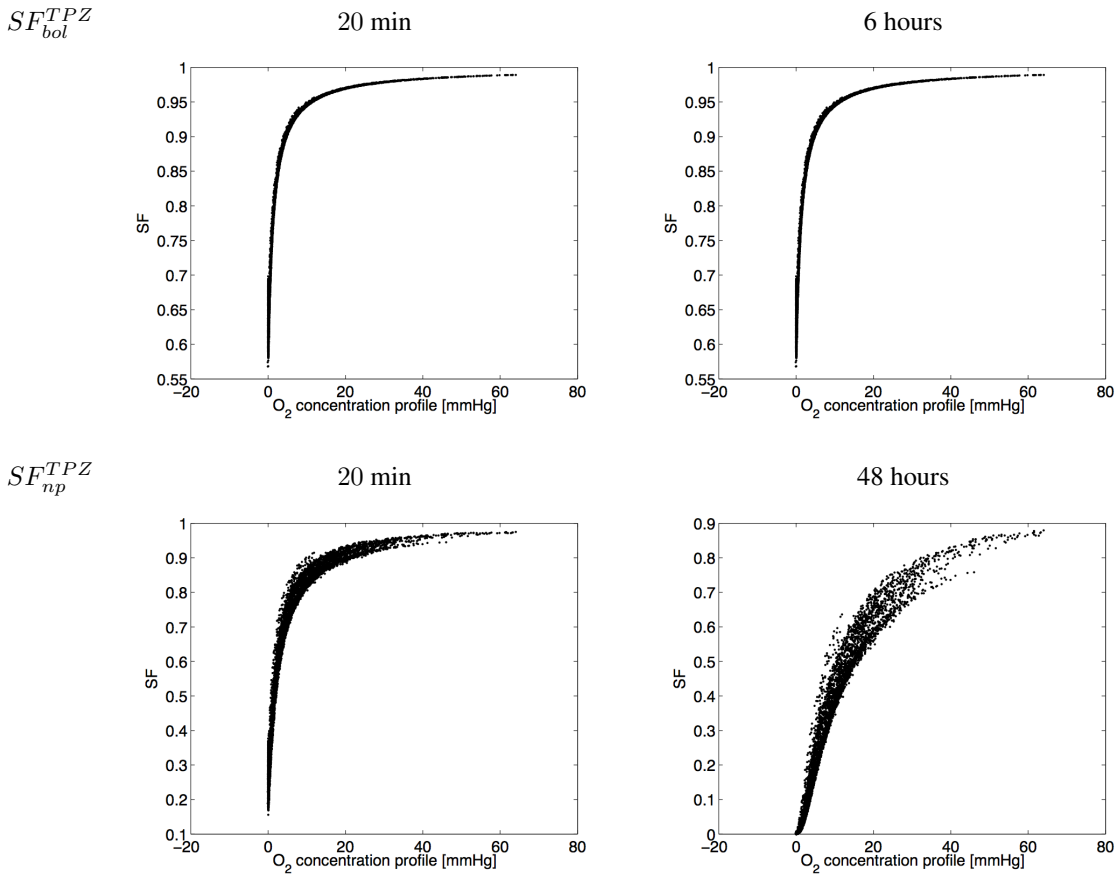

Figure 5.8: *Comparison of cell surviving fraction (SF) when TPZ released from bolus injection (subscript bol) and nanoparticle injection (subscript np).*

controlled delivery. Future developments of the model will indeed consider the tumor microenvironment as a dynamic system where angiogenesis, cell proliferation and drug treatment constantly interact. As discussed in [46, 54], the evolution of the tumor environment also affects how nanoparticles adhere to the capillary walls.

Further ramifications of this study will also be devoted to develop specific models for different types of cancer. We expect that tumors developing in the brain, breast, liver or lungs may feature significant differences in their transport properties. The physiology of these organs as well as available metrics for the transport properties of different types of cancer will be combined to set up specific variants of the model for different tumors.

Another line of development moves along with the rapid technological progress in designing different nanovectors to efficiently and selectively deliver drugs [40, 98, 110]. Indeed, the model can be refined with respect to the drug delivery platform. In addition to the currently adopted model for rigid nanoporous particles, we would like to build up a library of delivery models to account for liposomes and other drug carriers. Finally, we believe that the proposed modelling and computational approach may effectively complement, at a coarser scale of analysis, the extraordinary results that molecular dynamics methods are obtaining to boost the discovery and testing of new drugs [111].

Bibliography

[1] C. Annavarapu, M. Hautefeuille, and J.E. Dolbow. A robust Nitsche's formulation for interface problems. *Computer Methods in Applied Mechanics and Engineering*, 225-228:44–54, 2012.

[2] W. Arap, R. Pasqualini, and E. Ruoslahti. Cancer treatment by targeted drug delivery to tumor vasculature in a mouse model. *Science*, 279(5349):377–380, 1998.

[3] R.F. Ausas, G.C. Buscaglia, and S.R. Idelsohn. A new enrichment space for the treatment of discontinuous pressures in multi-fluid flows. *International Journal for Numerical Methods in Fluids*, 70(7):829–850, 2012.

[4] I. Babuška and J.M. Melenk. The partition of unity method. *International Journal for Numerical Methods in Engineering*, 40(4):727–758, 1997.

[5] M. Barzegar-Jalali, K. Adibkia, H. Valizadeh, M.R.S. Shadbad, A. Nokhodchi, Y. Omidi, G. Mohammadi, S.H. Nezhadi, and M. Hasan. Kinetic analysis of drug release from nanoparticles. *Journal of Pharmacy and Pharmaceutical Sciences*, 11(1):167–177, 2008.

[6] L.T. Baxter and R.K. Jain. Transport of fluid and macromolecules in tumors. i. role of interstitial pressure and convection. *Microvascular Research*, 37(1):77–104, 1989.

[7] L.T. Baxter and R.K. Jain. Transport of fluid and macromolecules in tumors ii. role of heterogeneous perfusion and lymphatics. *Microvascular Research*, 40(2):246–263, 1990.

[8] L.T. Baxter and R.K. Jain. Transport of fluid and macromolecules in tumors. iii. role of binding and metabolism. *Microvascular Research*, 41(1):5–23, 1991.

[9] L.T. Baxter and R.K. Jain. Transport of fluid and macromolecules in tumors: Iv. a microscopic model of the perivascular distribution. *Microvascular Research*, 41(2):252–272, 1991.

[10] R. Becker, E. Burman, and P. Hansbo. A Nitsche extended finite element method for incompressible elasticity with discontinuous modulus of elasticity. *Computer Methods in Applied Mechanics and Engineering*, 198(41-44):3352–3360, 2009.

[11] T. Belytschko and T. Black. Elastic crack growth in finite elements with minimal remeshing. *International Journal for Numerical Methods in Engineering*, 45(5):601–620, 1999. cited By (since 1996)1128.

[12] T.R. Blake and J.F. Gross. Analysis of coupled intra- and extraluminal flows for single and multiple capillaries. *Mathematical Biosciences*, 59(2):173–206, 1982.

[13] S. C. Brenner and L. R. Scott. 2008.

[14] F. Brezzi and M. Fortin. *Mixed and hybrid finite element methods*, volume 15 of *Springer Series in Computational Mathematics*. Springer-Verlag, New York, 1991.

[15] F. Brezzi and J. Pitkäranta. On the stabilization of finite element approximations of the Stokes equations. In *Efficient solutions of elliptic systems (Kiel, 1984)*, volume 10 of *Notes Numer. Fluid Mech.*, pages 11–19. Vieweg, Braunschweig, 1984.

[16] I. Brigger, C. Dubernet, and P. Couvreur. Nanoparticles in cancer therapy and diagnosis. *Advanced Drug Delivery Reviews*, 54(5):631–651, 2002.

[17] E. Burman. Ghost penalty [la pénalisation fantôme]. *Comptes Rendus Mathematique*, 348(21-22):1217–1220, 2010.

[18] E. Burman and P. Hansbo. Fictitious domain methods using cut elements : Iii. a stabilized Nitsche method for Stokes' problem. Technical Report 2011:06, School of Engineering, Jönköping University, JTH, Mechanical Engineering, 2011.

[19] E. Burman and P. Hansbo. Fictitious domain finite element methods using cut elements: Ii. a stabilized Nitsche method. *Applied Numerical Mathematics*, 62(4):328–341, 2012.

[20] Erik Burman and Peter Hansbo. Fictitious domain finite element methods using cut elements: II. a stabilized nitsche method. *Applied Numerical Mathematics*, In Press, Corrected Proof:–, 2011.

[21] Erik Burman and Paolo Zunino. A domain decomposition method based on weighted interior penalties for advection-diffusion-reaction problems. *SIAM J. Numer. Anal.*, 44(4):1612–1638 (electronic), 2006.

[22] Erik Burman and Paolo Zunino. Numerical approximation of large contrast problems with the unfitted nitsche method. Technical report, MOX, Department of Mathematics, Politecnico di Milano, 2011.

[23] G.C. Buscaglia and A. Agouzal. Interpolation estimate for a finite-element space with embedded discontinuities. *IMA Journal of Numerical Analysis*, 32(2):672–686, 2012.

[24] S. Canic, D. Lamponi, A. Mikelić, and J. Tambaca. Self-consistent effective equations modeling blood flow in medium-to-large compliant arteries. *Multiscale Modeling and Simulation*, 3(3):559–596, 2005.

[25] P. Carmeliet and R.K. Jain. Angiogenesis in cancer and other diseases. *Nature*, 407(6801):249–257, 2000.

[26] Formaggia L. Iori G. F. Scotti A. Cattaneo, L. and P. Zunino. Stabilized extended finite elements for the approximation of saddle point problems with unfitted interfaces. Technical report, MOX, Department of Mathematics, Politecnico di Milano, 25/2013.

[27] L. Cattaneo and P. Zunino. A computational model of drug delivery through microcirculation to compare different tumor treatment options. 2013.

[28] L. Cattaneo and P. Zunino. Computational models for fluid exchange between microcirculation and tissue interstitium. *Networks and Heterogeneous Media*, 2013. to appear. Available as MOX Report 25/2013.

[29] S.J. Chapman, R.J. Shipley, and R. Jawad. Multiscale modeling of fluid transport in tumors. *Bulletin of Mathematical Biology*, 70(8):2334–2357, 2008.

[30] Ramon Codina and Joan Baiges. Approximate imposition of boundary conditions in immersed boundary methods. *Internat. J. Numer. Methods Engrg.*, 80(11):1379–1405, 2009.

[31] F.E. Curry. *Mechanics and thermodynamics of transcapillary exchange*, chapter 8, pages 309–374. Hand Book of Physiology. Am. Physiol. Soc., Bethesda., 1984.

[32] C. D'Angelo. *Multiscale modeling of metabolism and transport phenomena in living tissues*. Phd thesis, 2007.

[33] C. D'Angelo. Finite element approximation of elliptic problems with dirac measure terms in weighted spaces: Applications to one- and three-dimensional coupled problems. *SIAM Journal on Numerical Analysis*, 50(1):194–215, 2012.

[34] C. D'Angelo and A. Quarteroni. On the coupling of 1D and 3D diffusion-reaction equations. Application to tissue perfusion problems. *Math. Models Methods Appl. Sci.*, 18(8):1481–1504, 2008.

[35] C. D'Angelo and P. Zunino. Robust numerical approximation of coupled Stokes' and Darcy's flows applied to vascular hemodynamics and biochemical transport. *ESAIM: Mathematical Modelling and Numerical Analysis*, 45(3):447–476, 2011.

[36] Carlo D'Angelo and Anna Scotti. A mixed finite element method for darcy flow in fractured porous media with non-matching grids. Technical report, MOX, Department of Mathematics, Politecnico di Milano, 2010.

[37] P. Decuzzi and M. Ferrari. The adhesive strength of non-spherical particles mediated by specific interactions. *Biomaterials*, 27(30):5307–5314, 2006.

[38] John Dolbow and Isaac Harari. An efficient finite element method for embedded interface problems. *Internat. J. Numer. Methods Engrg.*, 78(2):229–252, 2009.

[39] John Dolbow, Nicolas Moës, and Ted Belytschko. An extended finite element method for modeling crack growth with frictional contact. *Comput. Methods Appl. Mech. Engrg.*, 190(51-52):6825–6846, 2001.

[40] D.C. Drummond, O. Meyer, K. Hong, D.B. Kirpotin, and D. Papahadjopoulos. Optimizing liposomes for delivery of chemotherapeutic agents to solid tumors. *Pharmacological Reviews*, 51(4):691–743, 1999.

[41] Maksymilian Dryja. On discontinuous Galerkin methods for elliptic problems with discontinuous coefficients. *Comput. Methods Appl. Math.*, 3(1):76–85 (electronic), 2003. Dedicated to Raytcho Lazarov.

[42] A. Ern and J. Guermond. *Theory and practice of finite elements*, volume 159 of *Applied Mathematical Sciences*. Springer-Verlag, New York, 2004.

[43] Alexandre Ern and Jean-Luc Guermond. *Theory and practice of finite elements*, volume 159 of *Applied Mathematical Sciences*. Springer-Verlag, New York, 2004.

[44] A. Farina, A. Fasano, and J. Mizerski. A new model for blood flow in fenestrated capillaries with application to ultrafiltration in kidney glomeruli. *submitted.*

[45] D.A. Fedosov, G.E. Karniadakis, and B. Caswell. Steady shear rheometry of dissipative particle dynamics models of polymer fluids in reverse poiseuille flow. *Journal of Chemical Physics*, 132(14), 2010.

[46] M. Ferrari. Frontiers in cancer nanomedicine: Directing mass transport through biological barriers. *Trends in Biotechnology*, 28(4):181–188, 2010.

[47] S. Ferrati, A. MacK, C. Chiappini, X. Liu, A.J. Bean, M. Ferrari, and R.E. Serda. Intracellular trafficking of silicon particles and logic-embedded vectors. *Nanoscale*, 2(8):1512–1520, 2010.

[48] Silvia Ferrati, Sabeel Shamsudeen, Huw D. Summers, Paul Rees, James V. A. Abbey, Jeff Schmulen, Xuewu Liu, Stephen T. C. Wong, Andrew J. Bean, Mauro Ferrari, and Rita E. Serda. Inter-endothelial transport of microvectors using cellular shuttles and tunneling nanotubes. *Small*, 8(20):3151–3160, 2012.

[49] J. Fish and T. Belytschko. Elements with embedded localization zones for large deformation problems. *Computers and Structures*, 30(1-2):247–256, 1988.

[50] G.J. Fleischman, T.W. Secomb, and J.F. Gross. The interaction of extravascular pressure fields and fluid exchange in capillary networks. *Mathematical Biosciences*, 82(2):141–151, 1986.

[51] G.J. Flieschman, T.W. Secomb, and J.F. Gross. Effect of extravascular pressure gradients on capillary fluid exchange. *Mathematical Biosciences*, 81(2):145–164, 1986.

[52] L. Formaggia, D. Lamponi, and A. Quarteroni. One-dimensional models for blood flow in arteries. *Journal of Engineering Mathematics*, 47(3-4):251–276, 2003.

[53] Luca Formaggia, Alfio Quarteroni, and Alessandro Veneziani. Multiscale models of the vascular system. In *Cardiovascular Mathematics*, volume 1 of *MS&A. Model. Simul. Appl.*, pages 395–446. Springer Italia, Milan, 2009.

[54] H.B. Frieboes, M. Wu, J. Lowengrub, P. Decuzzi, and V. Cristini. A computational model for predicting nanoparticle accumulation in tumor vasculature. *PLoS ONE*, 8(2), 2013.

[55] M.H. Friedman. *Principles and Models of Biological Transport*. Springer New York, 2008.

[56] T.-P. Fries. A corrected xfem approximation without problems in blending elements. *International Journal for Numerical Methods in Engineering*, 75(5):503–532, 2008.

[57] T.-P. Fries and T. Belytschko. The extended/generalized finite element method: An overview of the method and its applications. *International Journal for Numerical Methods in Engineering*, 84(3):253–304, 2010. cited By (since 1996)97.

[58] A. Gerstenberger and W. A. Wall. An embedded Dirichlet formulation for 3D continua. *Internat. J. Numer. Methods Engrg.*, 82(5):537–563, 2010.

[59] V. Girault and P. Raviart. *Finite element methods for Navier-Stokes equations*, volume 5 of *Springer Series in Computational Mathematics*. Springer-Verlag, Berlin, 1986. Theory and algorithms.

[60] S. Gross and A. Reusken. *Numerical methods for two-phase incompressible flows*, volume 40 of *Springer Series in Computational Mathematics*. Springer-Verlag, Berlin, 2011.

[61] Sven Groß and Arnold Reusken. An extended pressure finite element space for two-phase incompressible flows with surface tension. *J. Comput. Phys.*, 224(1):40–58, 2007.

[62] D. Hanahan and R.A. Weinberg. The hallmarks of cancer. *Cell*, 100(1):57–70, 2000.

[63] A. Hansbo and P. Hansbo. An unfitted finite element method, based on Nitsche's method, for elliptic interface problems. *Computer Methods in Applied Mechanics and Engineering*, 191(47-48):5537–5552, 2002.

[64] Anita Hansbo and Peter Hansbo. A finite element method for the simulation of strong and weak discontinuities in solid mechanics. *Comput. Methods Appl. Mech. Engrg.*, 193(33-35):3523–3540, 2004.

[65] P. Hansbo, M. G Larson, and S. Zahedi. A Nitsche method for a Stokes interface problem. *arXiv preprint arXiv:1205.5684*, 2012.

[66] Isaac Harari and John Dolbow. Analysis of an efficient finite element method for embedded interface problems. *Comput. Mech.*, 46(1):205–211, 2010.

[67] F. Hecht. New development in freefem++. *J. Numer. Math.*, 20(3-4):251–265, 2012.

[68] K.O. Hicks, F.B. Pruijn, T.W. Secomb, M.P. Hay, R. Hsu, J.M. Brown, W.A. Denny, M.W. Dewhirst, and W.R. Wilson. Use of three-dimensional tissue cultures to model extravascular transport and predict in vivo activity of hypoxia-targeted anticancer drugs. *Journal of the National Cancer Institute*, 98(16):1118–1128, 2006.

[69] S.S. Hossain, T.J.R. Hughes, and P. Decuzzi. Vascular deposition patterns for nanoparticles in an inflamed patient-specific arterial tree. *Biomechanics and Modeling in Mechanobiology*, pages 1–13, 2013.

[70] S.S. Hossain, Y. Zhang, X. Liang, F. Hussain, M. Ferrari, T.J. Hughes, and P. Decuzzi. In silico vascular modeling for personalized nanoparticle delivery. *Nanomedicine*, 8(3):343–357, 2013.

[71] M. Intaglietta, N.R. Silverman, and W.R. Tompkins. Capillary flow velocity measurements in vivo and in situ by television methods. *Microvascular Research*, 10(2):165–179, 1975.

[72] R.K. Jain, R.T. Tong, and L.L. Munn. Effect of vascular normalization by antiangiogenic therapy on interstitial hypertension, peritumor edema, and lymphatic metastasis: Insights from a mathematical model. *Cancer Research*, 67(6):2729–2735, 2007.

[73] T. Koeppl and B. Wohlmuth. Optimal a priori error estimates for an elliptic problem with Dirac right-hand side. *SIAM Journal on Numerical Analysis*, 2013.

[74] H. Lei, D.A. Fedosov, B. Caswell, and G.E. Karniadakis. Blood flow in small tubes: Quantifying the transition to the non-continuum regime. *Journal of Fluid Mechanics*, 722:214–239, 2013.

[75] M. Lesinigo, C. D'Angelo, and A. Quarteroni. A multiscale darcy-brinkman model for fluid flow in fractured porous media. *Numerische Mathematik*, 117(4):717–752, 2011.

[76] J.R. Less, T.C. Skalak, E.M. Sevick, and R.K. Jain. Microvascular architecture in a mammary carcinoma: Branching patterns and vessel dimensions. *Cancer Research*, 51(1):265–273, 1991.

[77] W.K. Liu, D.W. Kim, and S. Tang. Mathematical foundations of the immersed finite element method. *Computational Mechanics*, 39(3):211–222, 2007.

[78] W.K. Liu, Y. Liu, D. Farrell, L. Zhang, X.S. Wang, Y. Fukui, N. Patankar, Y. Zhang, C. Bajaj, J. Lee, J. Hong, X. Chen, and H. Hsu. Immersed finite element method and its applications to biological systems. *Computer Methods in Applied Mechanics and Engineering*, 195(13-16):1722–1749, 2006.

[79] Y. Liu and W.K. Liu. Rheology of red blood cell aggregation by computer simulation. *Journal of Computational Physics*, 220(1):139–154, 2006.

[80] Y. Liu, L. Zhang, X. Wang, and W.K. Liu. Coupling of navier-stokes equations with protein molecular dynamics and its application to hemodynamics. *International Journal for Numerical Methods in Fluids*, 46(12):1237–1252, 2004.

[81] Panos Macheras and Athanassios Iliadis. *Modeling in biopharmaceutics, pharmacokinetics, and pharmacodynamics*, volume 30 of *Interdisciplinary Applied Mathematics*. Springer, New York, 2006. Homogeneous and heterogeneous approaches.

[82] J.M. Melenk and I. Babuška. The partition of unity finite element method: Basic theory and applications. *Computer Methods in Applied Mechanics and Engineering*, 139(1-4):289–314, 1996.

[83] N. Moës, J. Dolbow, and T. Belytschko. A finite element method for crack growth without remeshing. *International Journal for Numerical Methods in Engineering*, 46(1):131–150, 1999.

[84] Nicolas Moës, Eric Béchet, and Matthieu Tourbier. Imposing Dirichlet boundary conditions in the extended finite element method. *Internat. J. Numer. Methods Engrg.*, 67(12):1641–1669, 2006.

[85] J.A. Moore and C.R. Ethier. Oxygen mass transfer calculations in large arteries. *Journal of Biomechanical Engineering*, 119(4):469–475, 1997.

[86] L. Mu and S.S. Feng. A novel controlled release formulation for the anticancer drug paclitaxel (taxol®): Plga nanoparticles containing vitamin e tpgs. *Journal of Controlled Release*, 86(1):33–48, 2003.

[87] J. Nitsche. Über ein variationsprinzip zur lösung von dirichlet-problemen bei verwendung von teilräumen, die keinen randbedingungen unterworfen sind. *Abhandlungen aus dem Mathematischen Seminar der Universität Hamburg*, 36(1):9–15, 1971.

[88] Joaquim Peiró and Alessandro Veneziani. Reduced models of the cardiovascular system. In *Cardiovascular Mathematics*, volume 1 of *MS&A. Model. Simul. Appl.*, pages 347–394. Springer Italia, Milan, 2009.

[89] Karl Perktold, Martin Prosi, and Paolo Zunino. Mathematical models of mass transfer in the vascular walls. In *Cardiovascular mathematics*, volume 1 of *MS&A. Model. Simul. Appl.*, pages 243–278. Springer Italia, Milan, 2009.

[90] Charles S Peskin. The immersed boundary method. *Acta numerica*, 11(0):479–517, 2002.

[91] A. Quarteroni and A. Valli. *Numerical Approximation of Partial Differential Equations*. Springer-Verlag, Berlin, Heidelberg, New York, 1994.

[92] Alfio Quarteroni, Riccardo Sacco, and Fausto Saleri. *Numerical mathematics*, volume 37 of *Texts in Applied Mathematics*. Springer-Verlag, New York, 2000.

[93] Y. Renard and J. Pommier. *Getfem++: a generic finite element library in c++, version 4.2 (2012)*. http://download.gna.org/getfem/html/homepage/.

[94] Arnold Reusken. Analysis of an extended pressure finite element space for two-phase incompressible flows. *Comput. Vis. Sci.*, 11(4-6):293–305, 2008.

[95] Arnold Reusken and Patrick Esser. Analysis of time discretization methods for stokes equations with a nonsmooth forcing term. *Numerische Mathematik*, pages 1–27, 2013.

[96] A.M. Robertson and A. Sequeira. A director theory approach for modeling blood flow in the arterial system: An alternative to classical id models. *Mathematical Models and Methods in Applied Sciences*, 15(6):871–906, 2005.

[97] Anne M. Robertson, Adélia Sequeira, and Robert G. Owens. Rheological models for blood. In *Cardiovascular Mathematics*, volume 1 of *MS&A. Model. Simul. Appl.*, pages 211–241. Springer Italia, Milan, 2009.

[98] J.H. Sakamoto, A.L. van de Ven, B. Godin, E. Blanco, R.E. Serda, A. Grattoni, A. Ziemys, A. Bouamrani, T. Hu, S.I. Ranganathan, E. De Rosa, J.O. Martinez, C.A. Smid, R.M. Buchanan, S.-Y. Lee, S. Srinivasan, M. Landry, A. Meyn, E. Tasciotti, X. Liu, P. Decuzzi, and M. Ferrari. Enabling individualized therapy through nanotechnology. *Pharmacological Research*, 62(2):57–89, 2010.

[99] H. Sauerland and T.-P. Fries. The extended finite element method for two-phase and free-surface flows: A systematic study. *Journal of Computational Physics*, 230(9):3369–3390, 2011.

[100] Timothy W. Secomb, Axel R. Pries, Peter Gaehtgens, and Joseph F. Gross. Theoretical and experimental analysis of hematocrit distribution in microcirculatory networks. In Jen-Shih Lee and Thomas C. Skalak, editors, *Microvascular Mechanics*, pages 39–49. Springer New York, 1989.

[101] T.W. Secomb. *Microvascular network structures*. physiology.arizona.edu/people/secomb.

[102] T.W. Secomb, R. Hsu, R.D. Braun, J.R. Ross, J.F. Gross, and M.W. Dewhirst. Theoretical simulation of oxygen transport to tumors by three-dimensional networks of microvessels. *Advances in Experimental Medicine and Biology*, 454:629–634, 1998.

[103] T.W. Secomb, R. Hsu, E.Y.H. Park, and M.W. Dewhirst. Green's function methods for analysis of oxygen delivery to tissue by microvascular networks. *Annals of Biomedical Engineering*, 32(11):1519–1529, 2004.

[104] Rita E. Serda, Jianhua Gu, Rohan C. Bhavane, XueWu Liu, Ciro Chiappini, Paolo Decuzzi, and Mauro Ferrari. The association of silicon microparticles with endothelial cells in drug delivery to the vasculature. *Biomaterials*, 30(13):2440 – 2448, 2009.

[105] R.J. Shipley and S.J. Chapman. Multiscale modelling of fluid and drug transport in vascular tumours. *Bulletin of Mathematical Biology*, 72(6):1464–1491, 2010.

[106] M. Soltani and P. Chen. Numerical modeling of interstitial fluid flow coupled with blood flow through a remodeled solid tumor microvascular network. *PLoS ONE*, 8(6), 2013.

[107] F.S. Sousa, R.F. Ausas, and G.C. Buscaglia. Numerical assessment of stability of interface discontinuous finite element pressure spaces. *Computer Methods in Applied Mechanics and Engineering*, 245-246:63–74, 2012.

[108] Gilbert Strang and George J. Fix. *An analysis of the finite element method*. Prentice-Hall Inc., Englewood Cliffs, N. J., 1973. Prentice-Hall Series in Automatic Computation.

[109] Q. Sun and G.X. Wu. Coupled finite difference and boundary element methods for fluid flow through a vessel with multibranches in tumours. *International Journal for Numerical Methods in Biomedical Engineering*, 29(3):309–331, 2013.

[110] V.P. Torchilin. Recent advances with liposomes as pharmaceutical carriers. *Nature Reviews Drug Discovery*, 4(2):145–160, 2005.

[111] H. van de Waterbeemd and E. Gifford. Admet in silico modelling: Towards prediction paradise? *Nature Reviews Drug Discovery*, 2(3):192–204, 2003.

[112] Mikelić A. Pop I.S. Van Duijn, C.J. and C. Rosier. Effective dispersion equations for reactive flows with dominant péclet and damkohler numbers. *Advances in Chemical Engineering*, 2008.

[113] Colominas I. Vilanova, G. and Gomez H. Capillary networks in tumor angiogenesis: From discrete endothelial cells to phase-field averaged descriptions via isogeometric analysis. *International Journal for Numerical Methods in Biomedical Engineering*, 2013.

[114] X. Wang and W.K. Liu. Extended immersed boundary method using fem and rkpm. *Computer Methods in Applied Mechanics and Engineering*, 193(12-14):1305–1321, 2004.

[115] L. Zhang, A. Gerstenberger, X. Wang, and W.K. Liu. Immersed finite element method. *Computer Methods in Applied Mechanics and Engineering*, 193(21-22):2051–2067, 2004.

[116] A. Zilian and H. Netuzhylov. Hybridized enriched space-time finite element method for analysis of thin-walled structures immersed in generalized newtonian fluids. *Computers and Structures*, 88(21-22):1265–1277, 2010.

[117] P. Zunino. Analysis of backward euler/extended finite element discretization of parabolic problems with moving interfaces. *Computer Methods in Applied Mechanics and Engineering*, 258:152–165, 2013.

[118] P. Zunino, L. Cattaneo, and C.M. Colciago. An unfitted interface penalty method for the numerical approximation of contrast problems. *Applied Numerical Mathematics*, 61(10):1059–1076, 2011.